THE MAGNETO-OPTIC SPECTRA
OF
BISMUTH-SUBSTITUTED IRON GARNETS

by

Gary Alfred Allen

B.S. Physics,
Worcester Polytechnic Institute, 1987.

Submitted to the Department of Physics in
Partial Fulfillment of the Requirements
for the Degree of

Doctor of Philosophy

at the
Massachusetts Institute of Technology
September 1994

Signature of Author_____
Department of Physics
August 31, 1994

Certified by_____
Prof. Mildred S. Dresselhaus
Thesis Advisor

Accepted by_____
Prof. George F. Koster
Chairman, Department of Physics Graduate Committee

THE MAGNETO-OPTIC SPECTRA OF BISMUTH-SUBSTITUTED IRON GARNETS

by

Gary Alfred Allen

Submitted to the Department of Physics on August 31, 1994 in partial fulfillment of the requirements for the Degree of Doctor of Philosophy

ABSTRACT

The spectra for the dielectric constant, Kerr rotation and Kerr ellipticity between 2 eV and 4 eV for bismuth-substituted yttrium iron garnets investigated. The off-diagonal elements of the dielectric tensor are calculated. It is determined that substitution of bismuth into iron garnets increases the strength of transitions at 2.85 eV and 3.20 eV in both the diagonal and off-diagonal elements of the dielectric tensor. The off-diagonal elements of yttrium iron garnet are found to be composed entirely of paramagnetic transitions in this region. In contrast, the substitution of bismuth produces diamagnetic transitions at the above mentioned energies. The two-level excited state splittings associated with the diamagnetic transitions are 0.033 eV and 0.055 eV, respectively. A mixing of the excited state of the iron garnets with the ^3P excited state of Bi^{3+} can account for the observed excited state splittings. The mixing percentages are determined to be 1.6% and 2.6%, respectively, for these two transitions. Dilution of the tetrahedral and octahedral sublattices with aluminum and indium reduces the effect of bismuth substitution upon both the diagonal and off-diagonal elements. This reduction is equivalent for materials in which an equal percentage of either of the two sublattices are diluted. It is concluded that the increase in the diagonal and off-diagonal elements caused by bismuth substitution involves the joint population of the two iron sublattices. Based on this observation, the transitions at 2.85 eV and 3.20 eV are interpreted as intersublattice charge-transfer processes.

Thesis Supervisor: Dr. Mildred S. Dresselhaus

Title: Institute Professor of Physics and Electrical Engineering

Acknowledgments

It's two o'clock in the morning and I sit here alone in my office. The time and place have unfortunately occurred often in the last year or two,. And in each of these vigils, there always seems to come a point in the wee hours of the morning when I'll stop and think of the friends I know and or have known. So I suppose there is no more fitting time to write these acknowledgments than now.

I do not present this acknowledgement in any particular order of importance. And I also don't pretend to possess much in the way literary ability. So don't put too much into where your name appears or what I say about you. The one nice thing about this section is that it's the one part of this document that will not be proofread, corrected, reorganized, etc. Where to start? How about the folks most directly responsible for the completion of this work . . . the thesis committee.

I suppose the first to be thanked is Dr. Gerald Dionne. For almost a decade now he has been my mentor. The subject of this thesis developed out of his own interest, vision and effort and I am indebted to him for allowing me to be a part of it. I am grateful also to Dr. Hans Jenssen who showed some of that Viking spirit of adventure and chose to advise me in an area on the fringe of his field. Your support and generosity have been appreciated and invaluable. We even got to "battle the forces of evil" together, too, and I think we did pretty well if, I do say so. I am also honored to have been one of the "adopted orphans" of Prof. Mildred Dresselhaus. Your caring and kindness as well as your obvious love of science have made a lasting impression on me and have shown me that there are kind hearts in science. And thanks goes also to Dr. Simon Foner, primarily for his tolerance of some graduate student calling out of the blue every now and then to drag him over to building 13.

A special thanks must go to Prof. Jerald Weiss. Over the last decade you have indistinguishably been both mentor and friend and you have seen me grow from high school graduate to a Doctor of Science. Your love of science, your kind heart, your generous hospitality and your sense of humor of influenced my growth as both a scientist and as a human being.

Additional thanks must also go to Dr. Matthew G. Kemp. Your insight into the nature of the world is unrivaled. Your engaging intellectual conversations have often given me new perspectives on my research and on science as a whole . . . not to mention some good laughs.

I was told upon entering college that some of my strongest friendships were to be with the friends I made in college. This logically implies that even stronger friendships will result from graduate school. This hypothesis was scientifically proven during my graduate school career. I speak of the strong friendships I am fortunate to have with Jason Puchalla, Stefan Anderson and Ken Dinndorf. I don't know what it is about Minnesota (The soil? The air? The climate?), but the state produces some of the finest human beings made in the US of A. The three of you, over the course of my career at MIT, have given me some of my fondest memories at MIT and anywhere. Jason, you have gone half way across the country to finish your thesis and I wish you well. Stefan and Ken, you and Jenny and Linda have been the dearest friends imaginable to Debbie and myself. We're sad to see you go, but, we're happy that you have moved on in your life.

I have a new rule. No graduate physics thesis should be accepted without an acknowledgement of Peggy Berkowitz. Peggy is best described as the Den Mother of the graduate physics students. I, unfortunately, first got to know her only because of all the paperwork she constantly had to remind me to do at the beginning of each semester. I have grown, as many of my fellow students have, to rely on her warmth, kindness and caring. You have always been there for us and we thank you. You have made are lives here so much more enjoyable and pleasant.

I made a New Year's resolution last year to meet all those people you see in the hallway but don't say hello too. While I wished I had also kept some of my other resolutions, I did keep this one. As a result, I have seen my circle of friends increase and go beyond the boundaries of just the graduate student body. The majority of these new friends come from the Development Office. I thank you all for adopting me into your gang. You're all a great bunch of people and have given me a glimpse of what it's like to have "a real life". I have always enjoyed your company and hallway chats and thank you all for your friendship. You have made my days here much more enjoyable.

In particular, I am thankful for the friendship of Terri Flannery. You were a good friend at a time when the rest of my friends were leaving me. Try to remember the good times.

I thank, also, Traci Trotzer and Sally Gatewood for putting up with my dropping-ins from time to time. Your loss was also a loss for all of MIT. I hope that I've done

something along the way that made it easier for you. That way I can pay you back for your kindness. Let's stay in touch.

A special thank you goes to Mary Rowe. I am grateful for you and Dr. Wrighton's support in getting me out of a bad situation. Most of all I'd like to thank you for being my Guardian Angel here at MIT and giving me a untiring and sympathetic ear to gripe too.

Ooops. Almost forgot them wild Sengupta's. Scientifically, Louise and Somnath have been a great benefit. The experimental apparatus used in this work was suggested by the two of you, as well as your help with the ceramics. I am thankful to say, that we are also good friends and I thank you for being so. All five . . . er . . . six of you.

I must also acknowledge the love and support of my family. We Allens are a tight lip bunch. We're not too big into displaying affection (unless its a dog or a baby). We won't admit it, but, we *do* like each other. Well, let me step out of line for a moment. Mom, Dad, Glenn, Diane, I love you all and I thank you for your faith in me. Mom and Dad, you must have done something right if a goofball like me is getting his doctorate degree.

I lied when I said I wasn't presenting these acknowledgement in any order, because I have purposely left my wife for last. When two people marry, it is because they wish to join their lives together into one. Their dreams become one, their goals become one and their accomplishments become one. Unfortunately Deb, they will not let me put your name on this thesis. So let me state for all those who read this, that this document is the product of two authors. Debbie, your love and support have made me what I am today. I couldn't imagine life without you. Your unflagging support has allowed me . . . us to achieve one of our dreams. I am thankful that you were the one I got to share this achievement with. I love you and I am grateful that our son has such a wonderful mother.

To my wife, Debbie . . .

For nothing in particular, but, for everything in general.

. . . and to Zach.

Know O' Prince, that you can make your wildest dreams come true!

TABLE OF CONTENT

1. Introduction

1.1 Introduction

Bismuth-substituted iron garnets were first developed in the late 1960's for bubble memory devices. It was discovered, however, that the substitution of bismuth into iron garnets produced an unexpectedly large increase in the Faraday rotations. Investigations into the origins of the large Faraday rotation ensued and were conducted as part of the research effort into bubble memory materials in the 1970's. When research in this area ended in the latter part of the decade, the origin of the effect was left unresolved.

A new interest in these materials emerged in the mid to late 1980's. Bismuth-substituted iron garnets were desired for optical isolation devices and for magneto-optic memory. The materials' high ratio of Faraday rotation to absorption made them ideal for optical isolation devices in the near-infrared. For application to magneto-optic memory, the materials were desired for their large Kerr rotations and chemical stability. Although these materials are being applied successfully, the understanding of the origin of their magneto-optical properties has not changed in the last 15 years. The goal of this thesis is to investigate the origins of the large magneto-optic effect of iron garnets produced by bismuth substitution. It is hoped that a knowledge of the mechanism by which bismuth increases the magneto-optic activity of iron garnets will allow researches to tailor existing or develop improved materials for the two present areas of application.

In this chapter, we will review the history of magneto-optic effect of bismuth-substituted iron garnets leading up to the present. This chapter will conclude with an outline of the thesis.

1.2 The Magneto-optic Effect

The magneto-optic effect is defined as the change in the state of polarization of light upon interaction with a magnetic material. The first manifestation of the magneto-optic effect was discovered in 1846 by Michael Faraday[1] who found that the polarization of a beam of light was rotated upon passage through a piece of glass where a magnetic field was applied parallel to the direction of propagation (Figure 1.1a). A similar rotation

[1] M. J. Freiser, IEEE Transactions on Magnetics **MAG-4**, 152 (1968).

was observed by Voigt[2] in 1902 for a magnetic field applied perpendicular to the light beam (Figure 1.1b).

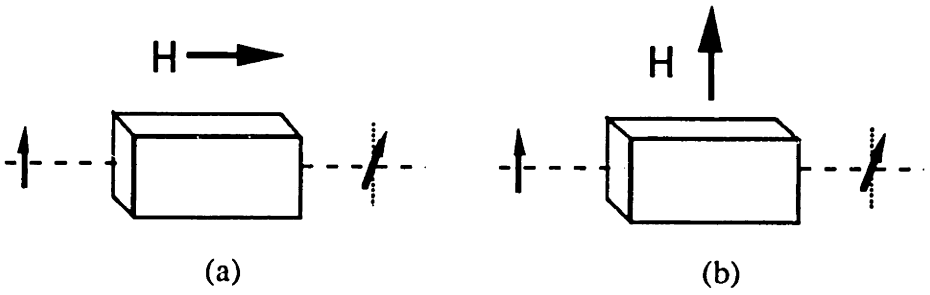

Figure 1.1. (a) The Faraday effect. (b) The Voigt effect.

In 1876, an analogous effect was found for *reflection* from a magnetic material by Kerr[1] and is now referred to as the magneto-optical Kerr effect. There are actually three different configurations possible for the magneto-optical Kerr effect, as is shown in Figure 1.2. Usually, the polar configuration (Figure 1.2a) is observed and for this reason, in the field of magneto-optics, the polar magneto-optical Kerr effect is simply referred to as the Kerr effect. This causes some confusion outside of the field, where the Kerr effect commonly refers to the electro-optical effect found by Kerr in 1875.

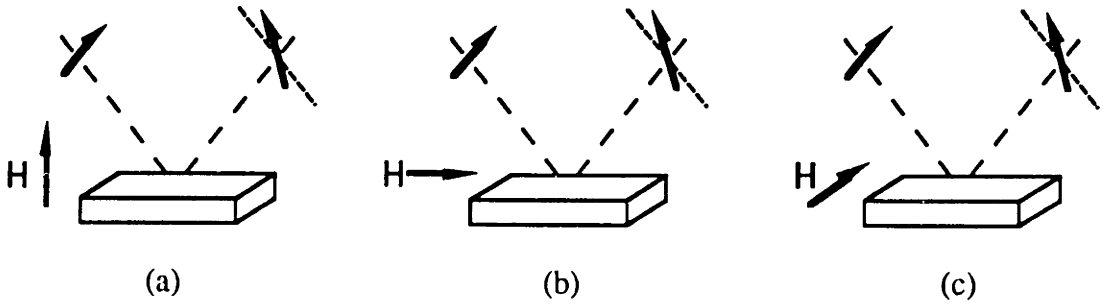

Figure 1.2. The magneto-optic Kerr effect. (a) The polar (b) longitudinal and (c) equatorial configurations.

All magneto-optical effects can be explained macroscopically as arising from differing indices of refraction for right and left circularly polarized light. For this reason, magneto-optical effects are often called *circular birefringence*. Similarly, the indices of absorption for right and left circularly polarized light will differ and produce *circular dichroism*. The circular birefringence and dichroism arise primarily from the Zeeman effect. In the Zeeman effect, two degenerate electronic states are split into two circular

---

2 W. Voigt, *Magneto- und Elektro-optik* (B. G. Teubner, Leipzig, 1908).

components (see Figure 1.3). Transitions to and from these states have the traditional dispersion and absorption line shapes.[3] If the excited state is split, transitions will have different energies. This creates a difference in the indices of refraction and absorption for right and left circular polarizations, since transitions to each state can be induced only by one or the other sense of polarization. This situation is called a *diamagnetic* transition, relating to the fact that the effect is temperature-independent.[4]

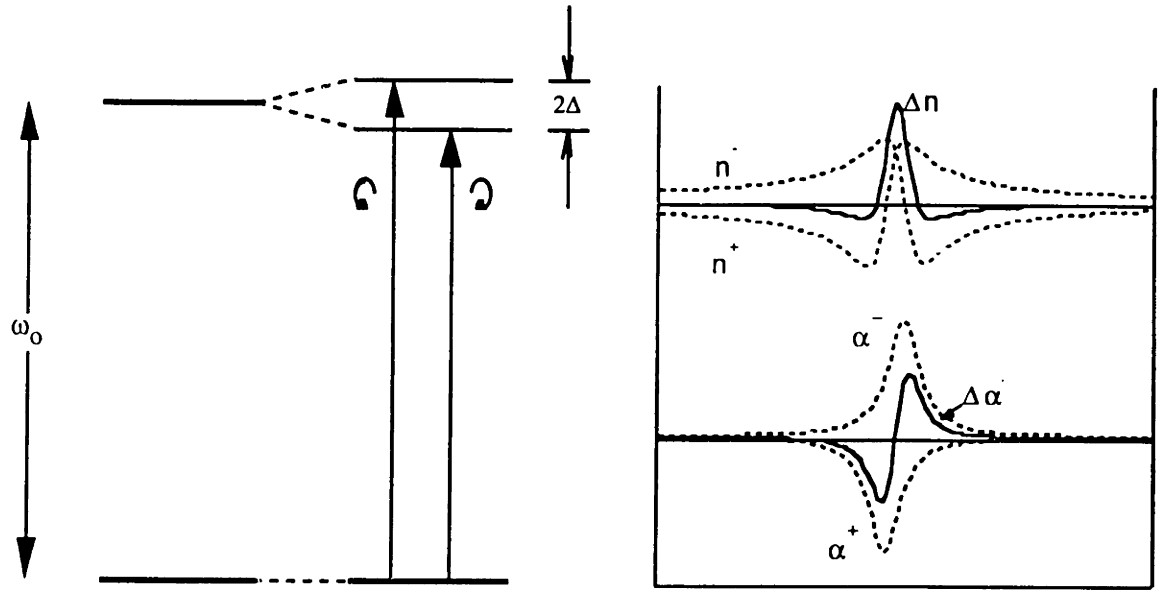

Figure 1.3. The diamagnetic transition arises from the difference in transition energy to a magnetically split excited state.

Another factor that contributes to circular birefringence and dichroism is a Zeeman-split ground state (Figure 1.4). The levels of a magnetically split ground state will have different populations according to the Boltzmann distribution, and thus, there is an unequal number of states available for making right and left handed transitions. This favoring of one sense of circular polarization over the other leads to a difference in indices of refraction and absorption, and hence, a magneto-optical effect. This situation is called a *paramagnetic* transition, since the material is in a paramagnetic state.[4]

---

3 F. A. Jenkins and H. E. White, *Fundamentals of Optics 4d* (McGraw-Hill, New York, 1976), p.474.

4 C. J. Ballhausen, *Introduction to Ligand Field Theory* (McGraw-Hill, New York, 1962), p.211

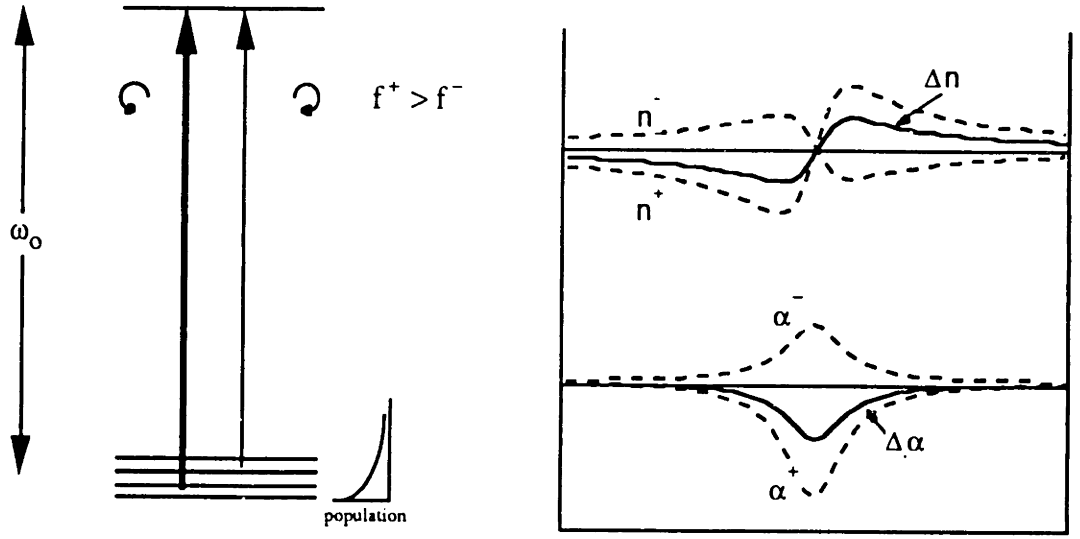

Figure 1.4. The paramagnetic transition arises from a magnetically-split ground state which possesses a thermal population distribution.

1.3 Magneto-optical Effects of Garnets

Soon after the discovery of synthetically-produced rare-earth iron garnets[5,6], Dillon[7] made the first optical and magneto-optical measurements on these new materials. He observed that they possessed a very large Faraday rotation that was associated with a strong absorption edge. The discovery stimulated much interest in the optical and magneto-optical properties of iron garnets as well as other iron oxide compounds[8]. Dillon's measurements, and those of others, were transmission measurements which are only possible in the garnets for wavelengths larger than ~500 nm due to the strong absorption edge at this wavelength.

Optical and magneto-optical measurements were made over the entire optical spectrum by Kahn *et al.*[9] by means of reflection techniques. In this study, Kahn *et al.* used the spectra of the Kerr effect in combination with optical data, to analyze the electronic transitions on a number of iron oxide compounds, including the iron garnets. Their techniques showed how magneto-optic spectroscopy can be used to determine the electronic states of magnetic compounds.

---

5 F. Bertaut and F. Forrat, Compt. Rend. **242**, 382 (1956).

6 S. Geller and M. A. Gilleo, Acta Crystal. **10**, 239 (1957).

7 J.F. Dillon, Jr., J. Phys. Radium **20**, 374 (1959).

8 F. J. Kahn, P. S. Pershan and J. P. Remeika, Phys. Rev. **186**, 891 (1969).

1.4 Bismuth-containing Iron Garnets

The first magneto-optical measurements on bismuth-containing iron garnets were reported by Chetkin[9] in the Soviet Union and Buhrer[10] in the United States. The materials investigated were of the form $Bi_{3-2x}Ca_{2x}Fe_{5-x}V_xO_{12}$. Bismuth was used in these materials as an inexpensive substitute for yttrium. The pentavalent vanadium ion was substituted for tetrahedrally coordinated Fe^{3+} in order to increase the Faraday rotation[11]. And lastly, the divalent calcium ion provided charge compensation for the vanadium ion. It was expected that the Faraday rotation would increase positively with vanadium content in the near infrared, but, in fact, the opposite was found† (Figure 1.5).

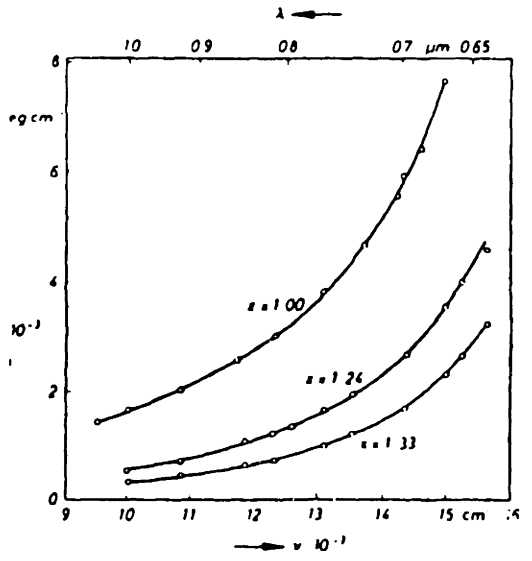

Figure 1.5. The Faraday rotation of $Bi_xCa_{3-x}V_xFe_{5-x}O_{12}$. After Buhrer[10].

Later, results on vanadium-free bismuth iron garnets proved that the bismuth ion was responsible for the decrease in the Faraday rotation of bismuth iron garnets in this region. Further Faraday rotation measurements on bismuth iron garnets of single crystal

---

9 M. V. Chetkin, I. G. Morozova and G. K. Tyutneva, Soviet Physics - Solid State **9**, 2852 (1968).

10 C. Buhrer, J. Appl. Phys. **40**, 4500 (1969).

11 H. Matthews, S. Singh and R. C. LeCraw, Appl. Phys. Lett. **7**, 165 (1965).

† Chetkin actually misinterpreted the sign of the Faraday rotation and thus did not realize the anomalous effect.

samples[12] and liquid-phase epitaxy (LPE) grown thin films[13] showed that the bismuth ion increased the magnitude of the Faraday rotation in iron garnets, often by an order of magnitude (Figures 1.6 and 1.7).

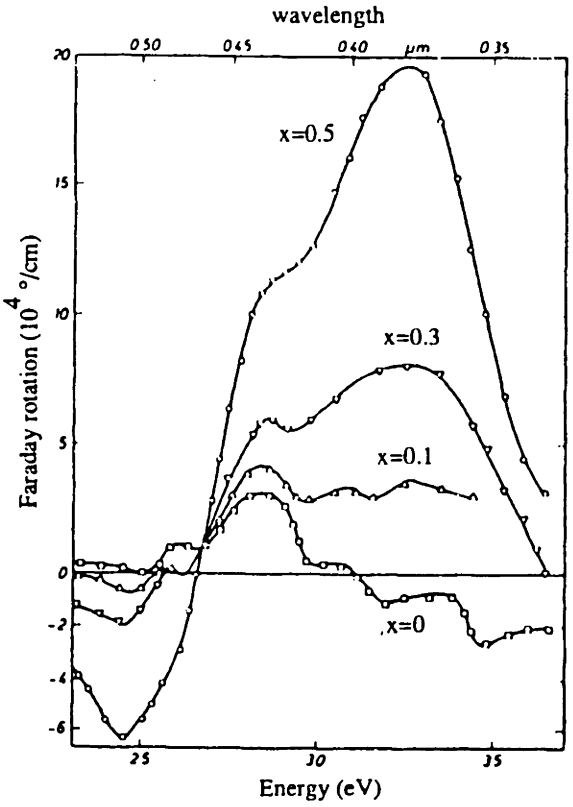

Figure 1.6. The Faraday rotation of $Bi_xY_{3-x}Fe_5O_{12}$ thin films. After Wittekoek *et al.*[14].

12 S. Wittekoek and D. E. Lacklison, Physical Review Lett. **28**, 740 (1972).

13 For a review article, see P. Hansen and J. -P. Krumme, Thin Solid Films **114**, 69 (1984).

14 S. Wittekoek, T. J. A. Pompa, J. M. Robertson and P. F. Bongers, Phys. Rev. B **12**, 2777 (1975).

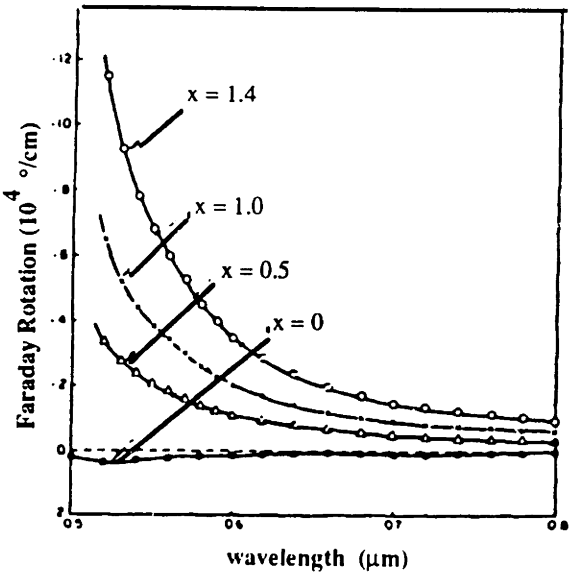

Figure 1.7. Faraday rotation of $Gd_{3-x}Bi_xFe_5O_{12}$. After Takeuchi[15].

Since transmission measurements could only be performed for wavelengths longer than 500 nm, the Kerr effect was employed for direct observation of the region of interest. Analysis on Faraday rotation measurements consisted of fitting the tails of magneto-optic lineshapes to theoretical expressions for diamagnetic and paramagnetic transitions[††] . The reflection measurements[12,13,16] allowed the entire magneto-optic spectra of the area of interest to be seen (Figure 1.7).

There are a number of explanations put forth to explain why bismuth, a diamagnetic ion, would produce such a large magneto-optical effect in the iron garnets when none would normally be expected at all[17]. First note (Figure 1.6) that the bismuth induced magneto-optical effect is attributed to a few magneto-optical transitions centered around 3.0 eV. Explanations have focused on the origins of these transitions.

Lacklison *et al.*[18] first suggested that the Bi^{3+} ion undergoes a $s^2 \rightarrow sp$ transition where the excited p state is magnetically split by the magnetization of the material. This

---

15 H. Takeuchi, Japan Journal of Applied Physics **14**, 1903 (1975).

†† These formulae are presented in chapter 3.

16 S. Wittekoek and T. J. A. Pompa, J. Appl. Phys. **44**, 5560 (1973).

17 A review of these theories and the research conducted in this field upto 1976 is given in G. B. Scott and D. E. Lacklison, IEEE Transactions on Magnetics **MAG-12**, 292 (1976).

18 D. E. Lacklison, H. I. Ralph and G. B Scott, Solid State Comm. **10**, 269 (1972).

seemed unlikely since such a transition would be expected to have an energy of greater than 32,000 cm^{-1}[16,19], yet the bismuth-induced transitions occur at lower energies of about 25,000 cm^{-1}. Another suggestion the authors gave was that the excitations were from charge-transfer transitions from the Fe^{3+} to the Bi^{3+} ion whose levels were split by spin-orbit coupling. Again, this seems unlikely since such transitions are expected at energies about 32,000 cm^{-1}[16,19]. A third scenario put forth by Wittekoek, *et al.*[14], is that the transitions of interest occur from charge transfer from the O^{2-} to Fe^{3+} on the tetrahedral site, the O^{2-} orbitals, being admixtures with the B^{3+} 6s orbitals. These 6s orbitals would contribute a large spin-orbit interaction which splits the ground state, thereby creating a magneto-optical effect. Data from Scott *et al.* on Fe^{3+} substituted yttrium gallium garnet[20], however, indicates that $O^{2-} \rightarrow Fe^{3+}$ transitions occur at energies in the vicinity of 35,000 cm^{-1}.

A final suggestion put forth by a number of authors[12,14,17,19,21] is that the large magneto-optic effect of bismuth iron garnets results from already present Fe^{3+} pair transitions (Chapter 2) being modified by a mixing of the Fe^{3+} orbitals with the Bi^{3+} orbitals. The Bi^{3+} ion has a large spin-orbit coupling in its first excited state; roughly 2 eV[12]. Therefore, even a small admixture of Bi^{3+} orbitals into the already existing Fe^{3+} states will give a substantial spin-orbit splitting. Wittekoek *et al.*[14] estimated the spin-orbit splitting to be $\approx$ 0.05eV. This would result from an admixture of only a few percent, which is quite reasonable. More recent analysis of Wittekoek et al.[14]'s data by Dionne and Allen[58] have determined even higher values of this parameter of 0.25 - 0.5 eV.

Further evidence for the mixing of bismuth and iron orbitals comes from the observed increase in Curie temperature with bismuth content.[22] An increase in the Curie temperature results from an increase in the coupling between the two iron sublattices. The increase may be caused by Bi^{3+} orbitals mixing with orbitals on both iron sublattices simultaneously, but the exact mechanism is uncertain.

The above two paragraphs represent the presently accepted explanation for the origins of the large magneto-optic effect in bismuth iron garnets.

1.5 Applications of Bismuth Iron Garnets

---

19 D. E. Lacklison, G. B. Scott and J.L. Page, Solid State Comm. **14**, 861 (1974).

20 G. B. Scott, D. E. Lacklison and J. L. Page, Phys. Rev. B **10**, 971(1974).

21 G. B. Scott, D. E. Lacklison and J. L. Page, J. Phys. C **8**, 519 (1975).

58 G. F. Dionne and G. A. Allen, J. Appl. Phys. **73**, 6127 (1993).

22 S. Geller, H. J. Williams, R. C. Sherwood and G. P. Espinosa, J. Appl. Phys. **35**, 1754 (1964).

Most of the research on the magneto-optic properties of bismuth-substituted garnets was conducted in the 1970's for bubble memory applications. Today, research on bismuth garnets is primarily for two types of applications: near infrared isolation devices and magneto-optic memory.

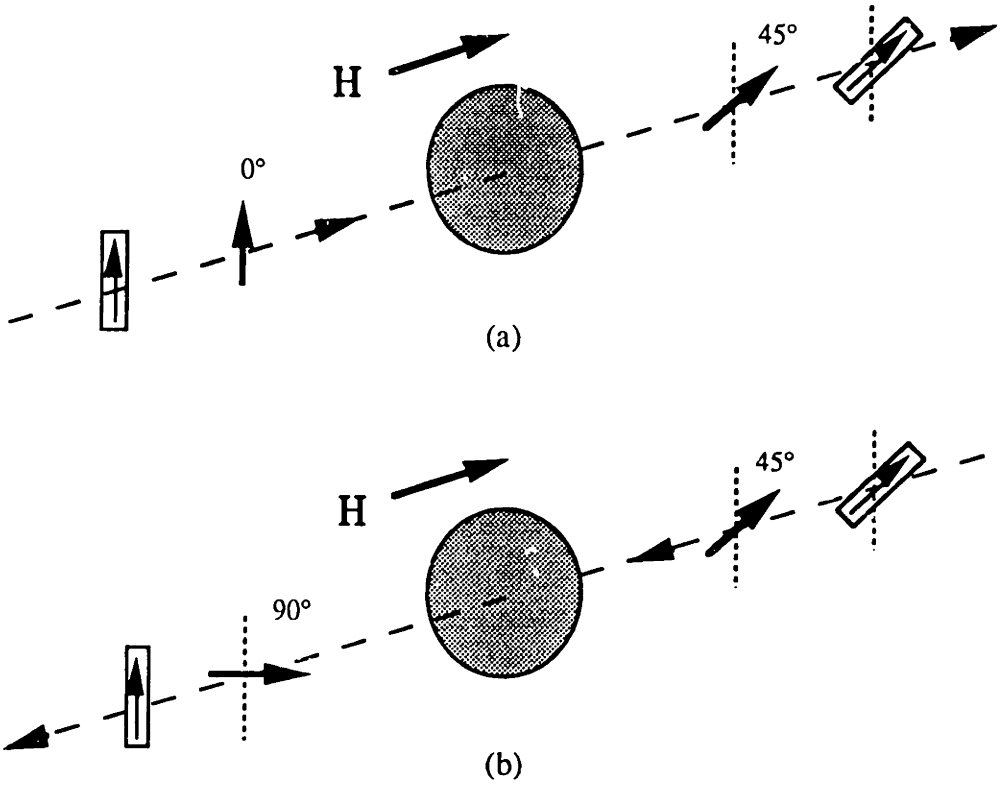

Figure 1.8. An optical isolator. In (a), outgoing linearly polarized light is Faraday rotated 45°. In (b), incoming light is linearly polarized and rotated -45° which makes it orthogonally polarized to the first polarizer.

An *optical isolator*, shown in Figure 1.8, uses the Faraday rotation of the material to differentiate between outgoing and incoming polarized light so as to reject the incoming light. Devices of this kind have been built for use at wavelengths longer than 1 μm where iron garnets are transparent. For wavelengths shorter than 1 μm, these materials are too absorbing to allow for transmission through a sufficient thickness for 45° of rotation necessary for a device. Bismuth-substituted garnets, however, have a large rotation per absorption ratio (called the figure of merit) compared to that of the unsubstituted material (Figure 1.9). Presently, the paramagnetic material terbium gallium garnet is used for NIR/visible isolators. Because it is a paramagnetic material, the device needs polarizing magnets for a uniform field and is temperature-sensitive both

intrinsically and through the magnetization of the polarizing magnets. A benefit of using bismuth-substituted iron garnets, which are ferrimagnetic materials, is the use of smaller polarizing magnets and temperature stability achieved by operating the material in a magnetically saturated state.

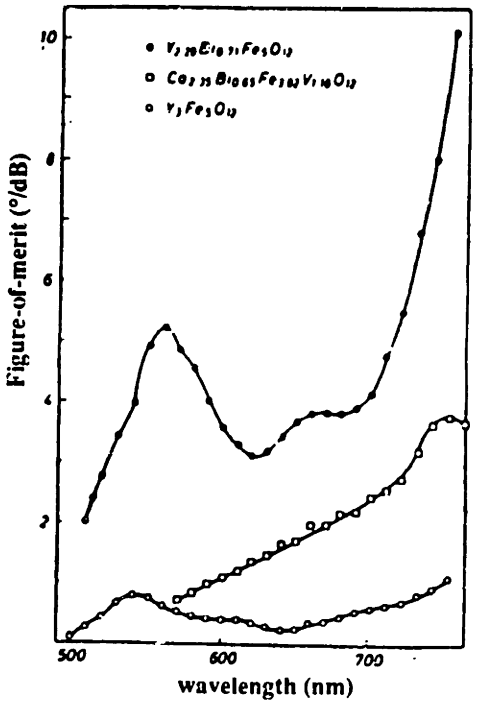

Figure 1.9. The figure-of-merit of YIG and some bismuth-substituted garnets in the near infrared region. After Lacklison *et al.*[23].

Bismuth-substituted iron garnets are also being exploited for use as a materials for magneto-optical memory. Such a system uses the Kerr rotation of a material to store and read digital information. Here, the important quantity is the Kerr rotation times the reflectivity[24]. Bismuth-substituted iron garnets are suitable materials for this application below ~500 nm, which, at the time of this writing, is the shortest wavelengths achieved by diode lasers, the light source of choice for magneto-optical memory devices.

---

23 D. E. Lacklison, G. B. Scott, H. I. Ralph and J. L. Page, IEEE Transactions on Magnetics **MAG-9**, 457 (1973).

24 F. J. A. M. Greidanus and W. B. Zeper, Mat. Res. Soc. Bull. **15**, 31 (1990).

1.6 Goal of Thesis

The goal of this thesis is to identify the origins of the magneto-optic effect of bismuth-substituted iron garnets. Additionally, we will also examine the role of the two iron sublattices in this effect. Data will be obtained by measurement of the complex dielectric constant spectra and the spectra of the Kerr rotation and ellipticity of selected materials. The spectra will be obtained for bismuth-substituted yttrium iron garnet and yttrium iron garnet. A comparison of these two materials will reveal the bismuth ion's contribution the magneto-optic effect. The role of the two iron sublattices will be elucidated by comparison of aluminum and indium-substituted yttrium iron garnet, both with and without bismuth substitution. The substitution of aluminum represents a reduction of iron in the tetrahedral sublattice, while substitution by indium will show the effect of a reduction of octahedral iron.

All measured spectra will be fitted to theoretical lineshapes in order to extract quantitative results.

1.7 Outline of Thesis

In this chapter, we reviewed the history of the problem addressed in this thesis; that is, explaining the origin of the magneto-optic effect of bismuth-substituted iron garnets. In the next chapter, we present an exposition of the properties of the magnetic garnets. The magnetic garnets are a family of magnetic materials of which yttrium iron garnet and its derivatives are members. The properties discussed are the structural, magnetic, optical and magneto-optical properties. Chapter 3 is devoted to the quantum theory of optical transitions. In this chapter, we derive expressions for the dielectric tensor elements. The diagonal elements of this tensor are the familiar dielectric constants, while the off-diagonal elements are responsible for magneto-optical effects. Also in this chapter, we derive some useful expressions for extracting information from the spectra of the dielectric tensor elements.

In this study, we measured both the dielectric constant and the Kerr spectra of iron garnet samples. To measure the spectra of the dielectric constant we constructed a photoelastic-modulated ellipsometer. This device is described in Chapter 4, where we discuss its theory of operation, errors of measurement and the details of the working instrument. Kerr spectra were measured by the magneto-optic spectrometer described in Chapter 5. We, again, present the theory of operation, errors of measurement and the details of the system constructed for this study.

In Chapter 6 is a description of the production and characterization of the ceramic samples measured in this work. Finally, in Chapters 7 and 8 a· presented the experimental results and an interpretation of these results, respectively.

2. Magnetic Garnets

There is a class of synthetic magnetic materials called magnetic garnets. These materials are generally ferrimagnetic and electrically insulating. Their crystal structure is the same as that of the precious gem *garnet*, and hence, they are referred to as *magnetic garnets*.

Magnetic garnets were first developed in the mid-fifties[5,6]. Since then a wide variety of magnetic garnets have been developed. They have been extensively used for magnetic devices and studies in systems and experiments involving microwaves (ν = 1-10 GHz). Much of the development of this class of materials through the 60's and 70's was for radar applications. Within the last decade or so, attention has turned towards using magnetic garnets in magneto-optical systems (i.e. fiber optical systems, magneto-optical recording) where the behavior of these materials in the near infrared and optical region is of interest.

The prototypical magnetic garnet is yttrium iron garnet, commonly referred to as YIG. In this Chapter, we review some of the basic properties of YIG as an illustration of the magnetic garnets. In particular, we will discuss the crystal structure, magnetic and optical properties. Two excellent sources for review of magnetic garnets are the books *Physics of Magnetic Garnets*[25] and *Magnetic Garnets*[26]. Also, a wealth of experimental data appears in reference Landbolt-Borntein[27].

2.1 Crystal Structure

Yttrium iron garnet, $Y_3Fe_5O_{12}$, derives its name from having the garnet crystal structure. The garnet structure has the space group symmetry of Ia3d (O_h^{10}, space group 230)*, The structure is body centered cubic and the unit cell contains 8 formula units of $Y_3Fe_5O_{12}$ (160 atoms per unit cell). The crystal structure is shown in Figure 2.1.

---

25 A. Paoletti, ed., *Physics of Magnetic Garnets* (North-Holland Publishing Company, Amsterdam, 1978).

26 Gerhard Winkler, *Magnetic Garnets* (Friedr. Vieweg and Sohn, Braunschweig/Weisbaden, 1981).

27 Landolt-Börnstein, "Magnetic and other properties of Oxides and Related Compounds: Garnets and Perovskites", *Numerical Data and Functional Relationships in Science and Technology, New Series, III/12a.* (Springer-Verlag, Berlin, 1978).

* Strictly speaking, a material with a magnetization can not possess cubic symmetry. It was found by x-ray diffraction by Popma *et al.*[m] and later by Chenavas *et al.*[n], that YIG as well as other garnets do not have a cubic structure. The actual structure has a trigonal symmetry and belongs to the space group

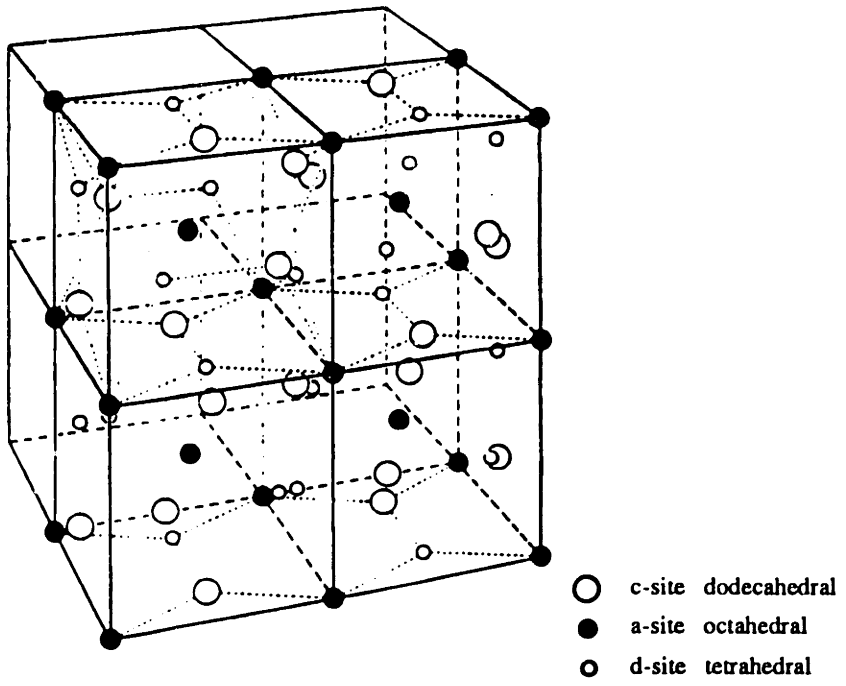

Figure 2.1. The unit cell of the garnet structure. After Geller.[29]

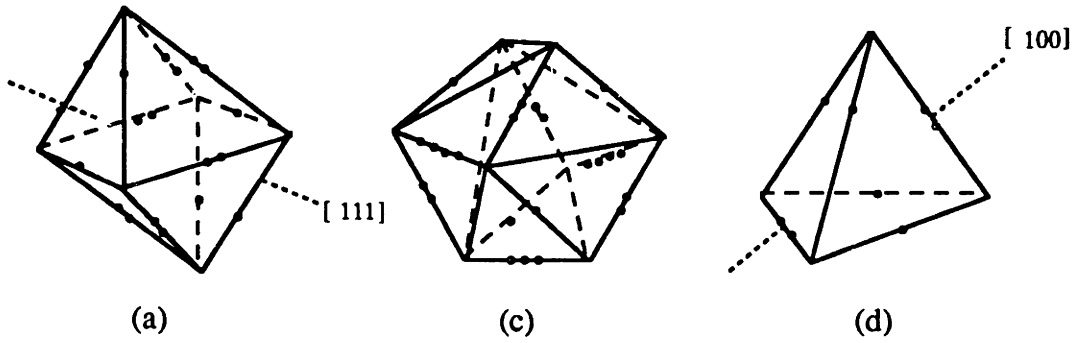

Figure 2.2. The cation sites. The a site; (•2.68Å, ••2.99Å). The c-site; (•2.68, ••2.81Å, •••2.87Å, ••••2.96Å). The d-site; (•3.16Å, ••2.87Å). After Geller.[29]

The structure possesses four different crystallographic sites. There are two a-sites or *octahedral* sites per formula unit. They are occupied by two of the Fe^{3+} ions. The remaining three Fe^{3+} ions reside in the d-sites or *tetrahedral* sites. The Y^{3+} ions occupy

R3. It is a very slight departure from the Ia3d symmetry, and hence, garnets are almost always considered to be cubic materials.

the c-sites or *dodecahedral* sites. The remaining oxygen anions occupy the h-sites which have no symmetry. As a way of keeping track of which cations reside in which sites, the chemical formula for YIG, as well as other garnets, can be expressed as,

$$\{Y_3\}[Fe_2](Fe_3)O_{12} \quad . \tag{2-1}$$

The occupants of the c-sites are contained in braces, { }; those of the octahedral sites in brackets, [] and the tetrahedral sites in parentheses, (). The usefulness of this convention becomes more important when other elements are substituted into the cation sites.

In actuality, none of the sites are of regular symmetry as their names suggest. The d-site (Figure 2.2a) is actually a tetragonally distorted tetrahedron along the crystals <100> directions and has the point symmetry $\bar{4}$. The a-site (Figure 2.2b) is actually a trigonally distorted octahedron being distorted along the <111> directions and has a point symmetry of C_{3i}. Lastly, the c-site (Figure 2.2c) is a highly-distorted cube possessing the point symmetry D_2. Listed in Figures 2.2a-c are the oxygen ion spacings for the three polyhedra in YIG. Even though the a and d sites are not truly octahedrons and tetrahedrons, they are nearly so and they are commonly referred to as the octahedral and tetrahedral sites.

An alternate way to view the sites of the crystal is to look at the surroundings of the oxygen ions as is shown in Figure 2.3. Here we see that each oxygen ion is part of two dodecahedral, one octahedral and one tetrahedral polyhedra. The distances between ions in Figure 2.3 are listed in Table 2.1 along with the bond angles between the oxygen and cations.

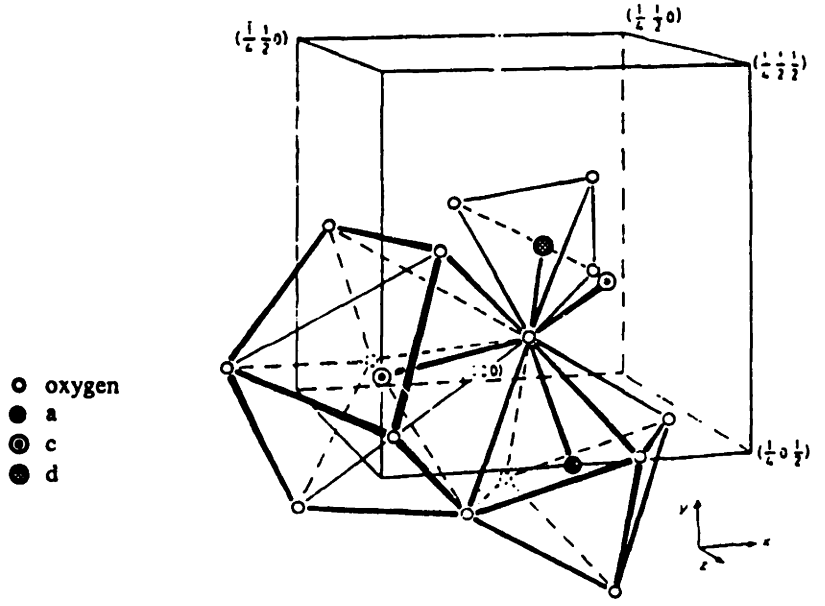

Figure 2.3. Arrangement of the cation sites in the garnet structure. After Geller.[29]

lattice constant	12.376 Å		
Oxygen coordinates	x	y	z
	-0.0271(1)	0.0567(1)	0.1504(1)

interatomic nearest neighbors distances

ion	#nn		distances (Å)	
O^{2-}	2	Y^{3+}	2.357	2.436
	1	$[Fe^{3+}]$	2.017	
	1	(Fe^{3+})	1.865	
	9	O^{2-}	2 x 2.692	2.789
			2.837	2.976
			2 x 3.005	2 x 3.146
Y^{3+}	4	$[Fe^{3+}]$	3.46	
	6	(Fe^{3+})	2 x 3.09	4 x 3.79
	8	O^{2-}	4 x 2.357	4 x 2.436
$[Fe^{3+}]$	2	Y^{3+}	3.46	
	6	(Fe^{3+})	3.46	
	6	O^{2-}	2.017	
(Fe^{3+})	6	Y^{3+}	2 x 3.09	4 x 3.79
	4	$[Fe^{3+}]$	3.46	
	4	O^{2-}	1.865	

interionic angles

configuration	angle (°)
$[Fe^{3+}] - O^{2-} - (Fe^{3+})$	125.9
$[Fe^{3+}] - O^{2-} - Y^{3+}$	101.5
$[Fe^{3+}] - O^{2-} - Y^{3+}$	104.3
$(Fe^{3+}) - O^{2-} - Y^{3+}$	123.0
$(Fe^{3+}) - O^{2-} - Y^{3+}$	93.5
$Y^{3+} - O^{2-} - Y^{3+}$	104.5
$[Fe^{3+}] - O^{2-} - [Fe^{3+}]$	147.2
$(Fe^{3+}) - O^{2-} - (Fe^{3+})$	86.6
$(Fe^{3+}) - O^{2-} - (Fe^{3+})$	78.8
$(Fe^{3+}) - O^{2-} - (Fe^{3+})$	74.7
$(Fe^{3+}) - O^{2-} - (Fe^{3+})$	74.6

Table 2.1. Distances and angles of the YIG crystal structure. After Winkler.[26]

Other elements can be put into YIG to replace the yttrium and iron and produce other magnetic garnets. In place of yttrium, we can substitute lanthanum or any of the rare-earths. The c-site is for this reason often referred to as the *rare-earth site*. In place of the iron can go other transition metals. Commonly used elements are aluminum and gallium which have a strong preference for substituting into the tetrahedral sites. Elements that prefer the octahedral site include indium and scandium.

Different elements are substituted into YIG to obtain desired magnetic properties. The use of the notation shown in (2-1) becomes particularly useful in describing the occupations of the three cation sites. As an example, if we substitute aluminum for one-tenth of the iron atoms in the material gadolinium iron garnet (GdIG) we would write the chemical formula of the material as

$$\{Gd_3\}[Fe_2](Al_{0.5}Fe_{2.5})O_{12} \quad ,$$

where we have assumed that all the aluminum ions reside in the tetrahedral sublattice.

As an example of the properties of magnetic garnets changing with different compositions, Figure 2.4 and Figure 2.5 show how the lattice constant changes with different rare-earth ions and varying amounts of iron substitutents.

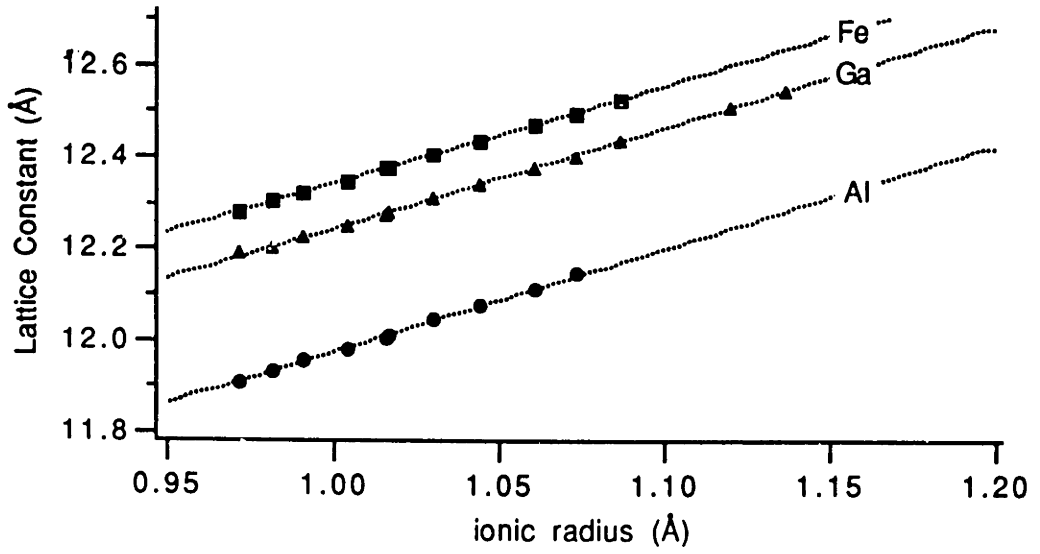

Figure 2.4. Lattice Constant of $RE_3M_5O_{12}$ versus ionic radius of rare-earth ion. After Winkler[26] and references therein.

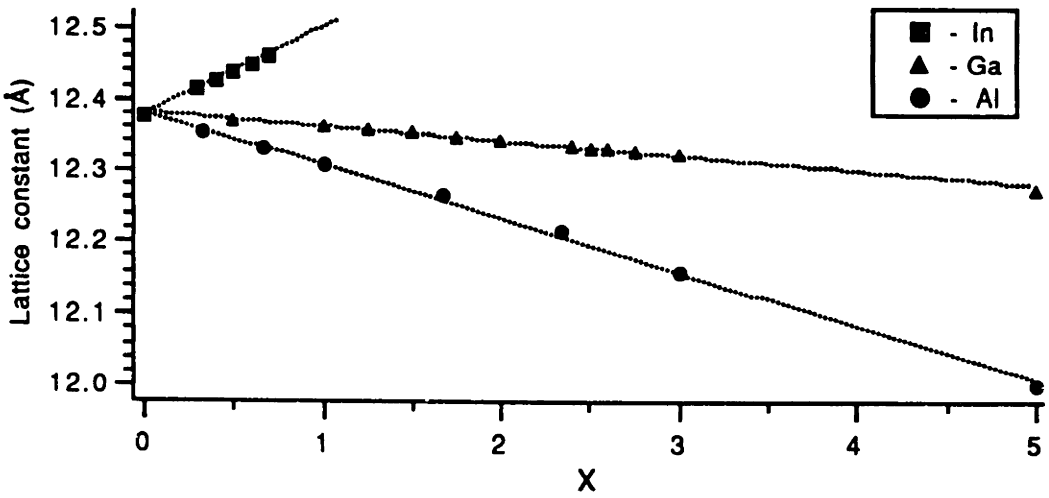

Figure 2.5. The lattice constant of $Y_3Fe_{5-x}M_xO_{12}$ for M = Al, Ga and In. After numerical data found in reference 27.

It is generally accepted that yttrium, lanthanum and the rare-earth elements only reside in the rare-earth or d-site. Transition metals, however, can and do go into both the octahedral and tetrahedral sites, although, they generally will have a preference for one of the sites. This site selectivity as it is called, depends not only on the size of the ion, but also the crystal field energy of the ions in the two sites. Also of importance is the material preparation technique.

Commonly substituted ions include the trivalent diamagnetic ions Al^{3+}, Ga^{3+}, In^{3+} and Sc^{3+}. Al^{3+} and Ga^{3+} have a strong preference to occupy the d-site[28]. At low concentrations, roughly 90% or more of these ions will occupy the d-site. In^{3+} and Sc^{3+} prefer to occupy the a-site[29].

The substituting ions need not be trivalent, provided that other non-trivalent ions are present for charge neutrality of the composition. Two such examples are

$$\{Y_{3-2x}Ca_{2x}^{2+}\}[Fe_2](V_x^{5+}Fe_{3-x})O_{12} \quad ,$$

where the V^{5+} ion goes exclusively into tetrahedral sites, and,

---

28 E. R. Czerlinsky, Phys. Stat. Sol. **34**, 483 (1969).

E. R. Czerlinsky and R. A. MacMillan Phys. Stat. Sol. **41**, 333 (1970).

29 S. Geller, "Crystal and Static Magnetic Properties of Garnets", *Physics of Magnetic Garnets*, ed. A. Paoletti (North-Holland Publishing Company, Amsterdam, 1978) p.1.

$$\{Y_{3-2x}Ca_x^{2+}\}[Zr_x^{4+}Fe_{2-x}](Fe_3)O_{12} \quad ,$$

where the Zr^{4+} goes exclusively into the octahedral site. In both cases, Ca^{2+}, a diamagnetic ion, has also been substituted for charge compensation. We will restrict work to trivalent diamagnetic ions.

2.2 Magnetic Properties

Yttrium iron garnet is an insulating ferrimagnetic material with a Curie temperature of 559 K. The magnetization of YIG comes from the Fe^{3+} ions which have a ground state electronic configuration of $^6S_{5/2}$, arising from a half-filled 3d shell. This gives the iron ions a magnetic moment of $5\mu_B$. The Y^{3+} ion has a closed shell configuration isoelectronic to Krypton, and hence, is diamagnetic, contributing nothing to the magnetization. Fe^{3+} ions in the tetrahedral sites prefer to align themselves parallel to one another. The Fe^{3+} ions residing in the octahedral sites also prefer to align parallel to one another. These two ferromagnetic sublattices, however, align anti-parallel to each other. Since there are three tetrahedral sites for every two octahedral sites, there is a net magnetization and the material is ferrimagnetic. At zero temperature, the magnetization of the material will be $5\mu_B$ per formula unit giving a magnetization of

$$4\pi M_0 = \frac{(8)(5\mu_B)}{(12.376\text{Å})^3} = 2459 \text{ Gauss.} \qquad (2\text{-}2)$$

This value has been found experimentally[30], lending credibility to the above model.

[30] Elmer E. Anderson, "Molecular Field Model and the Magnetization of YIG", Physical Review **134**, A1581 (1964).

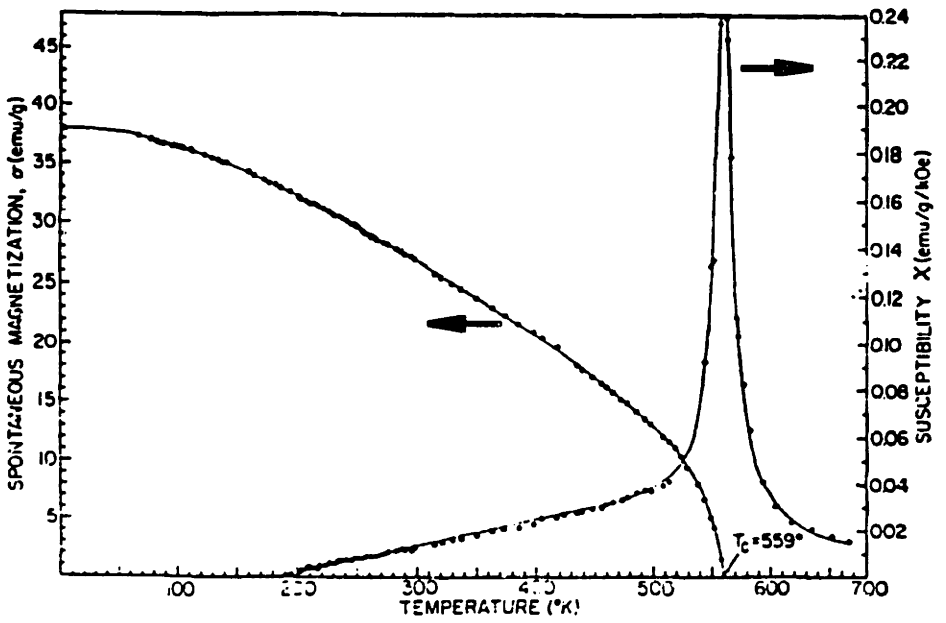

Figure 2.6. Saturation magnetization and magnetic susceptibility of YIG versus temperature. After Anderson.[30]

Figure 2.6 shows the thermomagnetization curve of YIG. The Néel Theory of ferrimagnetism can be used to explain the magnetization of YIG versus temperature[30,31]. The theory states that the total magnetization is the sum of the magnetizations of the tetrahedral and octahedral sublattices, M_d and M_a respectively. (We assign the octahedral sublattice a negative magnetization.);

$$M = M_d - M_a. \tag{2-3}$$

The sublattice magnetizations are calculated by treating the ions as paramagnetic moments under the influence of an effective magnetic field called an exchange field. This exchange field can be described as a Heisenberg exchange energy, $\mathcal{H}_{ex} = JS_1 \cdot S_2$, between ions on the same and different sublattices. Thus the sublattice magnetizations are given as follows:

---

31 Gerald F. Dionne, "Molecular Field Coefficients of Substituted Yttrium Iron Garnets", Journal of Applied Physics **41**, 4874 (1970).

$$M_a(T) = M_a(0)B_{5/2}\left(\frac{5\mu_B H_a}{kT}\right) \quad ,$$
$$M_d(T) = M_d(0)B_{5/2}\left(\frac{5\mu_B H_d}{kT}\right) \quad , \tag{2-4}$$

where

$$M_a(0) = 2\frac{(8)(5\mu_B)}{(12.376\text{Å})^3} \quad ,$$
$$M_d(0) = 3\frac{(8)(5\mu_B)}{(12.376\text{Å})^3} \quad , \tag{2-5}$$

and $B_{5/2}(x)$ is the Brillouin function for spin 5/2. The exchange fields, H_a and H_d, arise from the interactions (super-exchange) between the iron ions and are assumed to take the form of

$$H_a = \lambda_{aa}M_a + \lambda_{ad}M_d \quad ,$$
$$H_d = \lambda_{da}M_a + \lambda_{dd}M_d \quad . \tag{2-6}$$

The λ's are called molecular field coefficients and are proportional to the Heisenberg exchange constants as will be shown later.

Equations (2-4), (2-5) and (2-6) are solved simultaneously with different values for the λ's. The λ's are adjusted until a good fit with experimental data is achieved.

The exchange constants, J_{ij}, can be calculated from the λ's and compared with other experimentally determined values of J in the following way. The exchange energy of an ion is written as

$$H_i = \sum_j J_{ij}S_i \cdot S_j = \sum_{j=a,d} z_{ij}J_{ij}S_i \cdot S_j \quad , \tag{2-7}$$

where z_{ij} is the number of nearest j neighbors for ion i,. We can also write the exchange energy in terms of the exchange field,

$$H_{exchange,i} = g_i\mu_B S_i \sum_j \lambda_{ij}M_j \quad . \tag{2-8}$$

Equating (2-7) and (2-8) we find that

$$J_{ij} = \frac{g_i g_j}{z_{ij}} \mu_B^2 n_j \lambda_i \quad . \tag{2-9}$$

where n_j is the density of j-sites.

Values for the exchange constants derived from magnetization curves of some iron garnets are given in Table 2.2. Other experimentally determined values of the exchange constants for YIG are listed in Table 2.3. First note that the value of J_{ad} is positive, indicating that the two sublattice magnetizations prefer to align anti-ferromagnetically, while J_{aa} and J_{dd} are negative indicating ferromagnetism within the sublattices. Also, J_{ad} is in good agreement with other experiments, although this is less true for the smaller exchange constants J_{aa} and J_{dd}. However, it appears that the above model for the magnetization is a reasonably valid one.

Composition	J_{ad}	J_{aa}	J_{dd}	J_{ac}	J_{dc}
$Y_3Fe_5O_{12}$	25.36	-8.45	-11.86	0	0
	25.31	-8.50	-11.90	0	0
(a)	24.2	-5.54	-10.6	0	0
(b)	22.0	-3.22	-3.22	0	0
$Gd_3Fe_5O_{12}$	25.18	-8.43	-12.02	-0.22	3.38
	25.3	-8.49	-11.90	-0.90	4.70
$Er_3Fe_5O_{12}$	25.31	-8.50	-11.90	-0.20	0.98
$Sm_3Fe_5O_{12}$	25.31	-8.50	-11.90	0	0
$Eu_3Fe_5O_{12}$	25.31	-8.50	-11.90	0	0
$Tb_3Fe_5O_{12}$	25.31	-8.50	-11.90	-0.48	2.66
$Dy_3Fe_5O_{12}$	25.31	-8.50	-11.90	-0.89	3.10
$Ho_3Fe_5O_{12}$	25.31	-8.50	-11.90	-0.20	1.18
$Tm_3Fe_5O_{12}$	25.31	-8.50	-11.90	-0.27	6.28
$Yb_3Fe_5O_{12}$	25.31	-8.50	-11.90	-0.45	1.57
$Lu_3Fe_5O_{12}$	25.31	-8.50	-11.90	0	0

Table 2.2. Exchange constants for iron garnets in cm^{-1}. (a) Values derived from susceptibility measurements. (b) Values derived from spin-wave measurements. After numerical data found in reference 27 and references therein.

Method	J_{ad}	J_{aa}	J_{dd}
Optical absorption	19.8	0	-1.77
	22.0	-3.22	-3.22
Magnetization	25.36	-8.45	-11.86
	22.5	-0.5±0.5	2.0±0.5
	31.8	-6.35	-6.35
Susceptibility	24.2	-5.54	-10.6
	24.0	-	-0.83

Table 2.3. Some values for the exchange constants (cm^{-1}) of YIG, determined by various experimental methods. After Winkler[26] and references therein.

We can magnetically dilute the two sublattices to either increase (octahedral substitution) or decrease (tetrahedral substitution) the magnetization of YIG. When this occurs, the coupling constants will decrease[g]. For the material $\{Yd_3\}[A_xFe_{2-x}](D_yFe_{3-y})O_{12}$, where A and D are diamagnetic ions in the octahedral and tetrahedral sublattice, respectively, the molecular field coefficients obey the empirical relationship[g]

$$\begin{aligned} \lambda_{aa} &= -65.0(1-0.42y) \quad , \\ \lambda_{dd} &= -30.4(1-0.43x) \quad , \\ \lambda_{ad} &= +97.0(1-0.125x-0.127y) \quad . \end{aligned} \tag{2-10}$$

Also, the magnetizations of the sublattices are observed to decrease slightly more than can be explained by mere substitution. Empirically it is found that

$$\begin{aligned} M_a(0) &= (2-x)g_a\mu_B S_a N_A\left(1-\left(\frac{y}{3}\right)^{5.4}\right) \quad , \\ M_d(0) &= (3-y)g_d\mu_B S_d N_A(1-0.05x) \quad . \end{aligned} \tag{2-11}$$

First note that (2-10) and (2-11) are not simply the result of removing magnetic ions. If this were the case, the molecular field coefficients in (2-10) would not change and the factors of $\left(1-\left(\frac{y}{3}\right)^{5.4}\right)$ and $(1-0.05x)$ would not appear in (2-11). Also seen in (2-10) and (2-11) is the implication that substitution of a diamagnetic species in one sublattice affects the coefficients and magnetization of the *opposite* sublattice. These

affects have been attributed to a *canting* of the spins of the Fe^{3+} ions upon dilution of the sublattices. That is, when some of the Fe^{3+} ions are removed, the spins on the remaining Fe^{3+} ions on average become non-collinear, not aligning either parallel or anti-parallel with the magnetization.

We can also substitute rare-earth ions in place of the yttrium ion. Rare-earth ions in general possess a magnetic moment. Rare-earth ions in the c-sublattice align parallel to each other and anti-parallel to the resultant magnetization of the two iron sublattices. As can be seen in Table 2.2, the molecular field coefficients for the c-sublattice are an order of magnitude less than those of the iron sub-lattices. The addition of this third magnetic sublattice does significantly affect the magnetization of the material, however. A third magnetic sublattice implies the magnetization as a function of temperature can go to zero at the Curie temperature, T_C, and at a second temperature called the compensation temperature, T_{comp}. This is illustrated in Figure 2.7.

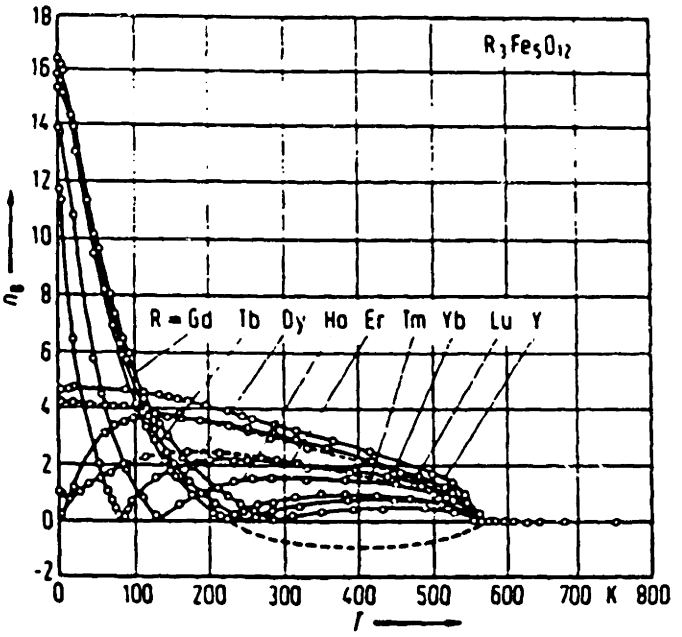

Figure 2.7. The thermomagnetization curves of rare-earth iron garnets. The y-axis denotes the number of Bohr magnetons per formula unit, n_B The dashed curve for $Dy_3Fe_5O_{12}$ indicates continuation of the magnetization curve; the magnetization being always positive. After Winkler[26] and references therein

2.3 Optical Absorption

As can be seen in Figure 2.8, YIG is transparent through much of the near-infrared spectrum. The optical window extends from roughly 1 to 5 μm in wavelength. At long wavelengths, the absorption is due to the excitation of optical phonons. At shorter wavelengths, the absorption comes from electronic transitions involving the Fe^{3+} ions. We will concern ourselves with the optical absorption in the visible region below 1 μm in wavelength.

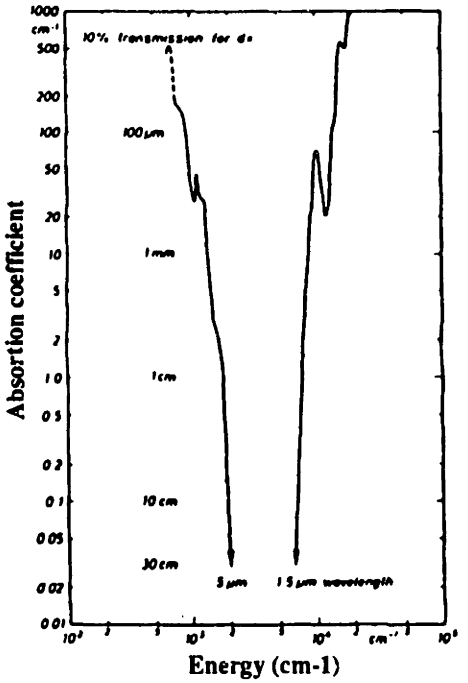

Figure 2.8. The absorption spectrum of YIG. After Wood and Remeika.[33]

The optical absorption of YIG is shown in Figure 2.9 for the range 10,000 cm^{-1} to 23,000 cm^{-1} (1000 nm - 400 nm)† and in Figure 2.10 for wavelengths 20,000 cm^{-1} to 40,000 cm^{-1} (500 nm - 250 nm). The spectrum can be split into three different regions

† The units of energy (electron volts, eV, and wavenumbers, cm-1) are used interchangeably with wavelength when talking about optical spectra. The wavenumber is the reciprocal of the wavelength of light. A useful equality to remember is that 1 eV = 8065 cm^{-1} = 1240 nm.

due to the different types of electronic processes proposed for the absorption in each region[32].

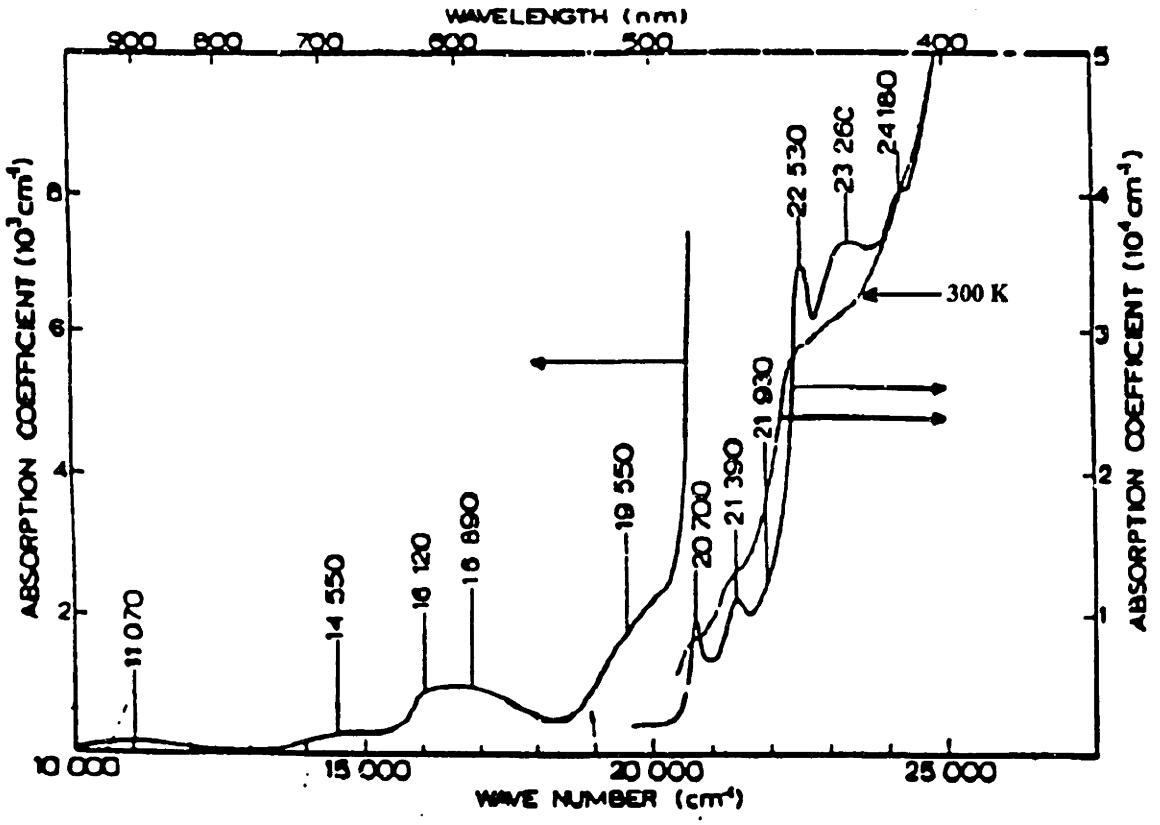

Figure 2.9. The absorption spectrum of YIG at 77 K (solid line) and 300 K (dashed line). After Scott *et al.*[20]

32 G. B. Scott, "The Optical Absorption and Magneto-optical Spectra of $Y_3Fe_5O_{12}$", *Physics of Magnetic Garnets*, ed. A. Paoletti, (North-Holland Publishing Company, Amsterdam, 1978) p.445.

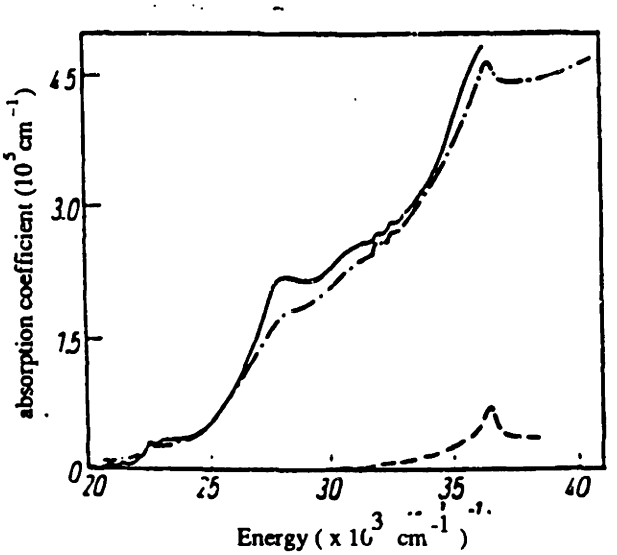

Figure 2.10. The absorption coefficient for a thin film of YIG at 77 K (–) and 300 K (– · –). The dashed curve at the bottom of the graph is the spectrum for the $Gd_3Ga_5O_{12}$ substrate. After Scott and Page.[38]

The absorption spectrum from 10,000 cm^{-1} to about 23,000 cm^{-1} is primarily from electronic transitions between the crystal field split levels of the Fe^{3+} ions in the octahedral and tetrahedral sites. It has been possible to decompose the optical absorption spectrum by fitting to a series of Gaussian peaks[20,33,34,35] and matching the resultant peaks to a crystal field splitting scenario for the Fe^{3+} ions based on the theory of Tanabe-Sugano's[36]. This modeling procedure is complicated by the fact that there are two crystal fields for the iron ions; one for the octahedral site and one for the tetrahedral site. The assignments made by Scott *et al.*[20] are listed in Table 2.4 with the energy levels shown schematically in Figure 2.11. The Gaussian peaks arising from the least-squares fit to the absorption spectrum is shown in Figure 2.12 and Figure 2.13.

---

33 D. L. Wood and J. P. Remeika, J. Appl. Phys **38**, 1038 (1967).

34 K. A. Wickersheim and R. A. Lefever, J. Chem. Phys. **36**, 844 (1962).

35 S. H. Wemple, S. L. Blank, J. A. Seman and W. A. Biolsi, Phys. Rev. B **9**, 2134 (1974).

36 Y. Tanabe, S. Sugano, J. Phys.Society of Japan **9**, 753 (1954).

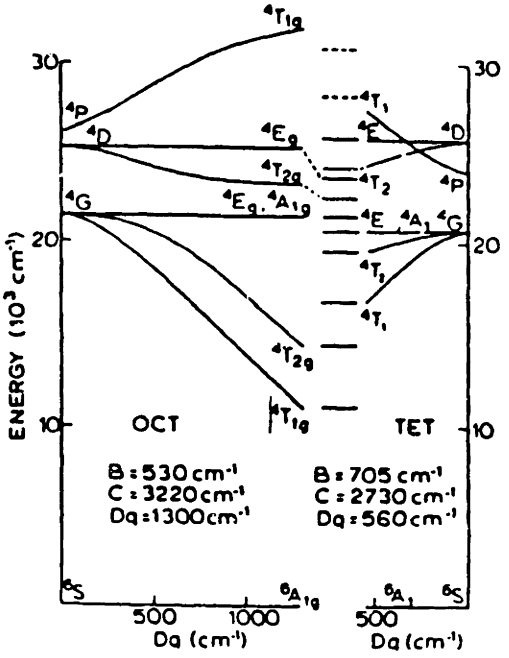

Figure 2.11. Diagram of the crystal field split energy levels of Fe^{3+} in the octahedral and tetrahedral sites. After Scott *et al.*[20]

Energy (cm^{-1})	Assignment	Site	Oscillator strength
11,070	$^6A_{1g}(^6S) \rightarrow {}^4T_{1g}(^4G)$	oct	2×10^{-5}
14550	$^6A_{1g}(^6S) \rightarrow {}^4T_{2g}(^4G)$	oct	2×10^{-5}
16120, 16890	$^6A_{1g}(^6S) \rightarrow {}^4T_1(^4G)$	tet	8×10^{-5}
19,718	$^6A_{1g}(^6S) \rightarrow {}^4T_2(^4G)$	tet	1.6×10^{-4}
20,710	$^6A_{1g}(^6S) \rightarrow {}^4E,{}^4A_1(^4G)$	tet	3.2×10^{-5}
21,390	$^6A_{1g}(^6S) \rightarrow {}^4E_g,{}^4A_{1g}(^4G)$	oct	2×10^{-5}
22,520	$^6A_{1g}(^6S) \rightarrow {}^4T_{2g}(^4D)$	oct	1×10^{-4}
24,150	$^6A_{1g}(^6S) \rightarrow {}^4T_2(^4D)$	tet	6×10^{-5}

Table 2.4. Assignments for crystal field transitions in YIG derived from Gaussian fitting of absorption spectrum 77 K. See Figure 2.11 for energy level diagram. After Scott *et al.*[32]

Energy (cm^{-1})	Half-width (cm^{-1})	Oscillator strength
23,100	1800	7.0×10^{-4}
25,600	1850	4.5×10^{-4}
27,700	3100	4.0×10^{-3}
30,700	3760	7.0×10^{-3}

Table 2.5. Transitions assignments derived from Gaussian fitting of absorption spectrum of YIG at 77 K. Oscillator strengths have been calculated assuming absorption is from $[Fe^{3+}]$-(Fe^{3+}) pairs. After Scott *et al.*[32]

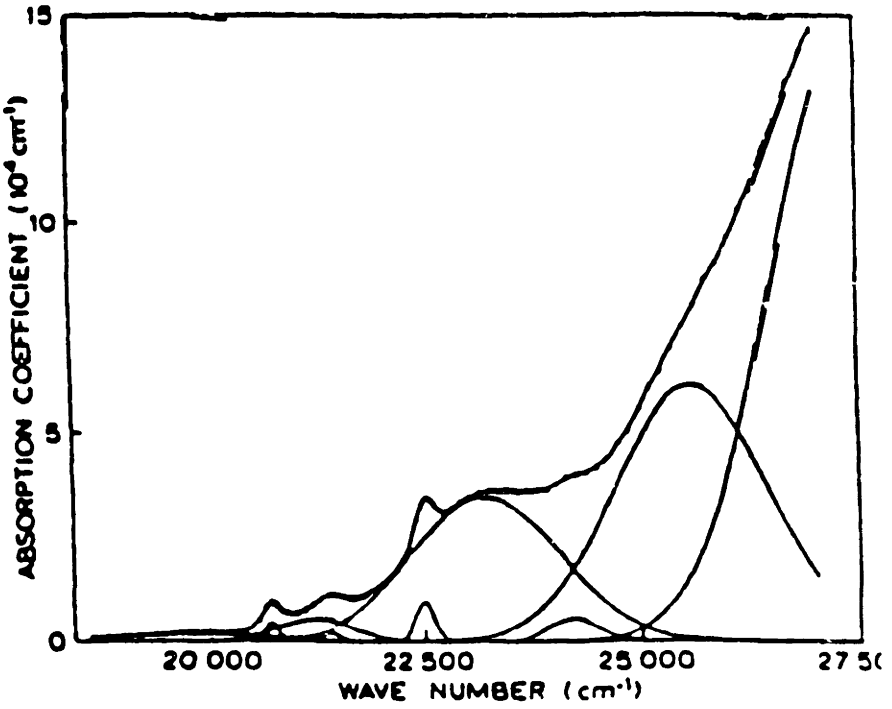

Figure 2.12. Gaussian curve fit to the absorption spectrum of YIG. After Scott *et al.*[20]

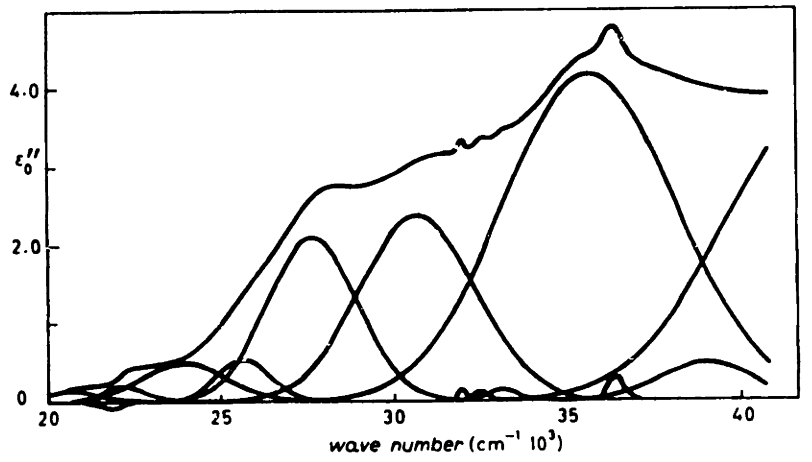

Figure 2.13. Gaussian curve fit to the imaginary part of the dielectric constant of YIG. After Scott and Page.[38]

It was noted, early on, that the strengths of these crystal field transitions did not scale linearly with the iron concentration of substituted iron garnets,[33,34] but instead, went approximately as the square of the concentration (see Figure 2.14). This suggested that the transitions actually involved pairs or groups of iron ions rather than single ions. Transitions of this type are referred to as pair transitions.

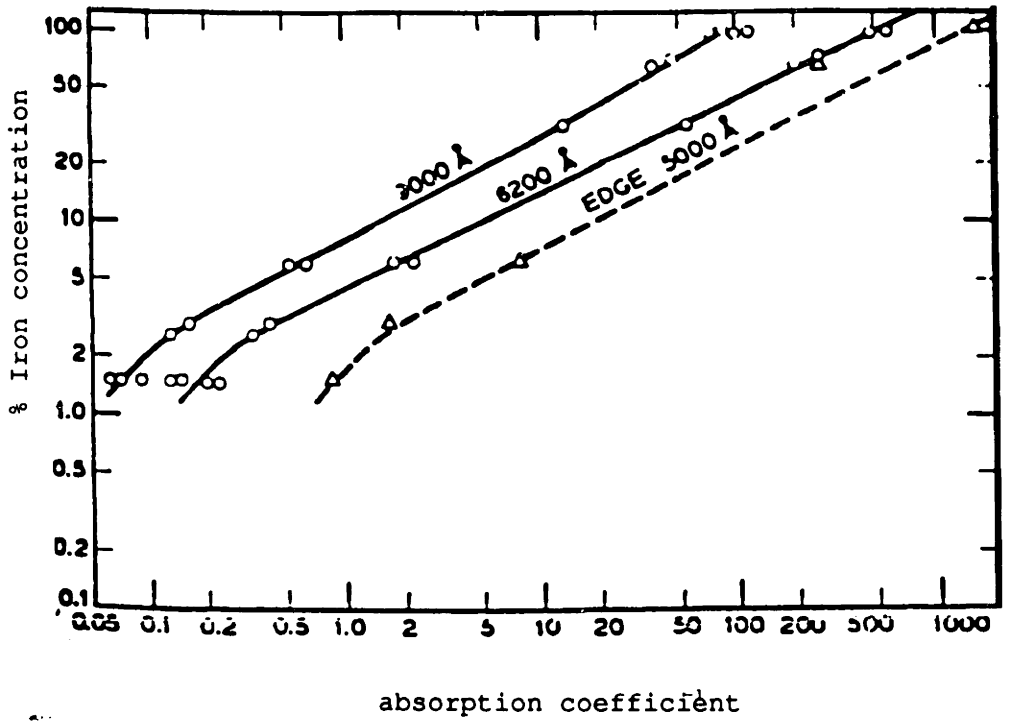

Figure 2.14. The dependence of absorption on iron concentration in Fe:$Y_3Fe_xGa_{5-x}O_{12}$. The top two curves are for crystal field transitions, while the bottom curve is at an arbitrary wavelength close to the absorption edge. The slopes are approximately equal to 1.8. After Wood and Remeika.[33]

This interpretation was used to explain the large oscillator strengths of the crystal field transitions. The ground state of the Fe^{3+} ions in either site contains a half-filled d-shell. Transitions to excited states of the ion require a spin flip and are therefore spin forbidden. Such transitions typically have oscillator strengths on the order of 10^{-7}.†† Yet, the observed oscillator strengths are on the order of 10^{-5} (see Table 2.4). If we assume the excitations to involve pairs of tetrahedral and octahedral iron, then the total spin change of the transition can remain zero if the spin flip of an ion is offset by a spin flip on

†† Transitions for the octahedral ion are also parity forbidden and expected oscillator strengths are on the order of 10^{-9}

an ion on the opposite sublattice. This is equivalent to producing a magnon or spin wave excitation. The interpretation was confirmed by van der Ziel *et al.*[37] who identified sidebands on the lowest energy absorption line of YIG which coincided with energies at peaks in the magnon density of states.

The second region of the absorption spectrum is in the range of 23,000 cm^{-1} to 30,000 cm^{-1}. Scott *et al.*[20] found that the absorption peaks implied by their Gaussian fit to the absorption spectrum in this region are an order of magnitude stronger than those assigned to transitions between crystal-field split levels. The first three of these levels can be seen in Figure 2.12, beginning at 23,000 cm^{-1}. Others can be seen in Figure 2.13. Further, they found that in gallium-substituted YIG, the oscillator strengths of these transitions depended upon the concentration of iron, indicating that the transitions also involve pairs of Fe^{3+} ions. It is suggested that the process responsible for these absorption lines is charge transfer between the iron sublattices.[38] These transitions are described as

$$\left[Fe^{3+}\right]+\left(Fe^{3+}\right)+h\upsilon \rightarrow \left[Fe^{2+}\right]+\left(Fe^{4+}\right) \quad ,$$
$$\left[Fe^{3+}\right]+\left(Fe^{3+}\right)+h\upsilon \rightarrow \left[Fe^{4+}\right]+\left(Fe^{2+}\right) \quad .$$

The four transitions of this type that were identified by Scott and Page[38] are listed in Table 2.5.

The third region of the spectrum is for energies greater than 35,000 cm^{-1}. Scott and Page[38] found very intense transitions in this region with oscillator strengths on the order of 0.1. The first of these transitions can be seen in Figure 2.13 at 35,000 cm^{-1}. Unlike the transitions assigned to charge transfer between the iron sites, the strength of these strong transitions did not change with the concentration of iron in gallium substituted YIG. These transitions were assigned to the process of charge transfer from the oxygen ions to the Fe^{3+} ions.

2.4 Magneto-optic Spectra

The magneto-optic spectra of YIG are less well understood than even that of the absorption spectra. The Faraday rotation and the magnetic circular dichroism of YIG are

---

37 J. P. van der Ziel, J. F. Dillon and J. P. Remeika, Proc. 18th Conf. Mag. and Mag. Mat., 254 (1971).

38 G. B. Scott and J. L. Page, Phys. Stat. Solidi. b 79, 203 (1977).

shown in Figures 2.15 - 2.17. The Faraday rotation is the resultant rotation of polarized light as it propagates through a magnetic material. It is the result of differing indices of refraction for right and left circularly polarized light. Magnetic circular dichroism is the difference in the absorption coefficients for right and left circularly polarized light. The circular dichroism manifests itself as an ellipticity in an initially linearly polarized light.

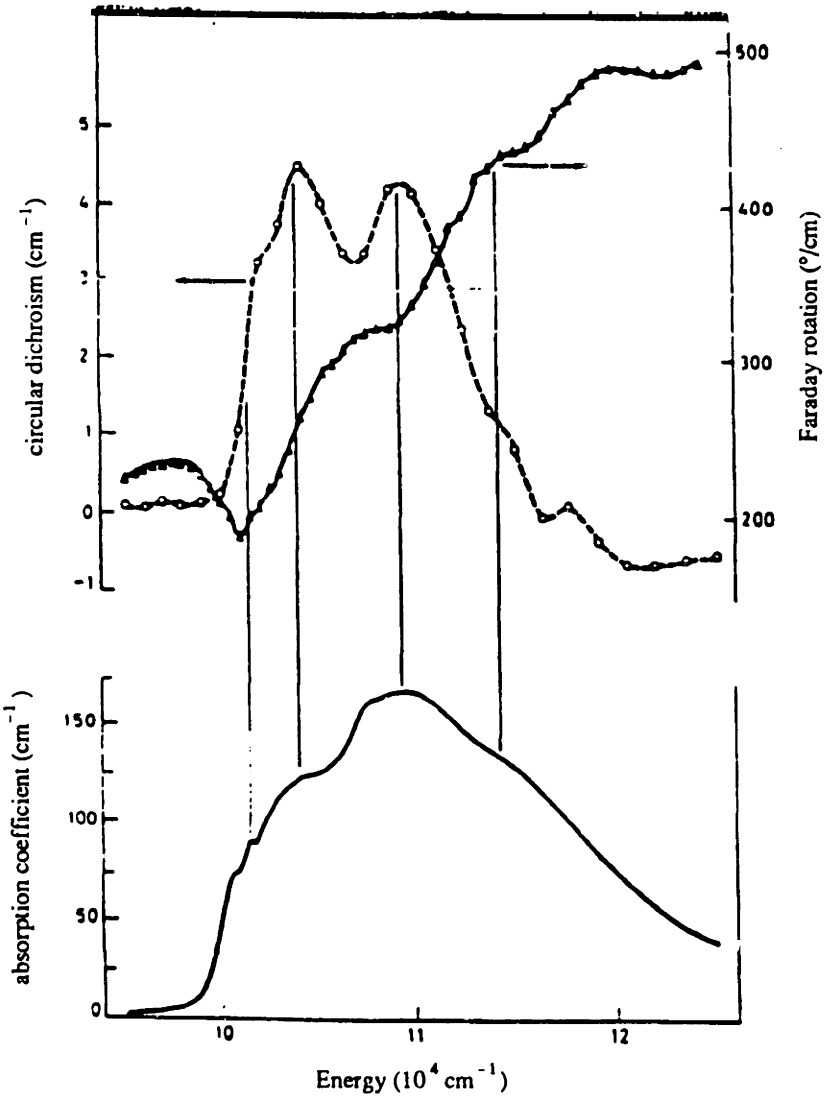

Figure 2.15. The Faraday effect and absorption spectra of YIG at 77 K from 9,500 cm^{-1} to 12,500 cm^{-1}. After Scott *et al.*[39]

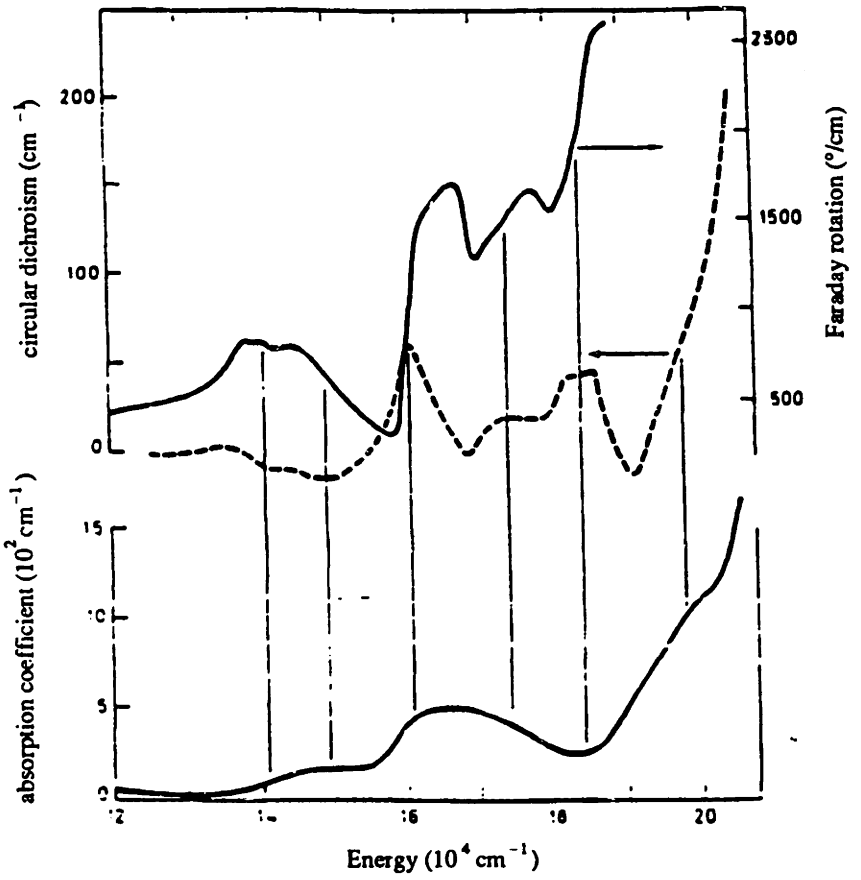

Figure 2.16. The Faraday effect and absorption spectra of YIG at 77 K from 12,000 cm^{-1} to 21,000 cm^{-1}. After Scott *et al.*[39]

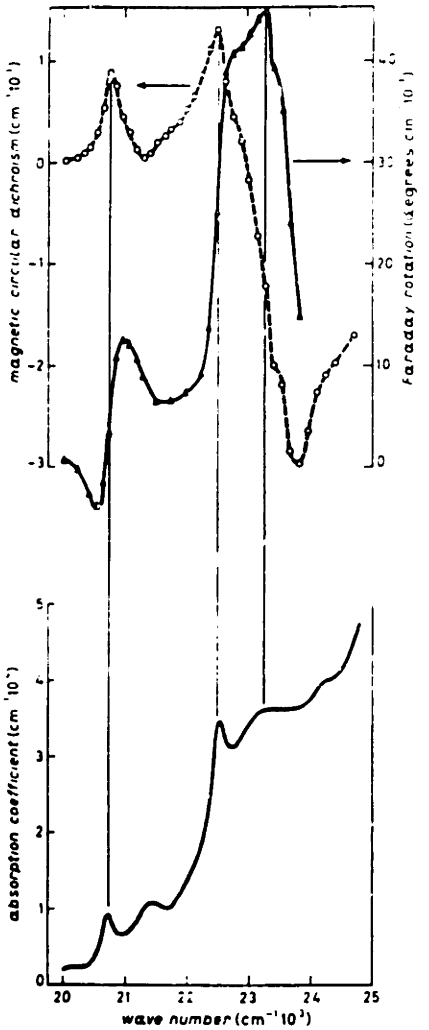

Figure 2.17. The Faraday effect and absorption spectra of YIG at 77 K from 20,000 cm^{-1} to 25,000 cm^{-1}. After Scott *et al.*[39]

Also shown in Figures 2.15 - 2.17 are the absorption spectra for the same spectral range. Scott *et al.*[39] have been able to match some of the absorption peaks of YIG with the magneto-optic transitions implied by the Faraday rotation and the magnetic circular dichroism spectra. To do this, it was assumed that all magneto-optic transitions are *paramagnetic* transitions with the exception of that at 23,100 cm^{-1} which appears to be a *diamagnetic* transition.†††

A paramagnetic transition arises from a magnetically-split ground state (see Figure 1.4) where the different indices of refraction for right and left circularly polarized

---

[39] G. B. Scott, D. E. Lacklison and J. L. Page, Physical Review B 12, 2562 (1975).

††† These two types of transitions derive there names from their temperature dependence and do not necessarily relate to the magnetization of the material.

light are due to the thermal distribution of ions in the ground state manifold. A diamagnetic transition, however, arises from a magnetically-split excited state (Figure 1.3), the difference of the indices of refraction for right and left circularly polarized light comes from the difference in the transitions energies. Based on this description, one would expect only diamagnetic transitions in YIG since the electronic ground state of Fe^{3+} is a singlet and hence can not be split. Yet, it would appear that the magneto-optic transitions are predominately paramagnetic. This point has not yet been explained.

Lastly, in Figure 2.18, is shown the magneto-optic spectra of YIG from 2 to 5 eV (620 - 250 nm). It is more physically correct to talk about magneto-optic phenomena in terms of the dielectric tensor, ε, which, for a cubic material, can be written as

$$\varepsilon = \begin{bmatrix} \varepsilon_0 & -i\varepsilon_1 & 0 \\ +i\varepsilon_1 & \varepsilon_0 & 0 \\ 0 & 0 & \varepsilon_0 \end{bmatrix} ,$$

for a magnetic field applied in the z-direction. The off-diagonal elements of this matrix, represented by the quantity ε_1, are responsible for magneto-optic properties. The real and imaginary parts of ε_1 for YIG are shown in Figure 2.18. Also shown in Figure 2.18 are the off-diagonal elements for $Bi_{0.25}Y_{2.75}Fe_5O_{12}$. As can be seen, ε_1 is increased in magnitude over that of YIG. Explaining this increase is the subject of this work.

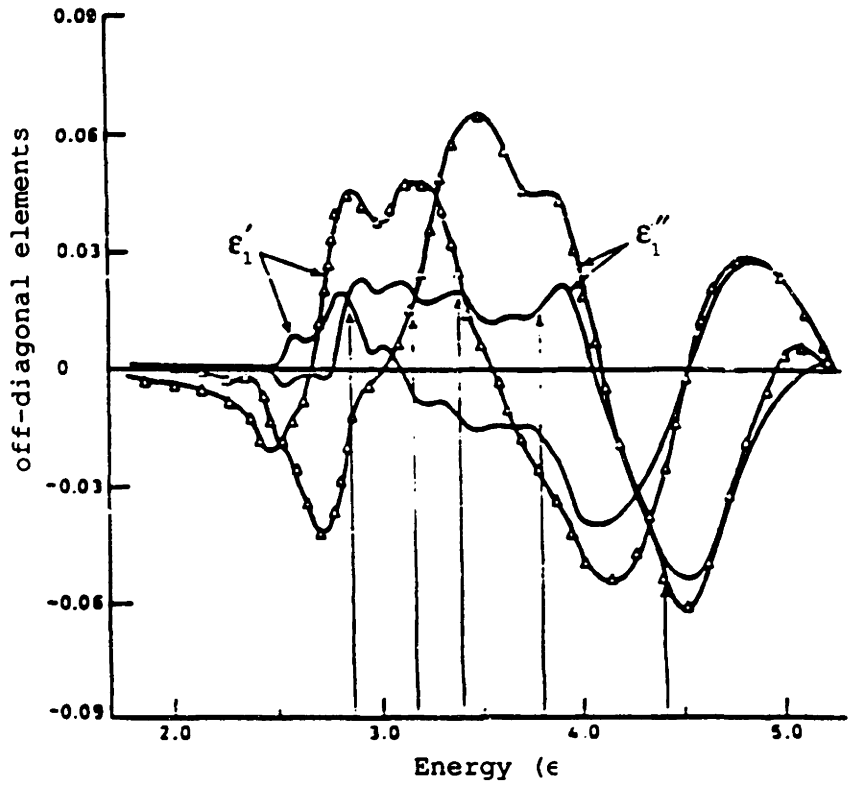

Figure 2.18. The off-diagonal elements of the dielectric tensor for YIG (solid lines) and $Bi_{0.25}Y_{2.75}Fe_5O_{12}$ (triangles). The off-diagonal elements are represented by the quantity ε_1. Arrows indicate energies of transitions found in absorption spectrum. After Wittekoek *et al.*[14]

2.5 Summary

We have given an overview of the properties of magnetic garnets. While the crystallographic and magnetic properties are somewhat well understood, the origins of the optical and magneto-optical properties of the magnetic garnets are far from resolved. In this thesis, we investigate the origins of these two properties and will focus on their change when bismuth is substituted into iron garnets.

3. Theory of Optical Transitions

In this chapter, we derive the quantum mechanical expression for the dielectric tensor of a cubic material. This is done by first finding the susceptibility tensor. We will use the expressions found for the complex diagonal and off-diagonal elements of the tensor to fit to experimental data.

The real and imaginary parts of the diagonal elements form the familiar dielectric constant of a material. The off-diagonal elements can take on two forms depending upon the configuration of the states involved in the transition. The two types of transitions that produce a non-zero off-diagonal element of the dielectric tensor are *diamagnetic* transitions and *paramagnetic* transitions. The diamagnetic transitions originate from magnetically-split excited states, while paramagnetic transitions originate from magnetically split ground states. The two types of transitions possess different lineshapes and thus, lend themselves as useful tools for determining the arrangement of states in a magnetic material.

The derivation of the dielectric tensor that follows uses the density matrix approach of quantum statistical mechanics[40]. This particular derivation is based on that of Shen[41].

3.1 Derivation of the Dielectric Tensor

For a system described by the wavefunction $|\psi\rangle$ in contact with a thermal reservoir, the density matrix operator, $\hat{\rho}$, is defined as,

$$\hat{\rho} = \overline{|\psi\rangle\langle\psi|} \quad , \tag{3-1}$$

where the bar indicates an ensemble average of the system. This is where the statistical mechanics comes in. An ensemble average of an observable, P, is then given by

$$\langle P \rangle = \overline{\langle\psi|P|\psi\rangle} = \mathrm{Tr}(\hat{\rho}P) \quad . \tag{3-2}$$

The time evolution of the density matrix operator is given by Ehrenfest's relation†

---

40 R. K. Pathria, Statistical Mechanics (Permagon Press, Oxford, 1985).

41 Y. R. Shen, The Principles of Nonlinear Optics, John Wiley and Sons, New York, p. 13 (1984).

† The equation of the time evolution of a density, such as (3-3) is usually called Liouville's equation.

$$\frac{\partial \hat{\rho}}{\partial t} = \frac{1}{i\hbar}[\mathcal{H}, \hat{\rho}] \quad . \tag{3-3}$$

We describe the Hamiltonian of the system as

$$\mathcal{H} = \mathcal{H}_0 + \mathcal{H}_{int} + \mathcal{H}_{random} \quad . \tag{3-4}$$

$\mathcal{H}_0$ is the Hamiltonian of the unperturbed system. The eigenstates of the unperturbed system, $\{|n\rangle\}$, and the eigenstate energies $\{E_n\}$ obey the relation

$$\mathcal{H}_0|n\rangle = E_n|n\rangle \quad . \tag{3-5}$$

The interaction Hamiltonian, $\mathcal{H}_{int}$, describes the interaction between light and electrons. We will treat this interaction semi-classically; that is, the light is described as an electromagnetic field and the electrons are in quantum states. We will neglect the magnetic interaction and thus have

$$\mathcal{H}_{int} = e\mathbf{r} \cdot \mathbf{E} \quad . \tag{3-6}$$

$\mathcal{H}_{random}$ is a phenomenological quantity that describes the random perturbations on the system due to contact with a thermal reservoir. These perturbations are responsible for stimulating transitions from excited states back to the ground state, in other words, the relaxation of the system.

With these three components of the Hamiltonian known, we can write (3-3) in more detail.

$$\frac{\partial \hat{\rho}}{\partial t} = \frac{1}{i\hbar}[\mathcal{H}_o, \hat{\rho}] + \frac{1}{i\hbar}[\mathcal{H}_{int}, \hat{\rho}] + \left(\frac{\partial \hat{\rho}}{\partial t}\right)_{relax} \quad , \tag{3-7}$$

where

$$\left(\frac{\partial \hat{\rho}}{\partial t}\right)_{relax} \equiv \frac{1}{i\hbar}[H_{random}, \hat{\rho}] \quad .$$

We define $\left(\frac{\partial\hat{\rho}}{\partial t}\right)_{relax}$ because we do not actually know $\mathcal{H}_{random}$. We will ,however, be able to determine its effect experimentally. We now give some descriptions for the matrix elements of this quantity.

For the matrix elements of $\left(\frac{\partial\hat{\rho}}{\partial t}\right)_{relax}$ we look at the separate cases of the diagonal elements and the off-diagonal elements. The diagonal elements correspond to a change in the population of a state $|n\rangle$. We can describe this by first defining a "thermaliy-induced" transition rate, W_{ij}, which is the rate at which the system in the state $|i\rangle$ makes a transition to the state $|j\rangle$. We can then write for a diagonal matrix element,

$$\left\langle n\left|\left(\frac{\partial\hat{\rho}}{\partial t}\right)_{relax}\right|n\right\rangle = \left(\frac{\partial\rho_{nn}}{\partial t}\right)_{relax} = \sum_{n'}\left[W_{n'\to n}\rho_{n'n'} - W_{n\to n'}\rho_{nn}\right] \quad . \tag{3-8}$$

At thermal equilibrium, (i.e. no applied electric field)

$$\left(\frac{\partial\rho^{(0)}_{nn}}{\partial t}\right)_{relax} = \sum_{n'}\left[W_{n'\to n}\rho^{(0)}_{n'n'} - W_{n\to n'}\rho^{(0)}_{nn}\right] = 0 \quad . \tag{3-9}$$

Combining (3-8) and (3-9), we then get

$$\frac{\partial}{\partial t}\left[\rho_{relax} - \rho^{(0)}\right]_{nn} = \sum_{n'}\left[W_{n'\to n}\left(\rho_{n'n'} - \rho^{(0)}_{n'n'}\right) - W_{n\to n'}\left(\rho_{nn} - \rho^{(0)}_{nn}\right)\right] \quad . \tag{3-10}$$

For the off-diagonal elements, we assume that there is a characteristic exponential decay rate, $\Gamma_{nn'}$, so that

$$\left(\frac{\partial\rho_{nn'}}{\partial t}\right)_{relax} = -\Gamma_{nn'}\rho_{nn'} \quad . \tag{3-11}$$

We now have all the components of (3-7) and can solve for the elements of the density matrix, ρ. It is not possible to do this in a closed form. Instead, we expand all quantities in orders of the applied electric field. Thus,

$$\rho = \rho^{(0)} + \rho^{(1)} + \rho^{(2)} + \quad \cdots \quad ,$$
$$\mathcal{H} = \mathcal{H}^{(0)} + \mathcal{H}^{(1)} + \mathcal{H}^{(2)} + \quad \cdots \quad , \tag{3-12}$$

Note that $\mathcal{H}_{int}$ is first order in the applied electric field. Applying (3-12) to (3-7), we get,

$$\frac{\partial \hat{\rho}^{(n)}}{\partial t} = \frac{1}{i\hbar}\left[H_o, \hat{\rho}^{(n)}\right] + \frac{1}{i\hbar}\left[H_{int}, \hat{\rho}^{(n-1)}\right] + \left(\frac{\partial \hat{\rho}^{(n)}}{\partial t}\right)_{relax} \quad . \tag{3-13}$$

For our purposes, we will only look at first order effects. Since the applied electric field is assumed to be sinusoidal in time, we assume that ρ is also sinusoidal in time. This leads to the relation

$$\frac{\partial}{\partial t}\hat{\rho}^{(n)}(\omega) = -i\omega\hat{\rho}^{(n)}(\omega) \quad . \tag{3-14}$$

By applying (3-11) and (3-14) to (3-13) we get an expression for the first-order density matrix.

$$\rho^{(1)}_{nn'}(\omega) = \frac{1}{\hbar}\frac{\langle n|H_{int}|n'\rangle}{\omega - \omega_{nn'} + i\Gamma_{nn'}}\left(\rho^{(0)}_{n'n'} - \rho^{(0)}_{nn}\right) \quad , \tag{3-15}$$

where

$$\hbar\omega_{nn'} = E_n - E_{n'} \quad .$$

The susceptibility tensor can now be found from (3-15) and from the ensemble average of the polarization vector, **P**, as given in (3-2).

$$\left\langle \chi^{(1)}_{ij}(\omega)\right\rangle = \frac{\left\langle P^{(1)}_i(\omega)\right\rangle}{E_j(\omega)} = -Ne\frac{\left\langle r^{(1)}_i(\omega)\right\rangle}{E_j} = -Ne\frac{Tr\left\langle \rho^{(1)}(\omega) r^{(1)}_i(\omega)\right\rangle}{E_j} \quad . \tag{3-16}$$

The trace appearing in (3-16) is

$$Tr\left(\rho^{(1)}(\omega) r_i\right) = \sum_n \sum_{n'} \left\langle n|\rho^{(1)}(\omega)|n'\right\rangle\left\langle n'|r_i(\omega)|n\right\rangle \quad , \tag{3-17}$$

leading to a susceptibility of

$$\chi_{ij}^{(1)}(\omega) = -\frac{Ne^2}{\hbar}\sum_{n}\sum_{n'}\frac{(r_j)_{nn'}(r_i)_{n'n}}{\omega-\omega_{nn'}+i\Gamma_{nn'}}\left(\rho_{n'n'}^{(0)}-\rho_{nn}^{(0)}\right) \quad , \tag{3-18}$$

We can put (3-18) in a different form by splitting the summations over states into two summations, one over the ground states of the system and the other over the excited states of the system. Since the excited states are not populated at thermal equilibrium (e.g. $\rho_n = 0$), we get

$$\chi_{ij}^{(1)}(\omega) = -\frac{Ne^2}{\hbar}\sum_{g}\sum_{n}\left[\frac{(r_i)_{ng}(r_j)_{gn}}{\omega+\omega_{ng}+i\Gamma_{ng}}-\frac{(r_j)_{ng}(r_i)_{gn}}{\omega-\omega_{ng}+i\Gamma_{ng}}\right]\rho_g^{(0)} \quad , \tag{3-19}$$

where n represents the excited states and g represents the ground states. Finally, the dielectric tensor will be given by

$$\varepsilon_{ij}^{(1)}(\omega) = \delta_{ij} + 4\pi\chi_{ij}^{(1)}(\omega) \quad . \tag{3-20}$$

In the discussion that follows, we will assume that the material of interest is cubic and that magneto-optic effects arise from a magnetic field in the z-direction. This implies that all the diagonal elements are equal and only the ε_{xy} and ε_{yx} off-diagonal elements are non-zero. The dielectric tensor can then be written as

$$\varepsilon = \begin{bmatrix} \varepsilon_0 & -i\varepsilon_1 & 0 \\ +i\varepsilon_1 & \varepsilon_0 & 0 \\ 0 & 0 & \varepsilon_0 \end{bmatrix} \quad . \tag{3-21}$$

We proceed now to derive expressions for the quantities ε_0 and ε_1.

3.2 Diagonal Elements

Consider first the diagonal elements of the dielectric tensor. These three elements correspond to the dielectric constants of the material. As we have just mentioned, for a

cubic, the diagonal elements are all equal, having a value of ε_0. From (3-20), the expressions for the diagonal elements are (we have kept the subscripts of ε for generality)

$$\varepsilon_{ii}(\omega) = 1 + \omega_p^2 \sum_g \sum_n f_{ng}^i \frac{\left(\omega^2 - \omega_{ng}^2 - \Gamma_{ng}^2\right) - i\left(2\omega\Gamma_{ng}\right)}{\left(\omega^2 - \omega_{ng}^2 - \Gamma_{ng}^2\right)^2 + 4\omega^2\Gamma_{ng}^2} \rho_g^{(0)} \quad , \tag{3-22}$$

where

$$\omega_p^2 = \frac{4\pi N e^2}{m} \qquad \text{and} \qquad f_{ng}^i = \frac{2m\omega_{ng}}{\hbar} \left|\langle g|r_i|n\rangle\right|^2 .$$

The quantity ω_p^2 is called the plasma frequency and is proportional to the density of absorbers in the material[††] . The quantity f_{ng}^i is the oscillator strength of the electronic transition $|g\rangle \rightarrow |n\rangle$. The superscript denotes the particular polarization of the transition.

The frequency dependence of the dielectric constants is shown in Figure 3.1. We see that the lineshape of the real part is dispersive and the imaginary part is absorptive, as is expected. The maximum value of the imaginary part occurs at approximately the center frequency ω_0 where the value is

$$\varepsilon_0''(\omega_0) = \frac{\omega_p^2 f}{2\omega_0\Gamma} + O\left(\frac{\Gamma}{\omega_0}\right)^2 \quad . \tag{3-23}$$

The ratio of the width to the center energy is usually much less than one for optical transitions and we neglect it here.

Equation (3-23) allows us to determine the oscillator strength from ε_0''. The oscillator strength is

$$f = \frac{2\omega_0\Gamma\varepsilon_0''}{\omega_p^2} \mathcal{L}(\varepsilon_0) \quad . \tag{3-24}$$

The quantity $\mathcal{L}(\varepsilon_0)$ is the Lorenz-Lorentz correction. It accounts for the increased electric field seen inside a dielectric[42]. It is equal to

---

†† A useful relationship is $\omega_p^2 = 830.4\ (N/N_A)\ eV^2$ where N_A is Avogadro's number.

42 J. D. Jackson, *Electrodynamics* (John-Wiley, New York, 1986).

$$\mathcal{L}(\varepsilon_0)=\left(\frac{3}{n^2+2}\right)^2 \quad , \tag{3-25}$$

where n is the real part of the index of refraction.

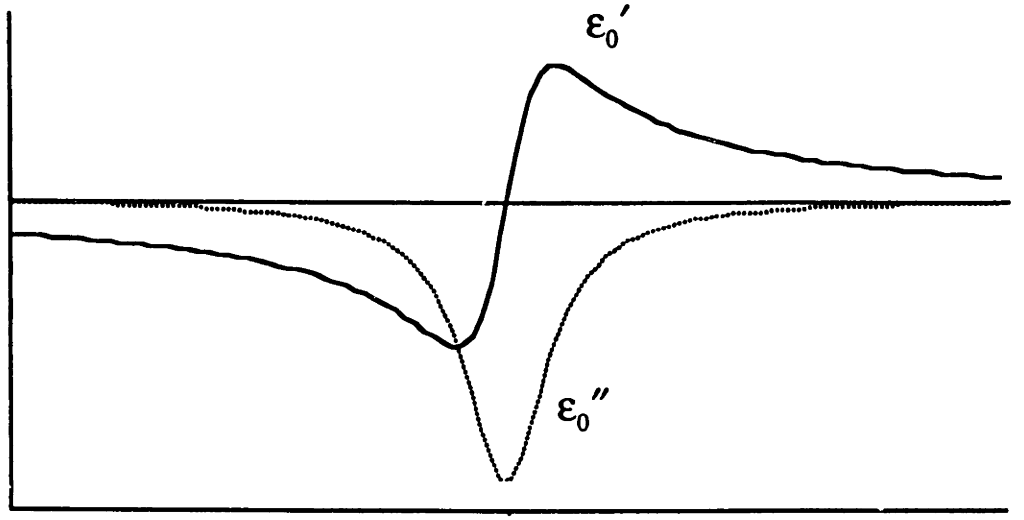

Figure 3.1. The real and imaginary part of the dielectric constant, ε_0. The real part of the dielectric constant is centered around the vacuum value of one.

3.3 Off-diagonal Elements

Consider now the off-diagonal elements of the dielectric tensor. We assume a cubic material magnetized in the z-direction. The off-diagonal elements of the dielectric tensor can then be represented by the quantity ε_1, as is shown in Equation (3-21). Finding an expression for ε_1 is not as straight forward as for the diagonal elements. However, in the geometry we have chosen (e.g. the magnetic field in the z-direction), which is often called the polar configuration, it can be shown that

$$\varepsilon_1(\omega)=\omega_p^2\sum_g\sum_n \frac{f_{ng}^+ - f_{ng}^-}{2}\frac{\left(\omega^2-\omega_{ng}^2-\Gamma_{ng}^2\right)-i\left(2\omega\Gamma_{ng}\right)}{\left(\omega^2-\omega_{ng}^2-\Gamma_{ng}^2\right)^2+4\omega^2\Gamma_{ng}^2}\frac{\omega+i\Gamma_{ng}}{\omega_{ng}}\rho_g^{(0)} \quad , \tag{3-26}$$

where

$$f_{ng}^i=\frac{2m\omega_{ng}}{\hbar}\left|\left\langle g\left|\frac{x\pm iy}{\sqrt{2}}\right|n\right\rangle\right|^2 .$$

Magneto-optic effects occur when the off-diagonal elements of the dielectric tensor are non-zero. This arises from two types of electronic transitions: *paramagnetic* and *diamagnetic.*

Paramagnetic transitions occur from a magnetic splitting of the ground state (see Figure 3.2). The ground state manifold is thermally populated and as such, there is a difference in the number of right and left handed states available for absorption. If we assume that the ground state splittings are small compared to the transition energy†††, ω_0, and also that all transition widths are equal, $\Gamma = \Gamma_{ng}$, then (3-26) becomes

$$\varepsilon_1(\omega) = \omega_p^2 \frac{(\omega^2 - \omega_0^2 - \Gamma^2) - i(2\omega\Gamma)}{(\omega^2 - \omega_0^2 - \Gamma^2)^2 + 4\omega^2\Gamma^2} \frac{\omega + i\Gamma_0}{\omega_0} \left[\frac{\sum_g f_g^+ \rho_g - \sum_g f_g^- \rho_g}{2} \right] \quad . \qquad (3\text{-}27)$$

The term in brackets is the effective difference in oscillator strengths Δf. We see that the value of ε_1 is directly proportional to Δf. Notice also that ε_1 for a paramagnetic transition is temperature dependent through the term ρ_g, having its greatest value at zero Kelvin and vanishing at infinite temperatures. This is the same temperature dependence as the susceptibility of a paramagnet, and hence, the name paramagnetic transition[4].

††† This is usually the case since in order to have a thermal distribution of states, the splitting of these states must be on the order of kT; typically ~ 1meV. The transition energies, however, are on the order of 1 eV.

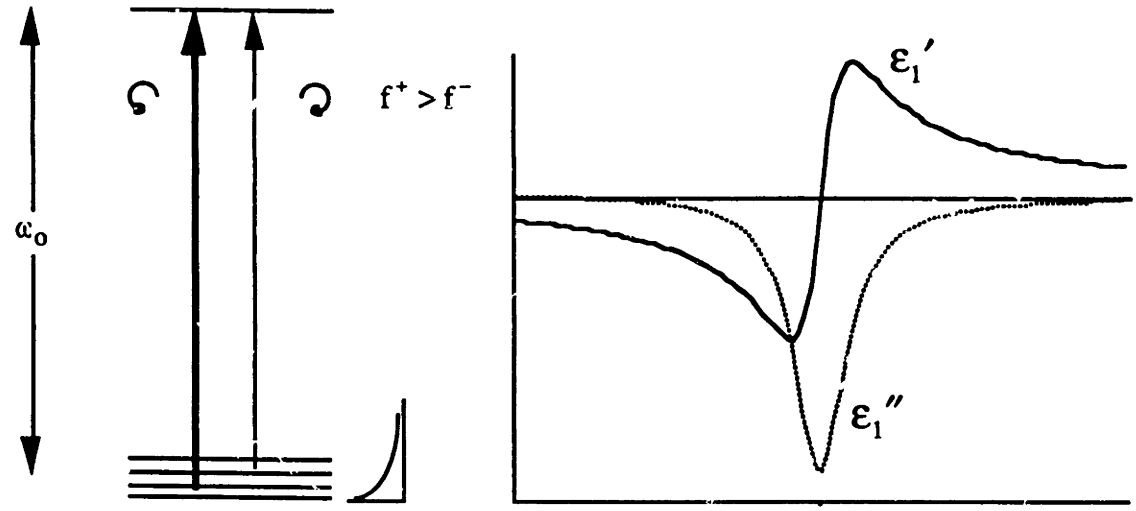

Figure 3.2. A paramagnetic transition. The ticks on the zero axis indicate the full width of 2Γ. The graph next to the ground state represents the population of the states.

The frequency dependence of ε_1 is shown in Figure 3.2 where we see that the real part of ε_1, has a dispersive lineshape and the imaginary part an absorptive lineshape. The value of ε_1'' at ω_0 to first order is

$$\varepsilon_1''(\omega_0) = \frac{\omega_p^2 \Delta f}{2\omega_0 \Gamma} \quad . \tag{3-28}$$

This leads to the relation

$$\frac{\varepsilon_1''(\omega_0)}{\varepsilon_0''(\omega_0)} = \frac{\Delta f}{f} \quad , \tag{3-29}$$

which will be of use in analyzing the magneto-optic spectra presented in Chapter 7.

A *diamagnetic* transition occurs due to a magnetic splitting of the excited state. The simplest example of this is illustrated in Figure 3.3 where the excited state is split into two components which differ from the central energy, ω_0, by an amount Δ. Due to the magnetic senses of these states, the upper state will have all of its oscillator strength in the positive sense, $f^+ = f/2$, while for the lower state, $f^- = f/2$. In the absence of a splitting (e.g. $\Delta = 0$), the contributions to ε_1 from these two states will exactly cancel. When there is a splitting, however, the slight difference in transition energy to these two states produces a non-zero ε_1 as is illustrated in Figure 3.4. There is no simple expression for ε_1

in the diamagnetic case. However, at the center frequency, ω_0, the real part of ε_1 has a value to first order, of

$$\varepsilon_1'(\omega_0) = \frac{\omega_p^2 f}{2\omega_o \Gamma} \frac{\Delta}{\Gamma} \quad . \tag{3-30}$$

This leads to the relation

$$\frac{\varepsilon_1'(\omega_0)}{\varepsilon_0''(\omega_0)} = \frac{\Delta}{\Gamma} \quad , \tag{3-31}$$

which will be useful in obtaining information from the magneto-optic spectra presented in Chapter 7.

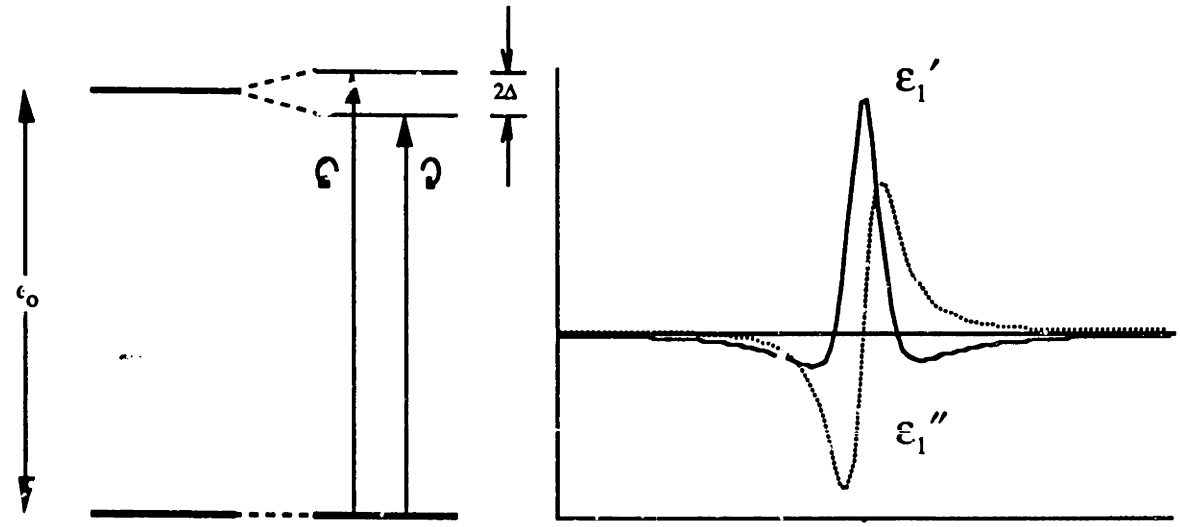

Figure 3.3. A diamagnetic transition. The ticks on the bottom axis indicate the full width of 2Γ.

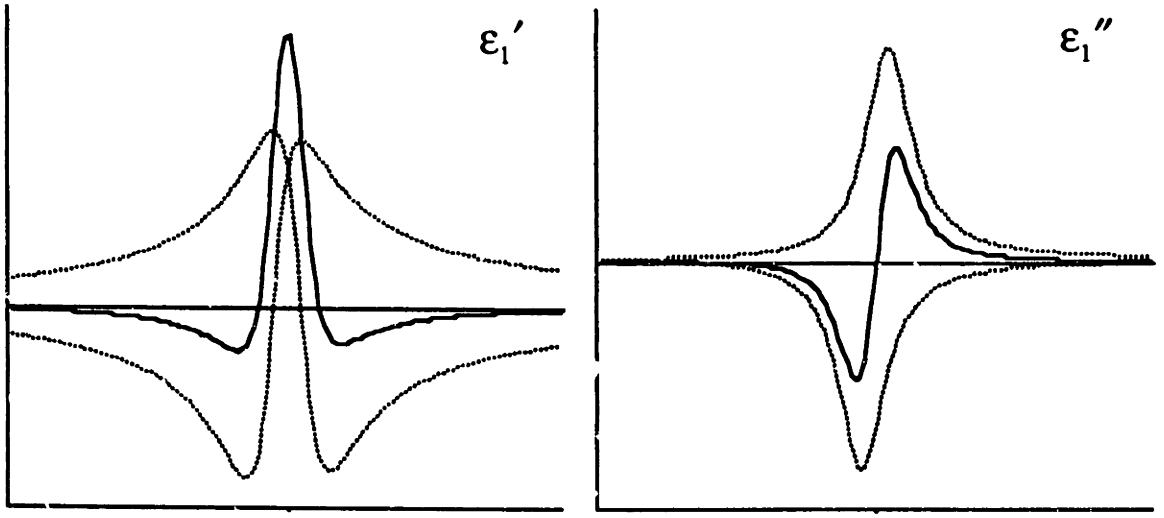

Figure 3.4. The off-diagonal of a diamagnetic transition arises from the shift in energy of two transitions with the opposite sense of rotation. Tick marks on the zero axis indicate the two transition energies. The dashed lines represent the components of e1 from right and left-handed absorbers. The solid line is the resultant difference.

Also, ε_1, is not explicitly temperature dependent as is the case with the susceptibility of a diamagnet. Any temperature dependence of ε_1 occurs due to a dependence of the oscillator strength or the linewidths on temperature[4]. The frequency dependence of ε_1 is shown in Figure 3.3 where we see that the real part has an absorptive lineshape and the imaginary part has a dispersive lineshape. This is the opposite of the paramagnetic case and because of this, the lineshapes of ε_1 can be used to determine the arrangement of the quantum states of a material.

3.4 Kramers-Kronig Relations

One last point in closing this Chapter is that the expressions for the elements of the dielectric tensor are analytic functions. As such, these expressions must obey Kramers-Kronig relations which relate the real and imaginary parts of analytic functions to each other. Mathematically, the Kramers-Kronig relations are

$$u(x_0) = \frac{1}{\pi} P \int_{-\infty}^{\infty} \frac{v(x)}{x - x_0} dx$$
$$v(x_0) = -\frac{1}{\pi} P \int_{-\infty}^{\infty} \frac{u(x)}{x - x_0} dx \quad , \tag{3-32}$$

where

$$f(x) = u(x) + iv(x) \quad ,$$

is an analytic function. Equations (3-32) allows one to find one part of an analytic function knowing the other. Equations (3-3) also imply the following:

$$\begin{pmatrix} \varepsilon'_{max} \\ \\ \varepsilon'_{min} \end{pmatrix} \leftrightarrow \begin{pmatrix} \left.\frac{d\varepsilon''}{d\omega}\right|_{max} \\ \\ \left.\frac{d\varepsilon''}{d\omega}\right|_{min} \end{pmatrix} \quad \text{and} \quad \begin{pmatrix} \varepsilon''_{max} \\ \\ \varepsilon''_{min} \end{pmatrix} \leftrightarrow \begin{pmatrix} \left.\frac{d\varepsilon'}{d\omega}\right|_{min} \\ \\ \left.\frac{d\varepsilon'}{d\omega}\right|_{max} \end{pmatrix} . \tag{3-33}$$

The above relations allows us to make a quick check on the sign and on the qualitative behavior of experimentally obtained dielectric data.

4. Photoelastic Modulated Ellipsometer

4.1 Ellipsometry

4.1.1 Introduction

Ellipsometry is the measurement of the change of polarization produced by reflection from a surface. The technique derives its name from the fact that the state of polarization of light is, in general, elliptical. The technique has been utilized for more than a century[43]. Its primary use has been to determine the dielectric constant of materials. In more recent decades, ellipsometry has been applied to measuring the thickness of thin films, often *in situ*, where it can be used to monitor film growth.

In this chapter, we describe a type of ellipsometer called a photoelastic modulated ellipsometer (PME). The PME is based on a device called a photoelastic modulator which was first described by James Kemp[44] in 1968. It was applied to ellipsometry a year later by Jasperson and Schnatterly[45] who developed the first PME to study metallic films. The PME described in this chapter is based on that of Bermudez and Ritz[46].

We will first introduce a system of matrices referred to as Jones' Matrices. Jones' matrices provide a method for calculating the change in polarization of light in an optical system. They will be used to describe the various configurations of the PME. Next, we will calculate the errors of the system. Finally, in closing the chapter, we describe the details of the PME constructed for this work.

4.1.2 Photoelastic Modulator

A photoelastic modulator is a device which modulates the state of polarization of light. It makes use of the *photoelastic effect* which is the birefringence exhibited by an optical material under mechanical stress. This stress is induced cyclically by a piezoelectric transducer and for this reason the device is sometimes called a piezo-birefringent or piezo-optical modulator.

---

43 For a review article on the history of ellipsometry, see A. C. Hall, Surface Science **16**, 1 (1969).

44 James C. Kemp, J. Opt. Soc. Am. **59**, 950 (1969).

45 S. N. Jasperson and Schnatterly, Rev Sci. Instr **40**, 761 (1969).

46 V. M. Bermudez and V. H. Ritz, Applied Optics **17**, 542 (1978).

As an example of a photoelastic modulator, we describe the one used in this work (see Figure 4.1). The modulator consists of two parts, an optical element and a piezoelectric transducer. The transducer is a bar of fused silica which is stressed by an oscillating applied electric field. The optical element of the modulator is also a fused silica bar. It is attached to the transducer which causes it to vibrate along its long direction. The transducer frequency is tuned to the natural resonant frequency of the optical bar (on the order of 10 kHz). The stress produced, and thus the birefringence of the material, is sinusoidal in profile with a peak at the center of the bar. The amount of birefringence depends upon the amplitude of the transducers vibration and, typically, only the center region of the bar is used to ensure that the birefringence is fairly constant across the light beam.

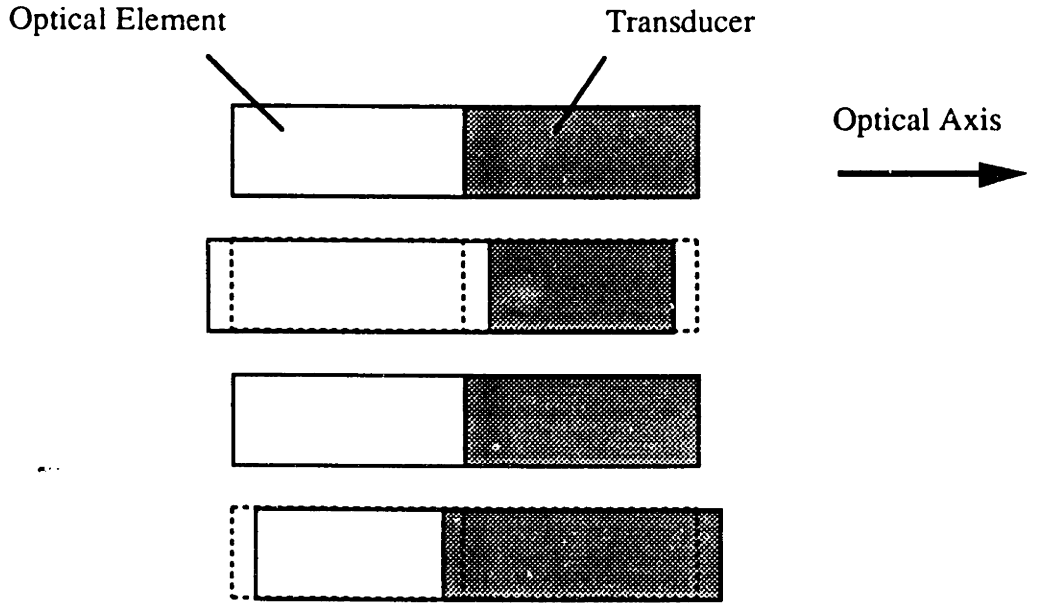

Figure 4.1. One cycle of a photoelastic modulator with a sinusoidal electric field applied perpendicular to the page.

The effect of a photoelastic modulator on polarized light is to modulate the phase between light polarized parallel and perpendicular to the stressed axis. If we modulate with a phase difference amplitude of 90°, we get the situation shown in Figure 4.2. Light polarized at 45° to the stressed axis is initially unaffected at the start of the modulation cycle. As the cycle progresses, the exiting light becomes elliptically polarized and eventually becomes right-circularly polarized. After returning again to linear polarized light at mid-cycle, the light becomes left-circularly polarized and then returns again to 45° linearly polarized light at the end of the cycle.

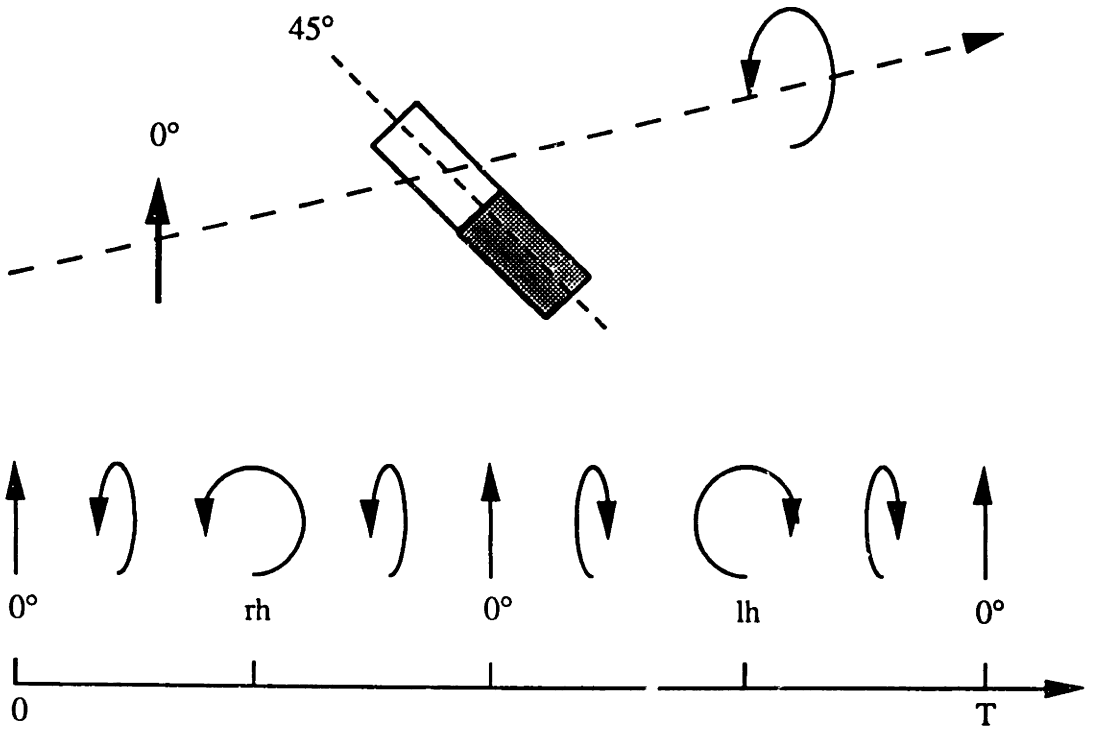

Figure 4.2. Effect of the photoelastic modulator on linearly polarized light. The amplitude of the phase difference is 90°.

4.2 Theory of Measurement

4.2.1 Jones' Matrices

We wish to describe the theory of operation of a photoelastic modulated ellipsometer (PME). To do this easily we introduce Jones' matrices. Jones' matrices and algebra were first introduced in 1943 by R. C. Jones[47] as a way to compute the change in polarization of light as it passes through an optical system. The basic premise is to define the polarization of the electric field of a light wave as a two dimensional vector. The basis of this vector can be any set of two orthogonal polarizations such as vertical and horizontal, left and right circular or two orthogonal elliptical polarizations. In the description that follows, we use x- and y-polarizations as our basis, where the x-axis will be the axis perpendicular to the plane of reflection of the sample under illumination, and the y-axis is parallel to the plane of reflection. The z-axis is the direction of propagation. In general, the polarization of the electric field of a light beam is written as

[47] R. C. Jones, J. Opt. Sci. Am. 31, 488 (1941).

$$\mathbf{E} = \begin{bmatrix} E_x \\ E_y \end{bmatrix} \quad . \tag{4-1}$$

Note, that the intensity of the light beam will be $I = \mathbf{E}^* \cdot \mathbf{E}$.

Optical components that affect the polarization of light are represented by matrices that operate on the left-hand side of the electric field vector:

$$\mathbf{E}_{final} = \mathbf{O} \cdot \mathbf{E}_{initial} \quad , \tag{4-2}$$

where $\mathbf{O}$ is a 2 x 2 matrix representing an optical component. Thus, we can compute the resultant polarization of a light beam passing through an optical system by doing a series of matrix multiplications. What we need to know are the matrix representations of the optical components of the system.

The first component we'll look at is a polarizer. A polarizer only lets light pass through that is polarized along its optical axis. If the optical axis of the polarizer is oriented along the x-axis, then the Jones matrix of the polarizer is

$$\mathbf{P} = \begin{bmatrix} 1 & 0 \\ 0 & 0 \end{bmatrix} \quad . \tag{4-3}$$

If we have the polarizer oriented at some angle θ to the x-axis, then we use a rotation matrix to rotate from the x-axis ($\theta = 0$) to the optical axis at θ:

$$\mathbf{P}(\theta) = \mathbf{P} \cdot \mathbf{R}(\theta) = \begin{bmatrix} 1 & 0 \\ 0 & 0 \end{bmatrix} \begin{bmatrix} \cos\theta & \sin\theta \\ -\sin\theta & \cos\theta \end{bmatrix} \quad . \tag{4-4}$$

Next is the photoelastic modulator. The modulator changes the phase difference between light polarized along its optical axis and light polarized orthogonal to its optical axis. For a modulator oriented along the x-axis,

$$\mathbf{M} = \frac{1}{\sqrt{2}} \begin{bmatrix} 1 & 0 \\ 0 & e^{i\delta_m} \end{bmatrix} \quad , \tag{4-5}$$

where the oscillating phase shift, $\delta_m = A\sin\omega t$. Here, ω is the modulation frequency and A is referred to as the *depth of modulation*. The prefactor of $1/\sqrt{2}$ gives the matrix a magnitude of one.

The Soliel-Babinet compensator also produces a phase shift between light polarized along its optical axis and light polarized perpendicular to its optical axis but the phase shift is constant. For a phase shift of δ_c, the compensator's Jones matrix is

$$C = \frac{1}{\sqrt{2}}\begin{bmatrix} 1 & 0 \\ 0 & e^{i\delta_c} \end{bmatrix} \quad . \tag{4-6}$$

For our use, however, the compensator will be used exclusively as a quarter-wave plate; that is $\delta_c = 90°$. Thus the compensator's matrix will be given by

$$C = \frac{1}{\sqrt{2}}\begin{bmatrix} 1 & 0 \\ 0 & i \end{bmatrix} \quad . \tag{4-7}$$

Lastly, we look at the Jones matrix of the sample. The sample reflects light polarized perpendicular to the plane of reflection with complex amplitude $r_\perp e^{i\delta_\perp}$ and light polarized in the plane of reflection with complex amplitude $r_\parallel e^{i\delta_\parallel}$. The sample matrix is thus

$$S = \begin{bmatrix} r_\perp e^{i\delta_\perp} & 0 \\ 0 & r_\parallel e^{i\delta_\parallel} \end{bmatrix} \propto \begin{bmatrix} 1 & 0 \\ 0 & \rho e^{i\Delta} \end{bmatrix} \quad , \tag{4-8}$$

where

$$\rho \equiv \frac{r_\parallel}{r_\perp} \qquad \text{and} \qquad \Delta \equiv \delta_\parallel - \delta_\perp \quad .$$

We ignore the prefactor $r_\perp e^{i\delta_\perp}$ since it will not play a role in the analysis that follows.

One final item to mention is that an incident light beam of unpolarized light is represented in an ad hoc manner by the vector

$$E_i = \begin{bmatrix} 1 \\ 1 \end{bmatrix} \quad . \tag{4-9}$$

We use this only if the light beam is incident upon a polarizer first, and hence, the beam becomes polarized and can be represented as a Jones' vector. E_i is <u>not</u> a Jones' vector. It

is merely a convenient way to express unpolarized light entering the system. If it were, it would represent light polarized at θ=45° with magnitude of $\sqrt{2}$.

4.2.2 CS configuration

We now wish to compute the effect of the different configurations of the PME on unpolarized light. The first configuration is the CS configuration (see Figure 4.3). The label CS refers to the quantities we obtain from this measurement. We find the resultant electric field of the measurement in Figure 4.3a using the Jones' matrices of the last section. The resultant electric field is

$$\begin{aligned}\mathbf{E}_f &= \mathbf{A}\cdot\mathbf{R}(+45°)\cdot\mathbf{S}\cdot\mathbf{M}\cdot\mathbf{R}(-45°)\cdot\mathbf{P}\cdot\mathbf{E}_i \\ &= \frac{1}{2\sqrt{2}}\begin{bmatrix}1+\rho e^{i\Delta}e^{i\delta_m}\\ 0\end{bmatrix} .\end{aligned} \tag{4-10}$$

The intensity measured by the photodetector is then

$$\begin{aligned}\mathbf{I} &= \mathbf{E}_f^*\cdot\mathbf{E}_f \\ &= \frac{1}{8}\left(1+\rho^2-2\rho\sin\Delta\sin\delta_m+2\rho\cos\Delta\cos\delta_m\right) .\end{aligned} \tag{4-11}$$

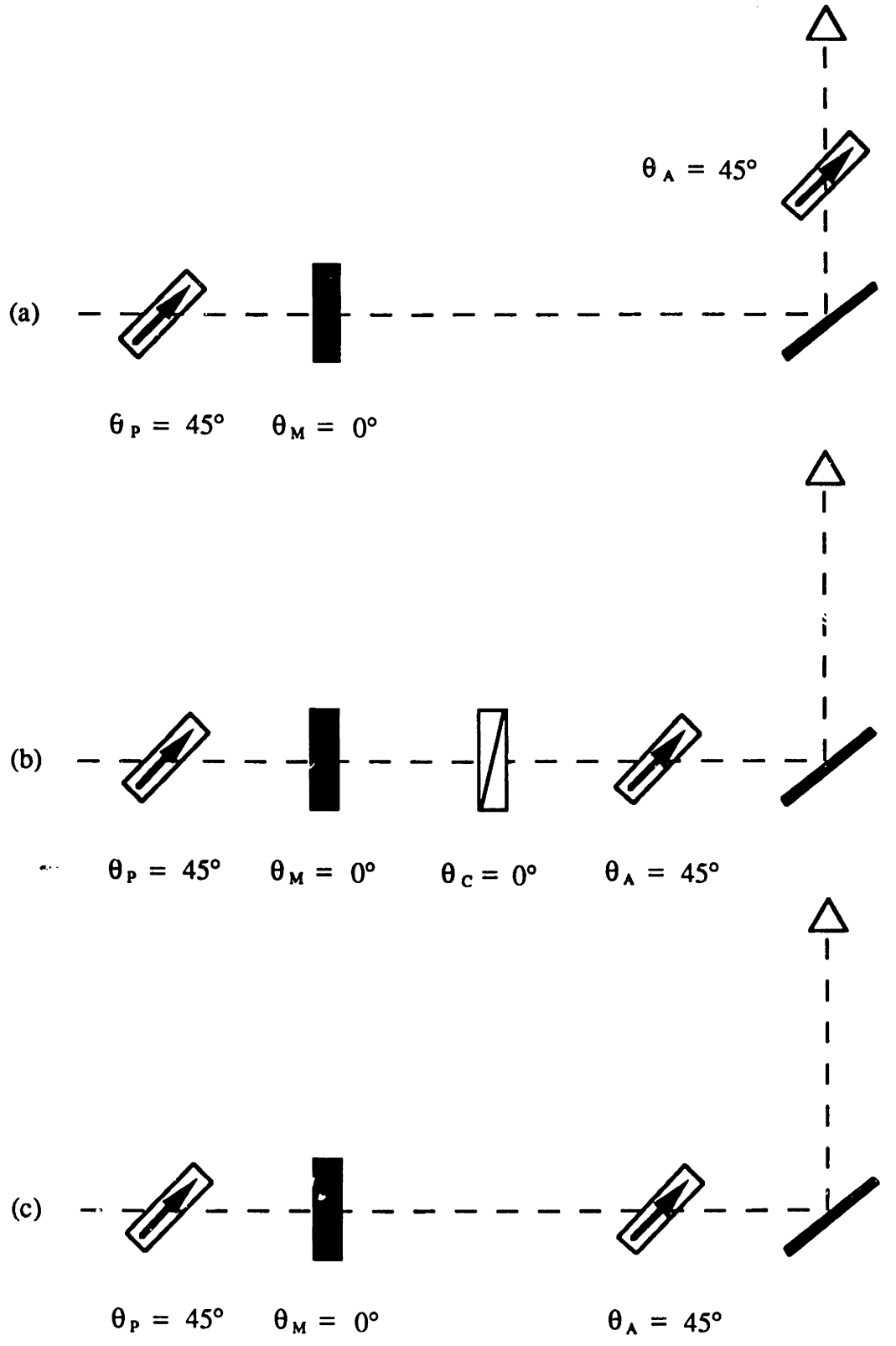

Figure 4.3. The CS configurations. a) measurement. b) 1f calibration. c) 2f calibration.

Note that we have sinusoidal functions of the modulator's phase shift, δ_m, which is itself a sinusoidal function. We can use the following identities to expand the sinusoidal terms into terms that are harmonics of the modulation frequency ω:

$$\begin{aligned}\sin(\delta_m) &= \sin(A\sin\omega t) = \sum_n 2J_{2n-1}(A)\cos[(2n-1)\omega t] \\ \cos(\delta_m) &= \cos(A\sin\omega t) = J_0(A) + \sum_n 2J_{2n}(A)\cos[2n\omega t] \quad ,\end{aligned} \tag{4-12}$$

where J_n is the n-th order Bessel function. Keeping only terms up to the second harmonic, the intensity of the CS measurement becomes

$$I^{CS} = \frac{1}{8}\left(1+\rho^2 - 2\rho\sin\Delta 2J_1(A)\cos\omega t + 2\rho\cos\Delta 2\left(J_0(A) + J_2(A)\cos 2\omega t\right) \quad ...\right) \quad . \tag{4-13}$$

By using lock-in amplifiers we can measure the individual frequency components of the intensity signal. We can then find ratios of the frequency components of the intensities which we define as follows:

$$R_{1f} \equiv \frac{I_f}{I_{dc}} \qquad \text{and} \qquad R_{2f} \equiv \frac{I_{2f}}{I_{dc}} \quad , \tag{4-14}$$

where I_f and I_{2f} are the ω and 2ω frequency components of the intensity and I_{dc} is the dc value of the intensity. For the CS measurement, the intensity ratios are

$$\begin{aligned}R_{1f}^{CS} &= -\frac{2\rho\sin\Delta}{1+\rho^2 + J_0(A)2\rho\cos\Delta}2J_1(A) \quad , \\ R_{2f}^{CS} &= +\frac{2\rho\cos\Delta}{1+\rho^2 + J_0(A)2\rho\cos\Delta}2J_2(A) \quad .\end{aligned} \tag{4-15}$$

Note that the denominators of the intensity ratios contain the term $J_0(A)$. We can make this term go to zero by setting the depth of modulation, A, to 2.405 radians (137.8°) which is the first zero of the zero order Bessel function. This gives the intensity ratios

$$\begin{aligned}R_{1f}^{CS} &= -S2J_1(A) \quad , \\ R_{2f}^{CS} &= +C2J_2(A) \quad ,\end{aligned} \tag{4-16}$$

where we have defined the quantities

$$S = \frac{2\rho \sin\Delta}{1+\rho^2} \quad ,$$
$$C = \frac{2\rho \cos\Delta}{1+\rho^2} \quad . \tag{4-17}$$

In actuality what is measured is

$$R_{1f}^{cs} = -\frac{a_{1f}}{a_{dc}} S 2J_1(A) \quad ,$$
$$R_{2f}^{cs} = +\frac{a_{2f}}{a_{dc}} C 2J_{21}(A) \quad , \tag{4-18}$$

where a_{dc}, a_{1f} and a_{2f} represent an effective gain for each of these channels. The effective gains take into account such things as the frequency response of the detector and amplifiers or the gain settings of the lock-in amplifiers. These quantities can be measured using the calibration configurations shown in Figure 4.3b and 4.3c.

The calibration of the 1f frequency channel can be obtained from the configuration shown in Figure 4.3b. The resultant electric field is

$$E_f = \frac{1+ie^{i\delta_m}}{4\sqrt{2}} \begin{bmatrix} 1 \\ \rho e^{i\Delta} \end{bmatrix} \quad , \tag{4-19}$$

which yields an intensity of

$$I^{call f} = \frac{1}{16}(1+\rho^2)[1-\sin\delta_m]$$
$$= \frac{1}{16}(1+\rho^2)[1-2J_1(A)\cos\omega t + \quad \ldots \quad] \quad . \tag{4-20}$$

Including effective gains for the frequencies, the intensity ratios become

$$R_{1f}^{call f} = \frac{a_{1f}}{a_{dc}} 2J_1(A) \quad ,$$
$$R_{2f}^{call f} = 0 \quad . \tag{4-21}$$

So we see that we will obtain S by dividing intensity ratios from the measurement and the 1f calibration:

$$S = -\frac{R_{1f}^{CS}}{R_{1f}^{cal1f}} \quad . \tag{4-22}$$

We do a similar thing for the calibration of the 2f frequency channel. The 2f calibration configuration is shown in Figure 4.3c. The configuration yields an intensity of

$$\begin{aligned} I^{cal2f} &= \frac{1}{8}(1+\rho^2)[1+\cos\delta_m] \\ &= \frac{1}{8}(1+\rho^2)[1+2J_2(A)\cos 2\omega t + \quad \ldots \quad] \quad , \end{aligned} \tag{4-23}$$

which gives the ratios

$$\begin{aligned} R_{1f}^{cal2f} &= 0 \quad , \\ R_{2f}^{cal2f} &= \frac{a_{2f}}{a_{dc}} 2J_2(A) \quad . \end{aligned} \tag{4-24}$$

By dividing R_{2f}^{CS} by the calibration ratio, we get C:

$$C = \frac{R_{2f}^{CS}}{R_{2f}^{cal2f}} \quad . \tag{4-25}$$

Knowing C and S is enough to solve for the two ellipsometric parameters ρ and Δ, and hence, the optical constants of the sample. It is helpful, however, to measure a third quantity, N, for reasons of accuracy and self consistency checking.

4.2.3 N configuration

In Figure 4.4 is shown the N configuration. The measurement configuration in Figure 4.4a gives us an intensity of

$$
\begin{aligned}
I^N &= \frac{1}{4}\left[1+\rho^2+(1-\rho^2)\cos\delta_m\right] \\
&= \frac{1}{4}\left[1+\rho^2+(1-\rho^2)2J_2(A)\cos 2\omega t + \quad \ldots \quad \right] \quad .
\end{aligned}
\tag{4-26}
$$

The intensity ratios for the N configuration are

$$
\begin{aligned}
R_{1f}^N &= 0 \\
R_{2f}^N &= \frac{a_{2f}}{a_{dc}}\frac{1-\rho^2}{1+\rho^2}2J_2(A) \\
&= \frac{a_{2f}}{a_{dc}}N2J_2(A) \quad ,
\end{aligned}
\tag{4-27}
$$

where we have defined the quantity

$$
N \equiv \frac{1-\rho^2}{1+\rho^2} \quad . \tag{4-28}
$$

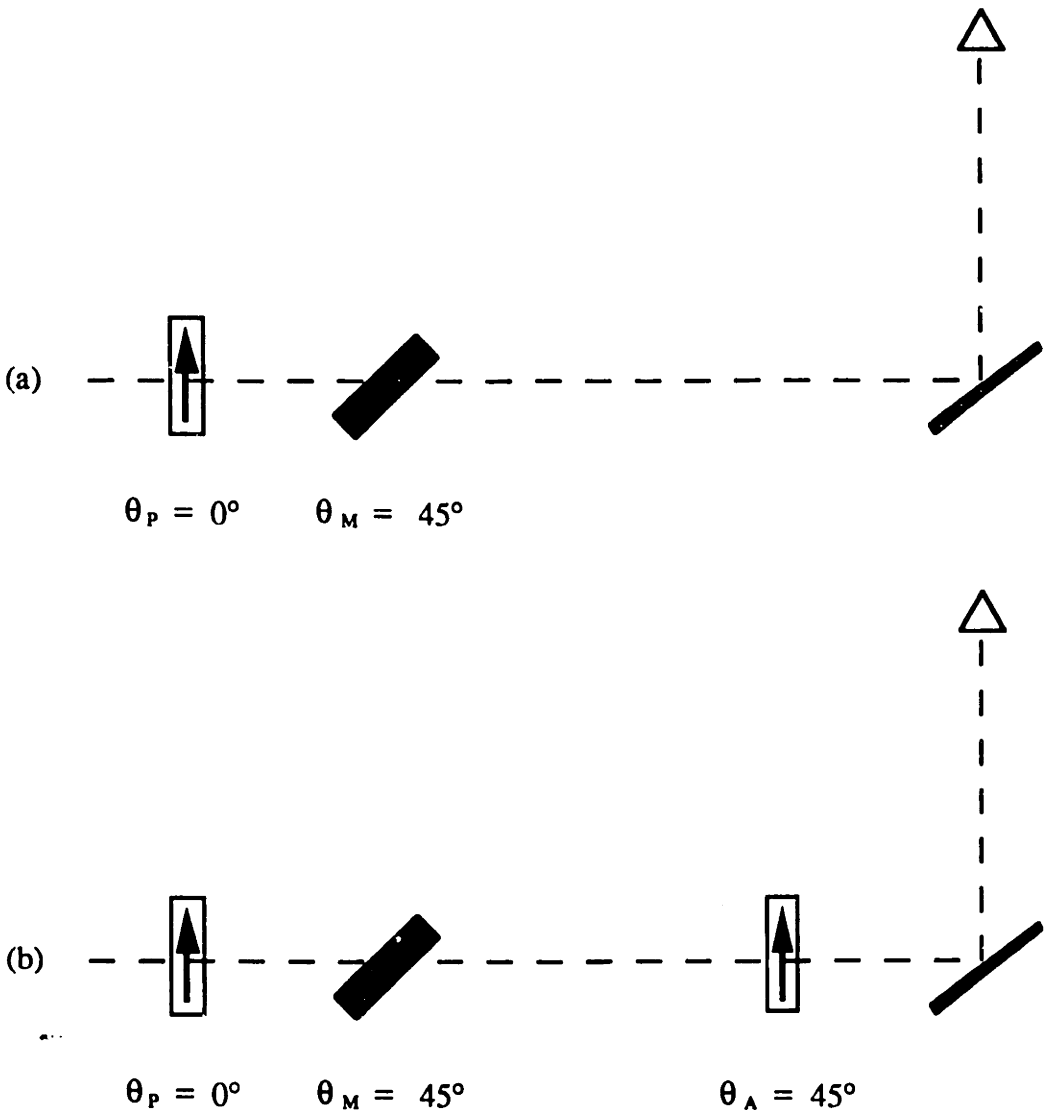

Figure 4.4. The N configurations. a) measurement. b) 2f calibration.

In Figure 4.4b is shown the configuration for the calibration of the 2f channel. The intensity of this configuration is

$$\begin{aligned} I^{cal2f} &= \frac{1}{4}(1+\cos\delta_m) \\ &= \frac{1}{4}(1+2J_2(A)\cos 2\omega t + \quad \ldots \quad) \quad , \end{aligned} \tag{4-29}$$

which yields the intensity ratios

$$R_{1f}^{cal2f} = 0 \quad ,$$
$$R_{2f}^{cal2f} = \frac{a_{2f}}{a_{dc}} 2J_2(A) \quad . \tag{4-30}$$

We see that, experimentally, we can find the quantity N by dividing the ratio R_{2f}^{N} by the 2f calibration

$$N = \frac{R_{2f}^{N}}{R_{2f}^{cal2f}} \quad . \tag{4-31}$$

4.2.4 NS configuration

One last independent configuration is the NS configuration shown in Figure 4.5. It is not used in this work, but is explained here for completeness. The measurement configuration is shown in Figure 4.5a. The intensity of this configuration is

$$\begin{aligned} I^{NS} &= \frac{1}{8}\left[1+\rho^2 - 2\rho\sin\Delta\sin\delta_m + (1-\rho^2)\cos\delta_m\right] \\ &= \frac{1}{8}\left[1+\rho^2 - 2\rho\sin\Delta 2J_1(A)\cos\omega t + (1-\rho^2)2J_2(A)\cos 2\omega t \quad \ldots \quad \right] \quad , \end{aligned} \tag{4-32}$$

which yields the intensity ratios (ignoring the effective gains)

$$R_{1f}^{NS} = S2J_1(A) \quad ,$$
$$R_{2f}^{NS} = N2J_2(A) \quad . \tag{4-33}$$

The 1f calibration in Figure 4.5b gives the ratios

$$R_{1f}^{cal1f} = 2J_1(A) \quad ,$$
$$R_{2f}^{cal1f} = 0 \quad , \tag{4-34}$$

and the 2f calibration shown in Figure 4.5c gives the ratios

$$R_{1f}^{cal2f} = 0 \quad ,$$
$$R_{2f}^{cal2f} = 2J_2(A) \quad . \tag{4-35}$$

Thus, we can find the quantities N and S by division of intensity ratios:

$$S = \frac{R_{1f}^{NS}}{R_{1f}^{cal1f}} \quad ,$$

$$N = \frac{R_{2f}^{NS}}{R_{2f}^{cal2f}} \quad . \qquad (4\text{-}36)$$

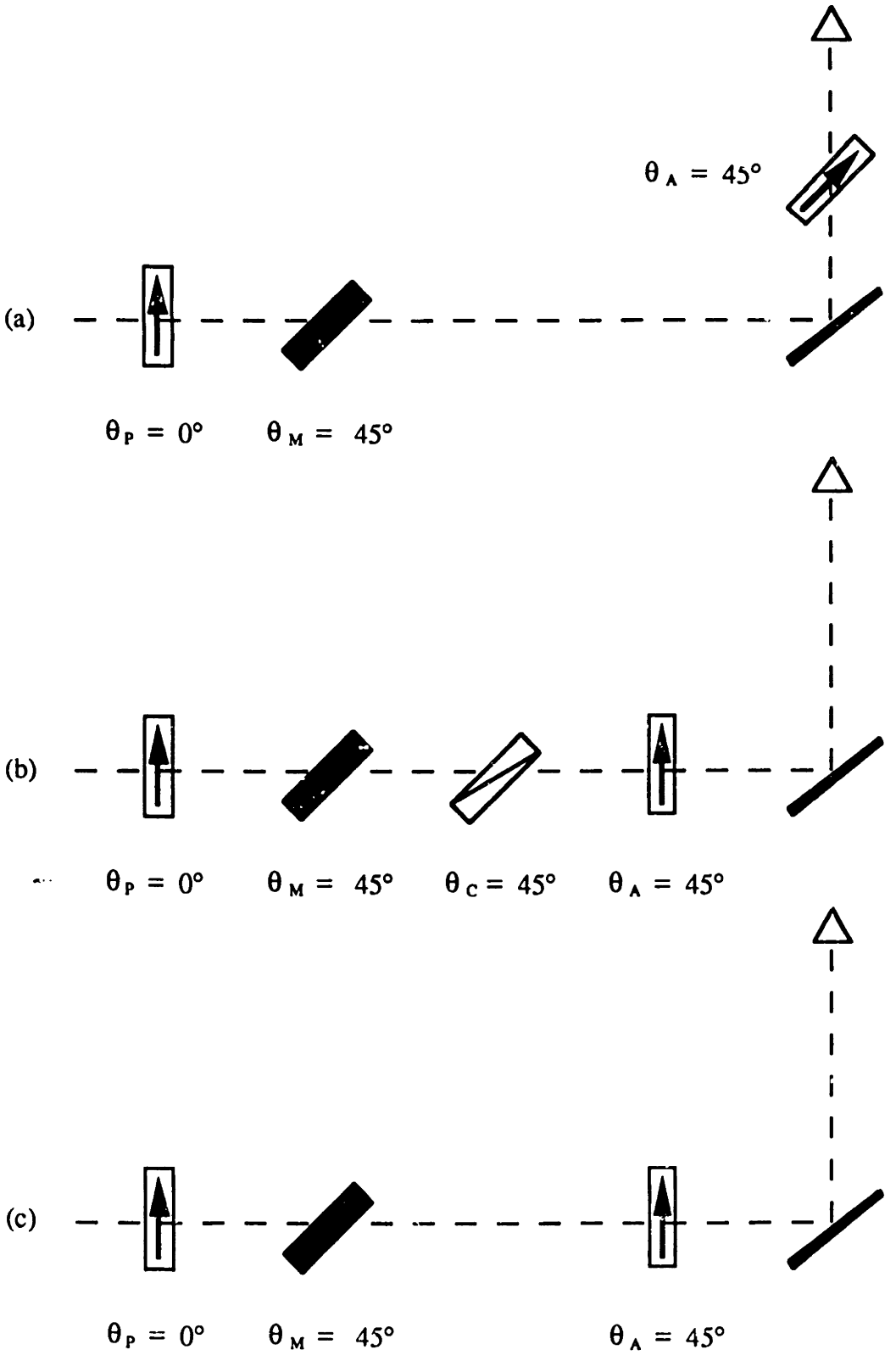

Figure 4.5. The NS configurations. a) measurement. b) 1f calibration. c) 2f calibration.

4.2.5 Extracting Data

Knowing N, C and S we can find the ellipsometric parameters ρ and Δ, and hence, the optical constants of the material. We actually only need two of the experimentally measured quantities to find the two unknowns ρ and Δ. One reason for measuring the three quantities N, C and S is to check the self consistency of the experiment. Note the following identity:

$$N^2 + C^2 + S^2 = 1 \ . \tag{4-37}$$

From our three experimentally found quantities then, we can define a quantity β:

$$\beta \equiv 1 - \left(N_{exp}^2 + C_{exp}^2 + S_{exp}^2 \right) , \tag{4-38}$$

whose closeness to zero indicates the degree of self-consistency of the PME.

Another reason for measuring the three quantities is that, usually for bulk dielectrics, N, C >> S, often by orders of magnitude. In these cases, N and C will be important in determining the real part of the dielectric constant and index of refraction. The imaginary part of these quantities is very small, however, and highly dependent upon a good measurement of S. So S is measured for its accuracy in determining these small quantities.

The goal in ellipsometry of any sort is to relate the ellipsometric parameters ρ and Δ (or equivalently for the PME, N, C and S) to the optical constants of the sample under study. This relation depends on the sample geometry and structure. Appendix B derives these relations for the case of an isotropic or cubic dielectric, which is the case for the materials studied in this work. The relations for other situations, such as multilayered dielectrics, can be found elsewhere[48].

We list below the equations for determining the optical constants of an isotropic dielectric material from the measured quantities N, C and S. For the dielectric constant,

---

[48] R. M. A. Azzam and N. M. Bashara, Ellipsometry and Polarized Light (North-Holland, Amsterdam, 1977).

$$\varepsilon = \varepsilon_0' + i\varepsilon_0''$$

$$\varepsilon_0' = \sin^2\theta\left[1 + \tan^2\theta\frac{N^2 - S^2}{(1+C)^2}\right] \qquad (4\text{-}39)$$

$$\varepsilon_0'' = \sin^2\theta\tan^2\theta\frac{2NS}{(1+C)^2} \quad .$$

From the complex dielectric constant we can get the complex index of refraction:

$$N = n + ik$$

$$n = \left[\frac{\left(\sqrt{\varepsilon_0'^2 + \varepsilon_0''^2}\right) + \varepsilon_0'}{2}\right]^{1/2} \qquad (4\text{-}40)$$

$$k = \left[\frac{\left(\sqrt{\varepsilon_0'^2 + \varepsilon_0''^2}\right) - \varepsilon_0'}{2}\right]^{1/2} \quad .$$

Also, the absorption coefficient can be related to the imaginary part of the index of refraction:

$$\alpha = \frac{4\pi}{\lambda}k \quad . \qquad (4\text{-}41)$$

4.3 Errors of Measurement

We now examine the errors of the PME. There are two types of errors with which we concern ourselves. The first are the component errors. These are errors occur because of the *non-idealness* of the optical components of the PME. The other type of error are associated with the precision errors of the components. These errors are due to the imprecision in the alignment of the components.

Much of the analysis shown here is based on the work done in reference[46] and deals with expanding errors to first order. A more elaborate method of error analysis can be done using the modified Jones' matrices developed by O'Handley[49]. In these matrices, the unmodulated and modulated components of light are treated separately, which lends

---

[49] R. C. O'Handley, J. Opt. Soc. Am. 63, 523 (1973).

them to be used in numerical calculations. A FORTRAN program using these matrices was developed by Bermudez[50] to calculate errors in a PME setup.

4.3.1 Component Errors and Corrections

In the previous section, we assumed all optical components to be ideal. Now, we show what the PME actually measures with non-ideal (realistic) components. The details of the mathematics of error analysis are presented in Appendix C and only the results are quoted here.

The non-idealness of the polarizer and analyzer comes from transmission of unwanted polarization. This transmission is characterized by the quantity α, which can be related to the extinction coefficient of the polarizers by the relation

$$\text{extinction} = \frac{I_{\perp}}{I_{\parallel}} = 2\alpha^2 \quad . \tag{4-42}$$

The extinction coefficient can be found by measuring the light intensity of two crossed polarizers. Also, manufacturers will often provide data on the extinction coefficient with the polarizers.

The photoelastic modulator can cause errors in three different ways. First, there is a static birefringence, δ_0. The static birefringence means that there is still some birefringence when there is zero applied electric field on the quartz plate of the modulator. The presence of a non-zero δ_0 means the sinusoidal phase shift of the modulator is centered around δ_0, rather than zero.

The photoelastic modulator can also have a different transmission coefficient for its stressed and unstressed axes. The ratio of the transmission coefficients, τ_0, characterizes this difference. As pointed out by Bermudez and Ritz[46], $\tau_0 = 1$ is an excellent approximation and we will assume it in our error analysis.

The third error of the modulator comes from an improper setting of the depth of modulation, A. Ideally, $A = A_0 = 2.405$ radians, at which the zero order Bessel function is equal to zero. Deviation from $A = A_0$ will cause the zero order Bessel function to have a non-zero value, leading to some of the 2f component of the intensity contributing to the dc intensity (see equation C-3).

---

50 V. M. Bermudez, Comput. Phys. Commun. 13, 207 (1977).

Lastly, the Soliel-Babinet compensator may not be set for 90° retardation. In general, the retardation will be 90° + δ_c, where δ_c is a small angle. It turns out that to first order, δ_c is negligible and thus, we drop it from our analysis.

In the following analysis, we look at the intensities of the two configurations of the PME using non-ideal components. In finding the intensities, we assume that our three error parameters α, δ_0, J_0 to be much less than one and we expand the intensities to first order. The mathematics is done in Appendix C and the results are just quoted here.

In the CS measurement of Figure 4.3a, the actual intensity ratios measured are

$$R_{1f}^{+} \equiv \frac{I_{1f}}{I_{dc}} = -\frac{S'}{1-2\alpha N + C'J_0(A)} 2J_1(A) \quad ,$$
$$R_{2f}^{+} \equiv \frac{I_{2f}}{I_{dc}} = +\frac{C'}{1-2\alpha N + C'J_0(A)} 2J_2(A) \quad , \tag{4-43}$$

where

$$C' = C - \delta_0 S \quad ,$$
$$S' = S + \delta_0 C \quad .$$

We can modify the CS measurement slightly by orienting the analyzer to ψ_A = -45°. The intensity-ratios for this modified configuration are

$$R_{1f}^{-} = +\frac{S'}{1-2\alpha N - C'J_0(A)} 2J_1(A) \quad ,$$
$$R_{2f}^{-} = -\frac{C'}{1-2\alpha N - C'J_0(A)} 2J_2(A) \quad . \tag{4-44}$$

We can average out the $J_0(A) \neq 0$ errors by averaging the intensity ratios of the two measurement configurations. We do this by defining the averages

$$\overline{R}_{1f}^{cs} \equiv \tfrac{1}{2}\left[R_{1f}^{+} - R_{1f}^{-}\right] = S'(1+2\alpha N)2J_1(A) \quad ,$$
$$\overline{R}_{2f}^{cs} \equiv \tfrac{1}{2}\left[R_{2f}^{+} - R_{2f}^{-}\right] = C'(1+2\alpha N)2J_2(A) \quad . \tag{4-45}$$

The same averaging scheme can be used for the 2f calibration of the CS measurement. The 2f calibration configuration of Figure 4.3c yields the ratios

$$R_{1f}^{cal2f} = -\delta_0 \frac{2J_1(A)}{1+J_0(A)} \quad ,$$

$$R_{2f}^{cal2f} = +\frac{2J_2(A)}{1+J_0(A)} \quad . \tag{4-46}$$

Orienting the analyzer to ψ_A=-45° produces the ratios

$$R_{1f}^{cal2f-} = +\delta_0 \frac{2J_1(A)}{1-J_0(A)} \quad ,$$

$$R_{2f}^{cal2f-} = -\frac{2J_2(A)}{1-J_0(A)} \quad . \tag{4-47}$$

We average these two configurations to remove the $J_0(A)$ dependence;

$$\overline{R}_{1f}^{cal2f} \equiv \tfrac{1}{2}\left[R_{1f}^{+} - R_{1f}^{-}\right] = -\delta_0 2J_1(A) \quad ,$$

$$\overline{R}_{2f}^{cal2f} \equiv \tfrac{1}{2}\left[R_{2f}^{+} - R_{2f}^{-}\right] = 2J_2(A) \quad . \tag{4-48}$$

The two 2f calibrations also provide us with a way to find $J_0(A)$. As shown in Appendix C;

$$J_0(A) = -\frac{R_{2f}^{cal2f+} + R_{2f}^{cal2f+}}{R_{2f}^{cal2f+} - R_{2f}^{cal2f+}} \quad . \tag{4-49}$$

There are no errors of concern in the 1f calibration. The intensity ratios are

$$R_{1f}^{cal1f} = -2J_1(A) \quad ,$$

$$R_{2f}^{cal1f} = -\delta_0 2J_2(A) \quad . \tag{4-50}$$

The error parameter δ_c does not contribute to the 1f calibration to first order, so, the PME is not very sensitive to the compensator's retardation.

In the N configuration, our only problem is with $J_0(A) \neq 0$. The N measurement of Figure 4.4a has the intensity ratios

$$R_{1f}^{N} = -\delta_0 \frac{N}{1+NJ_0(A)} 2J_1(A) \quad ,$$

$$R_{2f}^{N} = +\frac{N}{1+NJ_0(A)} 2J_2(A) \quad . \tag{4-51}$$

Unlike the CS measurement, there is not an averaging method for removing $J_0(A)$ terms from the N measurement. The same is true for the 2f calibration where we have

$$R_{1f}^{cal2f} = -\delta_0 \frac{1}{1+J_0(A)} 2J_1(A) \quad ,$$

$$R_{2f}^{cal2f} = +\frac{1}{1+J_0(A)} 2J_2(A) \tag{4-52}$$

We can now express C, N and S in terms of the measured quantities and the error parameters. If we define the measured values of C, N and S as C_{exp}, N_{exp} and S_{exp}:

$$C_{exp} \equiv \frac{\overline{R}_{2f}^{cs}}{\overline{R}_{2f}^{cal2f}} = C'(1+2\alpha N) \quad ,$$

$$N_{exp} \equiv \frac{R_{2f}^{N}}{R_{2f}^{cal2f}} = N\big(1+(1-N)J_0(A)\big) \quad , \tag{4-53}$$

$$S_{exp} \equiv \frac{R_{1f}^{cs}}{R_{1f}^{cal1f}} = S'(1+2\alpha N) \quad ,$$

then we find that

$$N = N_{exp}\Big[1-\big(1-N_{exp}\big)J_0(A)\Big] \quad ,$$

$$C' = C_{exp} \frac{1}{1+2\alpha N} \quad , \tag{4-54}$$

$$S' = S_{exp} \frac{1}{1+2\alpha N} \quad ,$$

where the subscript refers to the experimentally measured quantity. The primed quantities are defined in Equation (4-43).

4.3.2 Orientation Errors

While the component errors of the last section can be measured and corrected for, the precision or orientation errors described here cannot be corrected for and thus represent the uncertainty in the PME's measurements. The uncertainties of the measurements arise from the uncertainties in the angle of orientation of the optical components and the angle of incidence, θ_i, of the sample. These uncertainties translate into the uncertainties of the quantities we derive; the complex dielectric constant, ε_0 and the complex index of refraction, N. The uncertainty of a derived quantity can be expressed in the uncertainties of its dependent variables via partial derivatives[51]. For example, the uncertainty in the real part of the dielectric constant is expressed as

$$d\varepsilon_0'(N,C,S,\theta_i) = \frac{\partial \varepsilon_0'}{\partial N}dN + \frac{\partial \varepsilon_0'}{\partial C}dC + \frac{\partial \varepsilon_0'}{\partial S}dS + \frac{\partial \varepsilon_0'}{\partial \theta_i}d\theta_i \quad . \tag{4-55}$$

We then have to find the uncertainties in N, C and S which will depend on the precision of the optical components' orientations and the incident angle of the sample, θ_i. This analysis is carried out in Appendix D and the results are repeated here.

The uncertainties in the derived quantities $\varepsilon_0 = \varepsilon_0' + i\varepsilon_0''$ and $N = n + ik$ are

$$\begin{aligned}
d\varepsilon_0' &= \frac{1}{(1+C)^2}\left[|NdN| + |SdS| + \left|\frac{N^2 - S^2}{(1+C)}dC\right| + \left|\left[(1+C)^2 + 3\left(N^2 - S^2\right)\right]d\theta_i\right|\right] \quad , \\
d\varepsilon_0'' &= \varepsilon_0''\left[\left|\frac{dN}{N}\right| + \left|\frac{dS}{S}\right| + \left|\frac{2C}{1+C}\frac{dC}{C}\right| + \left|6d\theta_i\right|\right] \quad , \\
dn &= \frac{1}{4n\sqrt{\varepsilon_0'^2 + \varepsilon_0''^2}}\left[\left|\varepsilon_0' d\varepsilon_0'\right| + \left|\varepsilon_0'' d\varepsilon_0''\right|\right] + \frac{1}{2n}\left|d\varepsilon_0'\right| \quad ,
\end{aligned} \tag{4-56}$$

---

51 P. R. Bevington and D. K. Robinson, *Data Reduction and Error Analysis of the Physical Sciences* (McGraw-Hill, New York, 1992).

$$dk = \frac{1}{4k\sqrt{\varepsilon_0'^2 + \varepsilon_0''^2}}\left[\left[\varepsilon_0' - 2\sqrt{\varepsilon_0'^2 + \varepsilon_0''^2}\right]d\varepsilon_0'\right| + \left|\varepsilon_0'' d\varepsilon_0''\right|\Big] \quad ,$$

where

$$dN = dN|_{statistical} \quad ,$$

$$dC = 2NC(a_A + a_M + a_P) + dC|_{statistical} \quad ,$$

$$dS = 2NS(a_A + a_M + a_P) + dS|_{statistical} \quad .$$

Here, a_A, a_M and a_P are the uncertainties in the orientation angle of the analyzer, modulator and polarizer in radians (a_C does not contribute), $d\theta_i$ is the uncertainty in the angle of incidence of the sample in radians and $dN|_{statistical}$, $dC|_{statistical}$ and $dS|_{statistical}$ are the statistical errors of N, C and S.

4.4 Realization of the PME

The PME used in this work is diagrammed in Figure 4.6. The components of the PME are mounted on carriers which ride on rails. This allows for easy alignment and positioning of the components. The two rails of the ellipsometer are mounted on a tapped optical table at a 90° angle to each other, giving an angle of incidence on the sample of $\theta_i = 45° \pm 0.5°$.

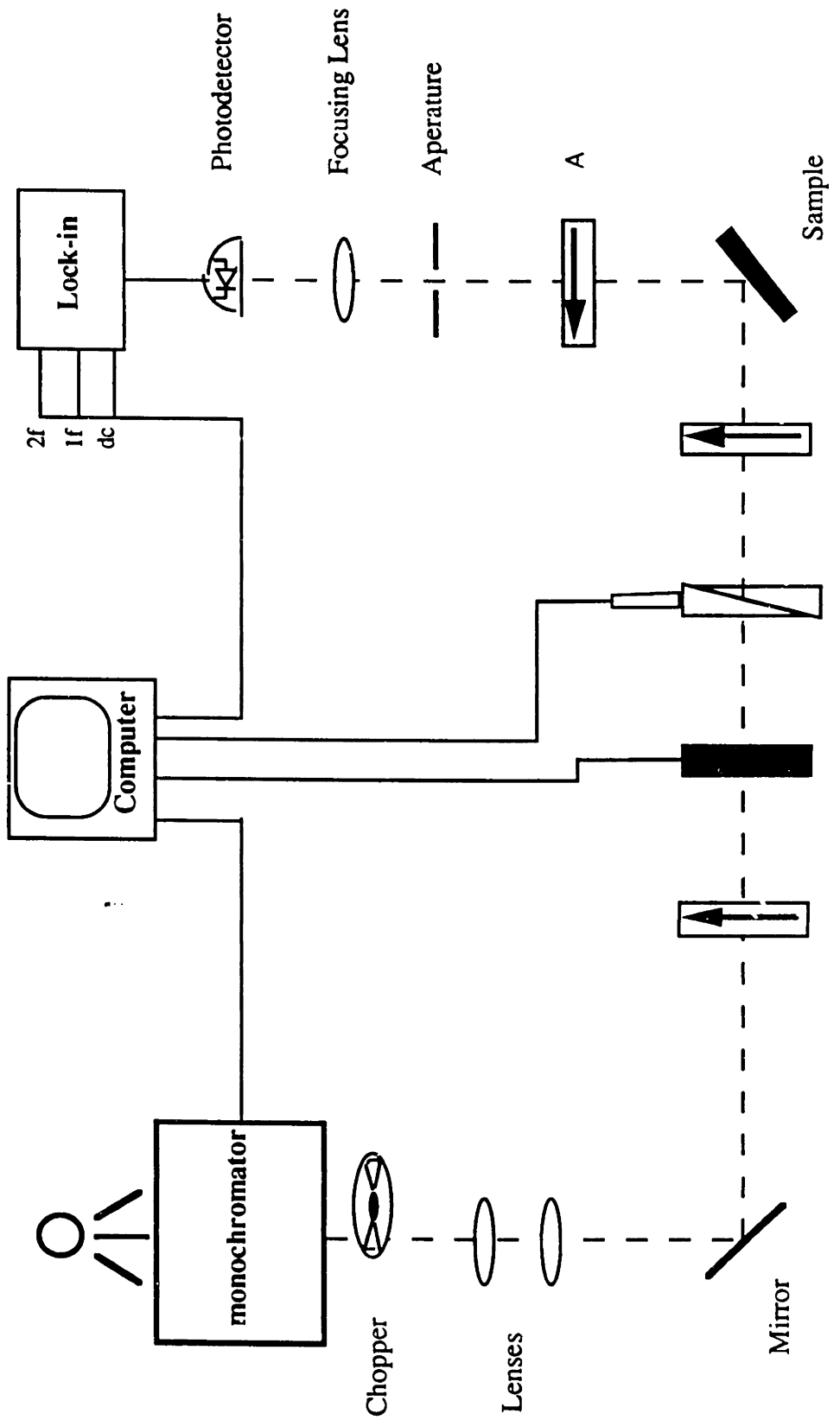

Figure 4.6. Schematic diagram of the photoelastic modulator

The polarizing optics of the PME are a polarizer, analyzer, photoelastic modulator and a Soleil-Babinet compensator.

The polarizer and analyzer are UV grade Glan-Thompson polarizers from the Karl Lambrecht Corporation. They have a minimum extinction coefficient of 10^{-5}, yielding, $\alpha \leq 2.25 \times 10^{-3}$. The polarizer and analyzer are mounted on rotators that can be positioned with a precision of 0.1°. The compensator is a calcite Soleil-Babinet compensator, also from the Karl Lambrecht Corporation. It is mounted in a similar rotator that has a precision of 0.1°. The retardation is adjusted by a computer controlled micrometer (Oriel encoder mike) which gives it a resolution of approximately 0.05 degrees of retardation at 500 nanometers.

The heart of the PME is the photoelastic modulator. The modulator used in this work is a PEM-90 series modulator from Hinds Instruments, Inc. It is made from infrasil grade quartz and is modulated at a frequency of 42 kHz. The spectral range of the modulator is roughly 200 to 2000 nm. The modulator is capable of being remotely controlled by a control voltage or by serial communication from a computer.

Other optics of the system include lenses and an iris. The iris is placed after the analyzer position on the reflection arm of the PME. This ensures that the final aperture of the system remains constant, regardless of whether the analyzer is located on the incident arm of the ellipsometer (as in the calibration configurations) or on the reflection arm. The aperture size of the iris is roughly one centimeter in diameter which corresponds to the aperture of the polarizer and analyzer. The lenses used are all quartz lenses to allow for operation in the ultraviolet region. The lenses are loosely mounted in circular mounts. It is important that the focusing and recollimating lenses, located before and after the sample, are mounted without any applied stress, particularly if three-point mounts are used. An applied stress causes birefringence in the lenses which will corrupt the incident and reflected polarization of the sample, particularly in the 1f channel.

Lastly, the sample under measurement is glued to a tiltable mount in order to obtain the proper reflection angle. It is also on an x-y stage to allow for additional positioning.

For generation of monochromatic light, a 450 watt xenon arc lamp is focused into a 0.25 meter double monochromator. The monochromator has gratings with 1200 grooves per inch and a slit size of typically 2.5 mm. This yields a resolution of 4.5 nm. The monochromator's wavelength is positioned by a stepping motor which is driven by a computer controlled logic circuit.

The detector for the PME is a silicon photodiode with a quartz window to allow for detection of light at wavelengths below 300 nm. The photodiode is part of a

transimpedance amplifier circuit. The bandwidth of the amplifier circuit is greater than 100 kHz to allow detection of the 42 kHz and 84 kHz components of the light intensity. Also, the light is chopped at approximately 100 Hz. This is referred to as the *dc* signal. It is acceptable to consider 100 Hz as zero frequency, since the frequency is rather small compared to the 1f and 2f frequencies of 42 kHz and 84 kHz. The light is chopped and synchronously detected, rather than measured as a dc signal because of the better signal-to-noise ratio that is obtained and also the immunity to a fluctuating dc ground, particularly at low signal strength.

The dc, 1f and 2f signals are measured via three lock-in amplifiers. Their readings are read through their analog outputs by an analog-to-digital converter (A/D) card in the computer.

Important to the operation of the PME is the alignment of the optical components. Alignment is done using a He-Ne laser and the system is realigned whenever the sample is changed. (The details of the alignment procedure are described in Appendix H.)

Operation of the PME is controlled by the computer via the A/D card and a serial port. The photoelastic modulator is controlled by applying an analog voltage that corresponds to the correct depth of modulation. Positioning of the monochromator's wavelength is accomplished by sending digital pulses to the stepping motor of the monochromator. The compensator is adjusted by positioning of its motorized micrometer. The micrometer is set, via a controller box, by serial communication with the computer. These instruments must, of course, be calibrated ahead of time.

After an initial one time calibration of the monochromator with a Hg pen lamp, the monochromator does not need to be recalibrated.

The compensator is calibrated by placing it between two crossed polarizers. The compensator can be set at any orientation to the polarizers, but, maximum sensitivity can be achieved by orienting the compensator at 45° to both polarizers. By moving the wedges of the compensator with the micrometer, (at least) two minima or extinctions can be found at a given wavelength. The first minima should be at the same position for all wavelengths. The second minima corresponds to one full wave of retardation. Hence, one quarter of this distance gives us the desired quarter wave of retardation.

The amount of translation required for a quarter-wave of retardation can be found for all wavelengths of the spectrum under study. It should be very close to a linear relation which we have assumed in the operation of the PME used in this work.

The J_0 calibration seems to be the most critical calibration. $J_0(A)$ at a given wavelength can be found from the 2f signals in the cal2f+ and cal2f- configurations of the CS configuration using Equation (4-49). Initially, the proper applied voltage sent to the

photoelastic modulator controller was found by varying the voltage at a fixed wavelength and measuring the 2f signal of both configurations. The voltage at which the 2f signals were equal in magnitude was the voltage corresponding to $J_0(A) = 0$. This procedure was repeated for all wavelengths across the spectrum under study. The relation between the applied voltage and the wavelength was found to be linear only over certain parts of the spectrum. Also, from day to day, and especially after a realignment of the ellipsometer, a new calibration relation between voltage and wavelength had to be obtained.

The controlling computer program of the PME has been named MARK5 for historical reasons. The program obtains the intensity ratios R_{1f} and R_{2f} at various wavelengths in the following manner. First, the monochromator, photoelastic modulator and, if necessary, the compensator are set to the desired wavelength. After a wait of five time constants of the lock-in amplifiers, approximately 100 readings are taken of the lock-in amplifiers' analog outputs in one second. The intensity ratios, R_{1f} and R_{2f} are calculated for each reading and are averaged and the results are stored. This procedure is repeated for all the wavelengths in the desired spectrum and multiple scans of each spectrum are usually taken to average out noise. The final R_{1f} and R_{2f} values are stored in data files.

The above procedure is done for all seven configurations of the PME that have been described in previous sections: CS+, CS-, cal1f, cal2f+, cal2f-, N, Ncal2f. A separate computer program combines the data for the configurations and makes the error corrections explained in section 4.3.1. The outputs of the program are the spectra of the optical constants of the sample: the real and imaginary part of the dielectric constant, ε, and the real and imaginary part of the index of refraction, N.

Also output from this program are the spectra of the two error parameters, J_0 and δ_0, as well as the self consistency parameter, β. J_0 is kept below an absolute value of 0.01 so that it is negligible to first order. The static birefringence, δ_0, is typically less than 0.003 radians across the spectrum considered in this work. β is usually less than 0.01 in magnitude.

5. Magneto-optic Spectrometer

5.1 Introduction

A magneto-optical spectrometer is any instrument that measures the spectra of any of the manifestations of the magneto-optic effect. Since there are a few different manifestations of the magneto-optic effect (Faraday, Voigt, the Kerr effects), there are many different spectrometer designs. In our case, we wished to measure the magneto-optic effect of bulk samples of iron garnets. Due to the strong absorption of these materials in the visible region, a reflection measurement was necessary. In particular, we designed an instrument to measure the ellipticity, ε_K, and the rotation, θ_K, of the polar magneto-optic Kerr effect.

The magneto-optic spectrometer (MOS) that was constructed to measure the Kerr effect of iron garnets is based on that of Krumme *et al.*[52] with some modifications. In this Chapter, we first describe its theory of operation with the aid of the Jones' matrices discussed in the previous Chapter. Next, we calculate the errors of measurement, and lastly, we describe the details of the actual MOS .

5.2 Theory of Measurement

5.2.1 Jones' Matrices

We can use Jones' matrices to describe the operation of the MOS. The Jones' matrices of the optical components of the MOS have already been given in Chapter 4. The one difference here is the Jones' matrix of the magneto-optical sample. The sample is oriented normal to the incident light of the MOS. At normal incidence, linear polarized light of any orientation will become elliptical and rotated upon reflection from a magnetized material with ellipticity ε_K and a major axis oriented at an angle θ_K from its original orientation.

The matrix that produces this transformation is the magneto-optic sample matrix:

$$S_{MO} = \begin{bmatrix} \cos\theta_K \cos\varepsilon_K - i\sin\theta_K \sin\varepsilon_K & -\sin\theta_K \cos\varepsilon_K - i\cos\theta_K \sin\varepsilon_K \\ \sin\theta_K \cos\varepsilon_K + i\cos\theta_K \sin\varepsilon_K & \cos\theta_K \cos\varepsilon_K - i\sin\theta_K \sin\varepsilon_K \end{bmatrix} \qquad (5\text{-}1)$$

---

52 J. -P. Krumme, V. Doorman and C. -P. Klages, Applied Optics **23**, 1184 (1984).

5.2.2 Measurement

We now wish to compute the effect of the different configurations of the MOS on unpolarized light. There are essentially only three different configurations of the MOS: a measurement configuration and two calibration configurations. The measurement configuration is shown in Figure 5-1a. The intensity of this configuration is

$$I_{MO} = 1 + \sin 2\varepsilon_K \sin \delta_m - \sin 2\theta_K \cos 2\varepsilon_K \cos \delta_m \quad . \tag{5-2}$$

We can expand the intensity according to (4-12) to obtain

$$I_{MO} = 1 + \sin 2\varepsilon_K 2J_1(A)\cos \omega t - \sin 2\theta_K \cos 2\varepsilon_K 2J_2(A)\cos 2\omega t \quad , \tag{5-3}$$

where we have assumed that the depth of modulation is set to A=137.8°, such that $J_0(A) = 0$. The Kerr ellipticity and rotation are much less than one; typically, they are rarely more than a tenth of a degree. By applying the small angle approximation the intensity ratios become

$$R_{1f}^{MO} = \frac{I_{1f}^{MO}}{I_{dc}^{MO}} = 2\varepsilon_K 2J_1(A) \quad ,$$

$$R_{2f}^{MO} = \frac{I_{2f}^{MO}}{I_{dc}^{MO}} = 2\theta_K 2J_2(A) \quad . \tag{5-4}$$

As was the case for the PME in Chapter 4, what is actually measured is

$$R_{1f}^{MO} = 2\varepsilon_K \frac{a_{1f}}{a_{dc}} 2J_1(A) \quad ,$$

$$R_{2f}^{MO} = 2\theta_K \frac{a_{2f}}{a_{dc}} 2J_2(A) \quad , \tag{5-5}$$

where a_{dc}, a_{1f} and a_{2f} are the effective gains of the frequency channels. We eliminate these unknown effective gains with the calibration configurations shown in Figures 5.1b and 5.1c.

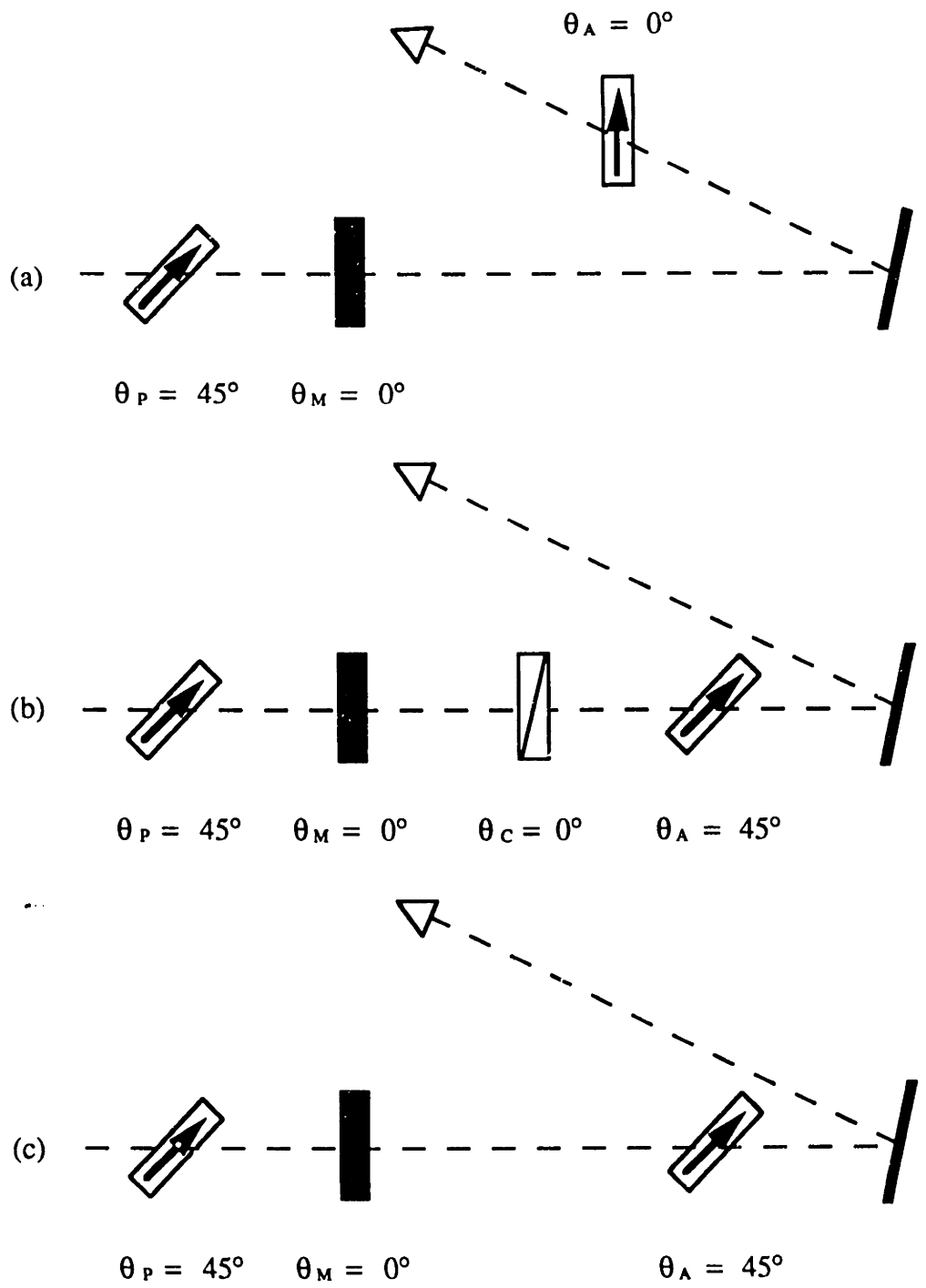

Figure 5.1. The MOS configurations: (a) measurement. (b) 1f calibration. (c) 2f calibration.

The calibration of the 1f channel can be obtained from the configuration shown in Figure 5.1b. The intensity ratios, including the effective gains, are

$$R_{1f}^{call\,f} = -\frac{a_{1f}}{a_{dc}} \cdot J_1(A) \quad ,$$
$$R_{2f}^{call\,f} = 0 \quad . \tag{5-6}$$

This is the same result as was found for the PME. Having the 1f calibration, we can now obtain the Kerr ellipticity, ε_K.

$$\varepsilon_K = \frac{1}{2}\frac{R_{1f}^{MO}}{R_{1f}^{call\,f}} \quad . \tag{5-7}$$

The calibration for the 2f channel is found using the configuration in Figure 5.1c. This configuration yields the intensity ratios

$$R_{1f}^{call\,f} = 0 \quad ,$$
$$R_{2f}^{call\,f} = \frac{a_{2f}}{a_{dc}} 2J_2(A) \quad . \tag{5-8}$$

The Kerr rotation of the material is thus

$$\theta_K = \frac{1}{2}\frac{R_{2f}^{MO}}{R_{2f}^{cal\,2f}} \quad . \tag{5-9}$$

5.3 Errors of Measurement

We now examine the errors of the MOS. As was the case for the PME, there are two types of errors to worry about. The first are the component errors due to the non-idealness of the optical components of the MOS. The second are the precision errors which are due to the uncertainty in the alignment of the optical components. The analysis of these errors is done in detail in Appendix E.

5.3.1 Component Errors and Corrections

In the previous section, we assumed all optical components to be ideal. Now, we show what the MOS actually measures with non-ideal (realistic) components. The details of the mathematics of error analysis are presented in Appendix E and just the results are quoted here.

We review the component errors described in the previous chapter. The non-idealness of the polarizer and analyzer comes from transmission of the unwanted polarization. This transmission is characterized by the quantity α, which can be related to the extinction coefficient of the polarizers by the relation

$$\text{extinction} = \frac{I_{\perp}}{I_{\parallel}} = 2\alpha^2 \quad . \tag{5-10}$$

The quantity α can be found by measuring the light intensity of two crossed polarizers.

The photoelastic modulator can cause errors in three different ways. First, there is a static birefringence, δ_0. The static birefringence is the birefringence when there is zero applied electric field on the quartz plate of the modulator. The presence of δ_0 means that the sinusoidal phase shift of the modulator is about δ_0, rather than zero.

The photoelastic modulator can also have a different transmission coefficient for its stressed and unstressed axes. The ratio of the transmission coefficients, τ_0, characterizes this difference, and is assumed to be equal to one, as it was in the case of the PME.

The third error of the modulator comes from an improper setting of the depth of modulation, A. Ideally, $A = A_0 = 2.405$ radians, at which the zero order Bessel function is equal to zero. Deviation from $A = A_0$ will cause the zero order Bessel function to have a non-zero value, leading to some contribution of the 2f component of the intensity to the dc intensity.

Lastly, the Soliel-Babinet compensator may not be set for 90° retardation. In general, the retardation will be $90° + \delta_c$, where δ_c is a small angle. To first order, δ_c is negligible and thus, we drop it from our analysis.

In the following analysis, we look at the intensities of the two configurations of the MOS using non-ideal components. In finding the intensities, we assume that our three error parameters are small (α, δ_0, $J_0 << 1$) and we expand all intensities to first order. The mathematics is done in Appendix D and the results are quoted here.

In the measurement configuration, the actual intensity ratios that are measured are

$$\begin{aligned} R_{1f}^{MO} &= +2\frac{\varepsilon_K + \delta_0\theta_K}{1-2\alpha}2J_1(A) \quad , \\ R_{2f}^{MO} &= -2\frac{\theta_K - \delta_0\varepsilon_K}{1-2\alpha}2J_2(A) \quad . \end{aligned} \tag{5-11}$$

The 1f and 2f calibrations of the MOS give the same results as the CS configuration of the PME. For the 1f calibration,

$$\begin{aligned} R_{1f} &= -2J_1(A) \quad , \\ R_{2f} &= -\delta_0 2J_2(A) \quad . \end{aligned} \tag{5-12}$$

For the 2f calibration we average the results with the analyzer in the plus and minus 45° positions:

$$\begin{aligned} \bar{R}_{1f}^{cal2f} &\equiv \tfrac{1}{2}\left[R_{1f}^{+} - R_{1f}^{-}\right] = \delta_0 2J_1(A) \quad , \\ \bar{R}_{2f}^{cal2f} &\equiv \tfrac{1}{2}\left[R_{2f}^{+} - R_{2f}^{-}\right] = 2J_2(A) \quad . \end{aligned} \tag{5-13}$$

If the error parameters are known, then we can determine ε_K and θ_K. We define the measured quantities E" and R" as

$$\begin{aligned} E'' &= \frac{R_{1f}^{MO}}{R_{1f}^{cal1f}} \quad , \\ R'' &= \frac{R_{2f}^{MO}}{\bar{R}_{2f}^{cal2f}} \quad . \end{aligned} \tag{5-14}$$

Then, the Kerr ellipticity and rotation are (keeping only first order terms)

$$\begin{aligned} \varepsilon_K &= \frac{1}{2}(1-2\alpha)(E'' - \delta_0 R'') \quad , \\ \theta_K &= \frac{1}{2}(1-2\alpha)(R'' + \delta_0 E'') \quad . \end{aligned} \tag{5-15}$$

5.3.2 Orientation Errors

Unlike the PME, some of the orientation errors of the MOS can be corrected for. The first such error is the misorientation of the analyzer in the measurement configuration. If the analyzer is oriented at an angle θ_A, then the intensity ratios of the configuration for one of the field orientations become

$$R_{1f}^{MO+} = +2\frac{\varepsilon_K + \delta_0(\theta_K - \theta_A)}{1-2\alpha}2J_1(A) \quad ,$$
$$R_{2f}^{MO+} = -2\frac{(\theta_K - \theta_A) - \delta_0\varepsilon_K}{1-2\alpha}2J_2(A) \quad . \tag{5-16}$$

If we reverse the magnetic field on the sample, the Kerr ellipticity and rotation change sign. The intensity ratios of the reversed field case are then

$$R_{1f}^{MO+} = -2\frac{\varepsilon_K + \delta_0(\theta_K + \theta_A)}{1-2\alpha}2J_1(A) \quad ,$$
$$R_{2f}^{MO+} = +2\frac{(\theta_K + \theta_A) - \delta_0\varepsilon_K}{1-2\alpha}2J_2(A) \quad . \tag{5-17}$$

We can now eliminate θ_A by combining the intensity ratios of the forward and reversed field cases in the following way:

$$R_{1f}^{MO} = \frac{1}{2}\left[R_{1f}^{MO+} - R_{1f}^{MO-}\right] = +2\frac{\varepsilon_K + \delta_0\theta_K}{1-2\alpha}2J_1(A) \quad ,$$
$$R_{2f}^{MO} = \frac{1}{2}\left[R_{2f}^{MO+} - R_{2f}^{MO-}\right] = -2\frac{\theta_K - \delta_0\varepsilon_K}{1-2\alpha}2J_2(A) \quad . \tag{5-18}$$

The quantities ε_K and θ_K can then be found from to (5-14) and (5-15) of the last section. This cancellation of θ_A has a practical application in the sense that it allows us to be sloppy in orienting the analyzer in the measurement configuration.

There is a second reason for measuring the forward and reversed field cases. In order to obtain the true Kerr ellipticity and rotation, the angle of incidence in the measurement configuration must be zero; that is, normal incidence. At non-normal incidence, there is an additional ellipticity and rotation due to the different reflection coefficients of perpendicular and parallel polarized light. This is the ellipticity and rotation that is used by ellipsometry to determine the optical constants of the reflecting material and, though small, they will show up in the measurement of the Kerr ellipticity and rotation.

When we reverse the magnetic field on a magneto-optical material, we change the sign of the Kerr ellipticity and rotation, but the dielectric ellipticity and rotation remain the same. Thus, in combining the intensity ratios of the forward and reversed field case as we do in Equation (5-18), we also eliminate the ellipticity and rotation due to a non-zero angle of incidence.

There still is, however, a reduction in the magnitude of the Kerr effect at non-normal incidence. The result is that the reduction of the Kerr ellipticity and rotation is second order in the angle of incidence going approximately as θ_i^2/n^3, where n is the index of refraction of the material. For an angle of incidence of 10° and a worst case index of refraction of n = 1, this reduction amounts to 1.5%. In the materials measured in this work, the reduction is less than 1%.

We cannot, however, eliminate the misorientation errors of the polarizer and modulator. The uncertainties in these orientation angles translate into uncertainties in ε_K and θ_K. We can determine these uncertainties, as we did in the last section, by using partial derivatives[51]. The relations are:

$$\begin{aligned} d\varepsilon_K(\theta_P,\theta_M) &= \frac{\partial \varepsilon_K}{\partial \theta_P} d\theta_P + \frac{\partial \varepsilon_K}{\partial \theta_M} d\theta_M \quad , \\ d\theta_K(\theta_P,\theta_M) &= \frac{\partial \theta_K}{\partial \theta_P} d\theta_P + \frac{\partial \theta_K}{\partial \theta_M} d\theta_M \quad . \end{aligned} \tag{5-19}$$

We have neglected the misorientation of the compensator, as we did for the PME, because its effect is of second-order and does not contribute importantly to our measurements. We also ignore the reduction of ε_K and θ_K by non-normal incidence because it is second-order in the angle of incidence.

The analysis of Equation (5-19) is done in Appendix F and the results are repeated here:

$$\frac{d\varepsilon_K}{\varepsilon_K} = \frac{d\theta_K}{\theta_K} = \pm 2(a_P + a_M) \quad . \tag{5-20}$$

where a_P and a_M are the uncertainties in the orientation angle of the polarizer and modulator, respectively.

5.4 Realization of the MOS

The MOS used in this work is diagrammed in Figure 5.2. The MOS is constructed with the same components as the PME described in Chapter 4. The components of the MOS are mounted on carriers which ride on rails. This allows for easy alignment and positioning of the components. The two rails of the spectrometer are

mounted on a tapped optical table at a 14.4° angle to each other, giving an angle of incidence on the sample of $\theta_i = 7.2°$.

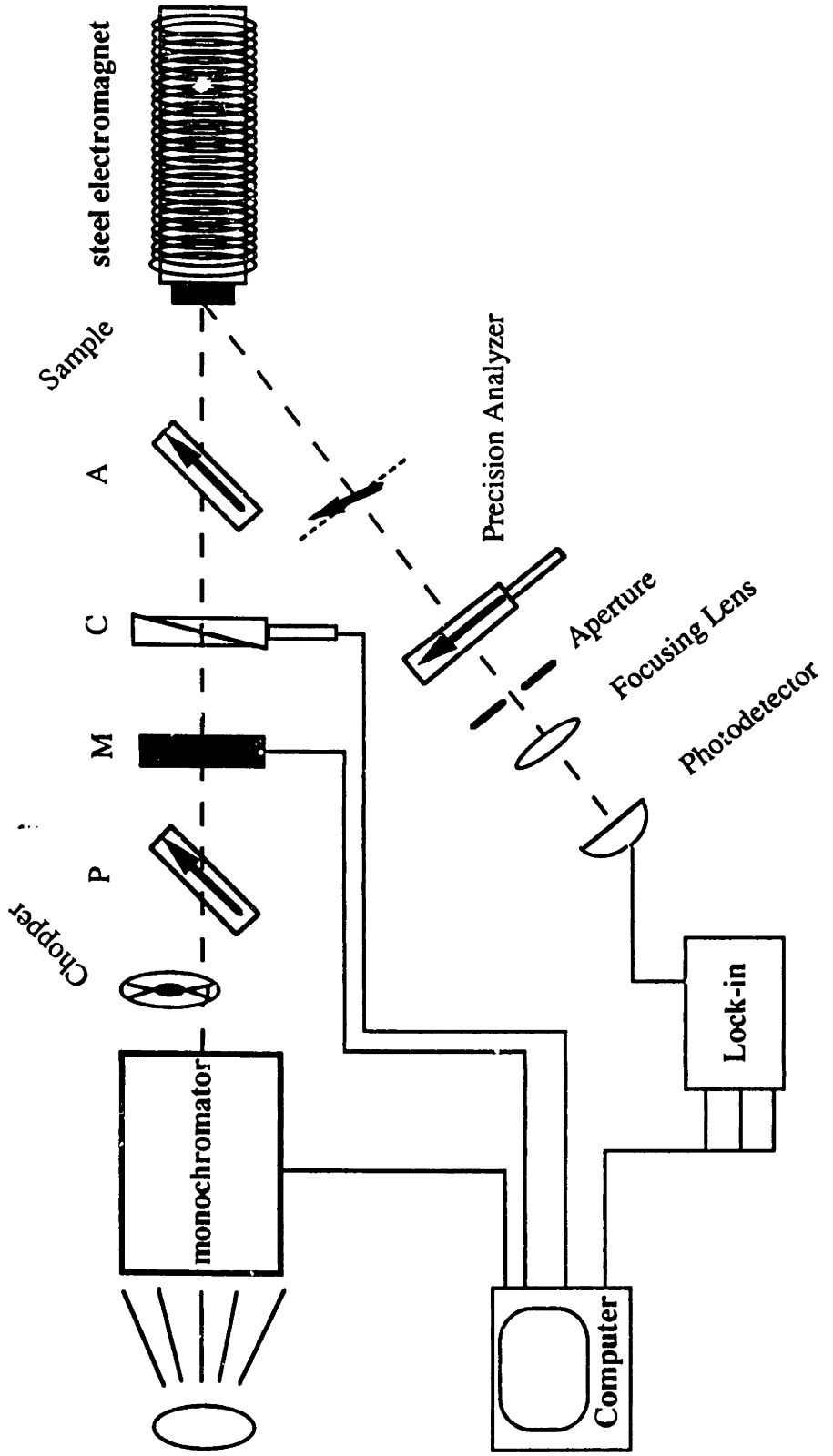

Figure 5.2. Schematic diagram of the magneto-optic spectrometer.

The optics of the system are mounted on movable carriers that ride on the rails. The polarizing optics of the MOS include a polarizer, analyzer, photoelastic modulator and a Soleil-Babinet compensator.

The polarizer and analyzer are UV grade Glan-Thompson polarizers from the Karl Lambrecht Corporation. They have a minimum extinction coefficient of 10^{-5}, yielding $\alpha \leq 2.25 \times 10^{-3}$. The polarizer is mounted on a rotator that can be positioned with a precision of 0.1°. The analyzer is mounted on a motorized precision rotation stage to obtain the higher orientation precision desired to measure the Kerr effect. The resolution of the rotator is better than 0.001°.

The compensator is a calcite Soleil-Babinet compensator also from the Karl Lambrecht Corporation. It is mounted in a rotator that has a precision of 0.1°. The retardation is adjusted by a computer controlled micrometer (Oriel encoder mike) which gives it a resolution of approximately 0.05 degrees of retardation at 500 nanometers.

The heart of the MOS is the photoelastic modulator. The modulator used in this work is a PEM-90 series modulator from Hinds Instruments, Inc. It is made from infrasil grade quartz and is modulated at a frequency of 42 kHz. The spectral range of the modulator is roughly 200 to 2000 nm. The modulator is remotely controlled by a control voltage from the computer.

Other optics of the system include lenses and an iris. The iris is placed after the analyzer position on the reflection arm of the MOS. This ensures that the final aperture of the system remains constant, regardless of whether the analyzer is located on the incident arm of the spectrometer (as in the calibration configurations) or on the reflection arm. The aperture size of the iris is roughly one centimeter in diameter which corresponds to the aperture of the polarizer and analyzer. The lenses used are all quartz lenses to allow for operation in the ultraviolet region. The lenses are loosely mounted in circular mounts. It is important that the focusing and recollimating lenses, located before and after the sample, are mounted without any applied stress, particularly if three-point mounts are used. An applied stress causes birefringence in the lenses which will corrupt the incident and reflected polarization of the sample, and give false readings primarily in the 1f channel.

Lastly, the sample is glued to the face of an iron electromagnet and magnetized to greater than 2000 Gauss. A schematic of the electromagnet is shown in Figure 5.3. The magnet is mounted on a tilt table to allow alignment of the sample. Because the sample is directly mounted onto the magnet pole, the sample is at a temperature of 315 Kelvin.

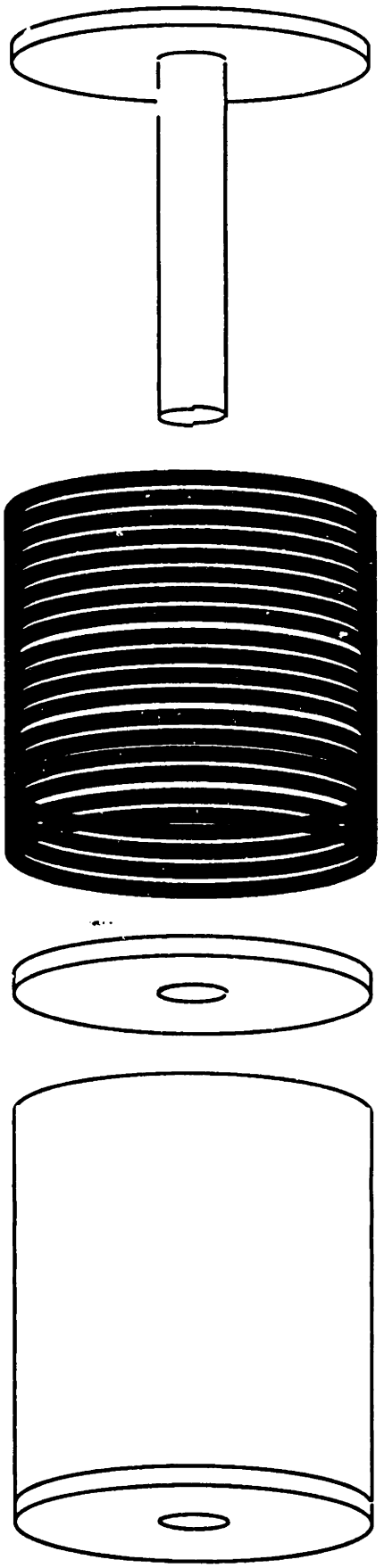

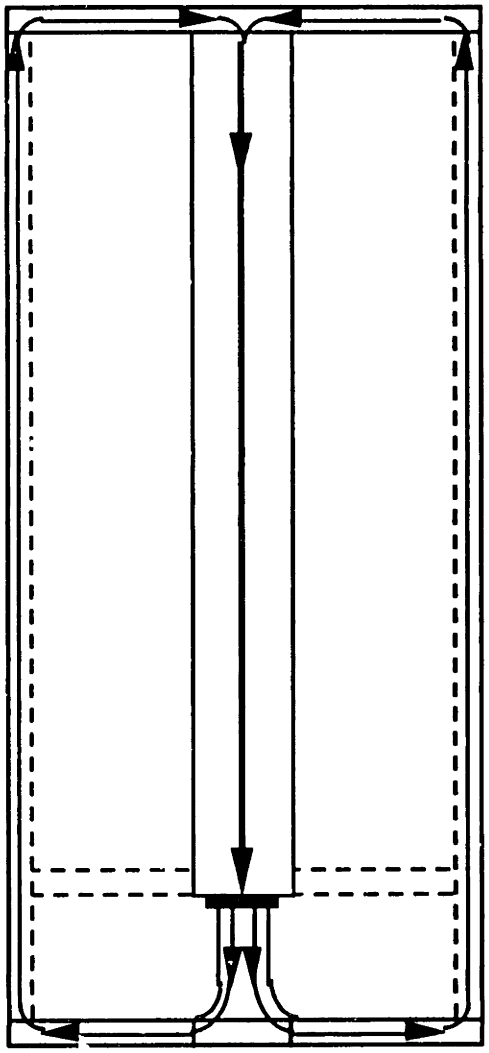

Magnetic flux path indicated by arrow

For generation of monochromatic light, a 450 watt xenon arc lamp is focused into a 0.25 meter double monochromator. The monochromator has gratings with 1200 grooves per inch and a slit size of typically 2.5 mm. This yields a resolution of 4.5 nm. The monochromator's wavelength is positioned by a stepping motor which is driven by a computer-controlled logic circuit.

The detector for the MOS is a silicon photodiode with a quartz window to allow for detection of light at wavelengths below 300 nm. The photodiode is part of a transimpedance amplifier circuit. The bandwidth of the amplifier circuit is greater than 100 kHz to allow detection of the 42 kHz and 84 kHz components of the light intensity. Also, the light is chopped at approximately 100 Hz. This signal is referred to as the *dc* signal, which is acceptable since the chopping frequency is small compared to the 1f and 2f frequencies of 42 kHz and 84 kHz. The light is chopped by a chopper wheel and synchronously detected to obtain an improved signal to noise ratio over that of the standardly used dc measurement.

The dc, 1f and 2f signals are measured via three lock-in amplifiers. Their readings are read through their analog outputs by an analog-to-digital converter (A/D) card in the computer.

Alignment of the MOS is done using a He-Ne laser and the system is realigned whenever the sample is changed. The details of the alignment procedure are analogous to those described in Appendix H. Alignment is not as crucial for the MOS as it is for the PME due to the lack of sensitivity in the angle of incidence.

Operation of the MOS is controlled by the computer via the A/D card and a serial port. The photoelastic modulator is controlled by applying an analog voltage that corresponds to the correct depth of modulation. Positioning of the monochromator's wavelength is accomplished by sending digital pulses to the stepping motor of the monochromator. The compensator is adjusted by positioning of its motorized micrometer. The micrometer is set, via a controller box, by serial communication with the computer. These instruments must, of course, be calibrated ahead of time.

After an initial one time calibration of the monochromator with a Hg pen lamp, the monochromator does not need to be recalibrated.

The compensator is calibrated by placing it between two crossed polarizers. The compensator can be set at any orientation to the polarizers but maximum sensitivity can be achieved by orienting the compensator at 45° to both polarizers. By moving the wedges of the compensator with the micrometer, (at least) two minima can be found at a given wavelengths. The first minima should be at the same position for all wavelengths.

The second minima corresponds to one full wave of retardation. Hence, one quarter of this distance gives us the desired quarter wave of retardation.

The amount of translation required for a quarter-wave of retardation can be found for all wavelengths of the spectrum under study. It should be very close to a linear relation which we have assumed in the operation of the MOS used in this work.

The J_0 calibration is not as critical here as it is for the PME. The calibration is done mainly to insure that J_0 is small and that second order effects in J_0 do not occur. Typically, J_0 values are less than 0.01 in magnitude during operation of the MOS and thus, second order effects are negligible.

$J_0(A)$ at a given wavelength can be found from the 2f signals in the cal2f+ and cal2f- configurations of the CS configuration using Equation (4-49). Initially, the proper applied voltage sent to the photoelastic modulator controller was found by varying the voltage at a fixed wavelength and measuring the 2f signal of the cal2f+ and cal2f- configurations. The voltage at which the 2f signals were equal in magnitude was the correct voltage for $J_0(A) = 0$. This procedure was repeated for wavelengths across the spectrum under study. The relation between the applied voltage and the wavelength was found to be linear only over certain parts of the spectrum. Also, from day to day, and especially after a realignment, a new calibration relation between voltage and wavelength had to be obtained.

The controlling computer program of the MOS has been named MARK5 for historical reasons. The program obtains the intensity ratios R_{1f} and R_{2f} at various wavelengths in the following manner. First, the monochromator, photoelastic modulator and, if necessary, the compensator are set to the desired wavelength. After a wait of five time constants of the lock-in amplifiers, approximately 100 readings are taken of the lock-in amplifiers' analog outputs in one second. The intensity ratios, R_{1f} and R_{2f}, are calculated for each reading, are then averaged and the results are stored. This procedure is repeated for all the wavelengths in the desired spectrum, and multiple scans of the spectrum are usually taken to average out noise. The final R_{1f} and R_{2f} values are stored in data files.

The above procedure is done for all five configurations of the MOS that have been described in previous sections: cal1f, cal2f+, cal2f-, and the measurement configuration with the applied field in the forward and reversed directions. A separate computer program combines the data for the configurations. The outputs of the program are the spectra of the Kerr ellipticity and rotation of the sample shown in Chapter 7.

Also output from this program are the spectra of the two error parameters, J_0 and δ_0. J_0 is kept below an absolute value of 0.01 so that it is negligible to first order. The

static birefringence, δ_0, is typically less than 0.003 radians across the spectrum considered in this work.

6. Sample Preparation and Characterization

The samples used in this work were all polycrystalline ceramics, prepared in air by standard techniques. Samples of greater than 90% density were obtained. Characterization of the samples was performed using x-ray powder diffraction for the determination of structure and lattice constants. The lattice constants, in turn, were used to determine the bismuth content of the samples.

6.1 Production of Ceramics

6.1.1 General Method

Production of the ceramic samples begins with the weighing of the proper amounts of the powder chemicals Y_2O_3, Bi_2O_3, Al_2O_3, In_2O_3 and Fe_2O_3. The chemicals used were nominally 99.9% pure or better. Powders were combined to make 0.1 moles of the desired compositions. The combined powders were ball mixed in ethanol with stainless steel milling balls for a period of three hours or longer. When completed, the mixed powder was oven-dried. The dried powder was packed into a platinum crucible and calcined at the calcining temperature for 12 hours. The calcine of the reacted powders was always green in color, indicative of the garnet phase.

The calcine was then ball milled in ethanol with stainless steel milling balls to produce a fine particle size. The resultant mixture was oven-dried and recalcined for 12 hours. After further ball milling and drying, the powder was ready to be fired into samples.

To make a sample, the calcined powder was often mixed in methanol with polyethyl glycol. The polyethyl glycol dissolves in methanol and acts as a binder for the powder during pressing and increases the density of the ceramics. The binder burns off at approximately 300°C and leaves no residue. The mixture was oven-dried to remove the methanol.

Next, the dried powder is packed into a die and uniaxially pressed. The die used was 1/4 square inches and typically between 8 and 60 kpsi of pressure was applied. The pressed pellets were then placed on a platinum sheet or crucible and sintered for 12 hours. The calcining and sintering temperatures are listed in Table 6-1.

After firing, the samples were cut, ground and polished into regular geometric shapes for volume measurement by a micrometer. The samples were weighed and declared acceptable if the density was above 90% of the expected density.

Material	Bismuth content	Calcine (°C)	Sinter (°C)	Density (g/cc)	Lattice Constant (Å)
$Y_3Fe_5O_{12}$	0	-	-	5.11 (99%)	12.3790 ± 0.0008
$Y_3Al_{0.5}Fe_{4.5}O_{12}$	0	1300	1535	5.08 (98%)	12.3431 ± 0.0008
$Y_3In_{0.33}Fe_{4.5}O_{12}$	0	1300	1480	4.98 (95%)	12.4149 ± 0.0009
$Bi_{0.47}Y_{2.53}Fe_5O_{12}$	0.471±0.012	1100	1160	5.06 (92%)	12.4156 ± 0.0010
$Bi_{0.48}Y_{2.52}Al_{0.5}Fe_{4.5}O_{12}$	0.479±0.013	1100	1160	5.08 (93%)	12.3832 ± 0.0110
$Bi_{0.46}Y_{2.54}In_{0.33}Fe_{4.5}O_{12}$	0.455±0.015	1075	1160	5.14 (92%)	12.4532 ± 0.0013

Table 6-1. Table of samples. The material $Y_3Fe_5O_{12}$ is the material G-113 from Trans-tech, Inc.

6.1.2 Bismuth Containing Samples

A complication arises in the production of bismuth-containing materials. In the sintering process, bismuth-oxide is released from the material. The amount of bismuth-oxide released increases with the sintering temperature. This phenomena was discovered by Geller *et al.*.[22] We used the lattice constants of the bismuth-containing samples to determine the final bismuth content of the material. The formula used was devised from lattice constants found in the literature[53] . For the material $Bi_xY_{3-x}Al_yIn_zFe_{5-y-z}O_{12}$, the lattice constant in Angstroms is

$$a = 12.376 + 0.084x - 0.067y + 0.118z \quad . \tag{6-1}$$

6.2 X-ray Diffraction

6.2.1 Structural Analysis

X-ray powder diffraction spectra were taken to determine the structural purity of the garnet materials. The accepted x-ray powder diffraction spectra for yttrium iron garnet is given in reference a and is representative of our samples. We found a good indicator of the presence of non-garnet phases to be the existence of a diffraction peak

---

[53] Bi: S. Geller, H. J. Williams, G. P. Espinosa, R. C. Sherwood and M. A. Gilleo, Appl. Phys. Lett. 3, 21 (1963). Al: reference 22. In: G. Winkler and P. Hansen, Phil. Res. Rept. 27, 151 (1972).

around $2\theta = 33.1°$. This peak is shown in Figure 6.1. It originates from unreacted Fe_2O_3. We declared a sample to be fully reacted and of a pure garnet phase when this peak could not be detected. No other non-garnet peaks were observed in the absence of this peak.

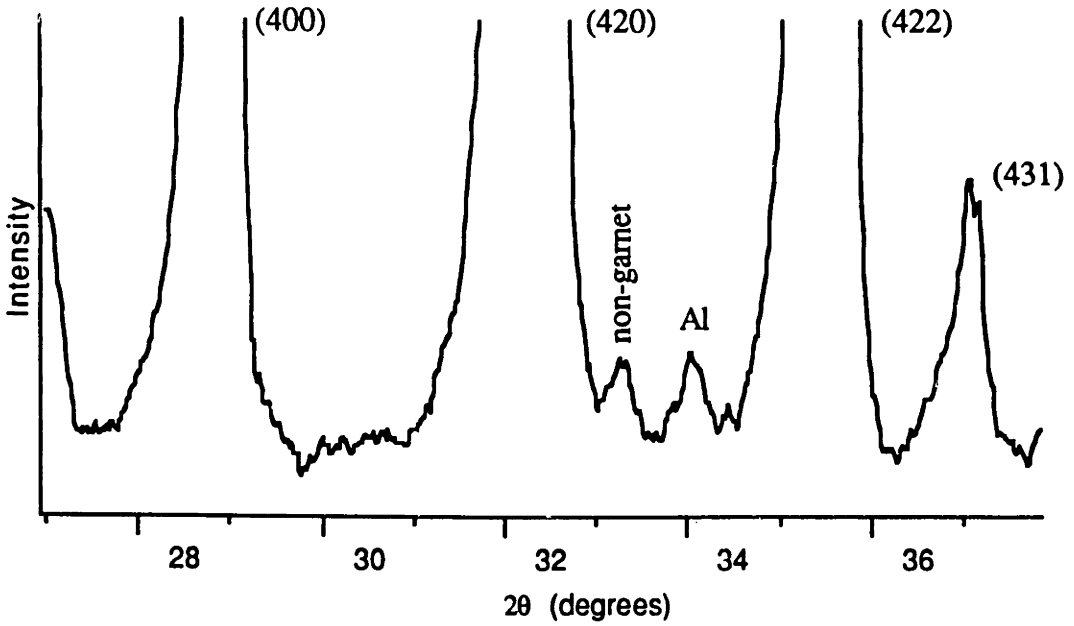

Figure 6.1. The x-ray powder diffraction spectrum for the garnet structure showing the peak used to detect a non-garnet phase. The radiation used is the copper K_α line. Labels refer to crystal planes. Also shown is an aluminum peak which originates from the sample holder.

6.2.2 Determination of Lattice Constants

The determination of the lattice constants was performed by x-ray powder diffraction. The powder diffraction technique was used to determine the angular positions of the diffraction peaks corresponding to the (12,0,0) , (12,2,0) and (12,2,2) planes of the garnet structure[54]. From these angles, the interplanar spacings, and thus the lattice constant of the material, can be determined. Only the position of one of the garnet peaks was necessary, but, three peaks were used to obtain greater accuracy; generally about ± 0.001Å. The calibration of the positions of the diffraction peaks were calibrated by adding a silicon powder standard obtained from the National Bureau of Standards to

[54] Card 18-1472 in the Inorganic Powder Diffraction File, Joint Committee on Powder Diffraction Standards, 1974

the powder sample. The angular scale was calibrated by assuming the silicon (511)/(333) peak to be at exactly 94.953°[55].

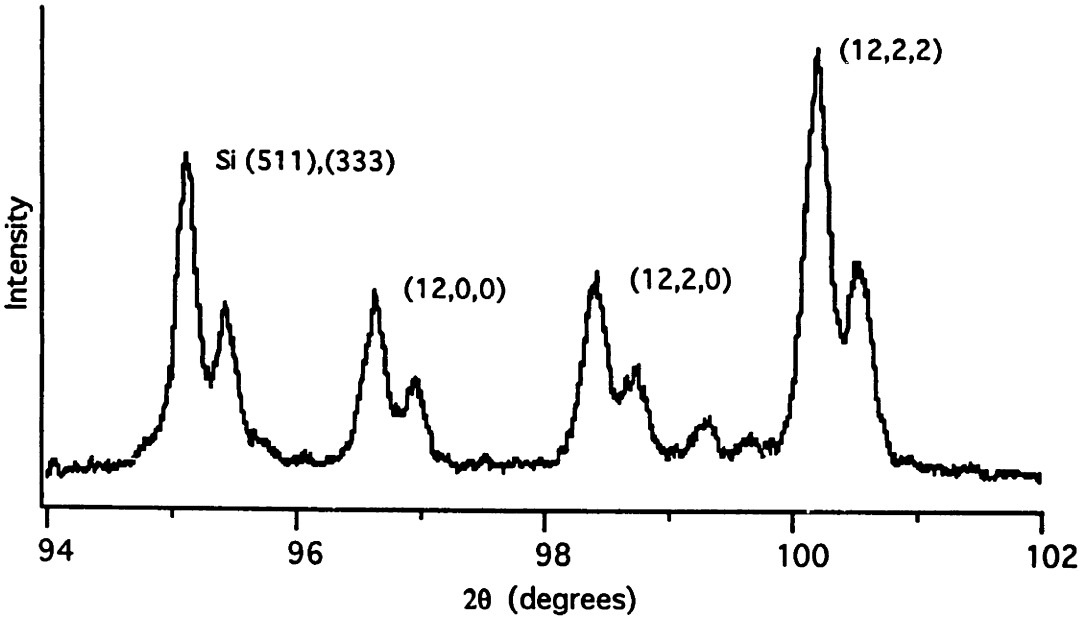

Figure 6.2. The x-ray powder diffraction peaks used to determine lattice constant. The large and small components of the double peaks correspond to reflection of the copper K_{α_1} and K_{α_2} radiation, respectively.

To obtain the lattice constants of a sample, pieces of the samples, generally from its center, were ground to a fine powder with a mortar and pestle. A roughly equal amount of silicon powder was added and the two powders thoroughly mixed. An x-ray diffraction scan of the powder was taken for a 2θ value range of 94° to 102°. A scanning speed was chosen that produced approximately 0.003° of angular resolution. The 2θ values of the silicon (511)/(333) diffraction peak and the garnet diffraction peaks for the (12,0,0) , (12,2,0) and (12,2,2) planes were obtained (Figure 6.2). The values were corrected so that the silicon (511)/(333) peak was at 94.953°. With the calibrated 2θ values for the three garnet peaks, the interplanar spacings for the respective planes were calculated using the p diffraction law,

$$d = \frac{1}{2}\frac{\lambda_{xray}}{\sin\theta} \quad . \tag{6-2}$$

55 National Bureau of Standards Certificate for Standard Reference Material 640b, 1987.

The radiation used was the copper K_{α_1} line with an assumed wavelength of $\lambda(Cu{:}K_{\alpha_1}) = 1.54050$ Å[56].

From the interplanar spacings, the lattice constant is found by multiplying the spacings by the appropriate scaling factors of $\sqrt{144}$, $\sqrt{148}$ and $\sqrt{152}$ for the (12,0,0), (12,2,0) and (12,2,2) planes respectively. The lattice constants for the samples used in this work are given in Table 6-1.

56 We have used the older value for the wavelength of the copper $K_{\alpha 1}$ line in order to be consistent with the references 53 from which we find the lattice constants. The most current value is l(CuKa1) = 1.5405981 Å from R. D. Deslattes and A. Hennins, Phys. Rev. Letts 31, 972 (1973).

7. Optical Measurements and Analysis

7.1 Introduction

The goal of these measurements is, first, to determine the change in the magneto-optic properties of $Y_3Fe_5O_{12}$ (YIG) due to substitution of bismuth, and secondly, to determine the contributions of the two iron sublattices to this effect. The first goal is realized by comparing the diagonal and off-diagonal elements of the dielectric tensor of $Bi_{0.47}Y_{2.5}Fe_5O_{12}$ ($Bi_{0.47}$YIG) to that of $Y_3Fe_5O_{12}$ (YIG). To elucidate the role that the two iron sublattices play in bismuth's enhancement of the magneto-optical effect, we compare the dielectric tensor elements of bismuth-substituted iron garnets in which the iron sublattices are diluted, with those of their non-bismuth containing counterparts. Specifically, we will compare $Bi_{0.48}Y_{2.5}Al_{0.5}Fe_{4.5}O_{12}$ ($Bi_{0.48}Al_{0.5}$YIG) and $Bi_{0.46}Y_{2.5}In_{0.33}Fe_{4.67}O_{12}$ ($Bi_{0.46}In_{0.33}$YIG) to the $Y_3Al_{0.5}Fe_{4.5}O_{12}$ ($Al_{0.5}$YIG) and $Y_3In_{0.33}Fe_{4.67}O_{12}$ ($In_{0.33}$YIG), respectively. If we assume that the aluminum and indium ions reside purely in the tetrahedral and octahedral sublattices, respectively, then the above samples represent materials in which the iron populations of the sublattices have been reduced by one-sixth in both cases. The overall reductions of iron, however, are different; namely, one-tenth of the total iron is removed in the aluminum-substituted materials, compared to one-fifteenth in the indium-substituted materials.

The off-diagonal elements of the dielectric tensor, which are represented by the complex quantity, ε_1, are obtained by measuring the complex dielectric constant, ε_0, and the Kerr rotation, θ_K, and ellipticity, ε_K. Having these quantities, ε_1 is found via the formulae derived in Appendix G:

$$\begin{aligned} \varepsilon_1' &= \varepsilon_K\left(n^3 - 3nk^2 - n\right) - \theta_K\left(k^3 - 3n^2k + k\right) \quad , \\ \varepsilon_1'' &= \varepsilon_K\left(k^3 - 3n^2k + k\right) + \theta_K\left(n^3 - 3nk^2 - n\right) \quad , \end{aligned} \tag{7-1}$$

where the complex quantity, ε_1, is written as

$$\varepsilon_1 = \varepsilon_1' + i\varepsilon_1'' \quad \text{and} \quad \sqrt{\varepsilon_1} = n + ik \quad .$$

Curve fitting is used to extract information on the transitions responsible for the measured spectra. A series of Gaussian peaks is fit to the imaginary part of the diagonal elements of the dielectric tensor of all the materials measured. The formulae for

paramagnetic and diamagnetic transitions derived in Chapter 3 are used to curve fit the calculated spectra of the off-diagonal dielectric tensor elements. From the results of these two sets of curve fits, we can extract information about the configurations of the magneto-optically active states of the materials using Equations (3-29) and (3-31). For paramagnetic transitions, the relation

$$\frac{\varepsilon_1'(\omega_0)}{\varepsilon_0''(\omega_0)} = \frac{\Delta f}{f} \quad , \tag{7-2}$$

is used to determine the difference in oscillator strengths for right and left-handed transitions that arise from a magnetically split ground state. For diamagnetic transitions, the relation

$$\frac{\varepsilon_1'(\omega_0)}{\varepsilon_0''(\omega_0)} = \frac{\Delta}{\Gamma} \quad , \tag{7-3}$$

is used to determine the excited state splitting responsible for the transitions, assuming a two-level excited state.

Due to the large amounts of figures in this chapter, the figures have been arranged as follows. Measurements of $\varepsilon_0(\omega)$ for the six materials studied in this work are presented in Figures 7.1 - 7.7. The spectra of the Kerr ellipticity, ε_K, and Kerr rotation, θ_K, for these materials are shown in Figures 7.8 - 7.11. From these two sets of data, we calculate the off-diagonal elements of the dielectric tensor represented by the quantity $\varepsilon_1(\omega)$. The spectra of ε_1 are shown in Figures 7.12 - 7.18 along with other data pertaining to this quantity. The rest of the figures in this chapter are devoted to the presentation of the curve fits to the experimental data. Figures 7.19 - 7.25 show the curve fits to the ε_0 spectra of the materials investigated in this work. Figures 7.26 - 7.28 present the curve fits to the spectra of ε_1, while Figures 7.29 - 7.32 present the curve fits to the *change* in $\varepsilon_1(\omega)$ produced by bismuth substitution. Lastly, Tables 7.1 - 7.6 present the numerical results of all curve fits.

Discussion and interpretation of the results will be presented in Chapter 8.

7.2 Bismuth-substituted YIG

7.2.1 Diagonal Tensor Elements

Figure 7.1, shows the effect of Bi^{3+} substitution in YIG on the diagonal elements of the dielectric tensor, $\varepsilon_0(\omega)$. We see that there is an overall increase in the imaginary part of $\varepsilon_0(\omega)$ at all energies. The real part of $\varepsilon_0(\omega)$ is increased at energies lower than 3.0 eV, but is relatively unaffected above this energy. The data compares reasonably well with that found in the literature[57] This is shown in Figure 7.4.

In Figure 7.7 are shown the contributions to the dielectric constant from bismuth substitution. The solid curves represent the differences between $Bi_{0.47}$YIG and YIG for the indicated quantities. Looking at the imaginary part of this contribution in Figure 7.7b, we see that bismuth substitution produces or enhances transitions at roughly 2.85 eV and 3.2 eV with some enhancement found in the shoulder at 2.7 eV and possibly some change is present at 3.6 eV. The two transitions are apparently quite strong compared to YIG. Note, in Figure 7.4, that at the peak of the bismuth contribution for $Bi_{0.47}$YIG at 3.2 eV, the contribution comprises roughly 50% of the imaginary part of the dielectric constant.

7.2.2 Gaussian Fitting

In order to identify the transitions responsible for the spectra of the diagonal elements of the dielectric tensor, we fit the imaginary part of this quantity to a series of Gaussian peaks. There is no reason to assume that the transitions responsible for the optical spectra produce Gaussian lineshapes in ε_0'' in such a concentrated system. In general, the actual lineshapes produced by a group of transitions is the integral of $\varepsilon_0''(\omega_0)$ (See Equation 3-19) weighted by the joint density of states $\mathcal{D}(\omega_0)$:

$$\varepsilon_0''(\omega) = \int_0^\infty \mathcal{D}(\omega_0)\varepsilon_0''(\omega;\omega_0)d\omega_0 \quad . \tag{7-4}$$

Unfortunately, we do not know the joint density of states. We do know, however, that the imaginary part of the dielectric constant consists of absorptive peaks. As such, we assume a Gaussian as a convenient approximation to these peaks.

---

57 V. Doorman, J. P. Krumme and C. P. Klages, Appl. Phys. A **34**, 223 (1984).

We note in passing that a Lorentzian lineshape, as given by Equation (3-22), was not used in the fitting of ε_0'', because the long tails of such functions made them unusable for fitting the data at low energies.

A fit was first performed on YIG. The results are shown in Figure 7.20 and Table 7.1. In order to add validity to our curve fitting, we used, as initial guesses, the energies shown in Figure 7.19 where the ε_0 spectrum of YIG is shown. The energies were chosen for their correspondence to features in the spectrum. The possible transition at 3.60 eV was found not to be necessary in the curve fitting and is not included in Table 7.1. Also, to match the data found in the literature[57] for $\varepsilon_0''(\omega)$ at energies above 4 eV, we initially assumed a strong transition centered at 4.35 eV. The Gaussian curve fit to the ε_0'' spectra of YIG compares reasonably well with fits achieved by previous authors.[20,38] Most notably, is the agreement that there is the onset of strong absorption peaks commencing at approximately 2.85 eV. (See Section 2.3).

The $\varepsilon_0''(\omega)$ spectra of $Bi_{0.47}YIG$ was obtained using the parameters for the YIG curve fit as initial guesses. The results are given in Figure 7.21 and Tables 7.4a and 7.4b where it can be noted that some of the transition energies found for $Bi_{0.47}YIG$ differ slightly from those of YIG. To our knowledge, there are no similar curve fits to $\varepsilon_0''(\omega)$ for bismuth-substituted YIG that can be used to make a comparison.

7.2.3 Kerr Effect Measurements

Measurements of the Kerr ellipticity and rotation were performed using the magneto-optic spectrometer of Chapter 5. The spectra of $Bi_{0.47}YIG$ and YIG are presented in Figure 7.8. The increase in the Kerr ellipticity and rotation due to bismuth substitution is clearly seen. Figure 7.9 is a comparison of our data with that of Wittekoek *et al.*[14]. The comparison is good if we assume that the rotations reported by Wittekoek *et al.* are actually negative rotations. The reason for this is that for regions where $\varepsilon_0' >> \varepsilon_0''$, ($\omega < 3$ eV for YIG), the rotation and ellipticity obey Kramer-Kronig relations where the rotation corresponds to the real function and the ellipticity corresponds to the imaginary (see Chapter 3). In order to satisfy these relations, in particular Equation (3-33), we must assume that the rotations in reported by Wittekoek *et al.* are negative rotations[†] .

[†] We could have chosen the ellipticities to be negative, but we have instead adopted the sign convention for rotations and ellipticities used in reference c.

7.2.4 Off-diagonal Tensor Elements

In order to analyze the magneto-optic data presented in the last section, it is convenient to express these data in terms of the off-diagonal elements of the dielectric tensor of a magnetic material. The off-diagonal elements of the tensor are represented by the quantity ε_1 which can be related to the measured spectra by Equation (7-1). Data for the real and imaginary part of ε_1 for the materials $Bi_{0.47}$YIG and YIG are shown in Figure 7.12. The increase in both parts of ε_1 due to bismuth substitution is clearly seen.

The effect of bismuth substitution on the magneto-optic properties of YIG can be seen in Figure 7.15, where the difference in $\varepsilon_1(\omega)$ between $Bi_{0.47}$YIG and YIG are shown. From inspection, it can be seen that the spectra of ε_1 induced by bismuth substitution is caused predominately by a diamagnetic transition. This comes from the dissipative line shape of the real part of ε_1 and the dispersive line shape of the imaginary part centered around the same energy. It will be shown in the next section that the spectra are actually caused by the presence of *two* diamagnetic transitions.

7.2.5 Curve fit to Off-diagonal Tensor Elements: YIG

We were able to simultaneously fit the real and imaginary parts of the ε_1 spectrum of YIG by assuming a series of paramagnetic transitions described by Equation (3-27). A fit to YIG is shown in Figure 7.26 and tabulated results are given in Table 7.1. Notice that the transition energies correspond closely to the energies found from fits to those of the dielectric constant spectra of these materials. The one exception is a transition centered at 3.93 eV which has no match in the Gaussian curve fit to $\varepsilon_0''(\omega)$. In order to agree with data in the literature[f] for energies above 4 eV, we initially assumed a strong paramagnetic transition in the vicinity of 4.4 eV (see Figure 7.16).

Of note in Figure 7.13 is the feature in the ε_1 spectrum at 2.85 eV. Previous authors[14,39] have attributed this feature to a diamagnetic transition due to the dispersive shape of the imaginary part. However, $\varepsilon_1''(\omega)$ for a diamagnetic transition is centered around a value of zero (see Figure 3.3), while the feature in the iron garnet spectra is not. In order for this feature to be a diamagnetic line, there must be transitions at energies less than 2.85 eV that will offset the dispersive lineshape to a value around 0.01. This does not seem likely. We have instead assumed this part of the spectrum to be due to two closely spaced paramagnetic transitions of opposite sign. This is shown in Figure 7.17. The assumption gains validity from the fact that the energies chosen closely correspond to energies found from the Gaussian curve fits of the diagonal elements; namely 2.73 eV

and 2.90 eV. Further, the 2.90 eV transition is stronger than the 2.73 eV transition which is also the case in the ε_0'' spectrum.

It can be seen from Table 7.1 that the linewidths of the magneto-optic peaks are generally smaller than those of the ε_0'' spectra. This is due in part to the two different line shapes used in our curve fits. We approximated the ε_0'' spectra with Gaussian peaks whose width, Γ_{Gauss}, is the width of the peak at e^{-1} of its maximum value. The Lorentzian line shape assumed in fitting the off-diagonal elements of the dielectric tensor have widths, $\Gamma_{Lorentz}$, equal to the halfwidth at half-maximum. A Gaussian lineshape must then have a larger value for its width, Γ_{Gauss}, in order to have the same width of a Lorentzian peak at half-maximum. This accounts for about 20% of the difference in the widths of the two different spectra. Another factor is the fact that Lorentzian peaks have much larger tails than Gaussians. We can not quantify how the large tails affect the linewidths of the observed lines.

Using the numerical results obtained from curve fits of $\varepsilon_0(\omega)$ and $\varepsilon_1(\omega)$, we can calculate the quantity $\Delta f/f$ for each transition using Equation (7-2). The results are given in Table 7.1. An interesting result of this calculation is illustrated in Figure 7.18. In this figure are plotted the magnitudes of $\Delta f/f$ for the first five paramagnetic transitions. Notice, that $\Delta f/f$ decreases monotonically with photon energy in a somewhat linear fashion. The solid line is a linear fit to the data of YIG. These results will be discussed in the next chapter.

7.2.6 Curve fit to Off-diagonal Tensor Elements: $Bi_{0.47}$YIG

Curve fits were performed on the *change* in $\varepsilon_1(\omega)$ between $Bi_{0.47}$YIG and YIG shown in Figure 7.15. By focusing our attention on the change in $\varepsilon_1(\omega)$, which we will call $\Delta\varepsilon_1(\omega)$, we have assumed that all the paramagnetic transitions of YIG found in the previous section are present in the bismuth iron garnets. The simultaneous fits to the real and imaginary parts of $\Delta\varepsilon_1(\omega)$ for $Bi_{0.47}$YIG are shown in Figure 7.29 and 7.30 with numerical results tabulated in Table 7.4a. In Figure 7.29 is also shown the components of the fits. The fits are reasonably good ones with the exception of the real part above 3.5 eV in energy.

In fitting simultaneously to the real and imaginary parts of the $\Delta\varepsilon_1(\omega)$ spectra of $Bi_{0.47}$YIG, we have assumed the presence of two diamagnetic transitions and three paramagnetic transitions. The rationale for these assignments is as follows. First, there appears to be a diamagnetic transition centered around 3.2 eV. Next, while we at first attempted to fit the region of the spectra around 2.85 eV with the two closely spaced

paramagnetic transitions assumed in the previous section, we found that a better fit could be obtained by assuming a single diamagnetic transition at this energy. Also, a strong paramagnetic transition was assumed at 4.33 eV in order to agree with data of Wittekoek *et al.*[14] for energies above 4 eV[††] . This corresponds to the paramagnetic transition that is present in YIG at this energy. A paramagnetic transition was assumed at 2.38 eV in order to reasonably fit the low energy region of the spectra. Lastly, a third paramagnetic transition was added at 3.73 eV to improve the fit at higher energies. The energy of 3.73 eV corresponds to an energy found in the curve fit to $\varepsilon_0''(\omega)$, although there is no corresponding transition in the ε_1 spectrum of the non-bismuth containing samples.

With numerical results for $\varepsilon_0(\omega)$ and $\varepsilon_1(\omega)$ for the bismuth-containing samples, we can calculate the quantity $\Delta f/f$ for the paramagnetic transitions using Equation (7-2) and the ratio Δ/Γ for the diamagnetic transitions using Equation (7-3). We must use the *change* in the quantity ε_0'' when applying these formula to the $\Delta\varepsilon_1$ spectra since they arise from the addition of bismuth. These results are given in Table 7.4.

We can calculate the upper state splittings of the diamagnetic transitions. Since the widths of the magneto-optic transitions differ from those of the same transitions in the $\varepsilon_0''(\omega)$ spectra, we will use the widths of the magneto-optic lines in calculating Δ for consistency. The splitting associated with the 2.85 eV and 3.20 eV transitions are found to be 0.138 eV and 0.057 eV, respectively. These values are listed in Table 7.4b.

It should be mentioned that the values of Δ were kept fixed at small values during the curve fitting process. This is acceptable since the shape of $\varepsilon_1(\omega)$ for a diamagnetic transition is insensitive to Δ for values of Δ/Γ less than about one-fourth. Letting the value of Δ vary during curve fitting resulted in large values which were inconsistent with the value found using Equation (7-3).

The above values can be compared to other reported estimates of Δ in the literature. Wittekoek *et al.*[14] estimated values using a cruder version of the procedure we have followed here. They estimated values of Δ = 0.01 eV and Δ = 0.06 eV for transitions at 2.8 eV and 3.3 eV, respectively, in the material $Bi_{0.25}YIG$. The second of these values agrees very well with our estimate of 0.055 eV, while the value for the 2.8 eV transition bears little resemblance to ours. It should be noted that the curve fit for the ε_0'' spectra of $Bi_{0.47}YIG$ does not qualitatively agree with what is shown in Figure 7.7b. This may explain the discrepancy. We will point out later in this chapter, however, that

---

[††] Wittekoek *et al.* assumed this line to be part of diamagnetic transitions. We believe a single paramagnetic transition at 4.33 eV provides a better fit and agrees with the transition energy assumed to be present in the spectrum of ε_0''.

our value is probably too high due to the inaccuracies of our curve-fitting procedure and a correction will produce a value for Δ of roughly 0.03 eV.

The only other published estimates of the excited state splittings in bismuth iron garnets are those of Dionne and Allen[58] who obtained values for Δ by fitting Wittekoek *et al.*'s data to the lineshapes of $\varepsilon_1(\omega)$ only. They obtained values of Δ for $Bi_{0.25}$YIG of 0.11 eV and 0.27 eV for diamagnetic transitions at 2.6 eV and 3.15 eV, respectively. The value obtained for the 2.6 eV transition is in good agreement with the value reported here for $Bi_{0.47}$YIG, although the transition energy is somewhat lower than what we have observed. The value for Δ at 3.15 eV, however, is much larger than the splitting reported here.

In the Chapter 8, we will discuss the origins of the diamagnetic transitions and their excited state splittings.

7.3 Dilution of the Iron Sublattices

7.3.1 Diagonal Tensor Elements

In Figures 7.5 and 7.6 can be seen the effect of Al^{3+} and In^{3+} substitution on the diagonal elements of the dielectric tensor of YIG and $Bi_{0.47}$YIG. When either of these two ions are substituted, there is an overall decrease in the imaginary part of the dielectric constant, ε_0''. This is not unexpected, since optical absorption in these materials comes from the Fe^{3+} ions. Substitution of these ions thus reduces the number of absorbers and the total absorption. The real part of the diagonal elements of $Bi_{0.47}$YIG and YIG is decreased by Al^{3+} and In^{3+} substitution below 3.25 eV, while it is increased above this energy. This suggests the reduction of a transition(s) centered around this energy is due to the dispersive shape of $\varepsilon_1'(\omega)$. Note, also, that substitution by $Al_{0.5}$ gives roughly the same effect as substitution by $In_{0.33}$, yet, they represent different amounts of iron substitution. If we make the assumption stated earlier, that all substituting ions reside in their preferred sites, this would imply that the transitions affected by iron substitution depend upon the iron population of both sublattices. This is in agreement with the suggestions of other authors, that transitions involving pairs of iron ions in different sites are responsible for the optical spectra in this region (see Section 2.3). We are unable, however, to resolve any of the crystal field transitions that have been identified below 2.5 eV.[e]

---

58 G. F. Dionne and G. A. Allen, J. Appl. Phys. **73**, 6127 (1993).

7.3.2 Gaussian Curve fit

We have performed a Gaussian curve fit to the ε_0'' spectra of aluminum and indium-substituted samples. The fits are shown in Figures 7.22 - 7.25 with the parameters of the fits listed in Tables 7.2, 7.3, 7.5 and 7.6. The ε_0'' spectra of $Al_{0.5}YIG$ and $In_{0.33}YIG$ were fitted using the peaks found for YIG as initial guesses. Initially, only the heights of the Gaussian peaks were allowed to vary, the energies and linewidths being kept fixed. This insured that the fitting program converged properly upon the data. The spectra were fit a second time with all three parameters of the peaks being allowed to vary. Fits to the ε_0'' spectra of $Bi_{0.48}Al_{0.5}YIG$ and $Bi_{0.46}In_{0.33}YIG$ were performed using the procedure described above, but with the parameters of the curve fit for $Bi_{0.47}YIG$ used as initial guesses.

7.3.2 Off-diagonal Tensor Elements

In Figures 7.10 and 7.11 are shown the Kerr ellipticity and rotation spectra for $Al_{0.5}YIG$, $In_{0.33}YIG$, $Bi_{0.48}Al_{0.5}YIG$ and $Bi_{0.46}In_{0.33}YIG$ along with YIG and $Bi_{0.47}YIG$. These spectra were used to calculate the spectra of the off-diagonal elements of the dielectric tensor by use of Equation (7-1). The spectra of the off-diagonal elements of the dielectric tensor of all six materials studied are shown in Figures 7.13 and 7.14.

In Figure 7.13, we see that the substitution of aluminum and indium into YIG reduces the overall intensity of $\varepsilon_1(\omega)$. We are able to fit these spectra with the paramagnetic transitions found for YIG, except with smaller amplitudes. The curve fits are shown in Figures 7.27 and 7.28 with values for the parameters of the transitions listed in Tables 7.2 and 7.3. With the numerical data derived from curve fits to $\varepsilon_0(\omega)$ and $\varepsilon_1(\omega)$, we can calculate the quantity $\Delta f/f$ for the paramagnetic transitions of $Al_{0.5}YIG$ and $In_{0.33}YIG$. Results are given in Tables 7.2 and 7.3. As was found for YIG, the magnitudes of $\Delta f/f$ for the first five paramagnetic lines of $Al_{0.5}YIG$ and $In_{0.33}YIG$ decrease with energy in a somewhat linear fashion. This relation is shown in Figure 7.18. Discussion on this observation is postponed until the next chapter.

For the bismuth-substituted materials $Bi_{0.48}Al_{0.5}YIG$ and $Bi_{0.46}In_{0.33}YIG$, we again focus on the change in $\varepsilon_1(\omega)$ caused by bismuth substitution, $\Delta\varepsilon_1(\omega)$. The $\Delta\varepsilon_1$ spectra are shown in Figure 7.15 along with that of $Bi_{0.47}YIG$. There are several of interesting results which can be derived by inspection of these spectra.

First, all curves have the same shape with roughly the same zero-crossings. This would indicate that all spectra, regardless of bismuth or iron content, are scalings of a single spectra. Secondly, we notice that the removal of iron from either sublattice reduces the bismuth contribution to ε_1, and further, removal of one-sixth of the iron in octahedral sites has the *same* effect as removal of one-sixth of the iron in the tetrahedral sites. This is significant because the two dilutions represent different total iron populations. From this we conclude that the magneto-optic effect produced by the substitution of bismuth into iron garnets is dependent on the joint population of the two iron sublattices.

Curve fits to the $\Delta\varepsilon_1$ spectra of $Bi_{0.48}Al_{0.5}YIG$ and $Bi_{0.46}In_{0.33}YIG$ have been performed and are presented in Figures 7.31 and 7.32. We again assumed the two diamagnetic transitions and three paramagnetic transitions that were used to fit $Bi_{0.47}YIG$ in section 7.2.6. Numerical results of the curve fits are listed in Tables 7.5 and 7.6. With the results from these curve fits for $\varepsilon_0''(\omega)$, we calculate the quantities $\Delta f/f$ and Δ/Γ using Equations (7-2) and (7-3). The results are listed in Tables 7.5b and 7.6b. Finally, we can calculate the splitting of the excited states responsible for the diamagnetic transitions from the ratio Δ/Γ. Using the linewidths of the diamagnetic transitions, we find for $Bi_{0.48}Al_{0.5}YIG$: $\Delta_{2.85eV} = 0.095$ eV and $\Delta_{3.20eV} = 0.055$ eV; and for $Bi_{0.46}In_{0.33}YIG$: $\Delta_{2.85eV} = 0.084$ eV and $\Delta_{3.20eV} = 0.052$ eV.

It can be noticed that the values for the splittings associated with the 3.20 eV transitions are approximately equal, having a value of approximately $\Delta = 0.055$ eV. The values for the 2.85 eV transitions, however, have a wide range. This may be due to the fact that the curve fits, from which we obtain our values of $\varepsilon_0''(\omega)$, do not accurately represent the increase in ε_0'' in the following way. From Figure 7.7 we would expect that the increase in $\varepsilon_0''(\omega)$ occurs at roughly 2.85 eV and 3.20 eV. The curve fits for $\varepsilon_0''(\omega)$ for the bismuth substituted materials, however, show most of this increase coming from the 2.73 eV transition (see Tables 7.2, 7.4 and 7.6). Since it appears that most of the intensity of the increase is represented in the 2.73 eV peak, we have tried to use the total change in *both* the 2.73 eV and the 2.85 eV peaks to find approximate values for the excited state splitting. Doing so, we obtain the following values:

$$\Delta_{BiYIG} = 0.036 \text{ eV} \quad , \quad \Delta_{BiAlYIG} = 0.033 \text{ eV} \quad , \quad \Delta_{BiInYIG} = 0.028 \text{ eV} \quad .$$

These values are more consistent than those obtained earlier and are used for the discussion in Chapter 8. We approximate these values collectively as $\Delta_{2.85} = 0.033$ eV.

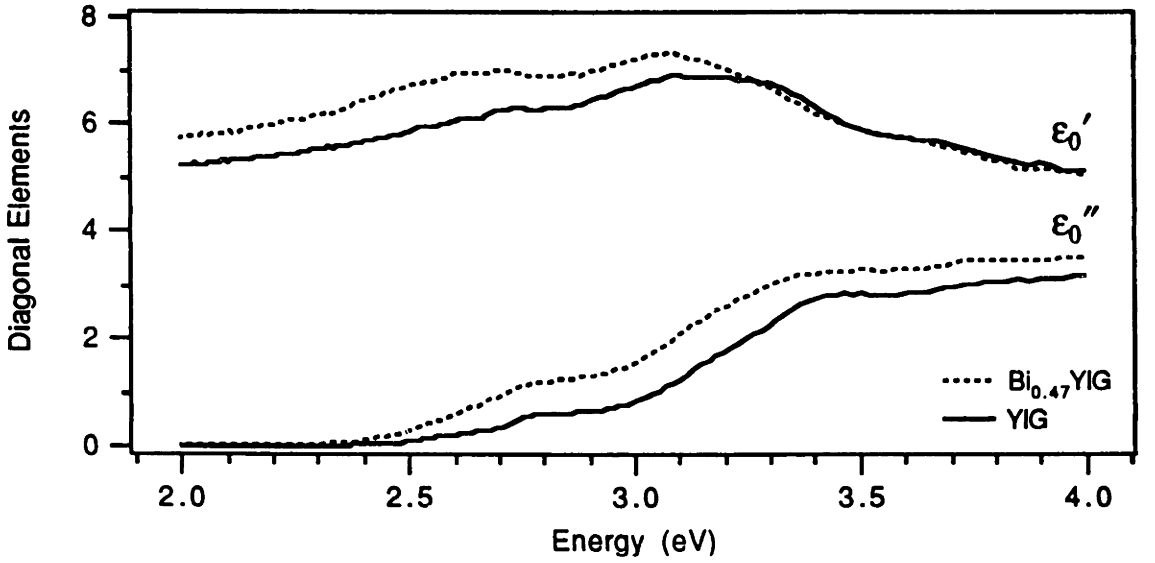

Figure 7.1. Off-diagonal elements of the dielectric tensor for $Bi_{0.47}Y_{2.53}Fe_5O_{12}$ and $Y_3Fe_5O_{12}$.

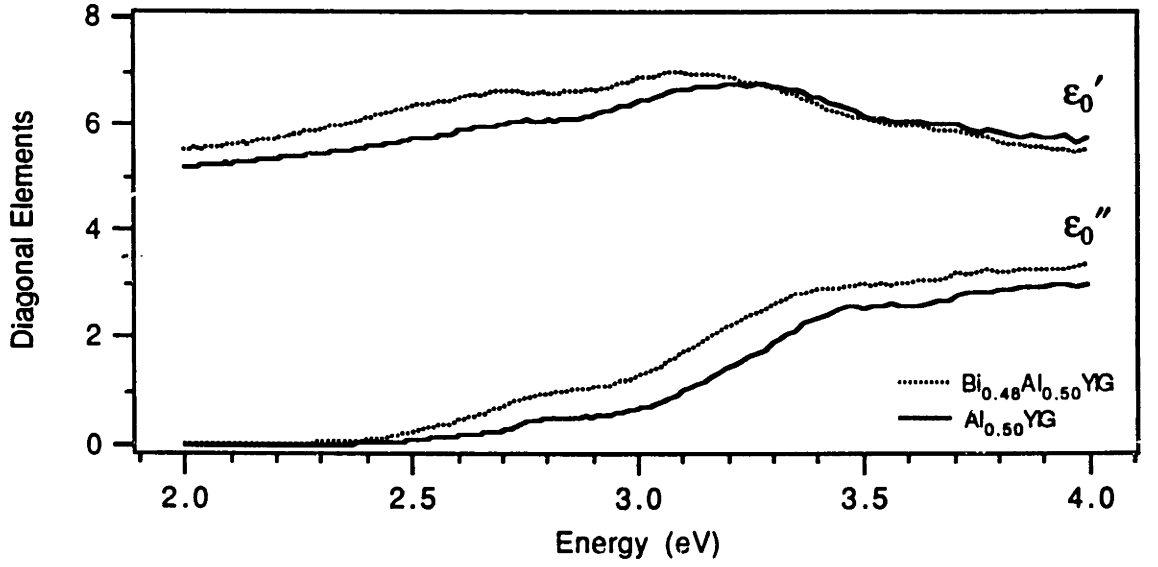

Figure 7.2. Off-diagonal elements of the dielectric tensor for $Bi_{0.48}Y_{2.52}Al_{0.5}Fe_{4.5}O_{12}$ and $Y_3Al_{0.5}Fe_{4.5}O_{12}$.

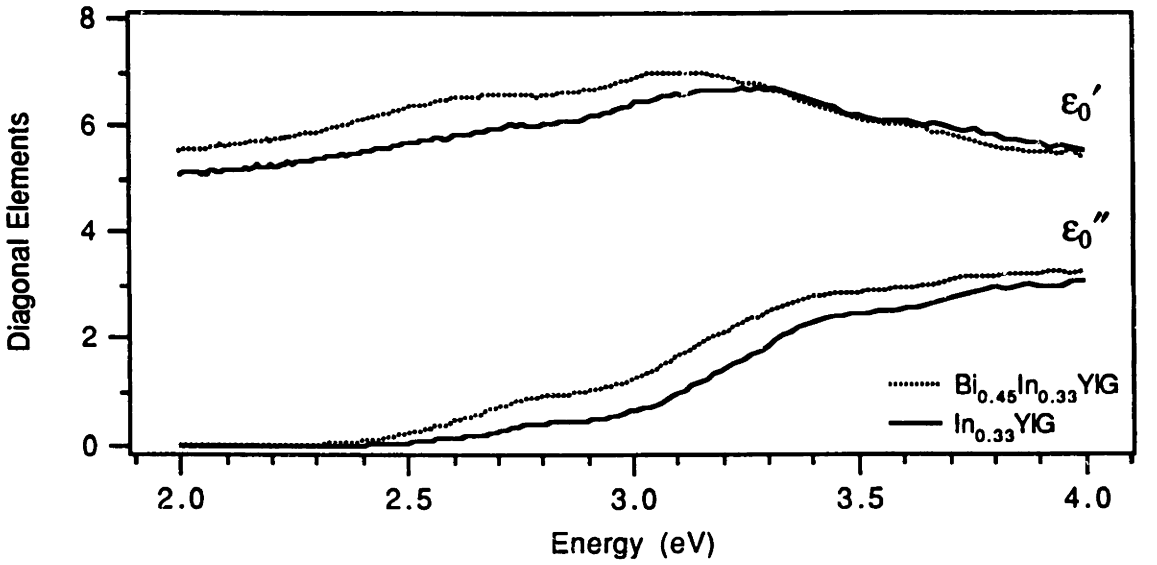

Figure 7.3. Off-diagonal elements of the dielectric tensor for $Bi_{0.46}Y_{2.54}In_{0.33}Fe_{4.67}O_{12}$ and $Y_3In_{0.33}Fe_{4.67}O_{12}$.

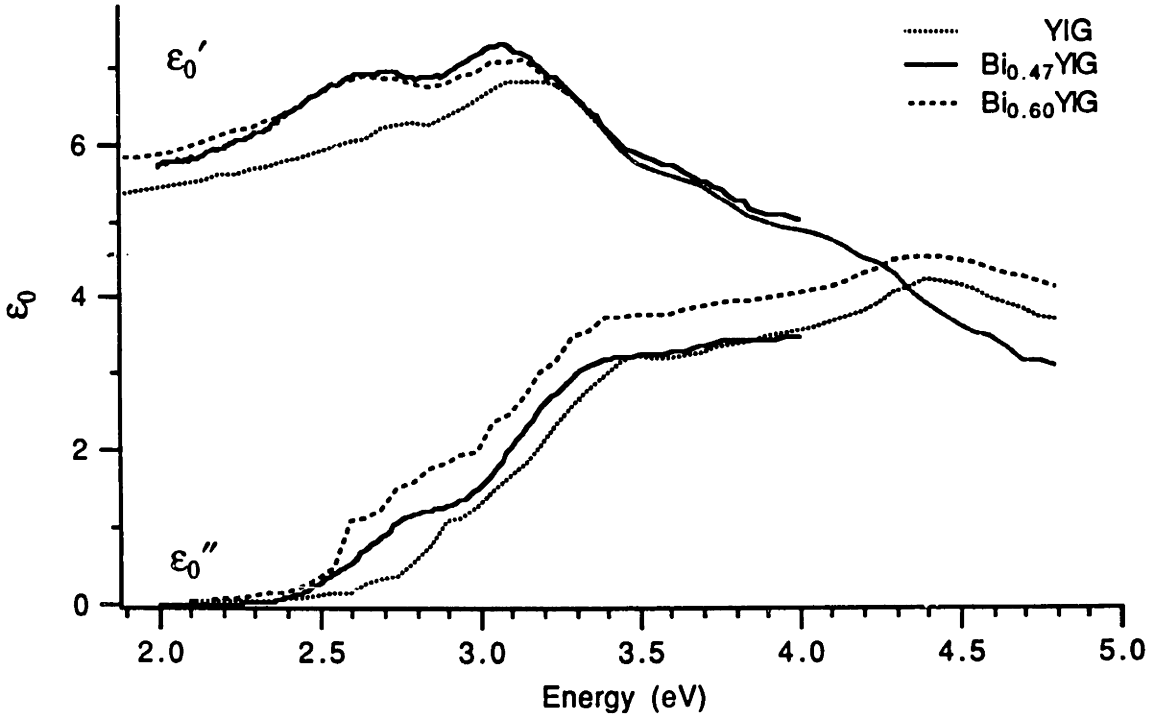

Figure 7.4. A comparison of the diagonal elements of the dielectric tensor of $Bi_{0.47}Y_{2.53}Fe_5O_{12}$ to spectra found in the literature. the spectra for $Y_3Fe_5O_{12}$ and $Bi_{0.60}Y_{2.40}Fe_5O_{12}$ are from Doorman *et al.*[57]

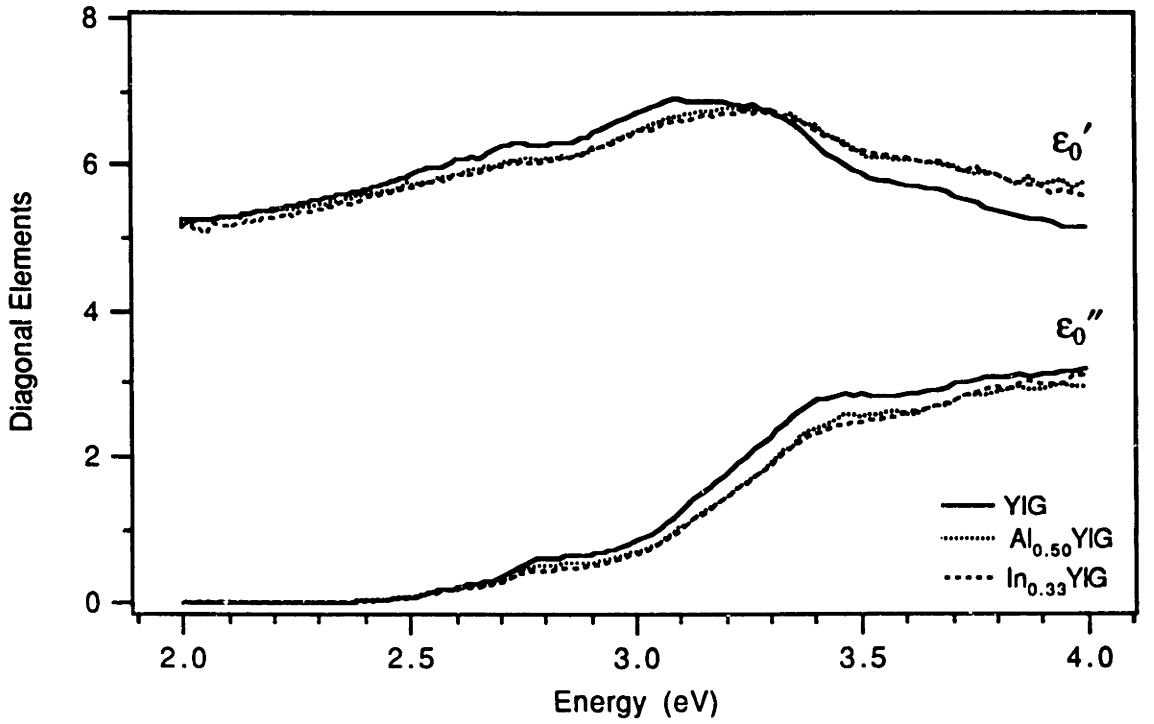

Figure 7.5. The diagonal elements of the dielectric tensor for $Y_3Fe_5O_{12}$, $Y_3Al_{0.5}Fe_{4.5}O_{12}$ and $Y_3In_{0.33}Fe4.67O_{12}$.

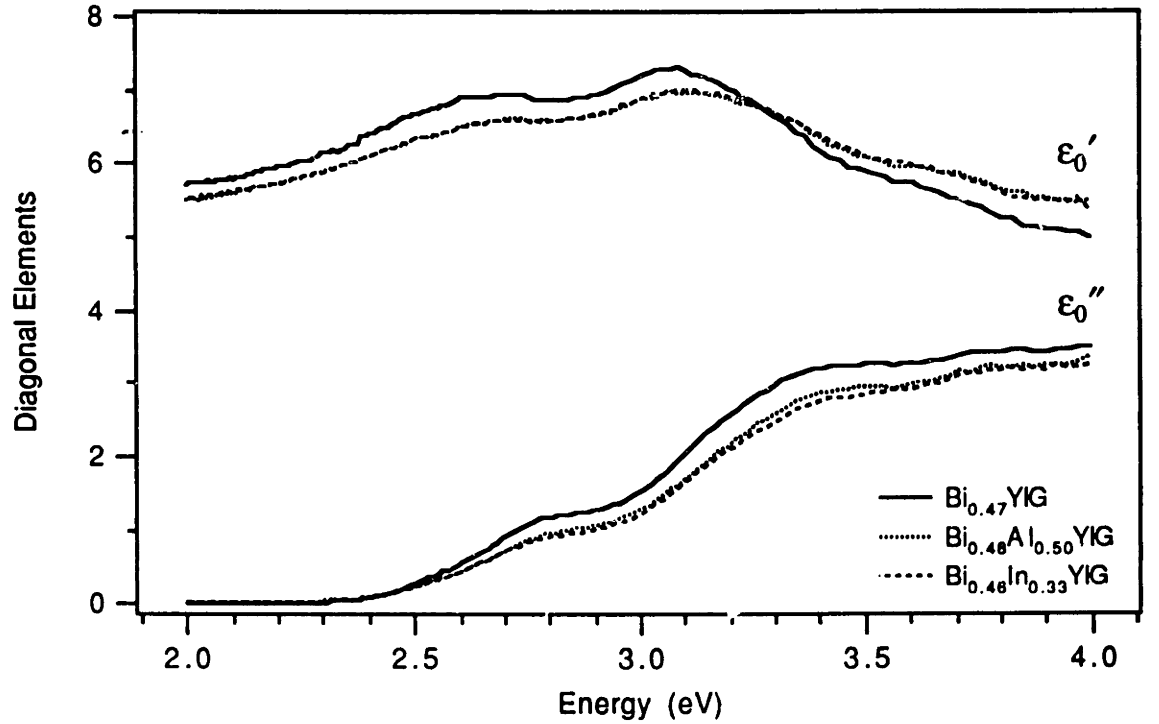

Figure 7.6. The diagonal elements of the dielectric tensor for $Bi_{0.47}Y_{2.53}Fe_5O_{12}$, $Bi_{0.48}Y_{2.52}Al_{0.5}Fe_{4.5}O_{12}$ and $Bi_{0.46}Y_{2.54}In_{0.33}Fe4.67O_{12}$.

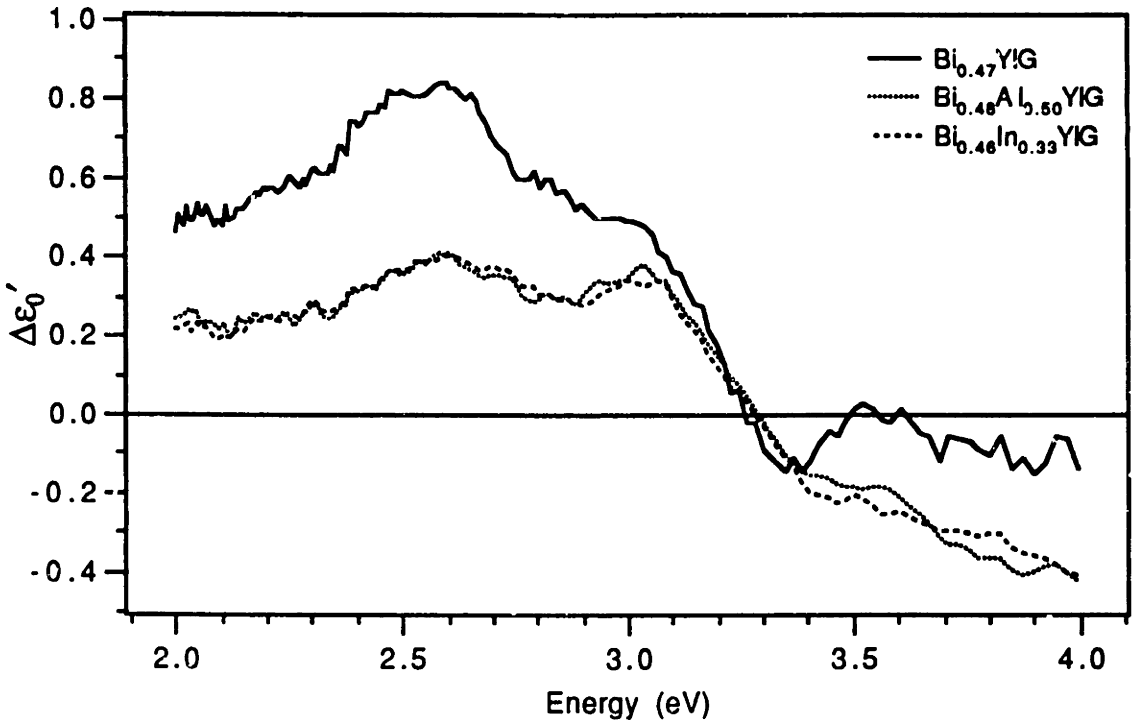

(a)

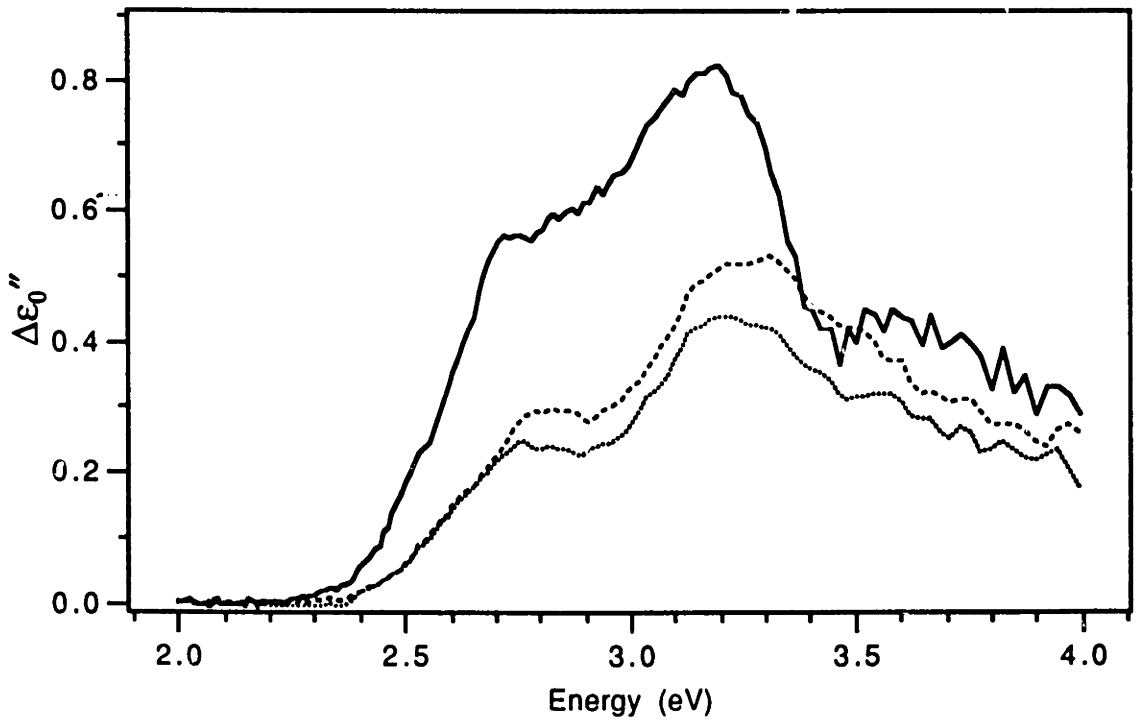

(b)

Figure 7.7. The change in the real (a) and imaginary (b) parts of ε_0 for YIG when substituted with bismuth.

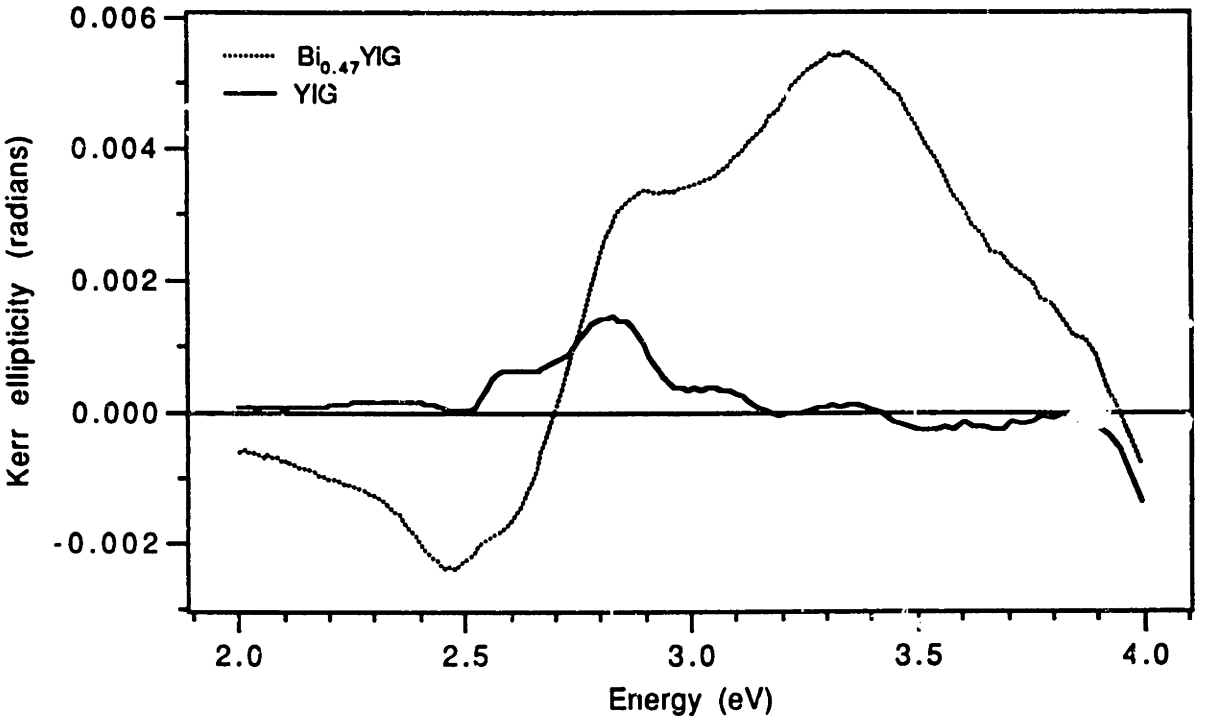

(a)

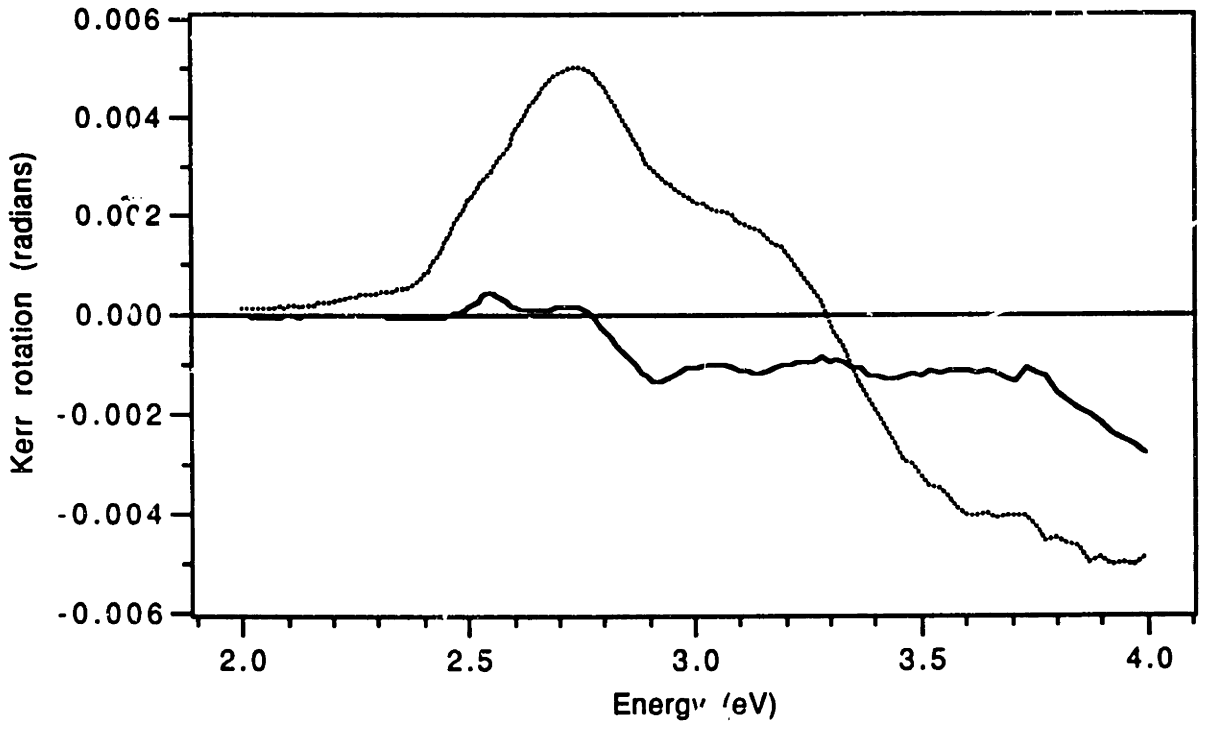

(b)

Figure 7.8. The Kerr spectra of $Y_3Fe_5O_{12}$ and $Bi_{0.47}Y_{2.53}Fe_5O_{12}$. (a) The Kerr ellipticity. (b) The Kerr rotation.

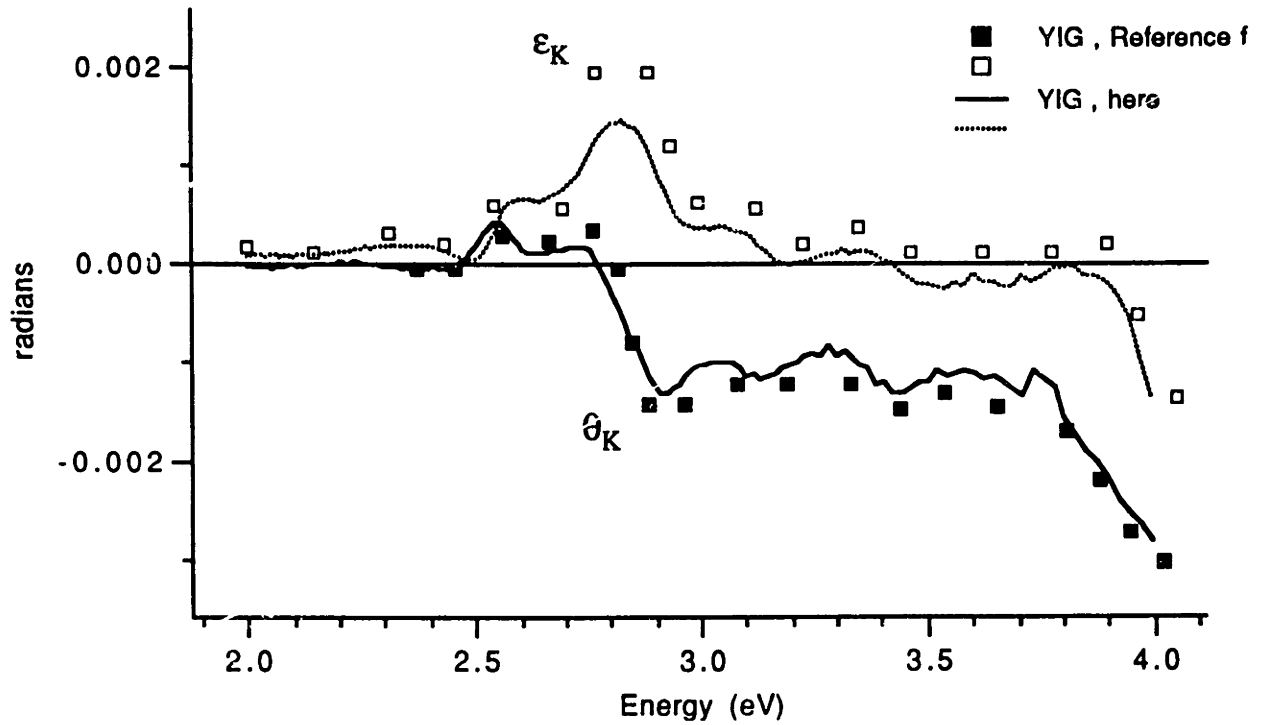

(a)

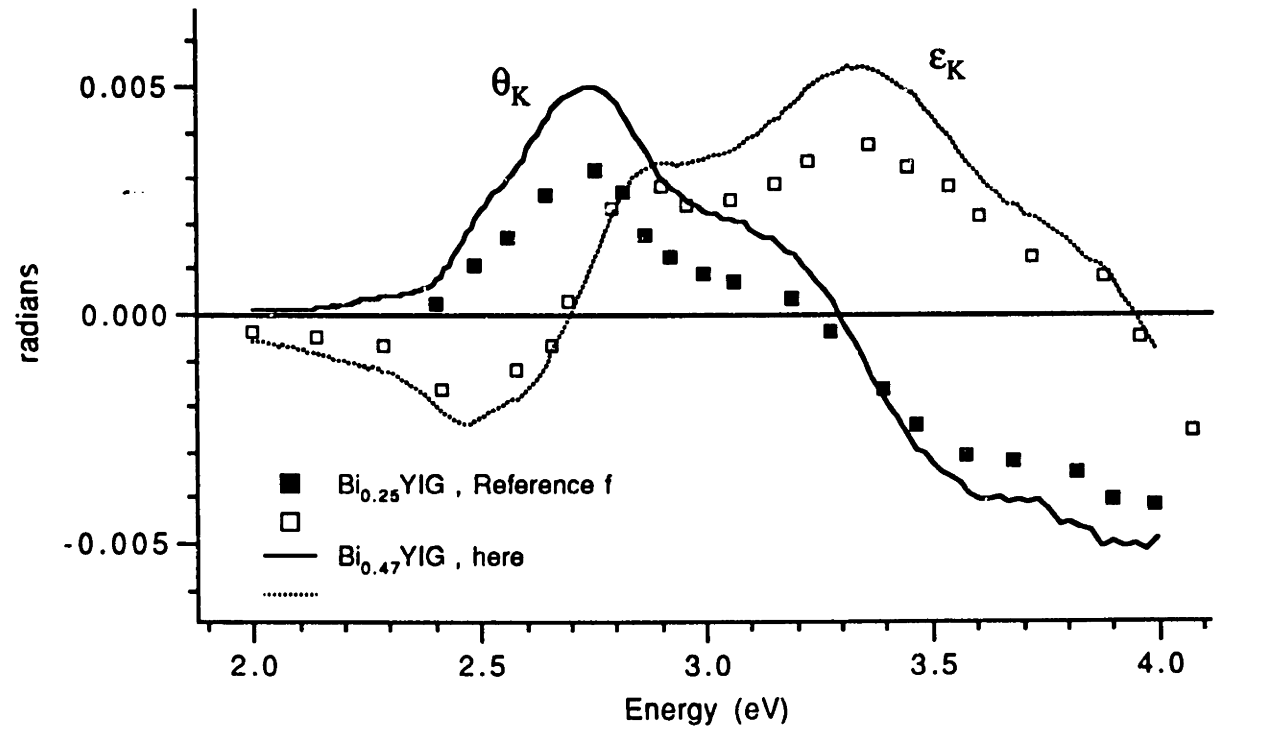

(b)

Figure 7.9. A comparison of the Kerr spectra measured by Wittekoek *et al.*[14] for $Bi_{0.25}Y_{2.75}Fe_5O_{12}$ and the Kerr spectra measured in this work for $Bi_{0.47}Y_{2.53}Fe_5O_{12}$. (a) The Kerr ellipticity. (b) The Kerr rotation.

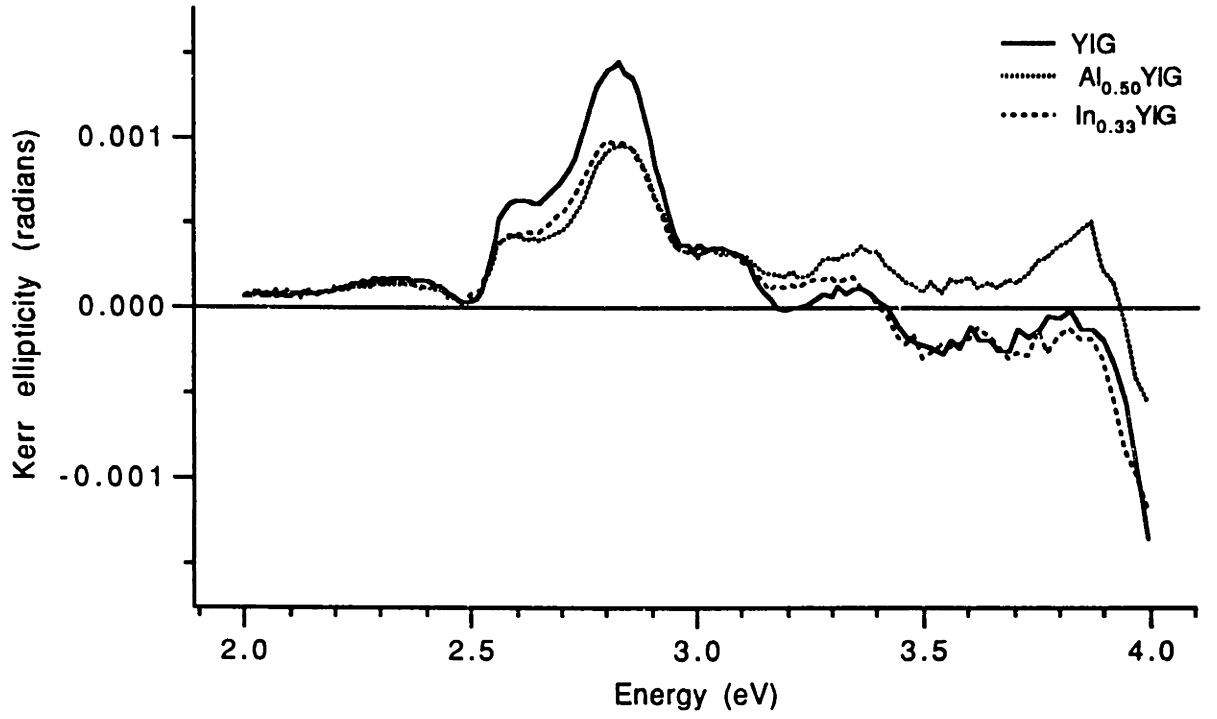

(a)

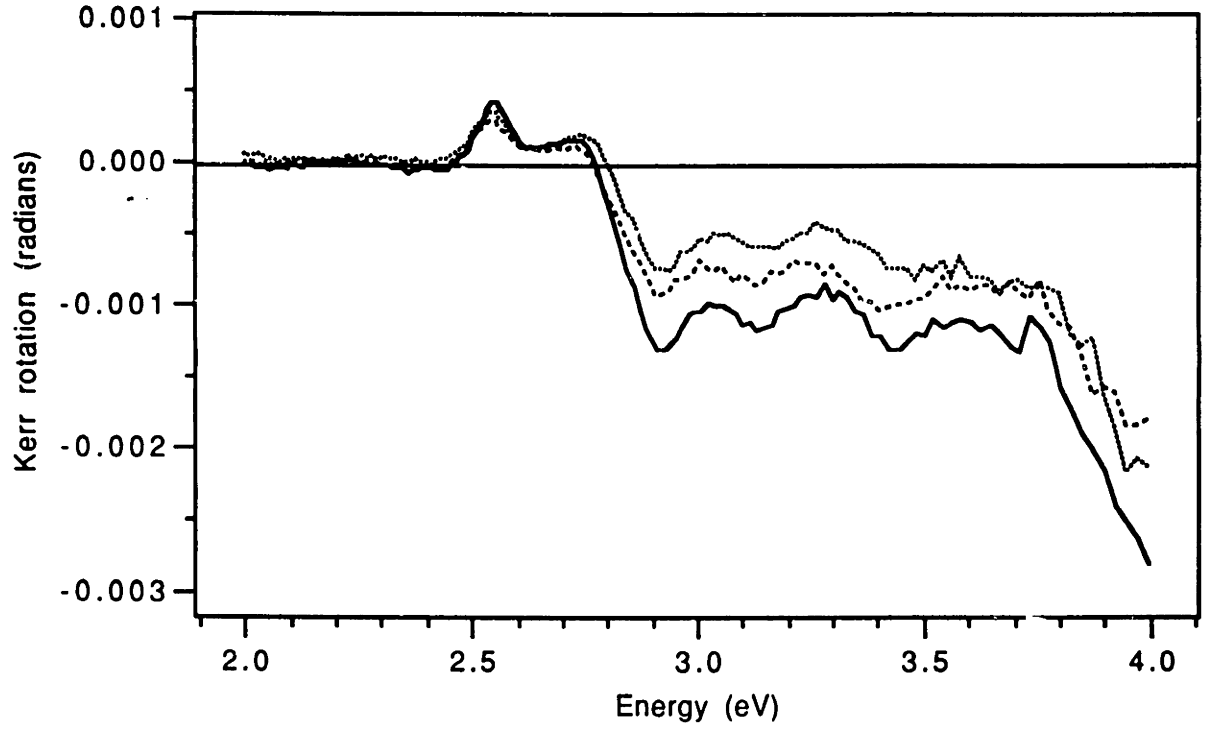

(b)

Figure 7.10. The Kerr spectra of $Y_3Fe_5O_{12}$, $Y_3Al_{0.5}Fe_{4.5}O_{12}$ and $Y_3In_{0.33}Fe4.67O_{12}$. (a) The Kerr ellipticity. (b) The Kerr rotation.

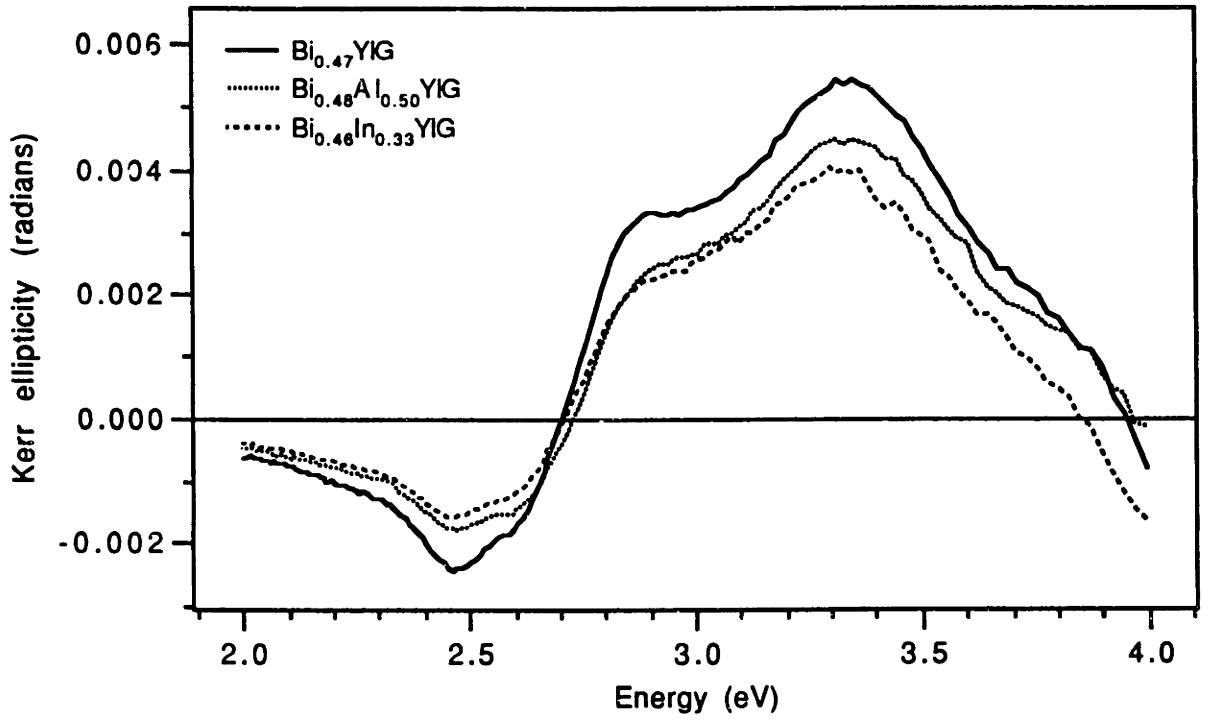

(a)

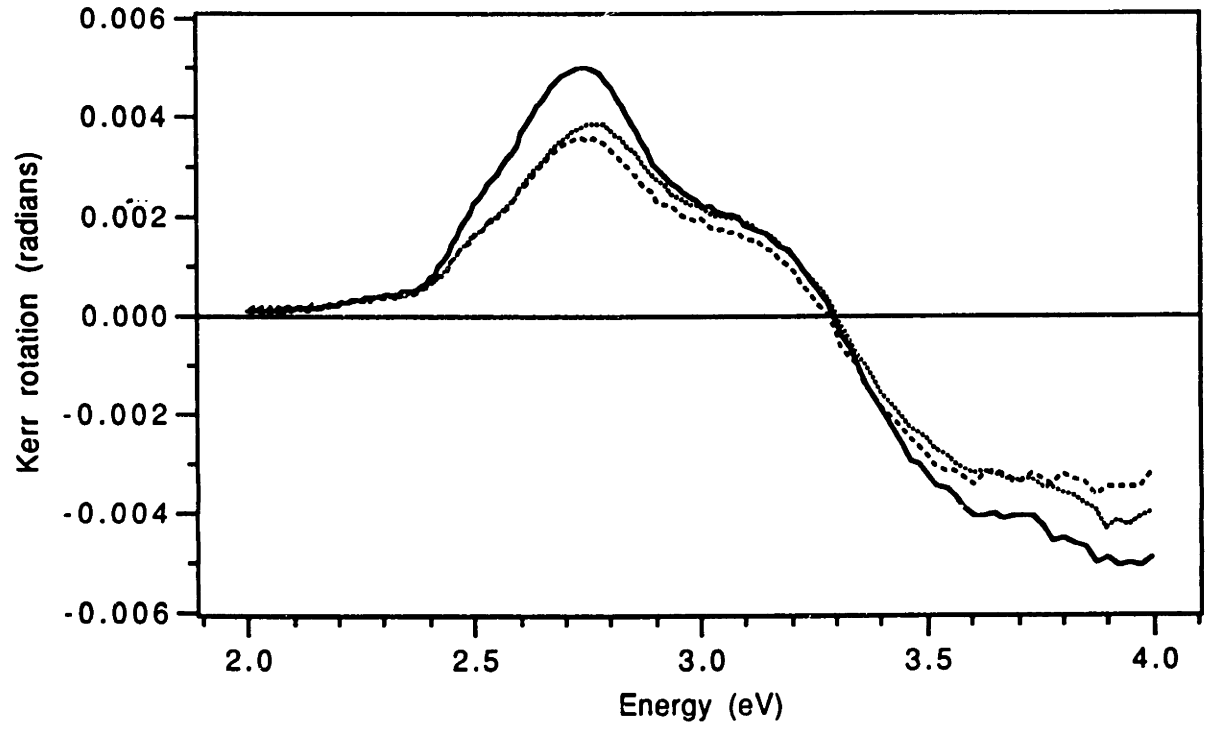

(b)

Figure 7.11. The Kerr spectra of $Bi_{0.47}Y_{2.53}Fe_5O_{12}$, $Bi_{0.48}Y_{2.52}Al_{0.5}Fe_{4.5}O_{12}$ and $Bi_{0.46}Y_{2.54}In_{0.33}Fe4.67O_{12}$. (a) The Kerr ellipticity. (b) The Kerr rotation.

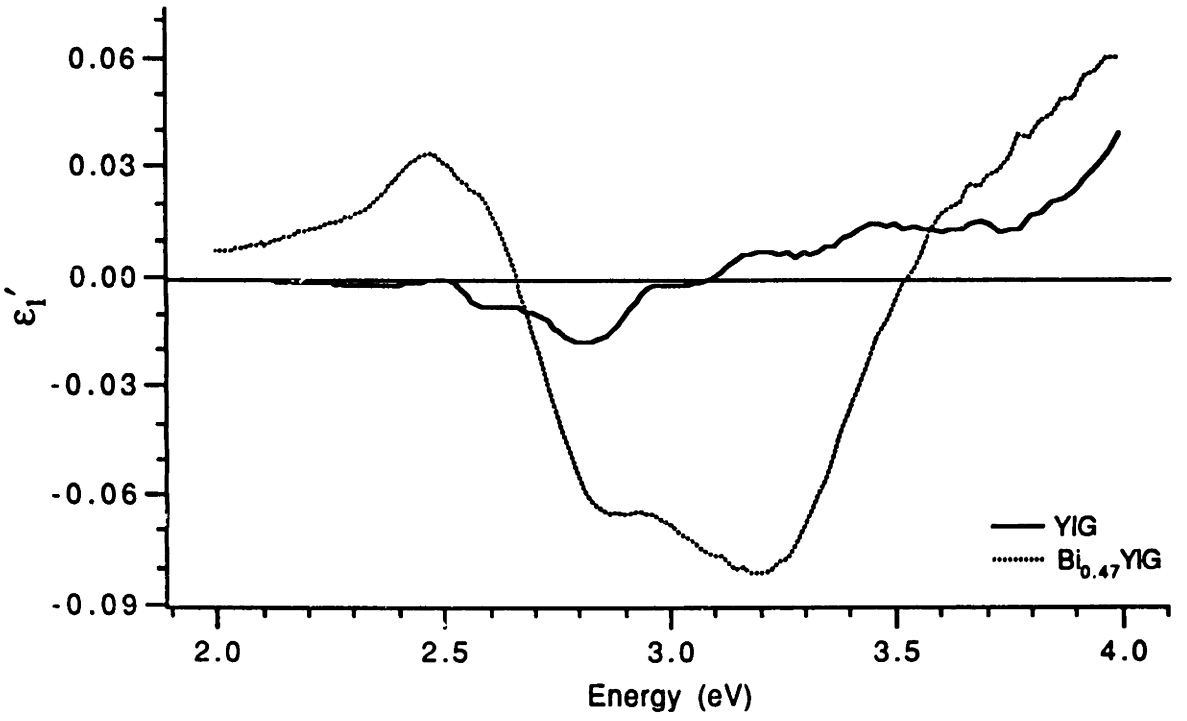

(a)

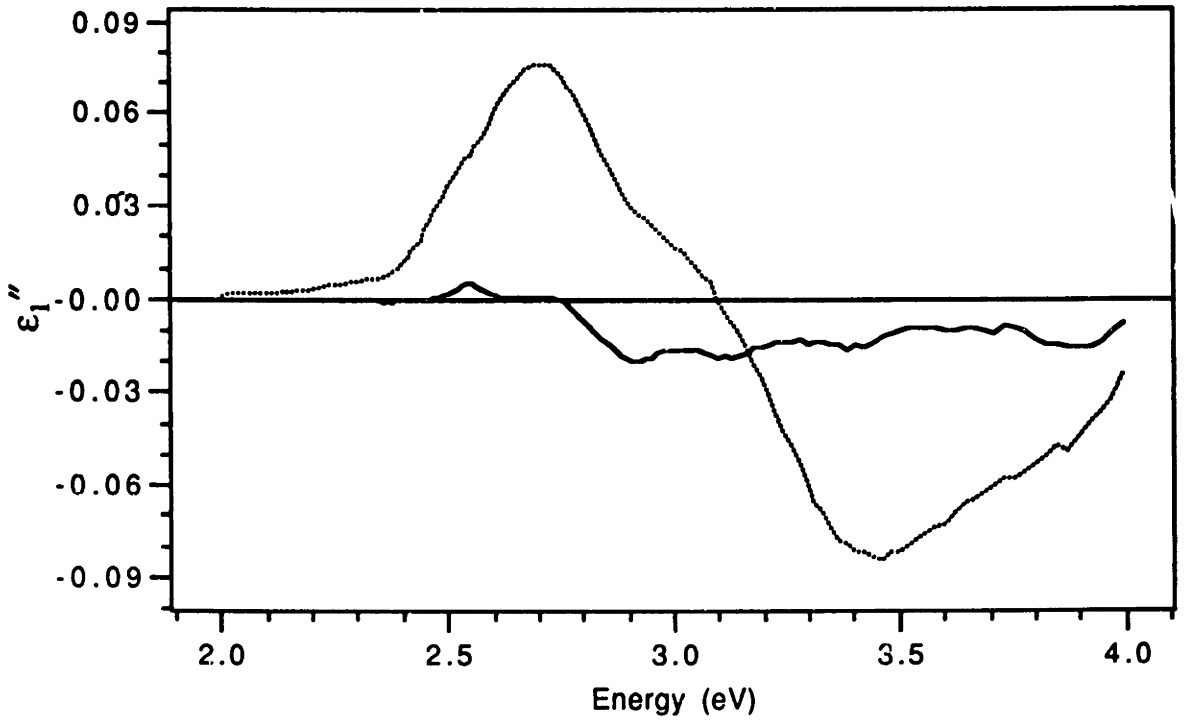

(b)

Figure 7.12. The real (a) and imaginary (b) parts of the off-diagonal elements of the dielectric tensor for $Y_{2.53}Fe_5O_{12}$ and $Bi_{0.47}Y_{2.53}Fe_5O_{12}$.

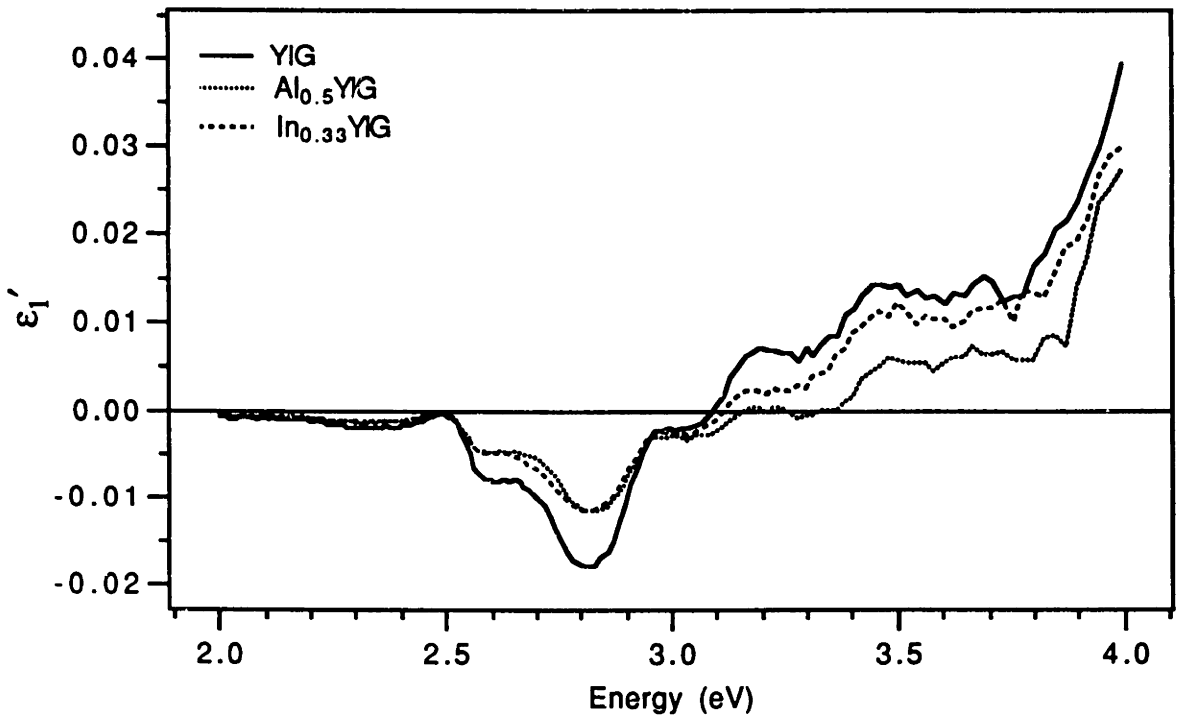

(a)

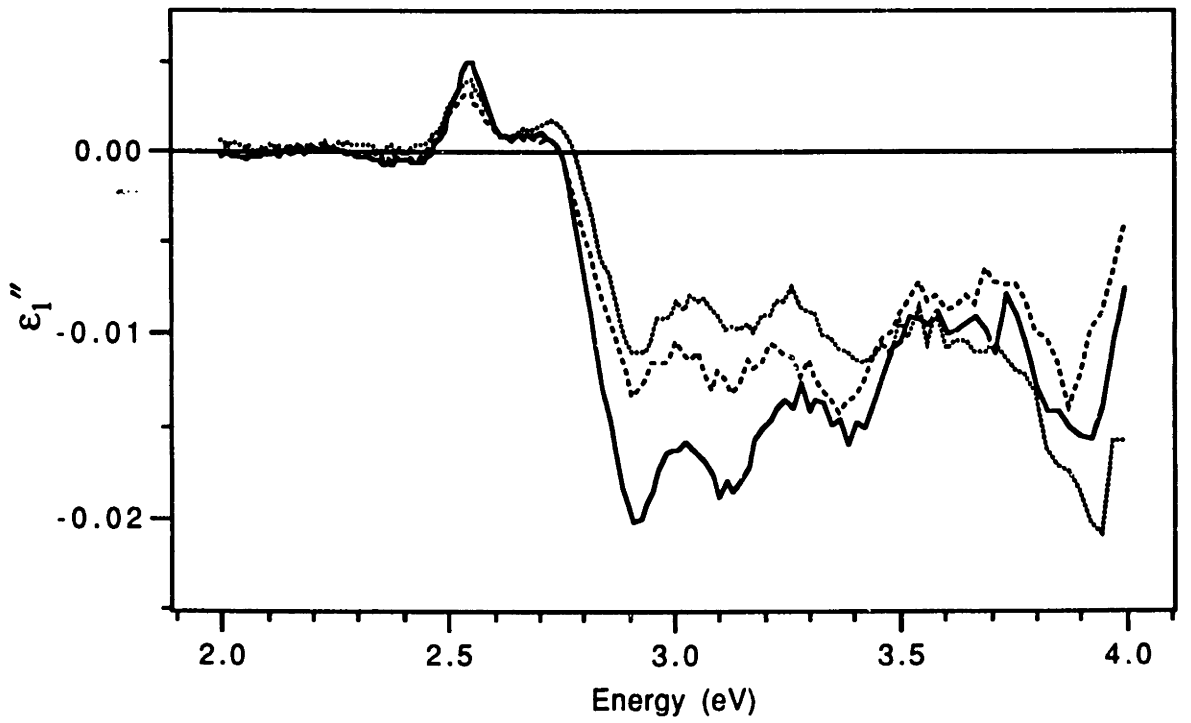

(b)

Figure 7.13. The real (a) and imaginary (b) parts of the off-diagonal elements of the dielectric tensor for $Y_3Fe_5O_{12}$, $Y_3Al_{0.5}Fe_{4.5}O_{12}$ and $Y_3In_{0.33}Fe4_{.67}O_{12}$.

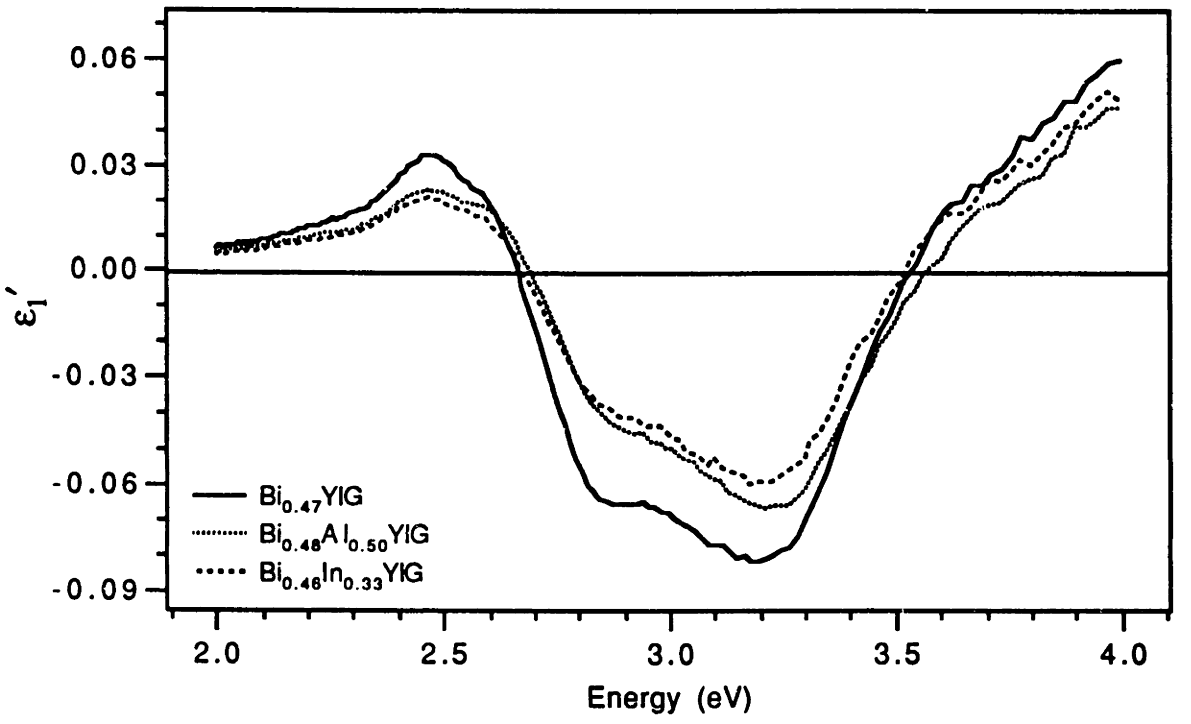

(a)

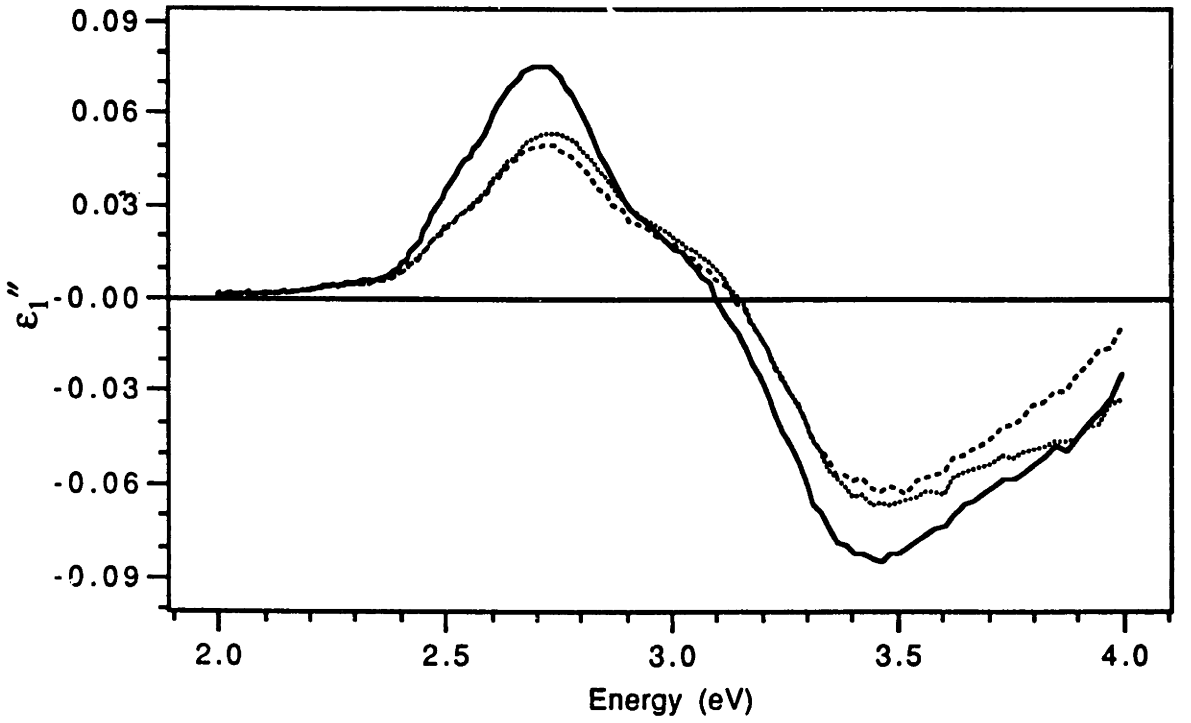

(b)

Figure 7.14. The real (a) and imaginary (b) parts of the off-diagonal elements of the dielectric tensor for the materials $Bi_{0.47}Y_{2.53}Fe_5O_{12}$, $Bi_{0.48}Y_{2.52}Al_{0.5}Fe_{4.5}O_{12}$ and $Bi_{0.46}Y_{2.54}In_{0.33}Fe4_{.67}O_{12}$.

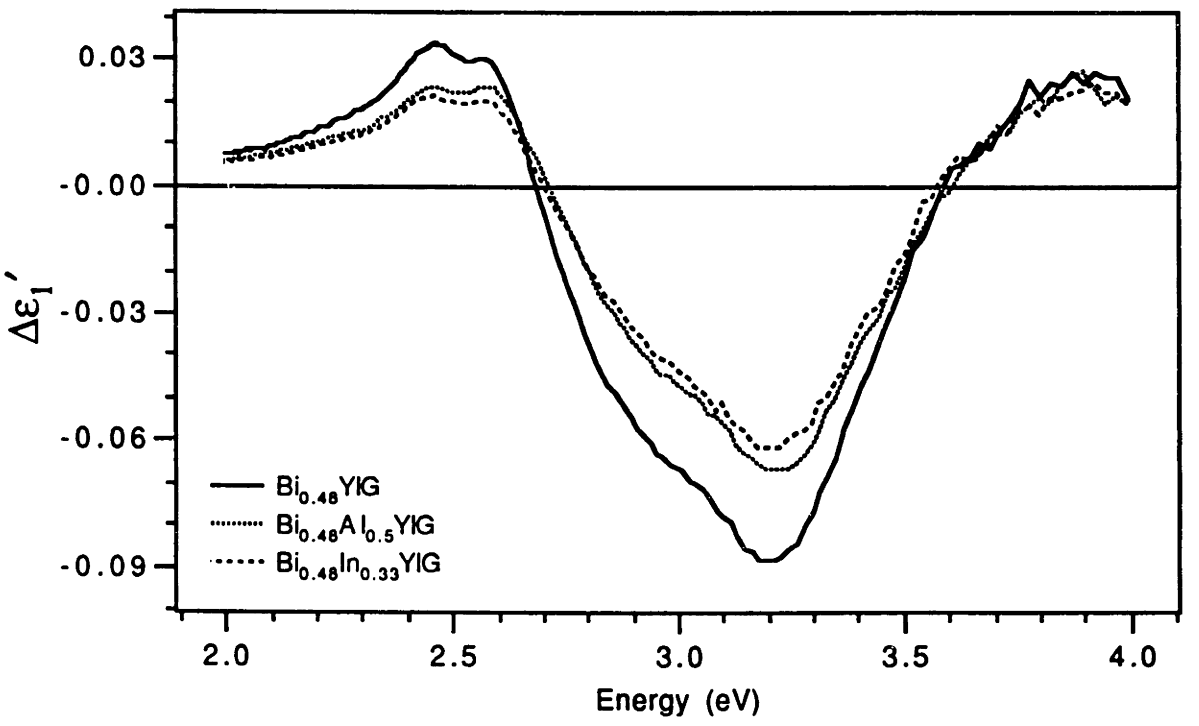

(a)

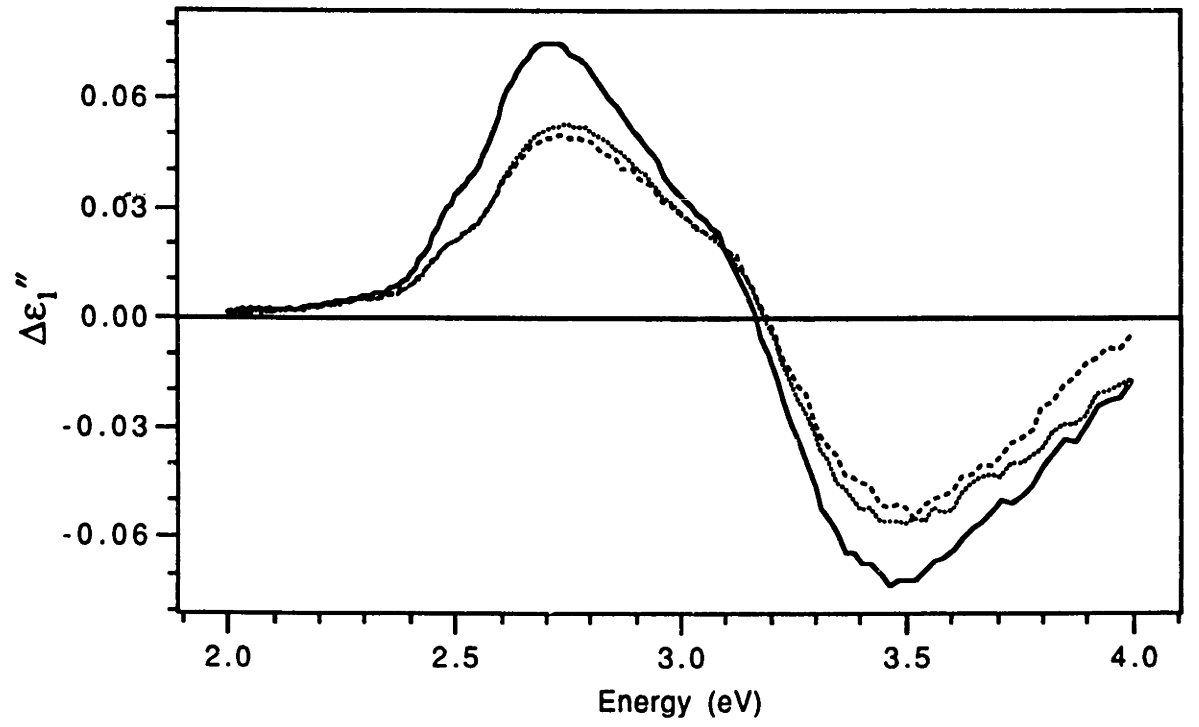

(b)

Figure 7.15. The change in the real (a) and imaginary (b) parts of ε_1 for $Bi_{0.47}Y_{2.53}Fe_5O_{12}$, $Bi_{0.48}Y_{2.52}Al_{0.5}Fe_{4.5}O_{12}$ and $Bi_{0.46}Y_{2.54}In_{0.33}Fe4_{.67}O_{12}$ as a result of bismuth substitution.

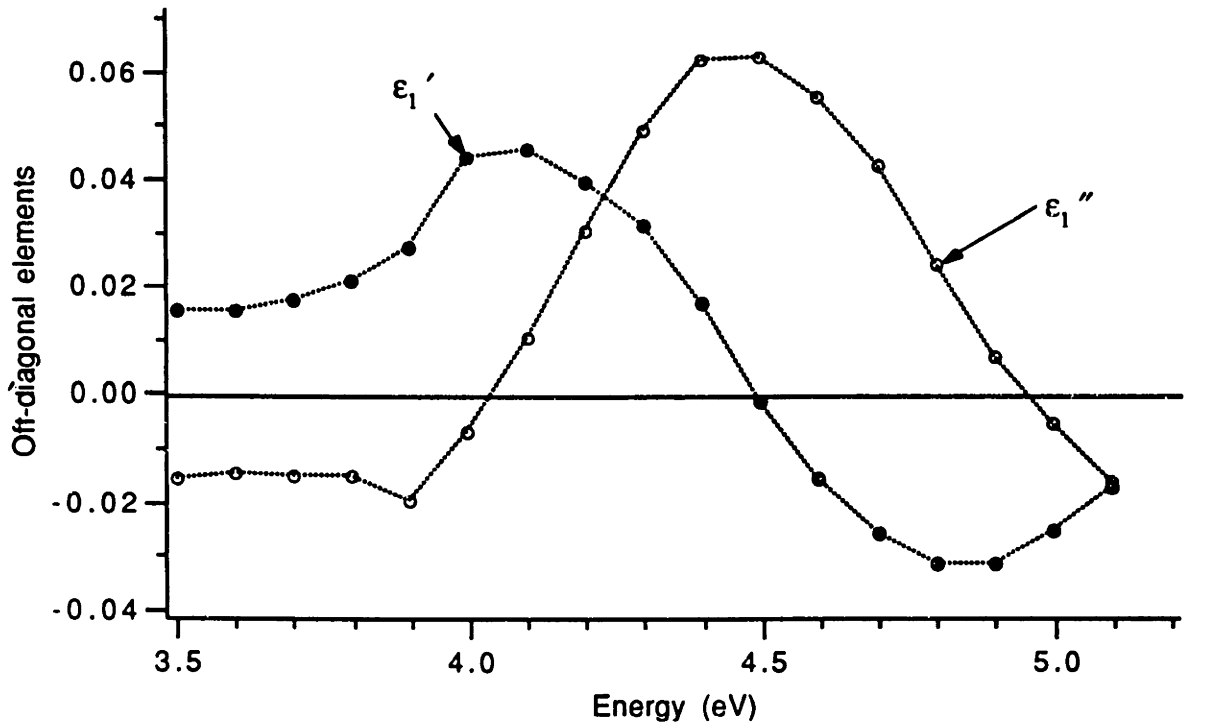

Figure 7.16. The off-diagonal elements of the dielectric tensor for $Y_3Fe_5O_{12}$ as reported by Wittekoek *et al.*[14] Notice the paramagnetic lineshape in the vicinity of 4.45 eV.

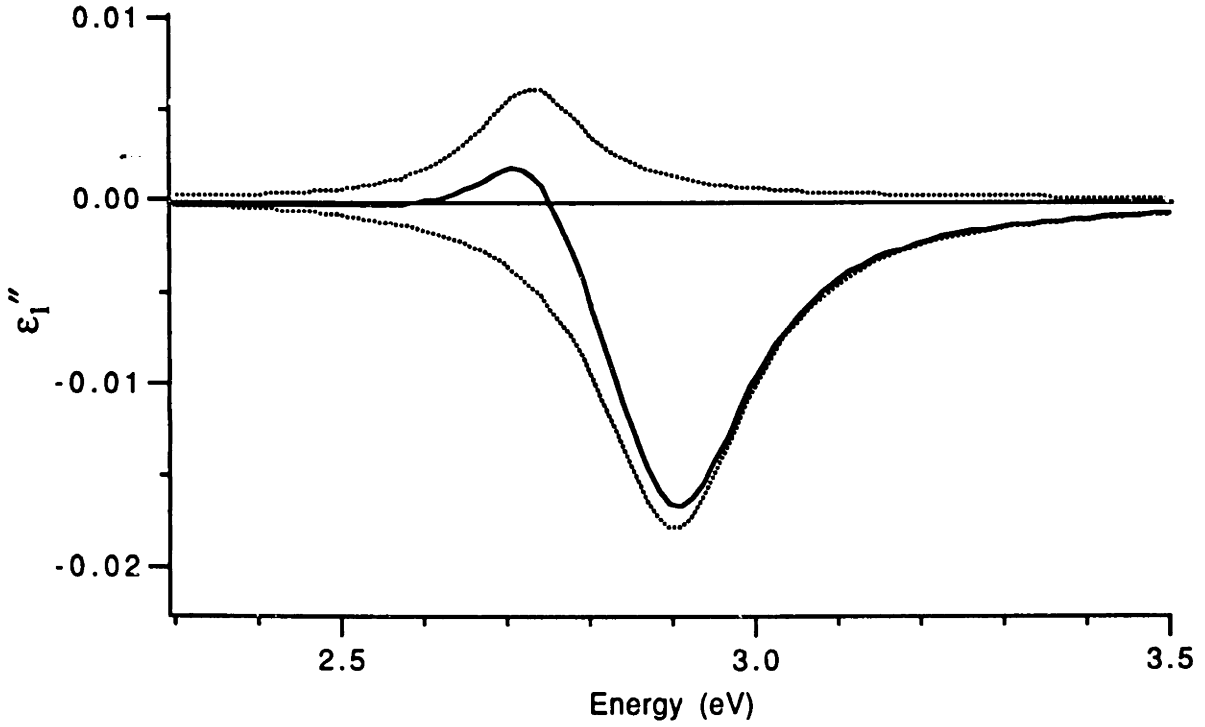

Figure 7.17. The two paramagnetic lineshapes that are components of the feature in the spectra of ε_1'' of $Y_3Fe_5O_{12}$ at 2.85 eV.

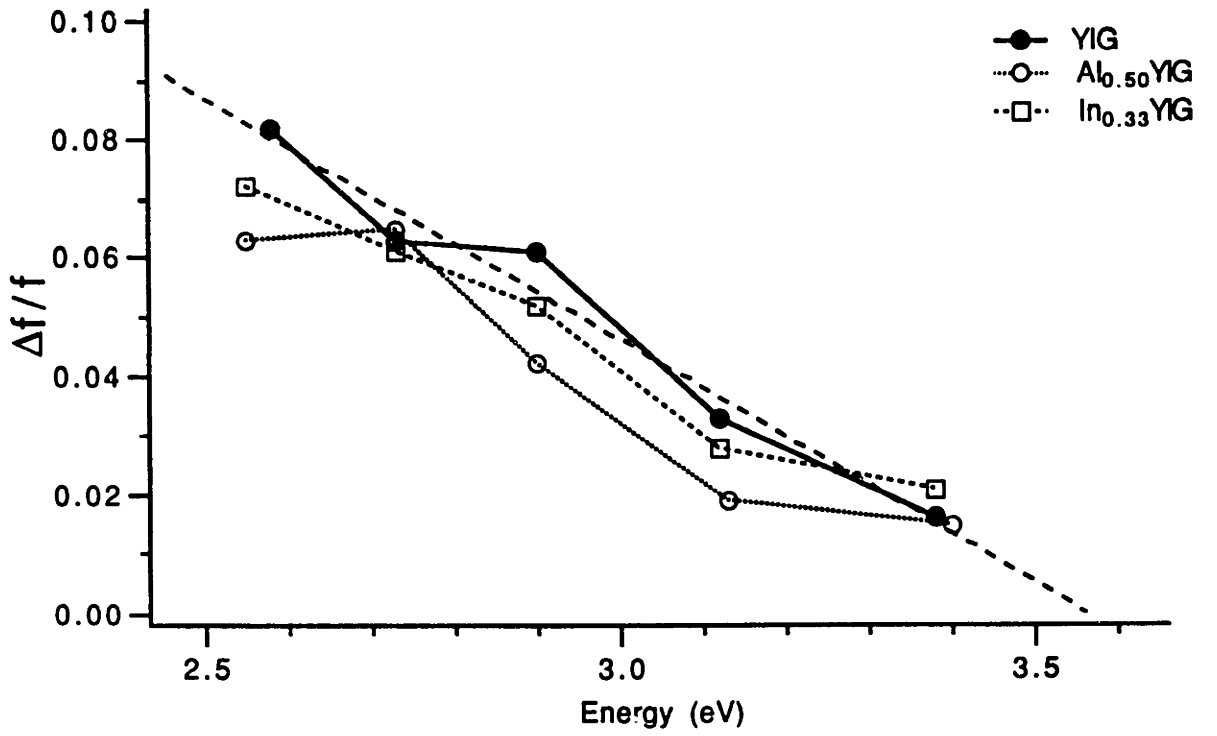

Figure 7.18. The calculated values of Δf/f versus energy for the first five paramagnetic transitions of $Y_3Fe_5O_{12}$, $Y_3Al_{0.5}Fe_{4.5}O_{12}$ and $Y_3In_{0.33}Fe4_{.67}O_{12}$. Dashed line is a least squares fit for $Y_3Fe_5O_{12}$.

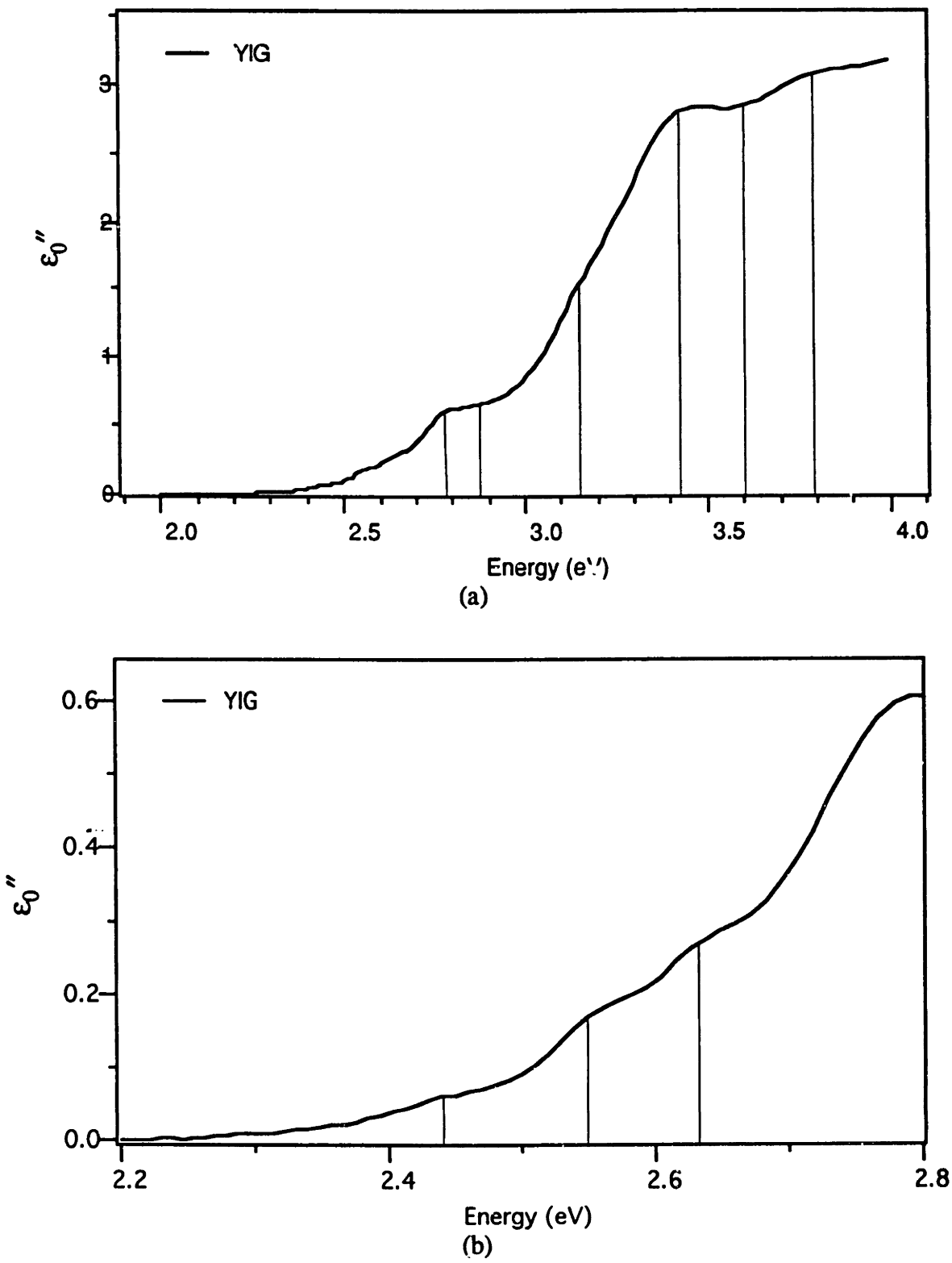

Figure 7.19. Energies used for initial guesses for Gaussian curve fitting of $\varepsilon_0''(\omega)$ for $Y_3Fe_5O_{12}$.

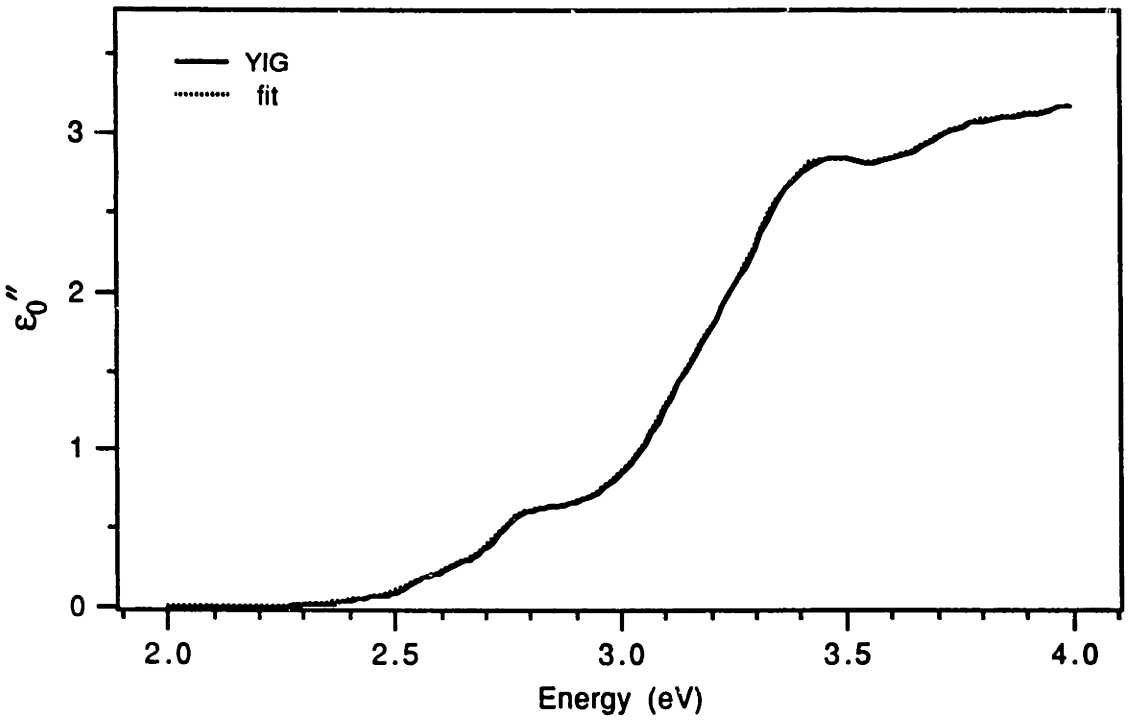

Figure 7.20. Gaussian curve fit to $\varepsilon_0''(\omega)$ for $Y_3Fe_5O_{12}$.

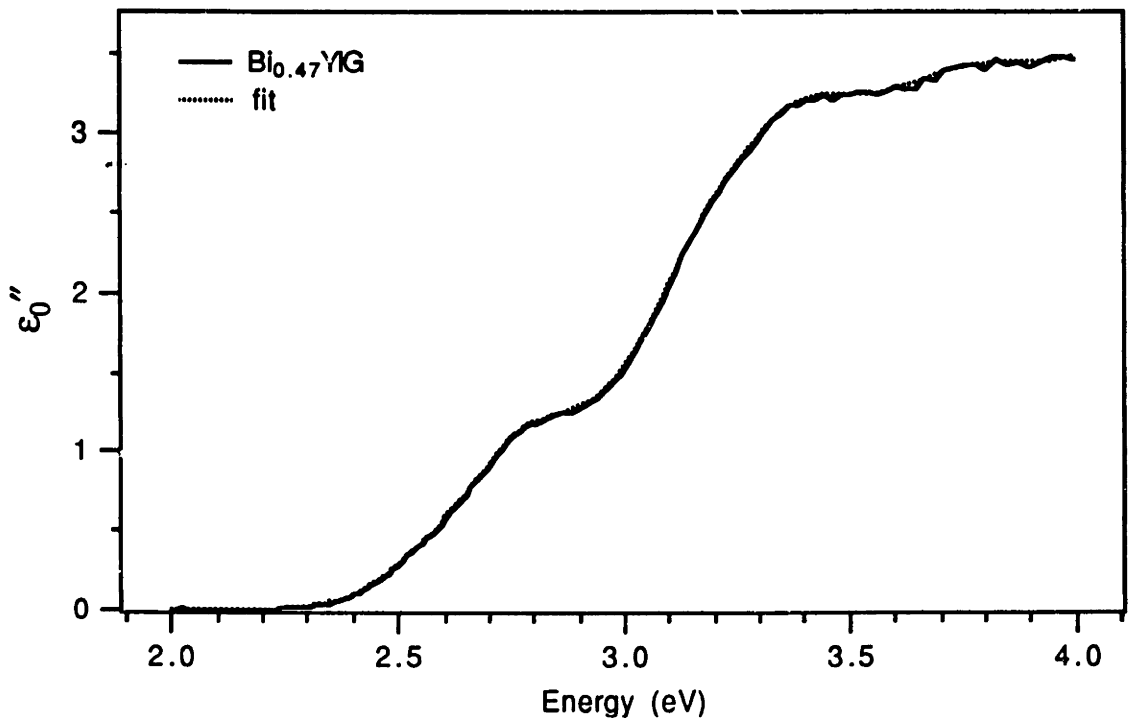

Figure 7.21. Gaussian curve fit to $\varepsilon_0''(\omega)$ for $Bi_{0.47}Y_{2.53}Fe_{4.5}O_{12}$.

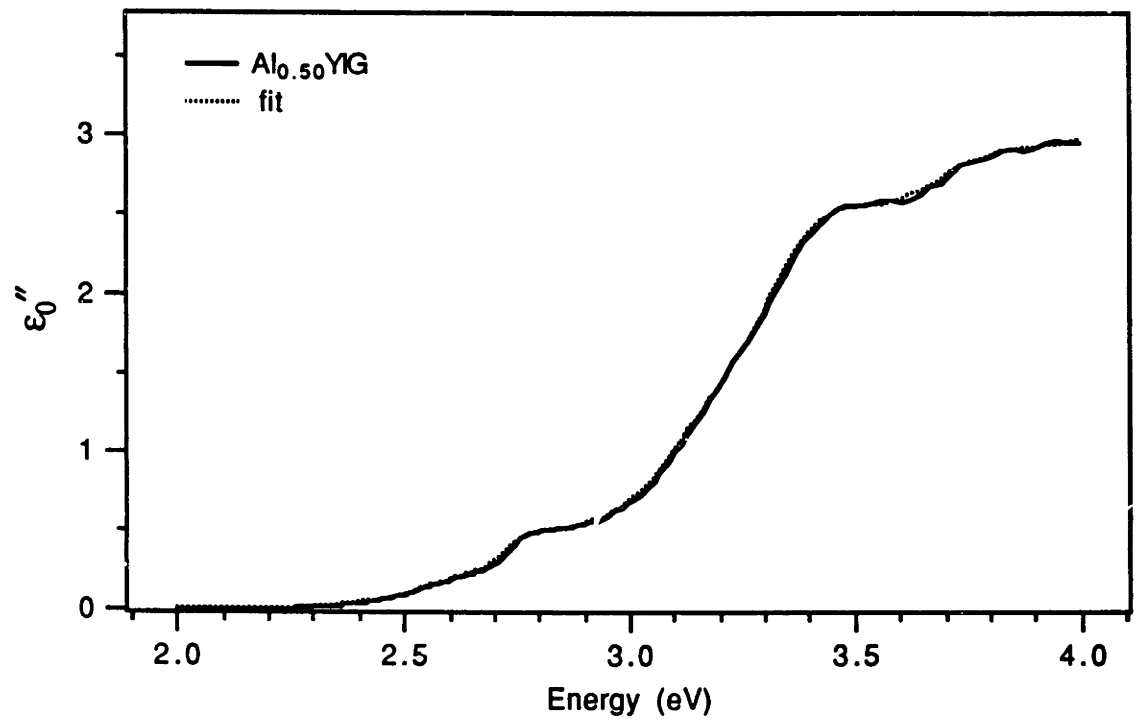

Figure 7.22. Gaussian curve fit to $\varepsilon_0''(\omega)$ for $Y_3Al_{0.5}Fe_{4.5}O_{12}$.

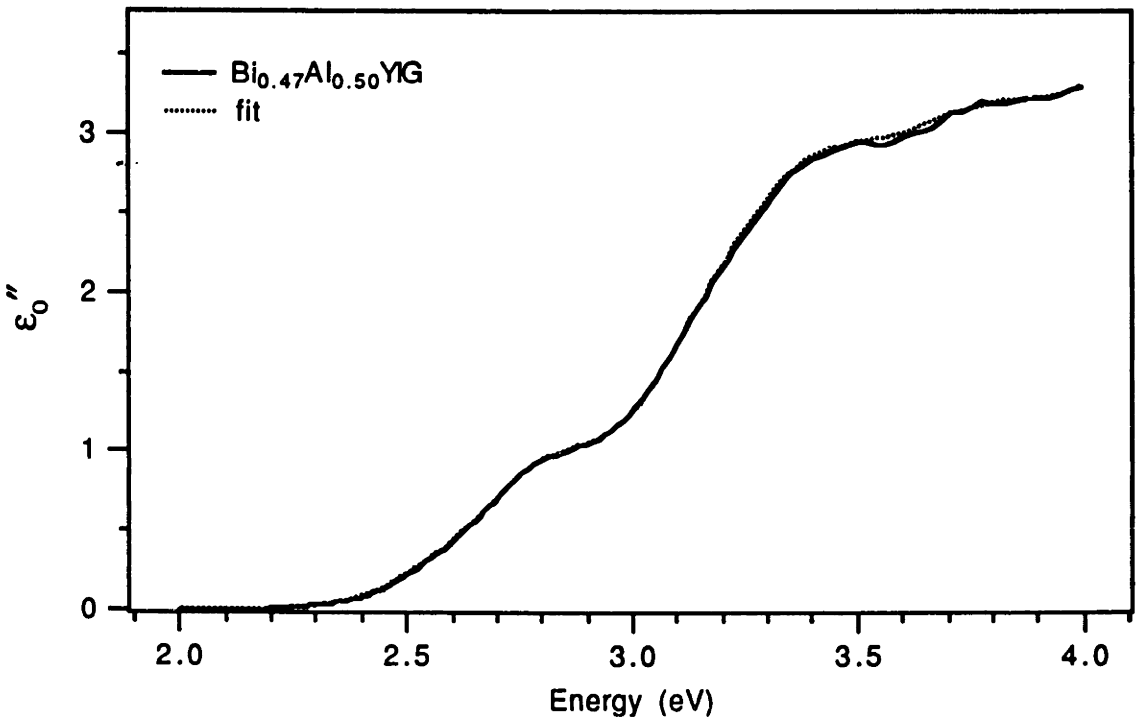

Figure 7.23. Gaussian curve fit to $\varepsilon_0''(\omega)$ for $Bi_{0.48}Y_{2.52}Al_{0.5}Fe_{4.5}O_{12}$.

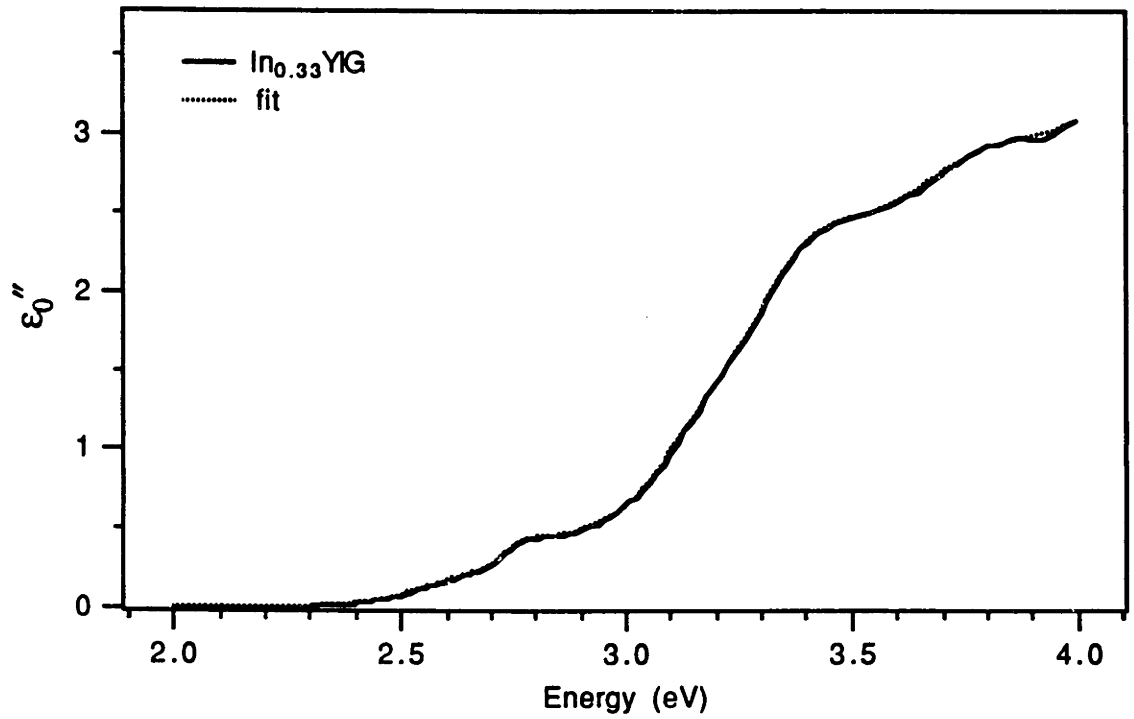

Figure 7.24. Gaussian curve fit to $\varepsilon_0''(\omega)$ for $Y_3In_{0.33}Fe_{4.67}O_{12}$.

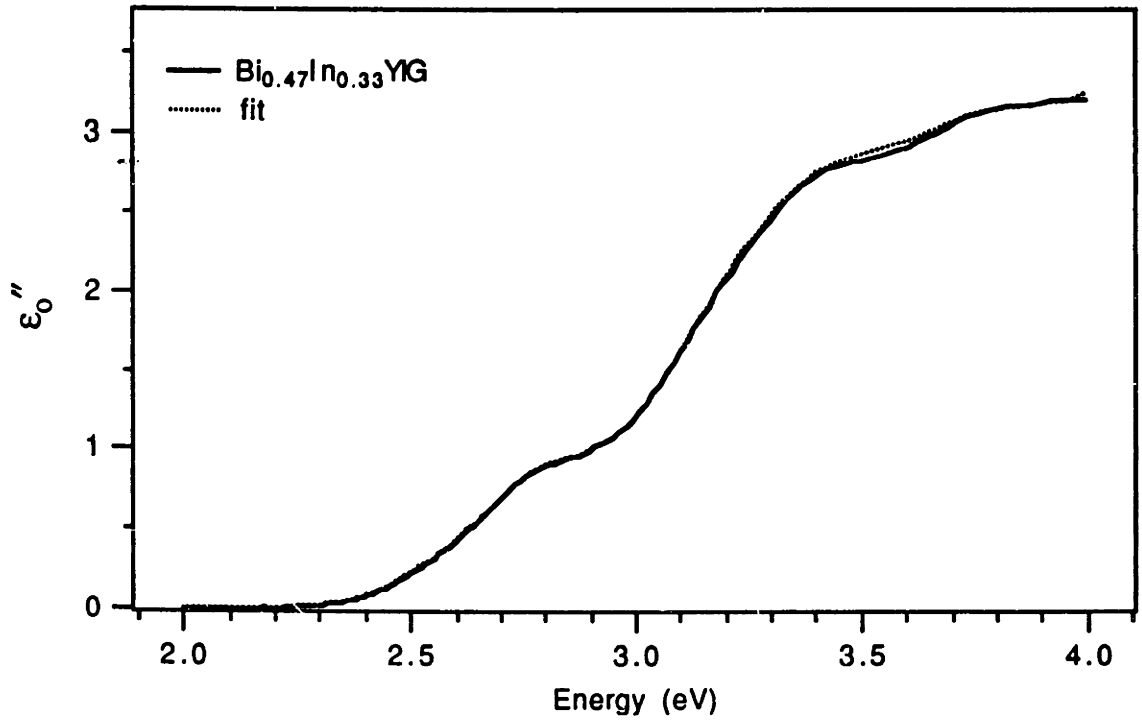

Figure 7.25. Gaussian curve fit to $\varepsilon_0''(\omega)$ for $Bi_{0.46}Y_{2.54}In_{0.33}Fe_{4.67}O_{12}$.

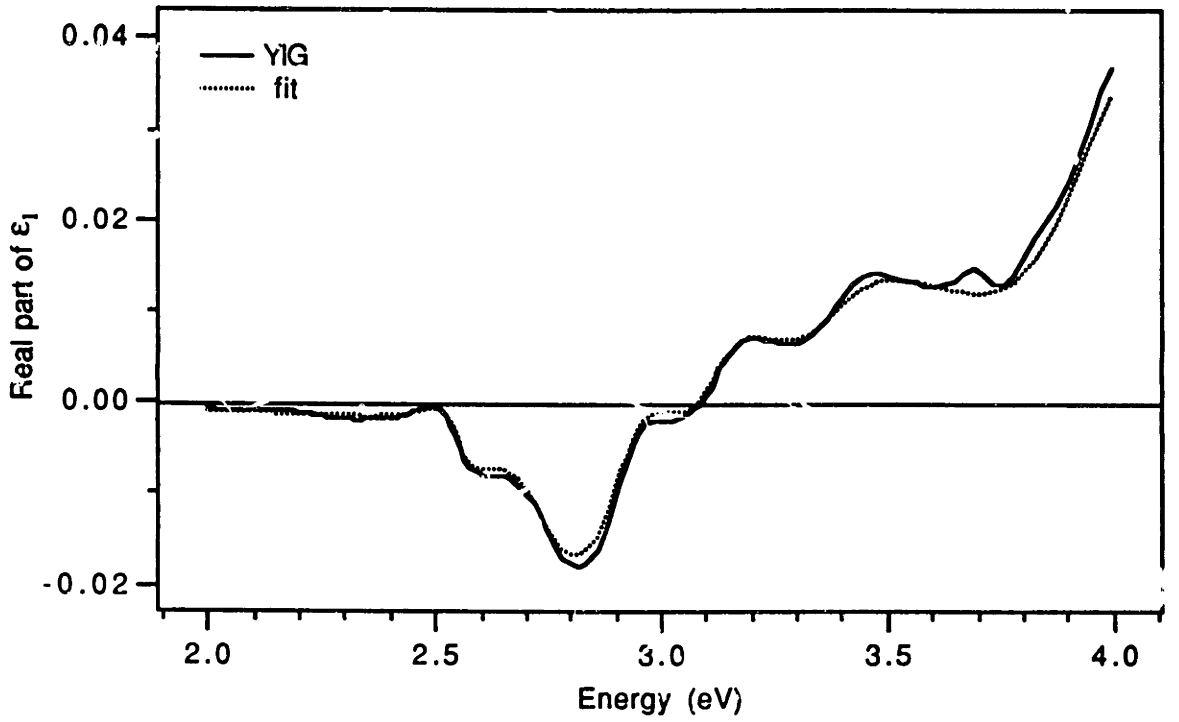

(a)

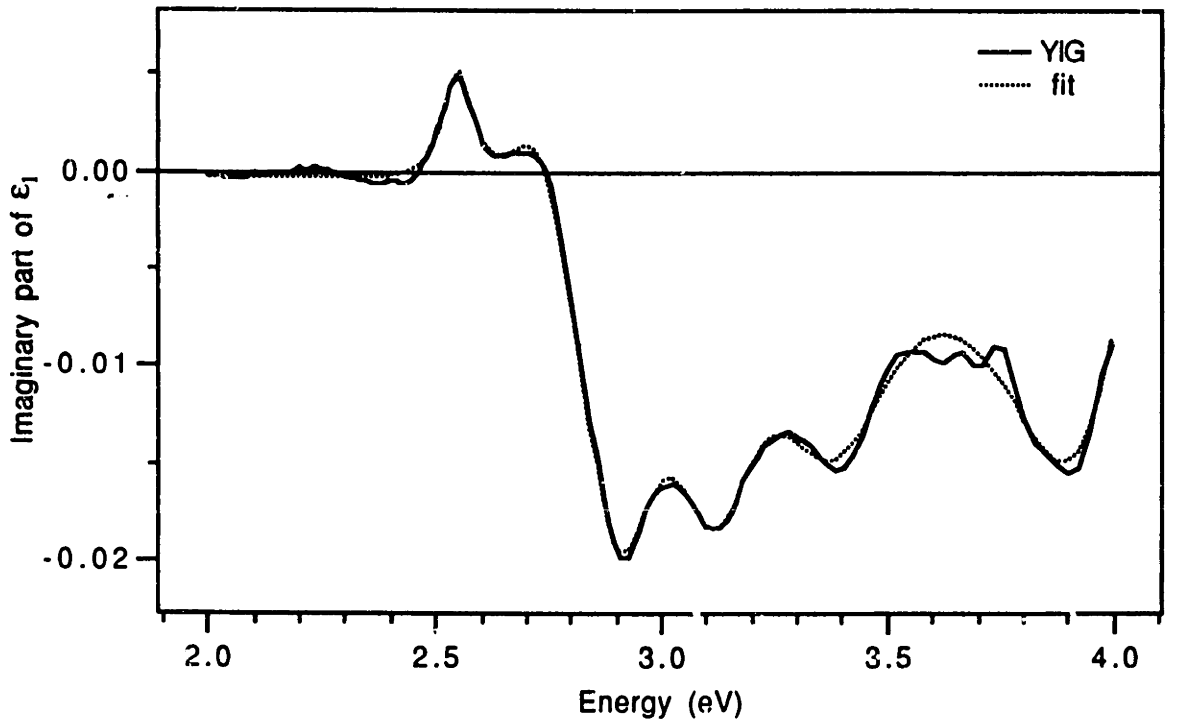

(b)

Figure 7.26. Curve fits to (a) real and (b) imaginary parts of the $\varepsilon_1(\omega)$ for $Y_3Fe_5O_{12}$.

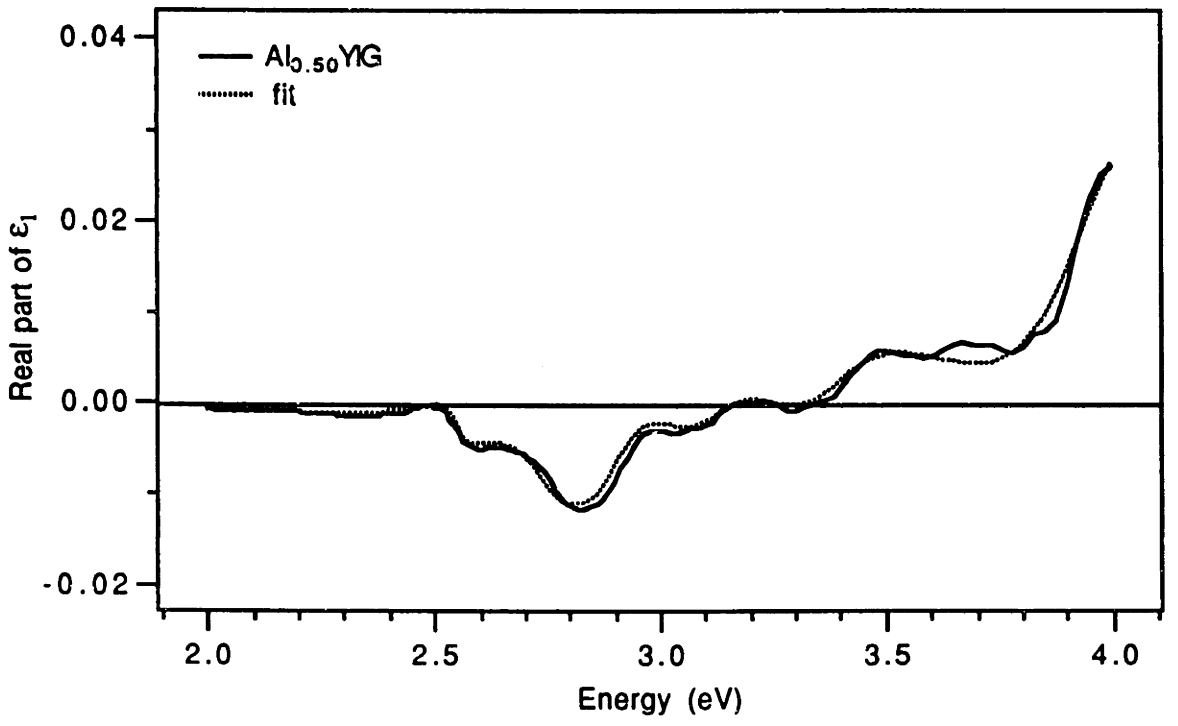

(a)

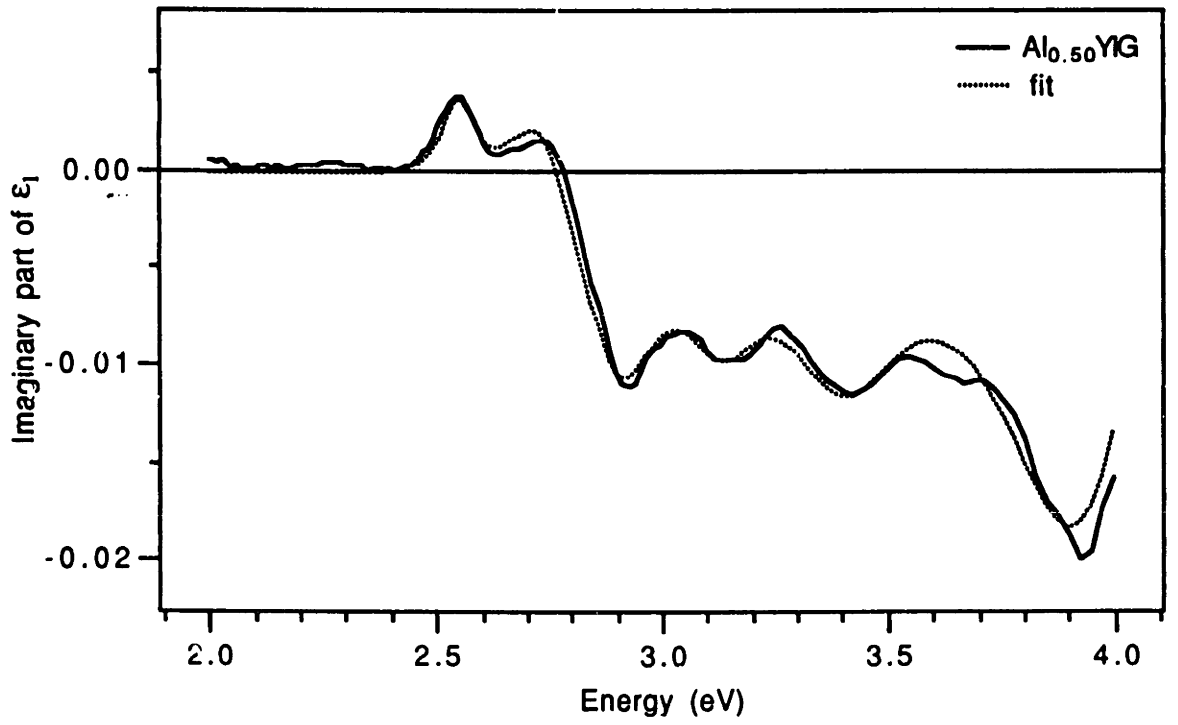

(b)

Figure 7.27. Curve fits to (a) real and (b) imaginary parts of the $\varepsilon_1(\omega)$ for $Y_3Al_{0.5}Fe_{4.5}O_{12}$.

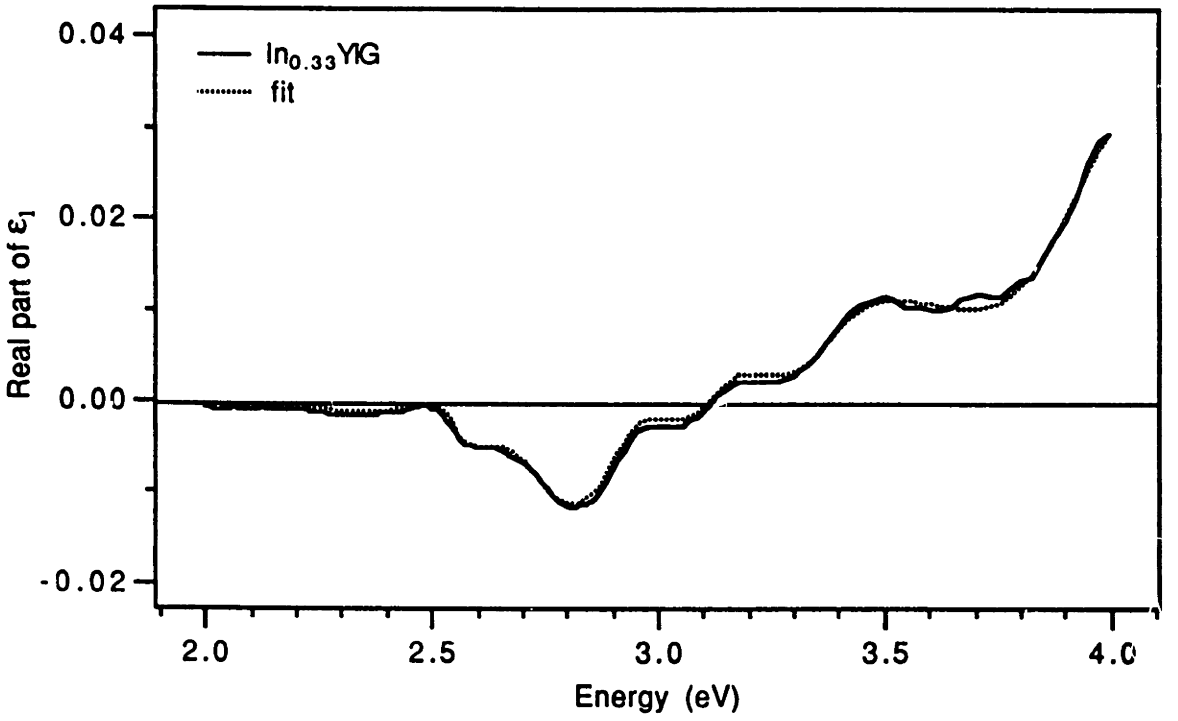

(a)

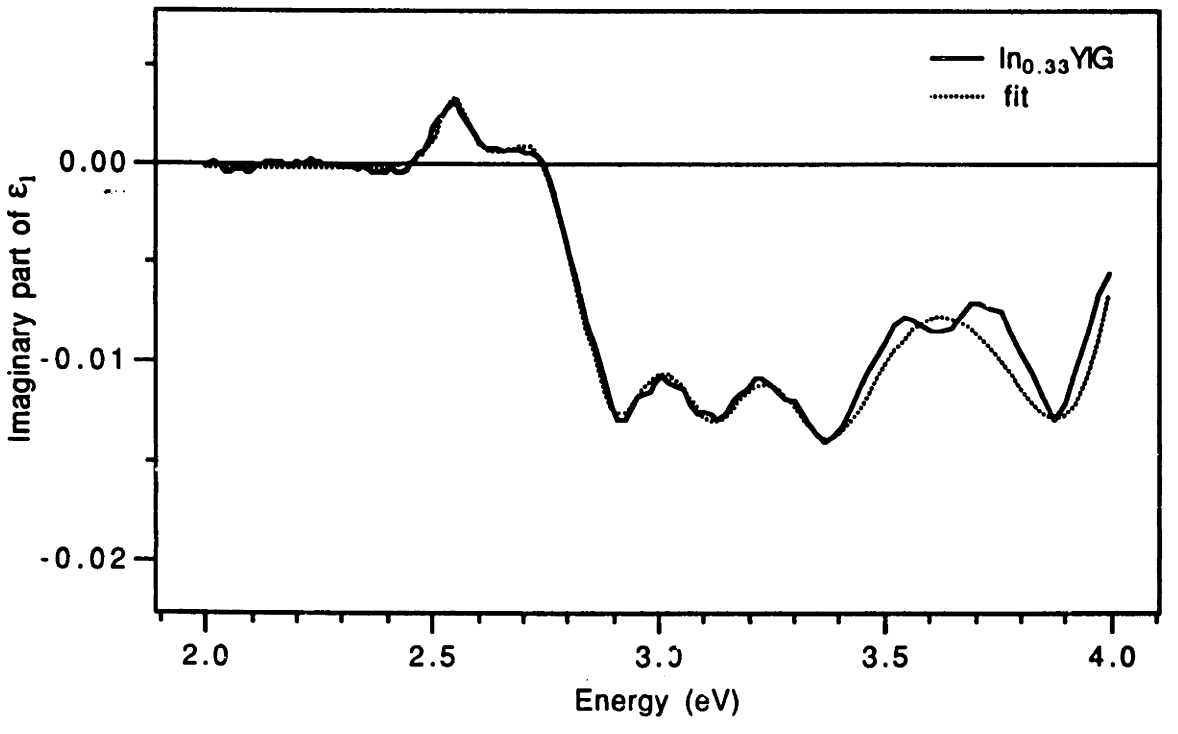

(b)

Figure 7.28. Curve fits to (a) real and (b) imaginary parts of the $\varepsilon_1(\omega)$ for $Y_3In_{0.33}Fe_{4.67}O_{12}$..

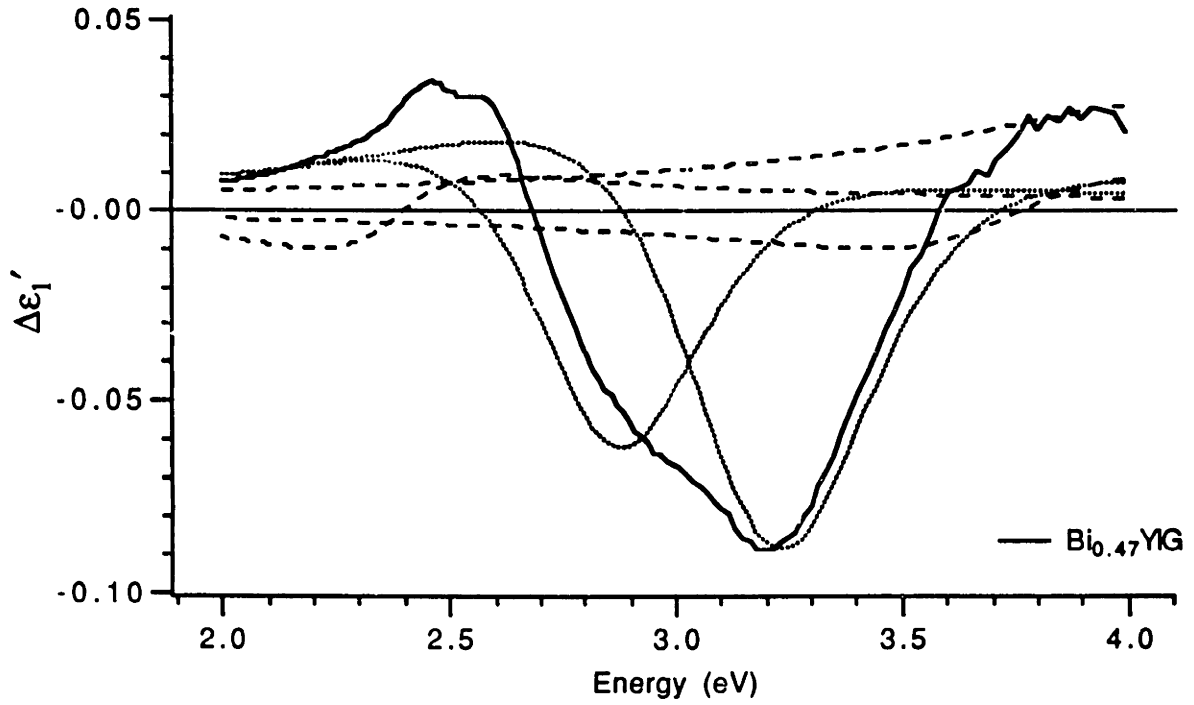

(a)

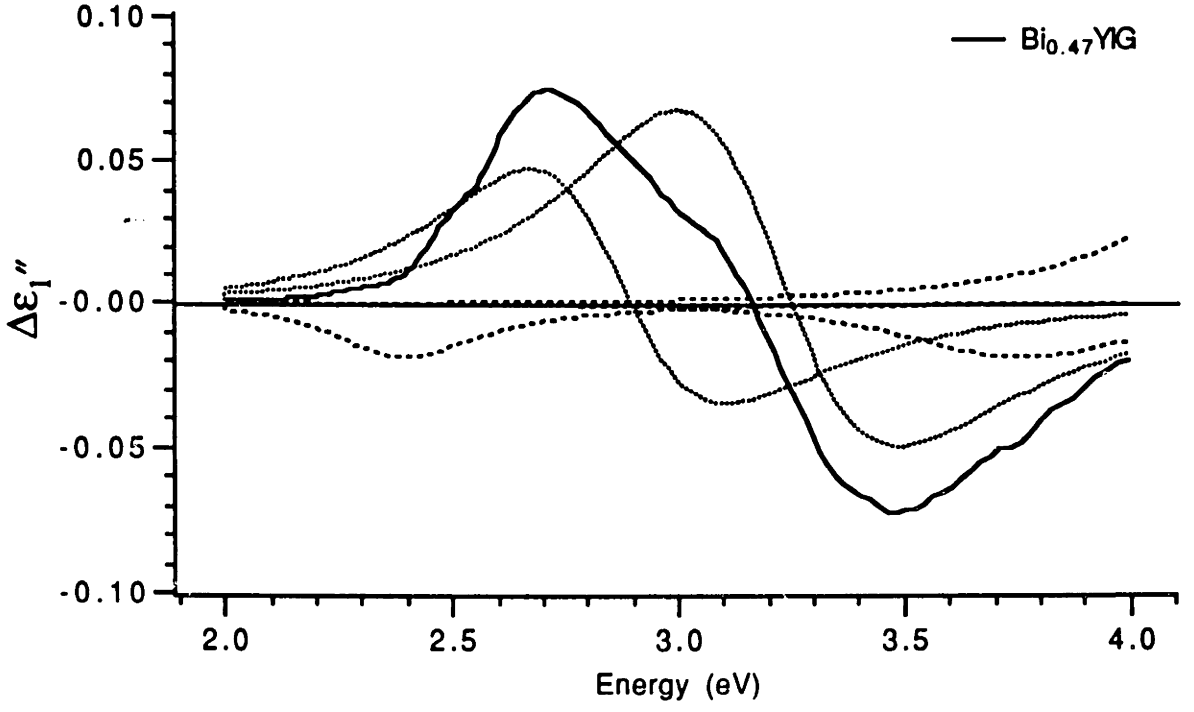

(b)

Figure 7.29. Curve fits to (a) real and (b) imaginary parts of the difference, $\Delta\varepsilon_1(\omega)$, between $\varepsilon_1(\omega)$ for $Bi_{0.47}Y_{2.53}Fe_5O_{12}$ and $Y_3Fe_5O_{12}$. The fine dashed lines are the two diamagnetic components. The coarse dashed lines are the three paramagnetic components.

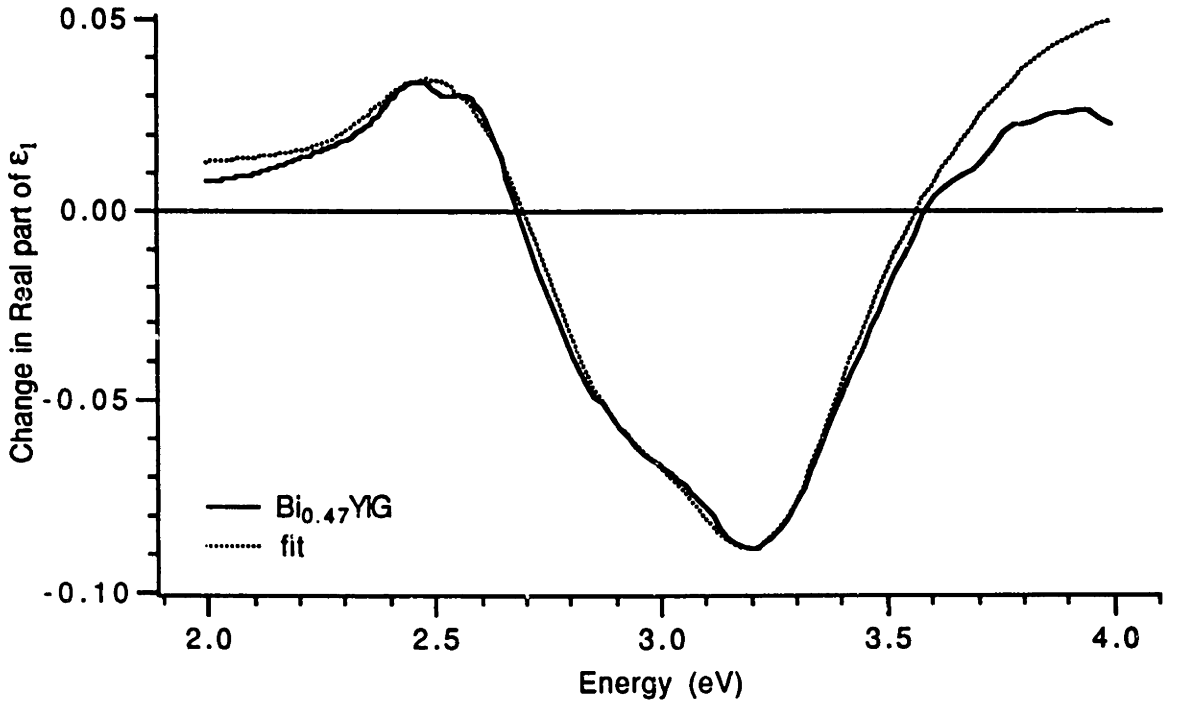

(a)

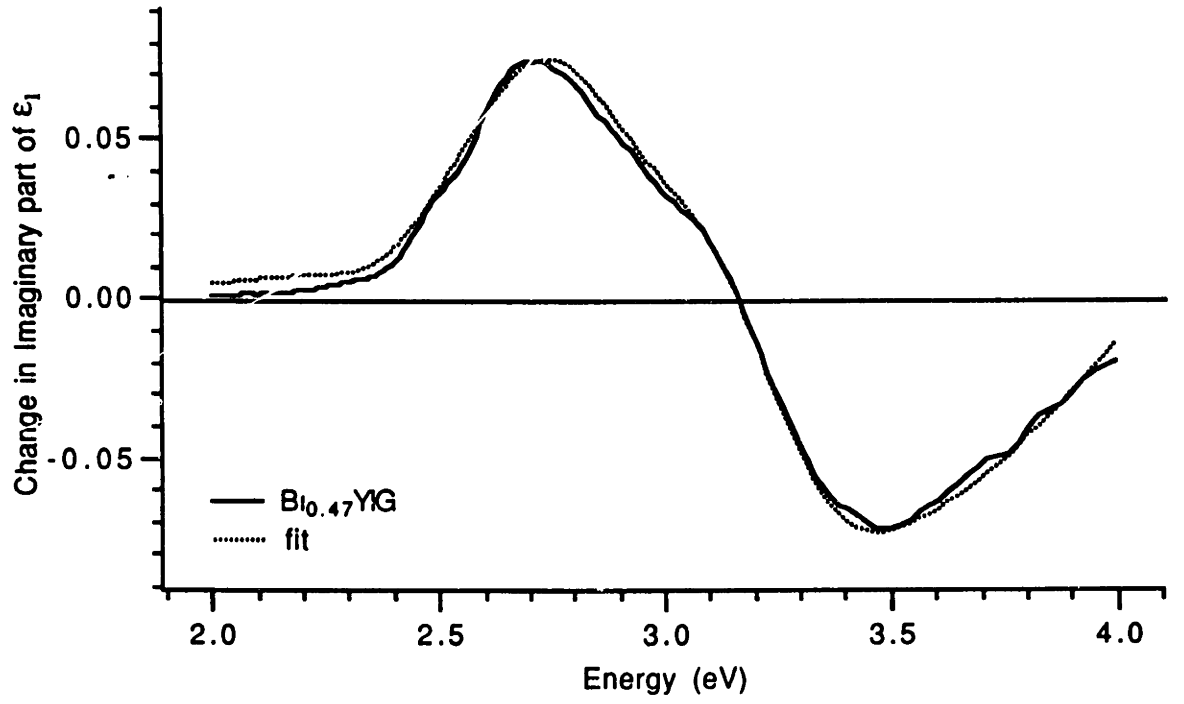

(b)

Figure 7.30. Curve fits to (a) real and (b) imaginary parts of the difference, $\Delta\varepsilon_1(\omega)$, between $\varepsilon_1(\omega)$ for $Bi_{0.47}Y_{2.53}Fe_5O_{12}$ and $Y_3Fe_5O_{12}$.

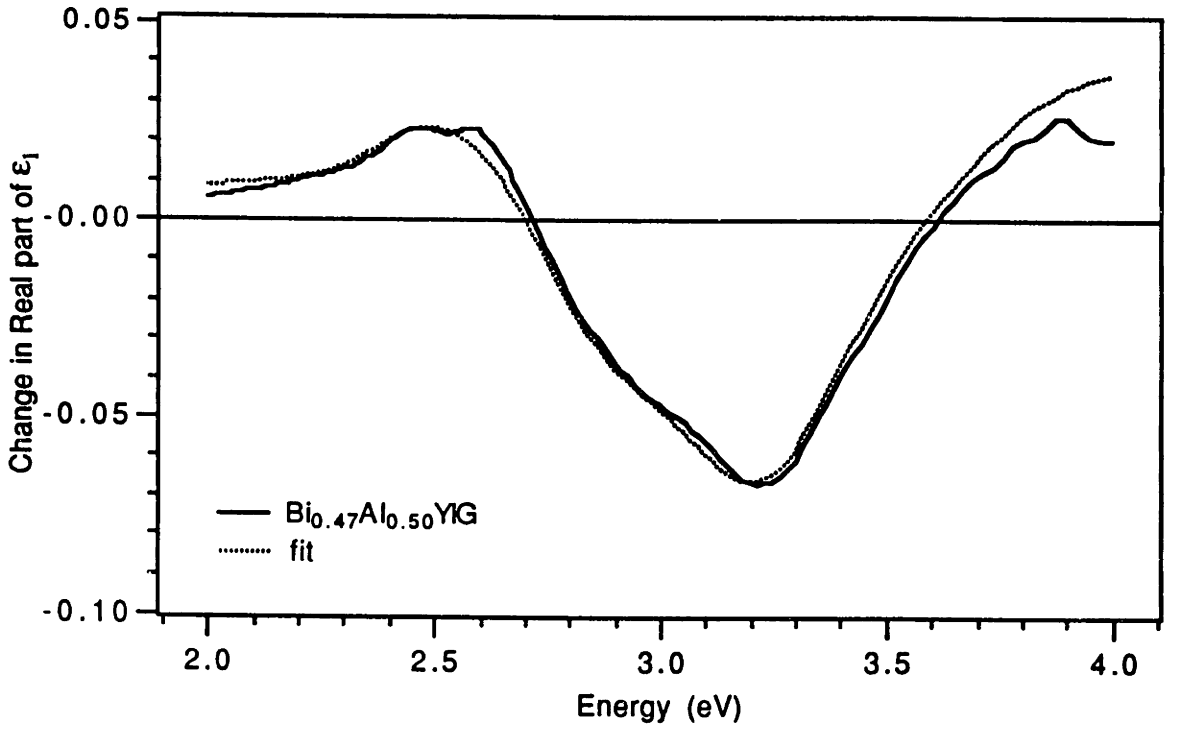

(a)

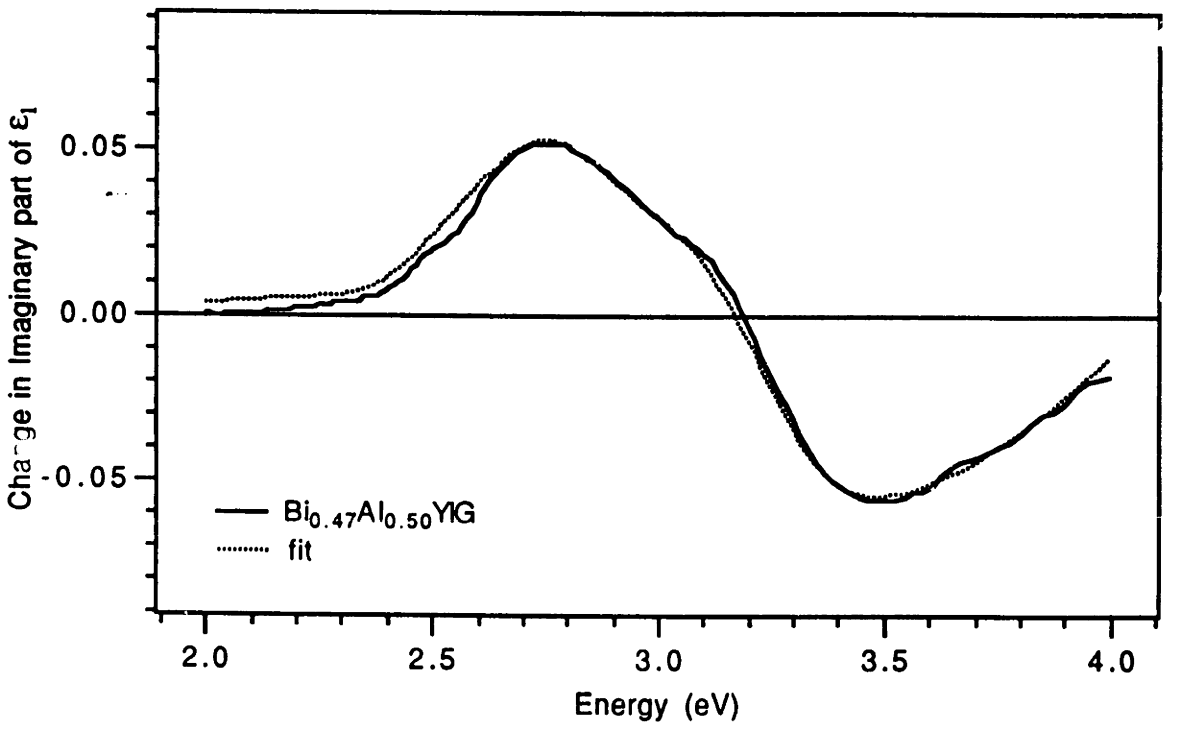

(b)

Figure 7.31. Curve fits to (a) real and (b) imaginary parts of the difference, $\Delta\varepsilon_1(\omega)$, between $\varepsilon_1(\omega)$ for $Bi_{0.48}Y_{2.52}Al_{0.5}Fe_{4.5}O_{12}$ and $Y_3Al_{0.5}Fe_{4.5}O_{12}$.

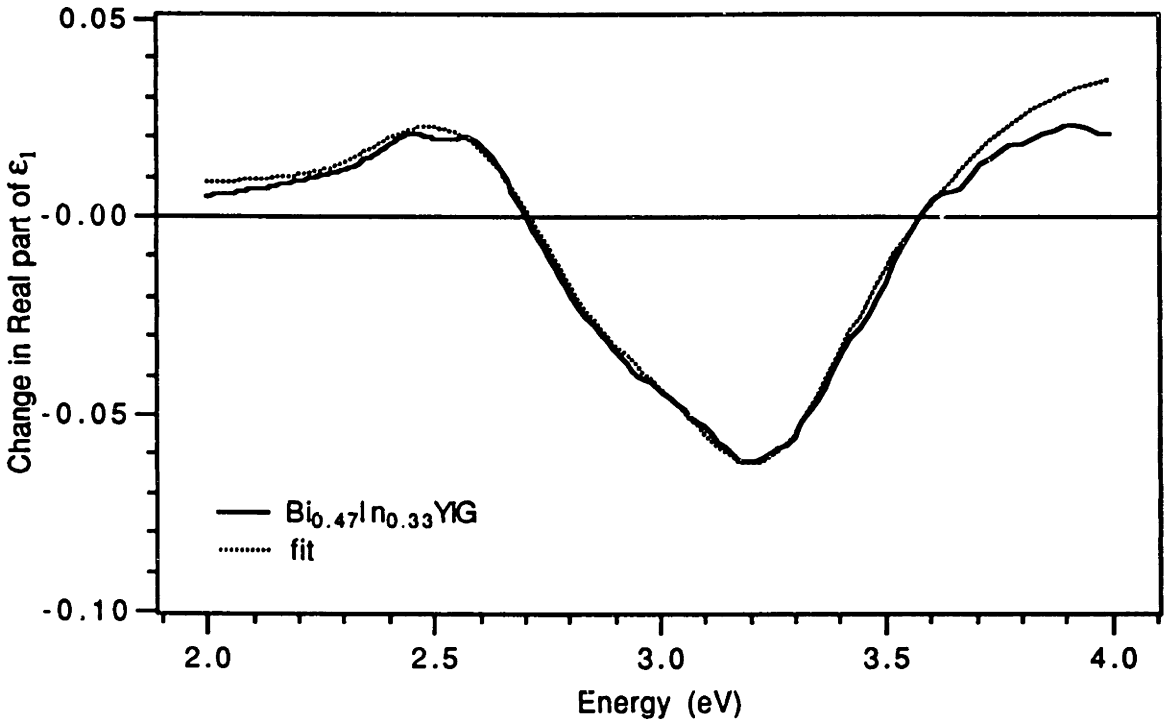

(a)

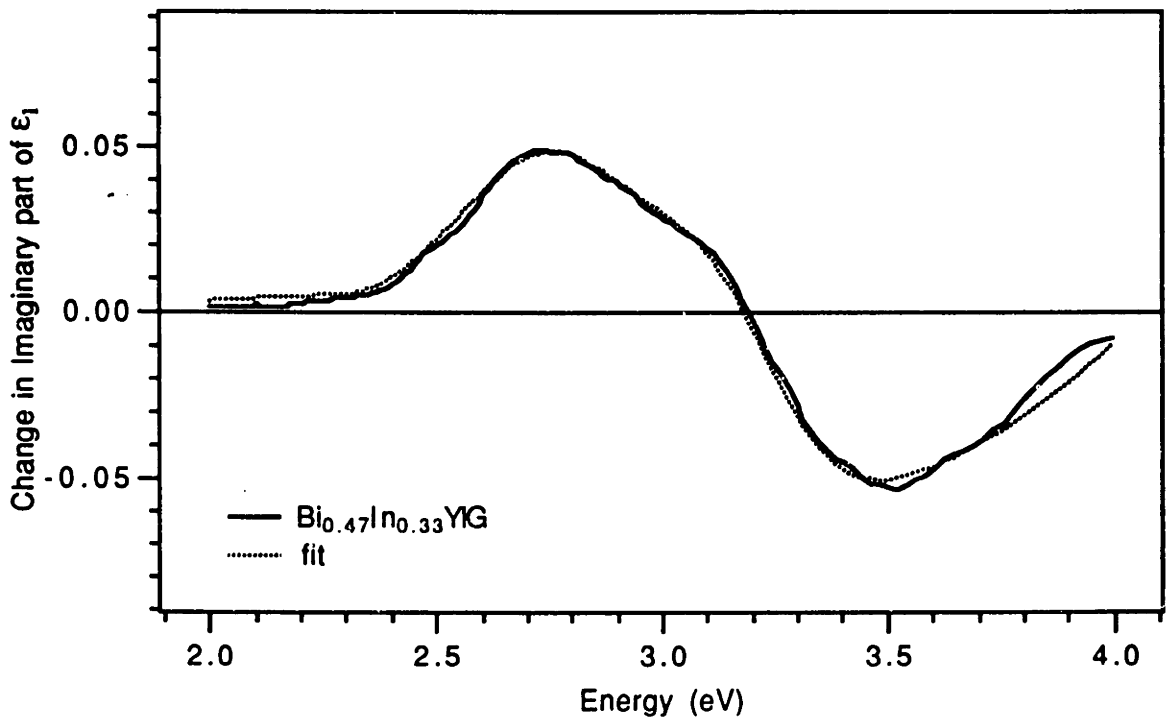

(b)

Figure 7.32. Curve fits to (a) real and (b) imaginary parts of the difference, $\Delta\varepsilon_1(\omega)$, between $\varepsilon_1(\omega)$ for $Bi_{0.46}Y_{2.54}In_{0.33}Fe_{4.67}O_{12}$ and $Y_3In_{0.33}Fe_{4.67}O_{12}$

ω_0 (eV)	ε_0''	Γ (eV)	ω_0 (eV)	ε_1''	Γ (eV)	$\Delta f/f$
2.41	0.030	0.082				
2.58	0.142	0.106	2.55	-0.0116	0.042	-0.082
2.64	0.044	0.039				
2.76	0.194	0.083	2.73	-0.0123	0.084	-0.063
2.91	0.588	0.207	2.90	0.0358	0.110	0.061
3.15	0.735	0.146	3.12	0.0240	0.108	0.033
3.37	1.412	0.188	3.38	0.0228	0.165	0.016
3.70	2.503	0.371				
			3.93	0.0536	0.238	
4.33	3.383	0.431	4.33	-0.0825	0.350	-0.024

Table 7.1. Results of curve fits to $\varepsilon_0''(\omega)$ and $\varepsilon_1(\omega)$ for $Y_3Fe_5O_{12}$.

ω_0 (eV)	ε_0''	Γ (eV)	ω_0 (eV)	ε_1''	Γ (eV)	$\Delta f/f$
2.41	0.033	0.082				
2.58	0.125	0.106	2.55	-0.0079	0.042	-0.063
2.64	0.024	0.039				
2.76	0.149	0.083	2.73	-0.0097	0.084	-0.065
2.91	0.480	0.207	2.90	0.0200	0.110	0.042
3.15	0.596	0.146	3.13	0.0112	0.108	0.019
3.38	1.204	0.188	3.40	0.0180	0.165	0.015
3.71	2.310	0.371				
			3.93	0.0556	0.238	-
4.33	3.041	0.431	4.33	-0.0629	0.350	-0.021

Table 7.2. Results of curve fits to $\varepsilon_0''(\omega)$ and $\varepsilon_1(\omega)$ for $Y_3Al_{0.5}Fe_{4.5}O_{12}$.

ω_0 (eV)	ε_0''	Γ (eV)	ω_0 (eV)	ε_1''	Γ (eV)	$\Delta f/f$
2.41	0.020	0.082				
2.58	0.109	^ 106	2.55	-0.0078	0.042	-0.072
2.64	0.030	0.039				
2.76	0.135	0.083	2.73	-0.0082	0.084	-0.061
2.91	0.429	0.207	2.90	0.0224	0.110	0.052
3.15	0.564	0.146	3.12	0.0160	0.108	0.028
3.37	1.104	0.188	3.38	0.0230	0.165	0.021
3.71	2.316	0.371				
			3.92	0.0450	0.238	-
4.33	3.287	0.431	4.33	-0.0700	0.350	-0.021

Table 7.3. Results of curve fits to $\varepsilon_0''(\omega)$ and $\varepsilon_1(\omega)$ for $Y_3In_{0.33}Fe_{4.67}O_{12}$.

ω_0 (eV)	ε_0''	Γ (eV)	ω_0 (eV)	ε_1	Γ (eV)	type
			2.38	0.0380	0.200	para
2.44	0.062	0.132				
2.57	0.319	0.113				
2.63	0.053	0.048				
2.73	0.629	0.118				
2.87	0.759	0.147	2.85	-0.0630	0.375	dia
3.12	1.397	0.202	3.20	-0.0900	0.420	dia
3.36	1.628	0.219				
3.70	2.791	0.364	3.73	0.0380	0.350	para
4.32	3.628	0.427	4.33	-0.1000	0.350	para

Table 7.4a. Results of curve fits to $\varepsilon_0''(\omega)$ and $\varepsilon_1(\omega)$ for $Bi_{0.47}Y_{2.53}Fe_5O_{12}$.

ω_0 (eV)	$\Delta\varepsilon_0''$	$\Delta\varepsilon_1$	$\Delta f/f^{**}$	Δ/Γ	Δ (eV)
2.38	?	0.0380	?	-	-
2.85	0.171	-0.0630	-	0.368	0.138
3.20	0.662	-0.0900	-	0.136	0.057
3.73	0.288	0.0380	0.132	-	-
4.33	0.245	-0.1000*	0.408	-	-

Table 7.4b. Differential oscillator strength and excited state splittings induced by bismuth substitution for $Bi_{0.47}Y_{2.53}Fe_{4.67}O_{12}$. *fixed. **relates only to portion induced by bismuth substitution.

ω_0 (eV)	ε_0''	Γ (eV)	ω_0 (eV)	ε_1	Γ (eV)	type
			2.38	0.0250	0.200	para
2.44	0.063	0.132				
2.57	0.237	0.113				
2.63	0.046	0.048				
2.73	0.460	0.118				
2.87	0.645	0.147	2.85	-0.0420	0.375	dia
3.12	1.100	0.202	3.20	-0.0660	0.420	dia
3.36	1.403	0.219				
3.70	2.562	0.364	3.73	0.0350	0.350	para
4.32	3.493	0.427	4.33	-0.0700	0.350	para

Table 7.5a. Results of curve fits to $\varepsilon_0''(\omega)$ and $\varepsilon_1(\omega)$ for $Bi_{0.48}Y_{2.52}Al_{0.5}Fe_{4.5}O_{12}$.

ω_0 (eV)	$\Delta\varepsilon_0''$	$\Delta\varepsilon_1$	$\Delta f/f$	Δ/Γ	Δ (eV)
2.38	?		?	-	-
2.85	0.165	-0.0420	-	0.255	0.095
3.20	0.504	-0.0660	-	0.131	0.055
3.73	0.252	0.0350	0.138	-	-
4.33	0.452	-0.0700*	0.155	-	-

Table 7.5b. Differential oscillator strength and excited state splittings induced by bismuth substitution for $Bi_{0.48}Y_{2.52}Al_{0.5}Fe_{4.5}O_{12}$. *fixed. **relates only to portion induced by bismuth substitution.

ω_0 (eV)	ε_0''	Γ (eV)	ω_0 (eV)	ε_1	Γ (eV)	type
			2.38	0.0236	0.200	para
2.44	0.057	0.132				
2.57	0.240	0.113				
2.63	0.046	0.048				
2.73	0.459	0.118				
2.87	0.591	0.147	2.85	-0.0365	0.375	dia
3.12	1.078	0.202	3.20	-0.0640	0.420	dia
3.36	1.310	0.219				
3.70	2.531	0.364	3.73	0.0290	0.350	para
4.32	3.434	0.427	4.33	-0.0700	0.350	para

Table 7.6a. Results of curve fits to $\varepsilon_0''(\omega)$ and $\varepsilon_1(\omega)$ for $Bi_{0.46}Y_{2.54}In_{0.33}Fe_{4.67}O_{12}$.

ω_0 (eV)	$\Delta\varepsilon_0''$	$\Delta\varepsilon_1$	$\Delta f/f$	Δ/Γ	Δ (eV)
2.38	?		?	-	-
2.85	0.162	-0.0365	-	0.225	0.084
3.20	0.514	-0.0640	-	0.125	0.052
3.73	0.215	0.0290	0.135	-	-
4.33	0.147	-0.0700*	0.476	-	-

Table 7.6b. Differential oscillator strength and excited state splittings induced by bismuth substitution for $Bi_{0.46}Y_{2.54}In_{0.33}Fe_{4.67}O_{12}$. *fixed. **relates only to portion induced by bismuth substitution.

8. Discussion

In this chapter we interpret and discuss the results presented in Chapter 7. We examine the ε_0'' spectra of YIG and the increase in $\varepsilon_0''(\omega)$upon bismuth substitution. The increase in $\varepsilon_0''(\omega)$ is interpreted as arising from two transitions present in the iron garnets at 2.85 eV and 3.20 eV, that are increased in strength by bismuth substitution. We postulate that the increased magneto-optic activity that arises from bismuth substitution of iron garnets can be explained by a mixing of excited states of Bi^{3+} and Fe^{3+} ions. A discussion is given on the plausibility of this mechanism. We conclude the chapter by briefly discussing the origins of the paramagnetic transitions that comprise the magneto-optic spectra of YIG.

8.1 The ε_0" spectrum of YIG

From inspection of the curve fit to the ε_0'' spectrum of YIG in Figure 7.20, the onset of strong absorption lines at 2.9 eV can be seen. These absorption lines were identified by a number of authors[59,60,35] including Scott *et al.*[20].who further found that the oscillator strengths of the transitions were dependent on the concentration of Fe^{3+} in the series of materials $Y_3Fe_{5-x}Ga_xO_{12}$. These transitions are generally accepted as originating from charge transfer between Fe^{3+} ions residing in different crystallographic sites. The rationale for this assignment is as follows.

First, the finding by Scott *et al.*[20] that the oscillator strengths of these transitions depend on the iron content of the material leads to the conclusion that the centers responsible for these transitions involve more than one iron ion. Secondly, the energies of these transitions coincide with the energies of the charge transfer processes. This fact comes from the photoconductivity measurements of Grant and Ruppel[61] and thermopower measurements of Metselaar and Larsen[62]. The photoconductivity measurements of gadolinium iron garnet showed photoconduction commencing at roughly 2.75 eV. Thermopower measurements of YIG revealed a band gap energy of either 2.85 eV, assuming band conduction, or 3.15 eV, if variable range hopping is

---

59 W. Wettling, B. Andlauer, P. Koidl, J. Schneider and W. Tolksdorf, Physica Status Solidi B **59**, 63 (1973).

60 S. Wittekoek, T. J. A. Popma and J. M. Robertson, Proc. 18th Conf. Mag. and Mag. Mat., 944 (1973).

61 P. M. Grant and W. Ruppel, Solid State Communications **5**, 543 (1967).

62 R. Metselaar and P. K. Larsen, Solid State Communications **15**, 291 (1974).

assumed. These two energies and the photoconductivity threshold at 2.75 eV, all lie in the region in which the strong absorption of interest commences. Lastly, Scott and Page[38] have shown that the first absorption peak of YIG whose oscillator strength is *not* dependent upon the population of Fe^{3+} occurs at 4.35 eV. They ascribed this transition to charge transfer from oxygen 2p states to excited states of iron due to the concentration independence of this transition and closeness in energy to the same transition in iron-doped yttrium gallium garnet. The interpretation of the absorption peaks of interest as intersublattice charge transfer transitions simultaneously explains the dependence of the oscillator strength on iron concentration and the onset of electronic conduction at 2.85 eV. We accept this interpretation and will refer to the above type of transition as *intersublattice transitions* . They are described as

$$\begin{aligned} [Fe^{3+}] + (Fe^{3+}) + h\nu &\longrightarrow [Fe^{2+}] + (Fe^{4+}) \\ [Fe^{3+}] + (Fe^{3+}) + h\nu &\longrightarrow [Fe^{4+}] + (Fe^{2+}) \end{aligned} \qquad (8\text{-}1)$$

Our data for $\varepsilon_0''(\omega)$ supports this interpretation. In Figures 8.1 and 8.2 are shown the reduction of the heights of the Gaussian peaks obtained from curve fits when iron is substituted by aluminum and indium in YIG. The data are representative of the actual ratio of the $\varepsilon_0''(\omega)$ spectra. Notice that the reduction of the intensity of $\varepsilon_0''(\omega)$ is roughly equal for $Al_{0.5}$ and $In_{0.33}$ substitution, which represent dilution by one-sixth of the tetrahedral and octahedral sublattices, respectively. This is in agreement with intersublattice transitions in the following way.

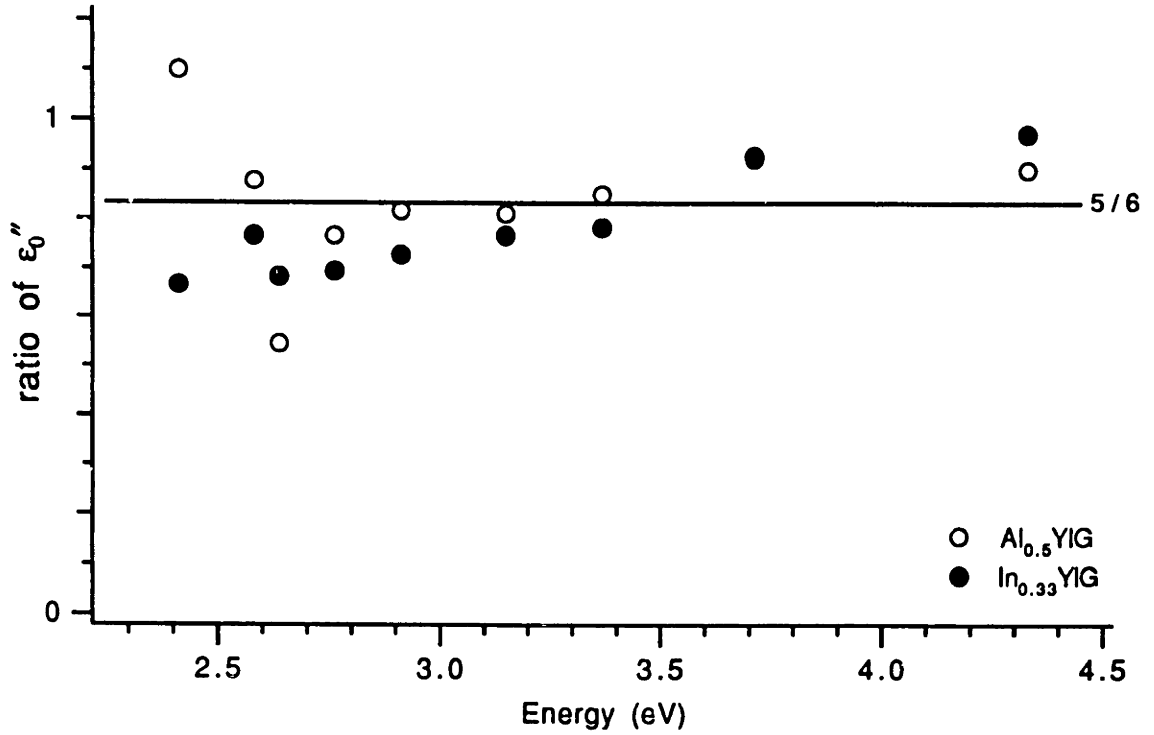

Figure 8.1. The ratios of the absorption peak heights of $Y_3Al_{0.5}Fe_{4.5}O_{12}$ and $Y_3In_{0.33}Fe_{4.67}O_{12}$ to those of YIG. Peak heights were obtained from Gaussian curve fitting.

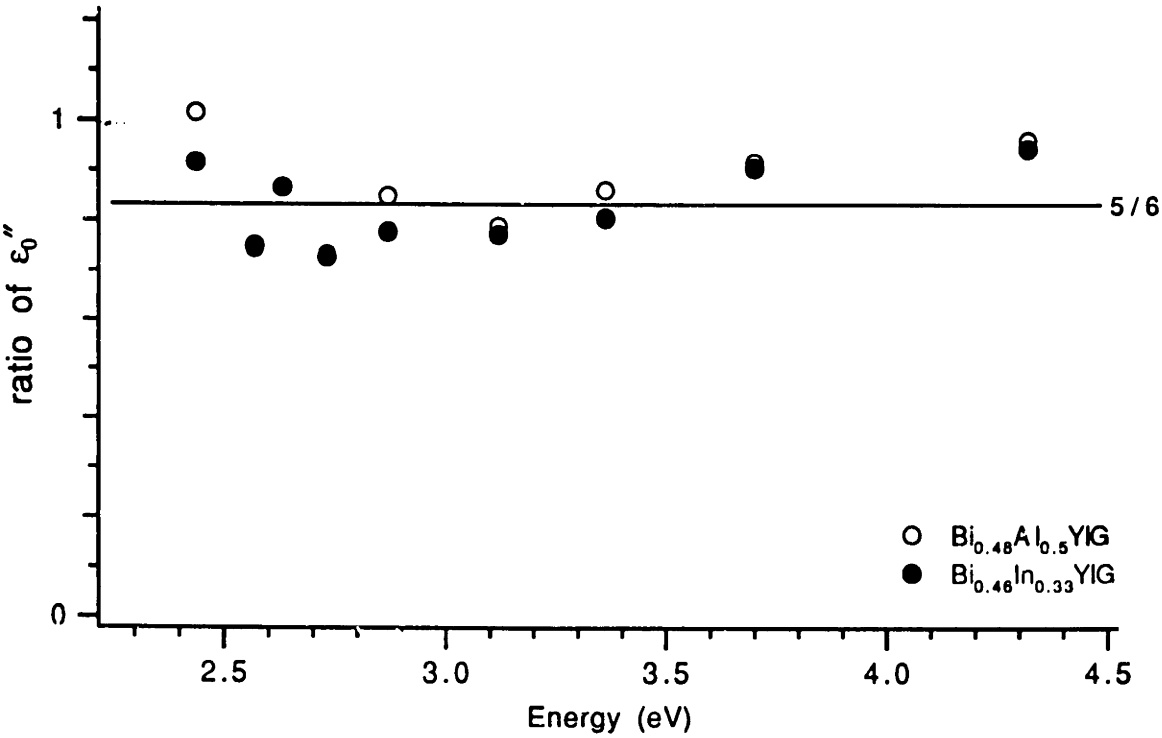

Figure 8.2. The ratios of the absorption peak heights of $Bi_{0.48}Y_{2.52}Al_{0.5}Fe_{4.5}O_{12}$ and $Bi_{0.46}Y_{2.54}In_{0.33}Fe_{4.67}O_{12}$ to those of $Bi_{0.47}Y_{2.53}Fe_5O_{12}$ Peak heights were obtained from Gaussian curve fitting.

The intersublattice transitions involve pairs of Fe^{3+} ions with each member of the pair belonging to a different sublattice. The two iron ions are linked by covalent bonds to the same oxygen ion that their sites share. Iron in an octahedral site has six nearest neighbor tetrahedral sites to which it is linked through the oxygen ions of the octahedra. This amounts to twelve *pairs* per formula unit. Equivalently, a tetrahedrally coordinated iron ion has four nearest neighbor octahedral sites, yielding the same twelve pairs per formula unit. Thus, removal of two octahedral ions destroys as many intersublattice pairs as the removal of three tetrahedral ions, and both will decrease the strength of the intersublattice transition by the same amount. We conclude that the substitution of $Al_{0.5}$ and $In_{0.33}$ represent an equivalent number of destroyed pairs; namely, the fraction of intersublattice pairs has been reduced to five-sixths. In Figures 8.1 and 8.2, we can see that the reductions of the heights of the transitions between 2.85 eV and 4.35 eV are not unreasonably far from the ratio five-sixths. It should be noted that, if we had assumed the strengths of the absorption peaks to be proportional to the iron concentration, the reductions of the peaks would have only been 90% and 93.4% for $Al_{0.5}$ and $In_{0.33}$ substitution, respectively.

Also seen in Figures 8.1 and 8.2 is an apparent linear trend in the ratios of the absorption peaks, increasing towards higher energy. We offer no explanation for this.

8.2 The ε_0'' Spectrum of Bismuth Iron Garnets

We have found that $\varepsilon_0''(\omega)$ of YIG has an overall increase in magnitude upon bismuth substitution (see Figures 7.1 - 7.3). This increase can be seen in Figure 8.3. The spectra shown are the differences in the dielectric constants between a material with and without bismuth substitution. (i.e. $\varepsilon_o''(Bi_{0.48}Al_{0.5}YIG) - \varepsilon_o''(Al_{0.5}YIG)$). As can be seen, the increase in ε_0''originates primarily from two transitions at 2.8 eV and 3.2 eV, the same energies of the two diamagnetic transitions found in the magneto-optic spectrum. There is also a shoulder at 2.75 eV and a broad absorption band around 3.6 eV, but, since these features appear to be much smaller than the peaks at 2.8 eV and 3.2 eV, we will not focus on them in this work.

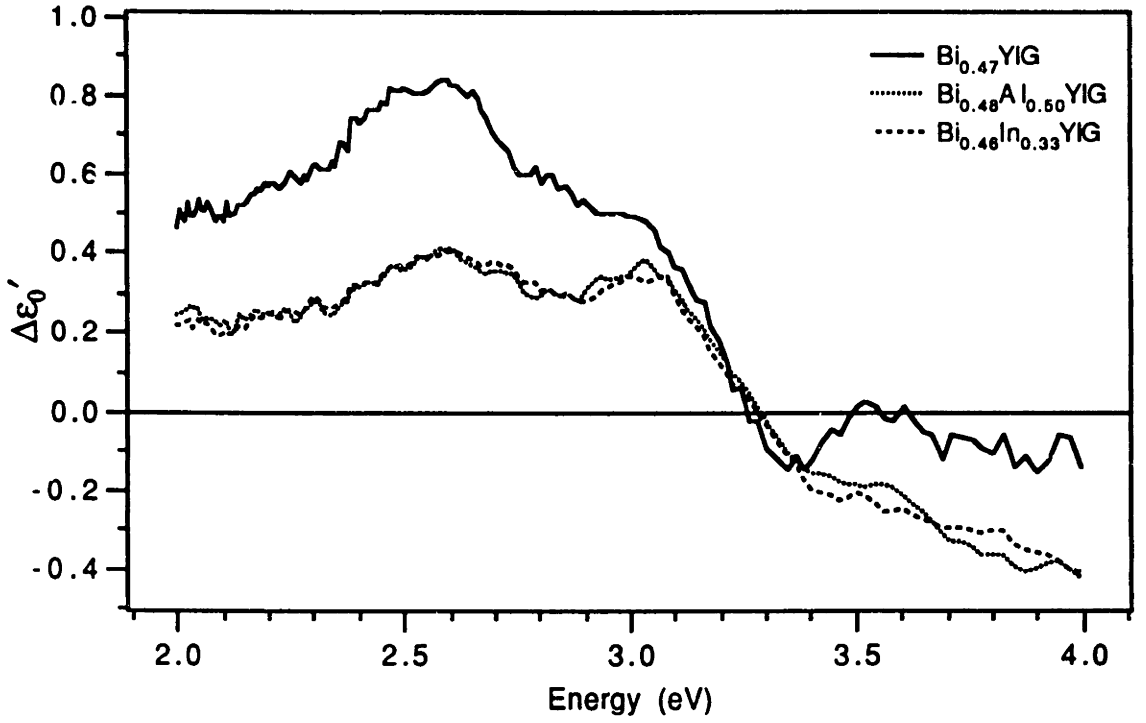

(a)

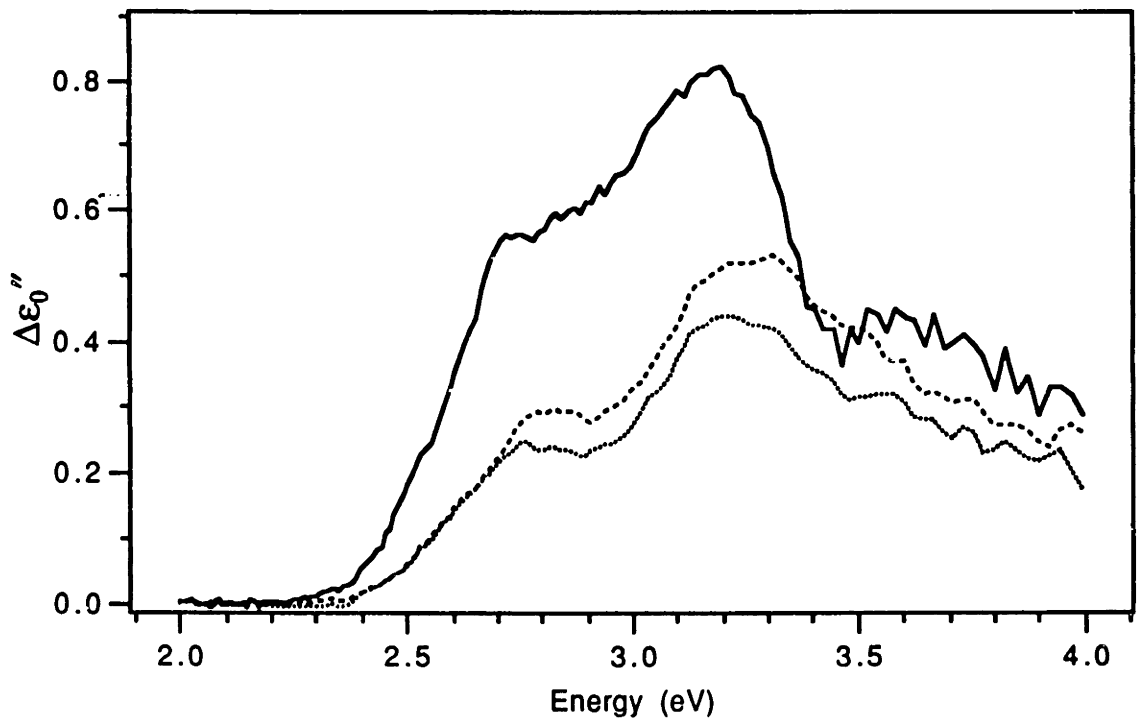

(b)

Figures 8.3. The change in the real (a) and imaginary (b) parts of $\varepsilon_0(\omega)$ due to bismuth substitution.

The transitions of interest lie in the region of the intersublattice transitions discussed in the last section and are very near in energy to those found in YIG at 2.91 eV and 3.15 eV. We reason then, that the increase in the dielectric constant of YIG caused by bismuth substitution arises, primarily, from a strengthening of intersublattice transitions already present in YIG at 2.91 eV and 3.15 eV.

Also shown in Figure 8.3 are the increases in dielectric constant when bismuth is added to $Al_{0.5}$YIG and $In_{0.33}$YIG. We see that the increase is not as great as when the full amount of Fe^{3+} is present. We expect this on the basis of our intersublattice transition interpretation. Since aluminum and indium substitution destroy intersublattice pairs, we expect there to be fewer transitions to be strengthened by the addition of Bi^{3+}. Furthermore, since $Al_{0.5}$ and $In_{0.33}$ substitution destroys approximately the same number of intersublattice pairs, (e.g. one-sixth of them), we would expect bismuth substitution to change the dielectric constant by an equivalent amount for both materials.

In Figure 8.3, we see that for the real part of the dielectric constant, $\varepsilon_0'(\omega)$, the change induced by bismuth is, indeed, equivalent for $Al_{0.5}$ and $In_{0.33}$, while for the imaginary part, $\varepsilon_0''(\omega)$, it is not.

Furthermore, we would expect the increase in the aluminum and indium substituted materials to be one-sixth smaller than the increase found for YIG. However, it appears, in Figure 8.3b, to be one-half of the increase found for YIG. We offer no explanation for this. We do note in closing, however, that the spectra of the change in dielectric constant caused by bismuth substitution in both aluminum and indium-substituted materials, has roughly the same overall shape; particularly below 3.5 eV.

8.3 The Magneto-optic Spectra of Bismuth Iron Garnet

From Figure 8.4, we see that the change in the ε_1 spectrum of YIG upon bismuth substitution is predominately due to the two diamagnetic transitions at 2.85 eV and 3.20 eV. We will focus on the origin of these transitions and neglect the paramagnetic transitions as they do not seem to be the main effect of bismuth substitution. The transition energies correspond to those present in the increase in the magnitude of $\varepsilon_0''(\omega)$ from bismuth substitution, which we attributed to a strengthening of already existing transitions in YIG. Thus, we conclude that the increase of the magneto-optic effect in YIG upon bismuth substitution, also originates from a strengthening of existing intersublattice transitions which, upon strengthening, acquire an excited state splitting.

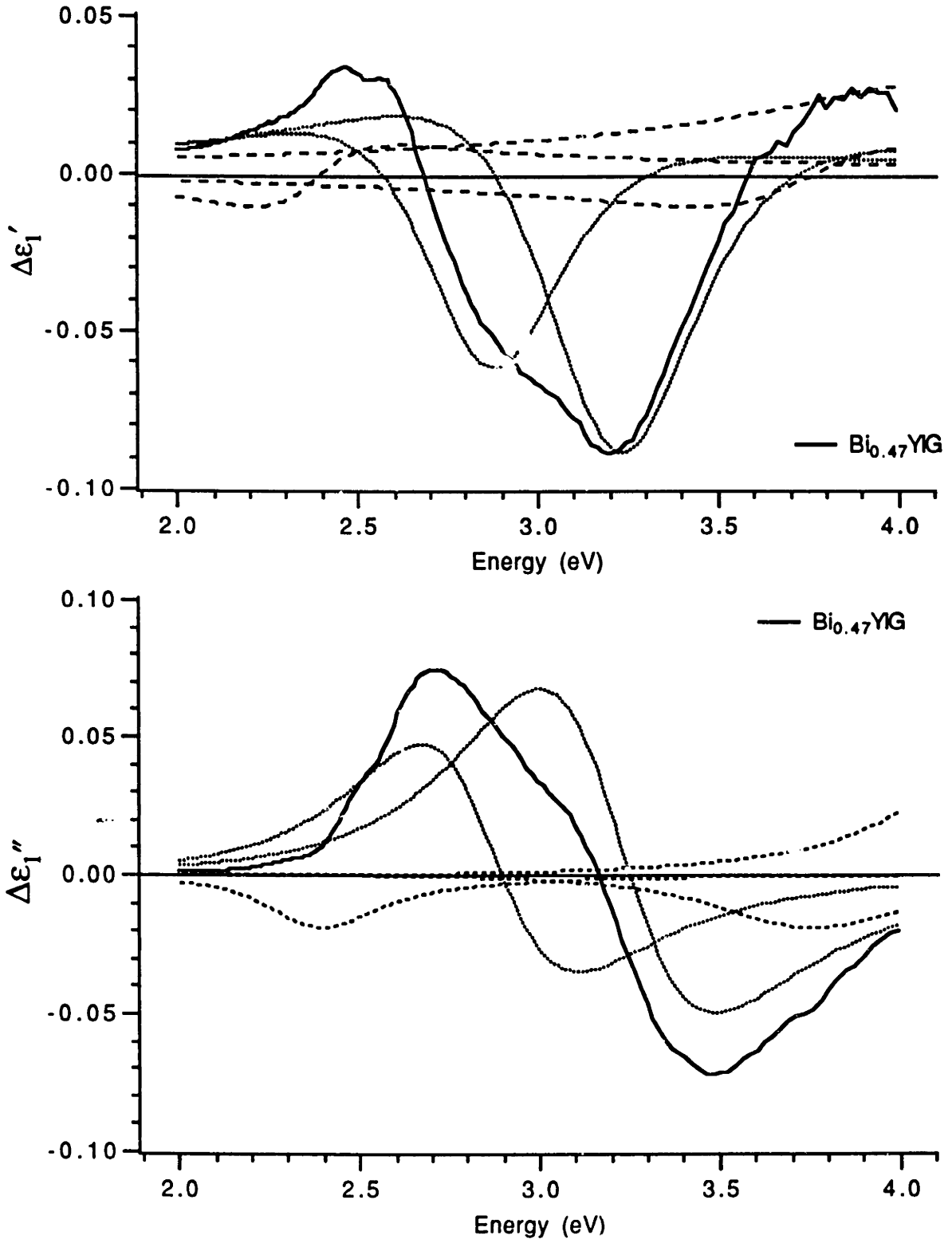

Figures 8.4. The curve fit to the change in the real (a) and imaginary (b) parts of ε_1 of $Bi_{0.47}Y_{2.53}Fe_5O_{12}$ from bismuth substitution. The solid line is the measured spectra. The fine dashed lines are the two diamagnetic transitions. The course dashed lines are the three paramagnetic transitions.

This interpretation is supported by examination of Figure 7.15. Here, we see that dilution of the iron sublattices by substitution of $Al_{0.5}$ and $In_{0.33}$ reduce bismuth's magneto-optic effect by the same amount. This supports the theory that the bismuth-induced magneto-optic effect arises from intersublattice transitions since both materials represent an equal number of destroyed intersublattice pairs.

In Figure 8.5 is shown the ratios of the magneto-optic peak heights of the iron reduced samples to those of $Bi_{0.47}YIG$. The peak heights are those obtained from the curve fits of the previous chapter and are representative of the actual ratio of the spectra. We notice that the ratios congregate around the value of two-thirds rather than the five-sixths that would be expected on the basis of the reduced number of intersublattice pairs.

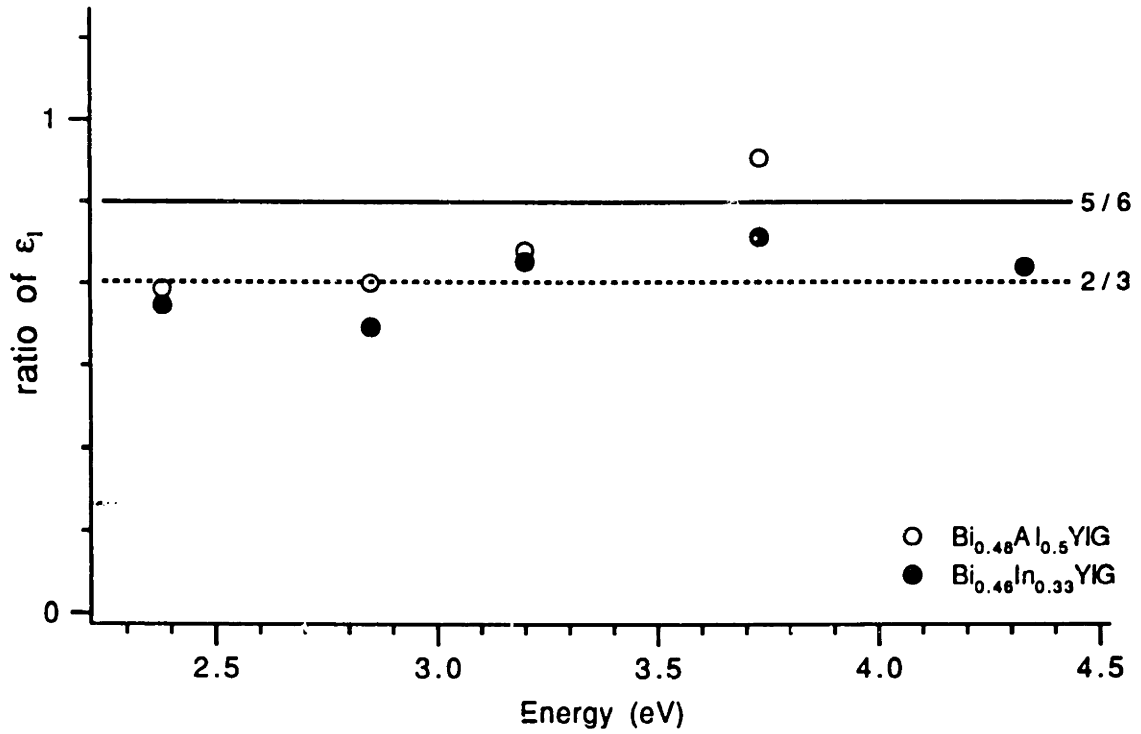

Figure 8.5. The energy dependence of the ratios of the heights of $\Delta\varepsilon_1'$ for $Bi_{0.48}Y_{2.52}Al_{0.5}Fe_{4.5}O_{12}$ and $Bi_{0.46}Y_{2.54}In_{0.33}Fe_{4.67}O_{12}$ to those of $Bi_{0.47}Y_{2.53}Fe_5O_{12}$.

8.4 Origin of excited state splittings

In Chapter 7, we found the excited state splittings responsible for the two diamagnetic transitions at 2.85 eV and 3.20 eV to be

$$\Delta_{2.85eV} = 0.033 \text{ eV} \quad \text{and} \quad \Delta_{3.20eV} = 0.055 \text{ eV}$$

We have also interpreted the origins of the two diamagnetic transitions as the result of a strengthening of intersublattice transitions already present in the iron garnets. The mechanism of this strengthening must then contribute a splitting in the excited state. We suggest, as many authors have[17], that this splitting arises from a mixing of the excited state of the iron ion with an excited state of the bismuth ion. The large spin-orbit coupling constant of Bi^{3+} ($\lambda_{Bi^{3+}} = 2.1eV$ for the free ion[14]), will contribute to the spin-orbit interaction and to the splitting of the new excited state. We assume an excited state that is a mixture of some excited state(s) of the Fe^{3+} ion and the Bi^{3+} ion. Details of this state will be described later. We write the mixed excited state as

$$|ex\rangle = \alpha|Fe\rangle + \beta|Bi\rangle \quad , \tag{8-2}$$

where $|\alpha|^2 + |\beta|^2 = 1$ and $|\alpha|^2 > 0.5$, implying that the state is predominately that of the iron ion. A spin-orbit coupling perturbation is applied to this state. The energy of the splitting is described as

$$E_{so} = \langle ex|\lambda \mathbf{L}\cdot\mathbf{S}|ex\rangle \quad . \tag{8-3}$$

There is, however, a spin exchange interaction present in YIG whose energy (E_{ex} ≈ 0.01eV to 0.1 eV) is expected to be on the order of the spin-orbit coupling interaction. This interaction is described by a Heisenberg exchange term, and is responsible for the magnetization of the material (cf. Chapter 2). As discussed by Dionne and Allen[63], the perturbation acts only on the spin and not on the orbital angular momentum. We must then treat the spin and orbital angular momentum separately. We follow the perturbation procedure outlined by Dionne and Allen and illustrated in Figure 8.6.

63 G. F. Dionne and G. A. Allen, J. Appl. Phys. **75**, 6372 (1994).

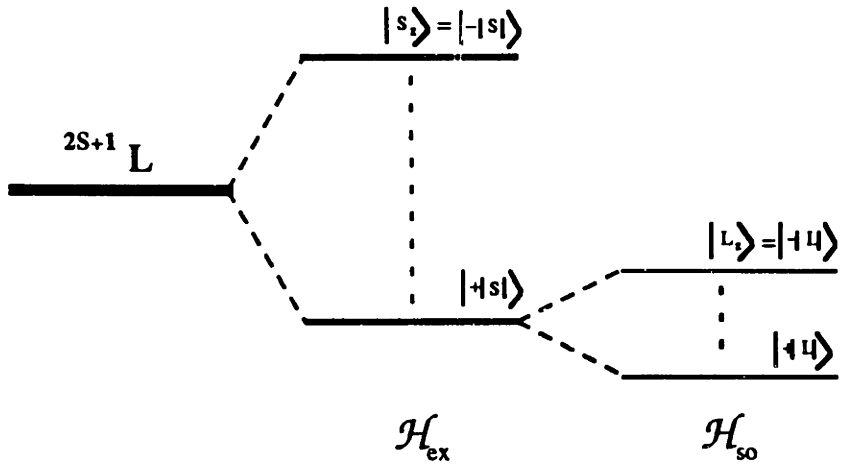

Figure 8.6. The exchange and spin-orbit coupling perturbations.

We first apply the exchange perturbation, which, for convenience and clarity, is approximated as an applied field, H_{ex}, that acts *only* on the spin† . The exchange interaction will split a ^{2S+1}L state into states corresponding to the 2S+1 values of S_z. Each of these states has a degeneracy of 2L+1. The degeneracy is removed by the spin-orbit coupling interaction. Since the spin components have already been separated, we model the interaction as[63,64]

$$\mathcal{H}_{so} = \lambda L_z S_z \quad . \tag{8-4}$$

The splittings of the mixed excited state becomes

$$E = 2\mu_B S_z H_{ex} + |\alpha|^2\langle Fe|\lambda_{Fe} L_z S_z|Fe\rangle + |\beta|^2\langle Bi|\lambda_{Bi} L_z S_z|Bi\rangle \quad . \tag{8-5}$$

The first two terms in (8-5) are the energy splitting associated with YIG. Since we do not observe any diamagnetic transitions in YIG, we assume that these terms do not produce an appreciable excited state splitting. We know that the exchange energy is significant, however, so we conclude that the spin-obit interaction for the excited state of the iron is negligible. (This is not to say that the spin-orbit interaction of Fe^{3+} is negligible, just the spin-orbit interaction for this state). Thus, we have for the energy splitting of our mixed excited state,

† This fictious field is on the order of a megagauss.

64 A. M. Clogston, Journal de Physique et le Radium 20, 151 (1959).

$$E = 2\mu_B S_z H_{ex} + |\beta|^2 \langle Bi|\lambda_{Bi} L_z S_z|Bi\rangle \quad . \tag{8-6}$$

Up to this point, we have ignored an actual description of either the Fe^{3+} or Bi^{3+} excited state. We now need a description of the excited state of Bi^{3+}.

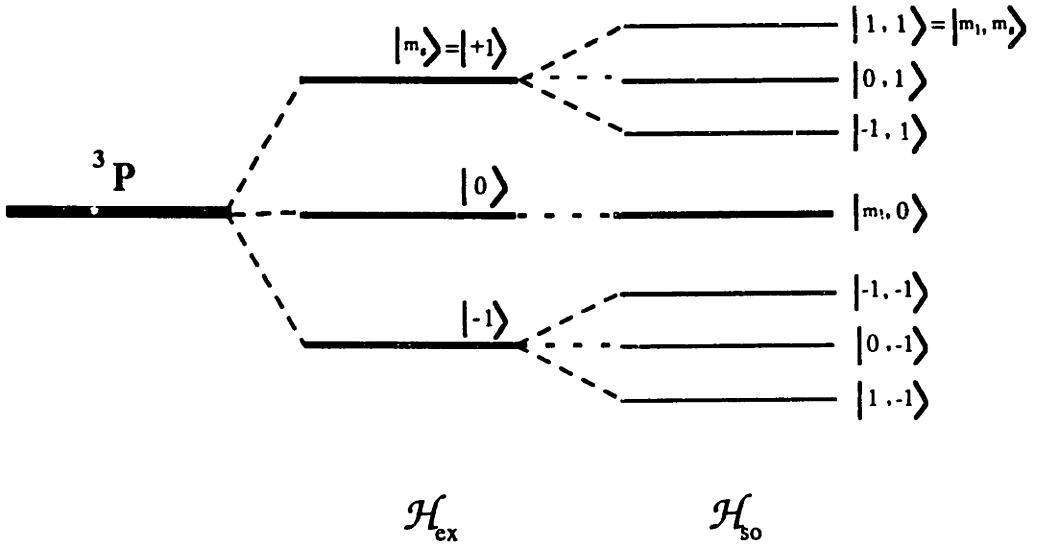

Figure 8.7. The exchange and spin-orbit coupling splittings of the ^3P-Bi^{3+}.

We assume that the bismuth state in question is the first excited state of the Bi^{3+} ion, which is a ^3P state. The nine ^3P substates will be split, according to Equation (8-6), into the energy levels depicted in Figure 8.7. We note that the $m_s = \pm 1$ states are split by the spin-orbit coupling. The upper and lower states of these groups have opposite senses of L_z, and thus, correspond to left and right-handed states. Since there is an energy difference between the right and left-handed states, they will produce a diamagnetic transition. Applying this to (8-6), we find that the excited state splitting, 2Δ, of $|e\rangle$ is

$$2\Delta = 2|\beta|^2 \lambda_{Bi} \quad . \tag{8-7}$$

We can estimate the admixture of Bi^{3+} orbital in the excited state that is necessary to explain the observed magneto-optic effect by using the free ion value of the spin-orbit coupling constant of Bi^{3+}: $\lambda_{Bi^{3+}} = 2.1\,eV$. The values calculated are

$$|\beta_{2.87}|^2 = 1.6\% \quad \text{and} \quad |\beta_{3.20}|^2 = 2.6\% \quad .$$

These are very reasonable values and indicate that the above mechanism is quite plausible.

This model is compared with the more in-depth model proposed by Dionne and Allen[63]. In this work, the authors considered the formation of a molecular bond between the excited states of the iron, bismuth and oxygen ions, using the method of Wolfsberg and Helmholtz[65]. In this method, the mixing of the states occurs due to the interaction caused by the overlap of the wavefunctions of the states. A large overlap of the wavefunctions produces a large mixing or covalency of the states. The overlap interaction also causes a shift in the energies of the states associated with molecular bonding. By assuming a downward shift in energy of the Fe^{3+} excited state, the authors were able to calculate the associated overlap and mixing of the iron and bismuth excited states.

We do not observe any shift in the energy of the excited state of the iron ion indicating that the overlap of the wave functions of the iron and bismuth excited states is small. The mixings we find are, indeed, small, being only a few percent, so there is no inconsistency between the two models. The difference lies, however, in the larger splittings Dionne and Allen assumed for the excited state that produces the diamagnetic transitions.

Notice also that in both models, the exchange interaction will not by itself produce a situation for a diamagnetic transition. Spin-orbit coupling is also necessary to split the L_z states. The reverse is also true. A spin-orbit interaction will split levels into eigenstates of the total angular momentum, J. These states have a zero expectation value for L_z. An exchange field is necessary for separation into states where the expectation value for L_z is non-zero in order for a diamagnetic transition to occur. In this case the excited state splitting, 2Δ, originates from the exchange interaction. We should mention in passing, that a third possibility for producing a diamagnetic transition is the application of a magnetic field. An applied magnetic field, in general, will always split atomic states into states with non-zero expectation values of L_z. The splittings, however, will never be much greater than 10^{-4} eV assuming a magnetic field from the magnetization of the material.

---

65 M. Wolfsberg and L. Helmholtz, J. Chem. Phys. 20, 837 (1952).

8.5 Origin of the Oscillator Strength

The mixed excited state in (8-2) must also be able to produce the observed increase in the imaginary part of the dielectric constant. This should occur from an increased oscillator strength of the transition upon mixing with the bismuth ion and will occur in the following way. If a fraction, x, of the excited states become mixed with Bi^{3+}, the dielectric constant becomes

$$\varepsilon_0^{new}(\omega) = \varepsilon_0(\omega) + x\left(\frac{f_m}{f_0} - 1\right)\varepsilon_0(\omega) \quad , \tag{8-8}$$

where f_m and f_0 are the oscillator strengths for transitions to the mixed and unmixed states, respectively. We have assumed no change in the transition energy or width. As was shown in Chapter 3, we can find the oscillator strengths from the peak values of $\varepsilon_0''(\omega)$. Doing so, we find

$$\begin{aligned} f_0 &= \frac{2\omega_0\Gamma}{\omega_p^2}\mathcal{L}_0\varepsilon_0''(\omega_0) \\ f_m &= f_0 + \frac{1}{x}f_0\left[\frac{\varepsilon_0^{new''}(\omega_0)}{\varepsilon_0''(\omega_0)}\frac{\mathcal{L}_{new}}{\mathcal{L}_0} - 1\right] \quad , \end{aligned} \tag{8-9}$$

where $\mathcal{L}$ is the Lorenz-Lorentz correction of the internal electric field of a material[42] and is equal to

$$\mathcal{L} = \frac{9}{(n^2+2)^2} \quad .$$

where n is the index of refraction. This yields for the two transitions of interest††

$$f_0^{2.87eV} = 1.2\times10^{-3} \qquad f_0^{3.20eV} = 1.1\times10^{-3}$$
$$f_m^{2.87eV} = 8.2\times10^{-3} \qquad f_m^{3.20eV} = 6.1\times10^{-3}$$

†† The oscillator strength for the mixed excited state at 2.85 eV was estimated by assuming that the increase in ε_0'' of both the 2.76 eV peak and the 2.91 eV peak of YIG found from curve fits, occured entirely at the latter transition. See section 8.2 for a rationale of this assumption.

To see if these are reasonable increases for our model, consider the following argument. The oscillator strength for a transition to the mixed excited state can be written as

$$\begin{aligned} f_m &= \frac{2m\omega}{\hbar}|\langle e|r|g\rangle|^2 \\ &= \frac{2m\omega}{\hbar}\left\{|\alpha|^2|\langle Fe|r|g\rangle|^2 + |\beta|^2|\langle Bi|r|g\rangle|^2 + 2\mathrm{Re}\left[\alpha^*\beta\langle Fe|r|g\rangle\langle Bi|r|g\rangle\right]\right\} \end{aligned} \quad . \tag{8-10}$$

If we assume that there is little change in the ground state upon bismuth substitution, then the first term in (8-10) is the oscillator strength of the unmixed state, f_0, multiplied by $|\alpha|^2$. The second term is the oscillator strength, f_{Bi}, of a transition to the excited state of the bismuth ion alone. To obtain an approximate value for f_{Bi}, we assume all matrix elements in (8-10) are real and positive. We find that

$$f_{Bi}^{2.87eV} \cong 0.20 \qquad f_{Bi}^{1.20eV} \cong 0.08 \quad .$$

These values are rather large. A more likely value for f_{Bi} would be less than that of 1.8×10^{-2}, as found for a Bi^{3+} transition in bismuth-substituted yttrium gallium garnet[19]. What this exercise implies is that, in order for the above model to be a valid one, the oscillator strength to the excited state of the iron ion, f_0, must be increased. This may be possible, if we drop our assumption that the ground state of the intersublattice transition is unaffected by bismuth substitution. A change in the ground state of the transition would be necessary to increase the dipole matrix element $\langle Fe|r|g\rangle$. We offer an explanation about how this might occur in the next section. We also point out that any explanation for the change in the ground state must preserve the magnetization of the material, since the magnetization is dependent upon the ground state and is found not to change significantly upon substitution of bismuth. A discussion of the ground state and the intersublattice transitions will be taken up in the next section.

8.6 Description of Intersublattice Transitions and the Ground State

An intersublattice transition is the transfer of an electron from an ion on one sublattice to an ion on the other sublattice. A reasonable probability for such transitions exist in YIG due to a mixing between the electron wavefunctions of Fe^{3+} on both of the

sublattices. The mixing occurs due to covalent bonding of the ions with the *same* oxygen orbital. This is illustrated in Figure 8.8. If the admixture of oxygen into the cation state is represented by γ, then the admixture of Fe^{3+} on one site into that of the other is $\gamma_a\gamma_d$, where the subscripts denote the site. There has been no formal theory, put forth in the literature, which describes intersublattice transitions and none will be developed here. It is largely felt, however, that the probability of such transitions will be proportional to the quantity $\gamma_a^2\gamma_d^2$. This is a reasonable assumption since this quantity represents the percentage that a state localized on one site is present on the other site.

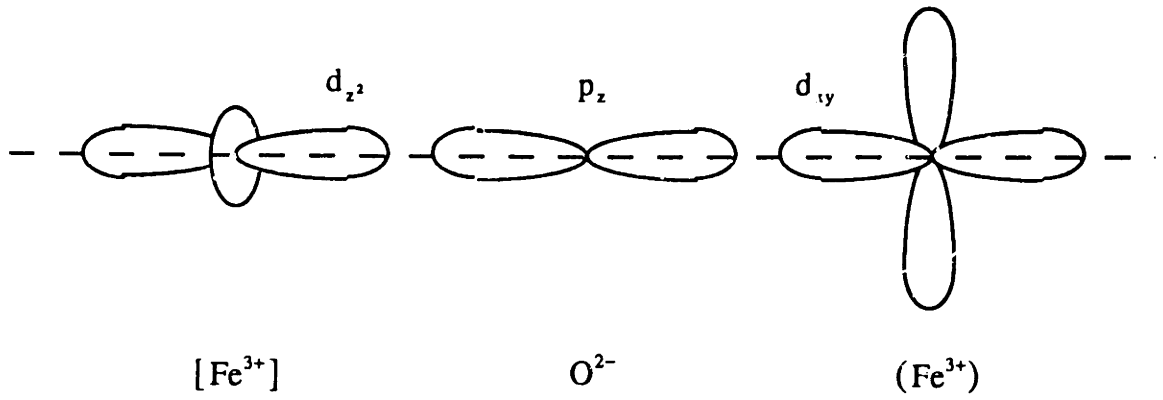

Figure 8.8. Schematic diagram of a pair of iron ions in different sites bonding to the same oxygen orbital. Only σ-bonding is shown.

We've postulated that substitution of Bi^{3+} into YIG increases the transition probability of intersublattice transitions. One mechanism by which this may be accomplished then, is for Bi^{3+} to increase the covalency of octahedral and/or tetrahedral Fe^{3+}; that is, increase the quantity $\gamma_a^2\gamma_d^2$. Evidence for an increase in covalency comes from magnetic measurements and the theory of superexchange. In the theory of superexchange[66], magnetic ions that are separated by an anion, have an antiferromagnetic Heisenberg exchange interaction, written as

$$\mathcal{H}_{SE} = J\vec{S}_1 \cdot \mathbf{S}_2 \quad .$$

The exchange constant, J, can be approximated as

$$J \approx \gamma_a^2\gamma_d^2 \frac{(\Delta E_{anion})^2}{U} \quad , \tag{8-11}$$

[66] H. J. Zeiger and G. W. Pratt, *Magnetic Interactions in Solids* (Clarendon Press, Oxford,1973), p.239.

where ΔE_{anion} is approximately the ionization energy of the anion and, U, is the repulsive energy of two electrons on the same ion; usually estimated to be about 10 eV. In YIG, the coupling constant, $J_{YIG} = 22\ cm^{-1}$. This value increases upon bismuth substitution and extrapolates for pure bismuth iron garnet to $J_{BIG} = 26\ cm^{-1}$. This increase can be accounted for with only about a 10% increase in the percentage γ_a^2 and γ_d^2. These are very plausible increases. Such changes may be detectable by NMR or EPR spectroscopy or other techniques capable of measuring the covalency of ions.

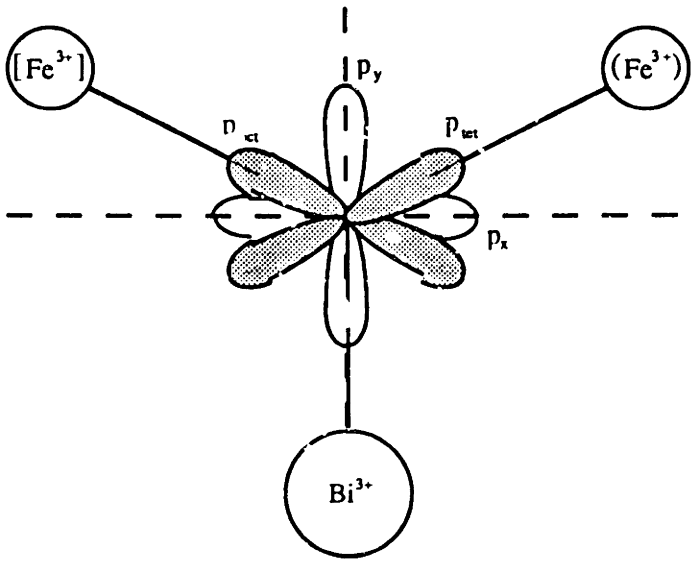

Figure 8.9. The covalent bonding of the ions in bismuth iron garnet. The arrangement of the cations is only approximate. Not shown is a second bismuth ion that is above the plane of the paper over the origin.

The most probable way in which the Bi^{3+} ion affects the covalency of the iron ions is through its own covalency with oxygen. This is illustrated in Figure 8.9, where we have simplified the arrangement of the ions for descriptive purposes. Assuming σ-bonding only, the octahedral and tetrahedral iron covalently bond with the oxygen orbitals p_{oct} and p_{tet} by the amounts γ_a and γ_d, respectively. The orbitals p_{oct} and p_{tet} have components of the p_y orbital, which itself is covalently bonded to the 6s orbitals of the Bi^{3+} ion. It is possible that the bismuth ion could affect the iron covalency through its mixing with the p_y orbital. Additionally, it can be seen that the Fe^{3+} states would possess a small percentage admixture of the bismuth wavefunction; $\gamma_a^2\gamma_{Bi}^2$ and $\gamma_d^2\gamma_{Bi}^2$.

A complete description of bismuth's effect on the iron-oxygen bond is beyond the scope of this work. We present the above model only as a plausibility argument for explaining the increase in the covalency of iron.

We note in concluding, however, that the increase in covalency of the iron determined from the magnetism, does not explain the observed increase in the oscillator strength of the intersublattice transitions. The increase in oscillator strength was determined in the last section to be about a factor of six, far larger than the 20% that would account for the magnetic properties. Another mechanism must come into play if our line of reasoning is a correct one. We suggest the possibility that the admixture of the bismuth ion with Fe^{3+} states may produce a significant increase in the oscillator strength.

8.7 The Magneto-optic Spectra of YIG

Before concluding this chapter, we comment on the magneto-optic spectra of YIG *without* the substitution of bismuth. We note that the spectra is composed entirely of paramagnetic transitions. This is quite surprising since the presumed ground state of the iron ions are ^6S states, possessing *no* orbital angular momentum. A paramagnetic lineshape arises from a thermally populated splitting of the ground state (c.f. Figure 3.2). The split states have different expectation values for L_z, and thus, have differing oscillator strengths for left and right-handed polarized light. If the ground state possesses no orbital angular momentum, there can not be a paramagnetic transition.

A mechanism by which the ground states of the Fe^{3+} ions could acquire some angular momentum was introduced by Clogston[64] and later refined by Scott *et al.*[39] The theory points out that the ground state of Fe^{3+} (in either site) can mix with the first excited state, $^4T_{1(g)}$, by means of the spin-orbit coupling interaction. This state has the character of a P state. If we were to carry out the perturbation process that was used in section 8.3 to explain the excited state splitting of bismuth iron garnet (exchange perturbation followed by a spin-orbit coupling), we get similar results for the splitting of states. Namely, the already exchange split states will split further into L_z states, and thus, provide the "handedness" needed for a paramagnetic transition. Scott *et al.* have shown that the mixing of the $^4T_{1(g)}$ state with the ground state would be about 5% and showed further that, this amount would account for the observed magnitude of the paramagnetic lines. Again, we wish to point out that, by themselves, the exchange interaction and the spin-orbit interaction will not alone produce a splitting of states with differing L_z values, but, the two interactions will do so in concert with each other.

Lastly, we point out that, we have found the quantity $\Delta f/f$ to decrease with transition energy in the iron garnets (see Figure 7.18). This is also quite surprising. The strength of the paramagnetic lines depends on the nature of the ground state, *not* the

excited state. This being the case, we do not expect to see any change in $\Delta f/f$ across the spectrum. We do not offer any explanation for this

9. Conclusions

In this work, we have measured the optical and magneto-optical spectra of polycrystalline samples of bismuth-substituted iron garnets and their non-bismuth counterparts. We have found that substitution of bismuth into iron garnets increases both spectra with peaks occurring at approximately 2.85 eV and 3.20 eV. We attribute these increases to a strengthening of intersublattice transitions that are already present in the unsubstituted materials.

This interpretation is supported by the optical and magneto-optical spectra of samples substituted with aluminum and indium. In these materials, the substituents reside primarily in the tetrahedral and octahedral sublattices, respectively, and represent a reduced iron population in the sublattices. It was found that substitution for iron in either sublattice produces an equivalent decrease in both the optical and magneto-optical spectra, when equal fractions of the iron in the sublattices are removed.

We have interpreted the increases in the magneto-optic effect of YIG from bismuth-substitution as originating predominately from two diamagnetic transitions located at 2.85 eV and 3.20 eV, the same energies at which transitions are found to increase in intensity in the optical spectra. The excited state splittings associated with the diamagnetic peaks are found to be approximately $\Delta_{2.85eV} = 0.033$ eV and $\Delta_{3.20eV} = 0.055$ eV. We propose, as others have, that this splitting originates from a spin-orbit coupling that is introduced by an excited state of the iron ions mixing with the ^3P state of the Bi^{3+} ion. Such a mixing was estimated to be 1.6% and 2.6% for the 2.85 eV and 3.20 eV transitions, respectively. From our work we have also concluded that any explanation as to the origin of the excited state splitting *must* include the combination of spin-orbit coupling and an exchange interaction.

In order for the above model to be correct, a change in the ground state must occur in order to explain the observed increase in oscillator strength. We suggest that the Bi^{3+} ion covalently bonds with the same oxygen ion that links the Fe^{3+} states on differing sites. This covalency could explain the increased mixing of the two iron sublattices and would admix the ground state of Bi^{3+} to the iron states.

We make the following suggestions for further investigations that would aid in the understanding the role of bismuth in the magneto-optical effect of bismuth iron garnets.

First, it would be useful to see how the optical and magneto-optical spectra of YIG and Bi-YIG change with the dilution of the two iron sublattices. We have only presented one piece of data for this; that of a one-sixth dilution of both iron sublattices.

Spectra for a series of diluted iron sublattices may shed light on the nature of the intersublattice transitions and the role that the two sublattices play in the magneto-optical effect. Along these lines, it would be helpful to have a theoretical description of intersublattice transitions.

The nature of both the ground state and the excited states responsible for the magneto-optic transitions also needs to be understood better. Some information of the nature of the excited states may be deduced through photoconductivity or thermopower measurements. For the ground state, of particular interest is the covalency between the two iron sites, as well as the covalency of bismuth with the intermediate oxygen ion. We have postulated, and indeed, magnetic measurements suggest, that the covalency between the two iron sublattices increases as a result of bismuth substitution. It may be possible to see this increase through NMR or EPR measurements, as well as any other techniques that can measure the effect of covalency.

Lastly, it is noted that a satisfactory explanation needs to be given for the increase in oscillator strength caused by bismuth substitution for the transitions of interest.

An understanding as to how Bi^{3+} produces such a large magneto-optic effect in iron garnets may allow researchers to produce stronger or more tailored magneto-optical materials for the present applications of optical isolation and magneto-optical recording.

A. Reflection Matrix for a Magneto-optic Material

In this appendix, we derive the Jones' matrix for reflection from an isotropic or cubic magneto-optic material. The derivation was formulated by Sprokel[67] and is adopted here for finding the reflection matrix. What we seek, exactly, is the matrix $\mathbf{R}(\theta)$ such that,

$$\mathbf{E}_{\text{reflected}} = \begin{bmatrix} E_x^r \\ E_y^r \end{bmatrix} = \mathbf{R}(\theta) \begin{bmatrix} E_x^i \\ E_y^i \end{bmatrix} = \mathbf{E}_{\text{incident}} \quad ,$$

where θ is the angle of incidence on the magneto-optic material surface (see Figure A.1). We will first use Maxwell's equations with no charges or currents to find the normal modes of propagation in the magneto-optic material. These modes are right and left circularly polarized light. Next, impedance relations for the normal modes are used in order to describe them in a single electric field component. Lastly, the electric fields for waves propagating in the initial material and the magneto-optical material are related by boundary conditions, and the reflection matrix is obtained by assuming light incident only from the incident material.

We begin by describing the magneto-optic material by its complex permittivity tensor,

$$\vec{\boldsymbol{\varepsilon}} = \begin{bmatrix} \varepsilon & -i\varepsilon_{12} & 0 \\ +i\varepsilon_{12} & \varepsilon & 0 \\ 0 & 0 & \varepsilon \end{bmatrix} = \varepsilon \begin{bmatrix} 1 & -ig & 0 \\ +ig & 1 & 0 \\ 0 & 0 & 1 \end{bmatrix} \quad ,$$

where ε, ε_{12} and g are in general complex and $g = \varepsilon_{12}/\varepsilon$. The off diagonal elements are what produce a magneto-optic effect. Typically, the magnitudes of these elements are small compared to the diagonal elements, i.e. $|g| << 1$. We also assume that the permeability, μ, of the magneto-optic material is one, since there are usually no significant magnetic moment contributions at optical wavelengths.

We start with the source free Maxwell's equations.

$$\nabla \times \mathbf{E} = -\frac{1}{c}\frac{\partial \mathbf{H}}{\partial t} \quad , \qquad \text{(A-1a)}$$

---

67 G.J. Sprokel, Applied Optics 23, 3983 (1984).

$$\nabla \times \mathbf{H} = \frac{1}{c}\boldsymbol{\varepsilon} \cdot \frac{\partial \mathbf{E}}{\partial t} \quad , \tag{A-1b}$$

By multiplying (A-1a) by $\nabla \times$ and using (A-1b) we obtain,

$$\nabla \times \nabla \times \mathbf{E} = \nabla(\nabla \cdot \mathbf{E}) - (\nabla \cdot \nabla)\mathbf{E} = -\frac{1}{c^2}\boldsymbol{\varepsilon} \cdot \frac{\partial \mathbf{E}}{\partial t} \quad , \tag{A-2}$$

At this point it is assumed that solutions to (A-2) have the form ,

$$\mathbf{E} = \mathbf{E}_0 e^{i(\mathbf{k}\cdot\mathbf{r}-\omega t)} \quad ,$$

and thus, we get a wave equation of the form,

$$\left(\frac{\omega}{c}\right)^2 \boldsymbol{\varepsilon} \cdot \mathbf{E} + \mathbf{k}(\mathbf{k} \cdot \mathbf{E}) - \mathrm{k}^2 \mathbf{E} = 0 \quad . \tag{A-3}$$

Equation (A-3) is a matrix equation ;

$$\begin{bmatrix} \mathrm{k}^2 - \mathrm{k}_x^2 - \left(\frac{\omega}{c}\right)^2 \varepsilon & -\mathrm{k}_x\mathrm{k}_y + ig\left(\frac{\omega}{c}\right)^2 \varepsilon & -\mathrm{k}_x\mathrm{k}_z \\ -\mathrm{k}_x\mathrm{k}_y - ig\left(\frac{\omega}{c}\right)^2 \varepsilon & \mathrm{k}^2 - \mathrm{k}_y^2 - \left(\frac{\omega}{c}\right)^2 \varepsilon & -\mathrm{k}_y\mathrm{k}_z \\ -\mathrm{k}_x\mathrm{k}_z & -\mathrm{k}_y\mathrm{k}_z & \mathrm{k}^2 - \mathrm{k}_z^2 - \left(\frac{\omega}{c}\right)^2 \varepsilon \end{bmatrix} \begin{bmatrix} \mathrm{E}_x \\ \mathrm{E}_y \\ \mathrm{E}_z \end{bmatrix} = 0 \quad .$$

Values of k that are a solution to (A-3) can be found by setting the determinant of the matrix equal to zero. This leads to the algebraic equation

$$\left[\mathrm{k}^2 - \left(\frac{\omega}{c}\right)^2 \varepsilon\right]^2 + g\left(\frac{\omega}{c}\right)\varepsilon\left[\mathrm{k}^2 - \mathrm{k}_z^2 - \left(\frac{\omega}{c}\right)^2 \varepsilon\right] = 0 \quad . \tag{A-4}$$

There are four solutions to (A-4),

$$k_{z1}^{+} = +\kappa_0\sqrt{1+g\frac{\frac{\omega}{c}\sqrt{\varepsilon}}{\kappa_0}} \qquad k_{z2}^{+} = +\kappa_0\sqrt{1-g\frac{\frac{\omega}{c}\sqrt{\varepsilon}}{\kappa_0}}$$

$$k_{z1}^{-} = -\kappa_0\sqrt{1-g\frac{\frac{\omega}{c}\sqrt{\varepsilon}}{\kappa_0}} \qquad k_{z2}^{-} = -\kappa_0\sqrt{1+g\frac{\frac{\omega}{c}\sqrt{\varepsilon}}{\kappa_0}} \quad , \tag{A-5}$$

where

$$\kappa_0^2 = \left(\frac{\omega}{c}\right)^2 \varepsilon - \left(k_x^2 + k_y^2\right) \quad .$$

Plus and minus refer to the direction of propagation in the z-direction while 1 and 2 are merely labels for the two solutions. Note that when there is no magneto-optical effect ($g = 0$), (A-5) reduces to only two solutions, $k_z = \pm\kappa_0$. These are the usual solutions for an isotropic material.

Before proceeding, we note that the solutions (A-5) are related in pairs and we therefore make the following definitions:

$$\begin{aligned} k_{z1} &\equiv k_{z1}^{+} = -k_{z2}^{-} \\ k_{z2} &\equiv k_{z2}^{+} = -k_{z1}^{-} \end{aligned} \quad . \tag{A-6}$$

Referring back to Figure A.1, we now assume that the plane of reflection and transmission is the y-z plane; k_x=0. We now derive impedance relations for electromagnetic waves in the magneto-optic material. With these relations we can describe the waves entirely by the quantity E_y.

Referring back to Maxwell's equations in (A-1), we find from the y-component of (A-1a)

$$H_y = \frac{c}{\omega} k_z E_x \quad . \tag{A-7}$$

Furthermore, by combining the z-component of (A-1b) with the x-component of (A-1a), we obtain

$$\mathbf{H}_x = -\frac{\frac{\omega}{c}\varepsilon}{k_0^2} k_z \mathbf{E}_y \quad . \tag{A-8}$$

Both (A-7) and (A-8) are true for any isotropic material, magneto-optic or otherwise. For the particular case of a magneto-optic material and propagation in the y-z plane, (A-1a) and (A-1b) give

$$\begin{aligned} \mathbf{E}_{x1} &= -i\frac{\frac{\omega}{c}\sqrt{\varepsilon}}{k_0}\mathbf{E}_{y1} \\ \mathbf{E}_{x2} &= +i\frac{\frac{\omega}{c}\sqrt{\varepsilon}}{k_0}\mathbf{E}_{y2} \end{aligned} \quad . \tag{A-9}$$

Equations (A-7)-(A-9) will be used to simplify equations by allowing us to use only independent variables.

Our next step is to relate the electromagnetic waves in the region of incidence, which will be assumed to be isotropic, to the electromagnetic waves in the magneto-optic materials (see Figure A.2). All electric and magnetic fields are indicated by the following convention:

$$\mathbf{E}^{\text{direction},\pm}_{(\text{material})(\text{component})(\text{solution}\#)} \quad .$$

We will include waves propagating in the negative z-direction in material 2 for generality. Later, the amplitude of these waves will be set to zero to obtain the reflectivity matrix.

Employing the boundary condition that tangential components (x and y) of the electric and magnetic fields must be continuous, we obtain the following equations:

$$E^+_{1x} + E^-_{1x} = E^+_{2x1} + E^-_{2x1} + E^+_{2x2} + E^-_{2x2} \tag{A-10a}$$

$$E^+_{1y} + E^-_{1y} = E^+_{2y1} + E^-_{2y1} + E^+_{2y2} + E^-_{2y2} \tag{A-10b}$$

$$H^+_{1x} + H^-_{1x} = H^+_{2x1} + H^-_{2x1} + H^+_{2x2} + H^-_{2x2} \tag{A-10c}$$

$$H^+_{1y} + H^-_{1y} = H^+_{2y1} + H^-_{2y1} + H^+_{2y2} + H^-_{2y2}. \tag{A-10d}$$

Now, apply the following three sets of operations:

1) use (A-7) and (A-8) to express (A-10c) and (A-10d) in terms of the electric field.

2) use (A-9) to put the right hand sides of (A-10) in terms of the E_y's

3) use the definitions in (A-6) to express (A-10) in terms of k_{1z},k_{2z1}, and k_{2z2}.

The resulting equations of (A-10) can then be expressed in the form of a matrix equation;

$$\begin{bmatrix} 0 & 0 & 1 & 1 \\ 1 & 1 & 0 & 0 \\ 0 & 0 & k_{1z} & -k_{1z} \\ k_{1z} & -k_{1z} & 0 & 0 \end{bmatrix} \begin{bmatrix} E_{1y}^{+} \\ E_{1y}^{-} \\ E_{1x}^{+} \\ E_{1x}^{-} \end{bmatrix} = \begin{bmatrix} \frac{1}{ia_2} & \frac{1}{ia_2} & \frac{-1}{ia_2} & \frac{-1}{ia_2} \\ 1 & 1 & 1 & 1 \\ \frac{k_{2z1}}{ia_2} & \frac{-k_{2z2}}{ia_2} & \frac{-k_{2z2}}{ia_2} & \frac{k_{2z1}}{ia_2} \\ bk_{2z1} & -bk_{2z2} & bk_{2z2} & -bk_{2z1} \end{bmatrix} \begin{bmatrix} E_{2y1}^{+} \\ E_{2y1}^{-} \\ E_{2x2}^{+} \\ E_{2x2}^{-} \end{bmatrix}, \quad \text{(A-11)}$$

where

$$a_2 = \frac{\kappa_{20}}{\frac{\omega}{c}\sqrt{\varepsilon_2}} \quad \text{and} \quad b = \frac{\kappa_{10}^2}{\varepsilon_1}\frac{\varepsilon_2}{\kappa_{20}^2} \ .$$

Expressing (A-11) with a single matrix, we have

$$\begin{bmatrix} E_{1y}^{+} \\ E_{1y}^{-} \\ E_{1x}^{+} \\ E_{1x}^{-} \end{bmatrix} = \begin{bmatrix} \frac{u_1+u_{21}}{2u_1} & \frac{u_1-u_{22}}{2u_1} & \frac{u_1+u_{22}}{2u_1} & \frac{u_1-u_{21}}{2u_1} \\ \frac{u_1-u_{21}}{2u_1} & \frac{u_1+u_{22}}{2u_1} & \frac{u_1-u_{22}}{2u_1} & \frac{u_1+u_{21}}{2u_1} \\ \frac{k_{1z}+k_{2z1}}{2ia_2k_{1z}} & \frac{k_{1z}-k_{2z2}}{2ia_2k_{1z}} & \frac{-k_{1z}-k_{2z1}}{2ia_2k_{1z}} & \frac{-k_{1z}+k_{2z1}}{2ia_2k_{1z}} \\ \frac{k_{1z}-k_{2z1}}{2ia_2k_{1z}} & \frac{k_{1z}+k_{2z2}}{2ia_2k_{1z}} & \frac{-k_{1z}+k_{2z2}}{2ia_2k_{1z}} & \frac{-k_{1z}-k_{2z2}}{2ia_2k_{1z}} \end{bmatrix} \begin{bmatrix} E_{2y1}^{+} \\ E_{2y1}^{-} \\ E_{2x2}^{+} \\ E_{2x2}^{-} \end{bmatrix}, \quad \text{(A-12)}$$

where we have made the further definitions

$$u_1 \equiv -\frac{\omega}{c}\varepsilon_1\frac{k_{1z}}{\kappa_{10}^2} \ , \qquad u_{21} \equiv -\frac{\omega}{c}\varepsilon_2\frac{k_{2z1}}{\kappa_{20}^2} \ , \qquad u_{22} \equiv -\frac{\omega}{c}\varepsilon_2\frac{k_{2z2}}{\kappa_{20}^2} \ .$$

Finally, we obtain the reflection matrix of the magneto-optic material. We do this by first assuming that no waves are propagating in the negative z-direction in the magneto-optical material; i.e., $E_{2y1}^{-} = E_{2y2}^{-} = 0$. And second, we want to find E_{1x}^{-} and E_{1y}^{-} in terms of E_{1x}^{+} and E_{1y}^{+}. By doing the first step we get two matrix equations:

$$\begin{bmatrix} E_{1x}^{+} \\ E_{1y}^{+} \end{bmatrix} = X_1 \begin{bmatrix} E_{2y1}^{+} \\ E_{2y2}^{+} \end{bmatrix} = \begin{bmatrix} \dfrac{k_{1z} + k_{2z1}}{2ia_2k_{1z}} & \dfrac{-k_{1z} - k_{2z2}}{2ia_2k_{1z}} \\ \dfrac{u_1 + u_{21}}{2u_1} & \dfrac{u_1 + u_{22}}{2u_1} \end{bmatrix} \begin{bmatrix} E_{2y1}^{+} \\ E_{2y2}^{+} \end{bmatrix} , \qquad \text{(A-13a)}$$

$$\begin{bmatrix} E_{1x}^{-} \\ E_{1y}^{-} \end{bmatrix} = X_2 \begin{bmatrix} E_{2y1}^{+} \\ E_{2y2}^{+} \end{bmatrix} = \begin{bmatrix} \dfrac{k_{1z} - k_{2z1}}{2ia_2k_{1z}} & \dfrac{-k_{1z} + k_{2z2}}{2ia_2k_{1z}} \\ \dfrac{u_1 - u_{21}}{2u_1} & \dfrac{u_1 - u_{22}}{2u_1} \end{bmatrix} \begin{bmatrix} E_{2y1}^{+} \\ E_{2y2}^{+} \end{bmatrix} . \qquad \text{(A-13b)}$$

By left multiplying (A-13a) by X_1^{-1} and then substitution into (A-13b), we obtain

$$\begin{bmatrix} E_{1x}^{-} \\ E_{1y}^{-} \end{bmatrix} = R \begin{bmatrix} E_{1x}^{+} \\ E_{1y}^{+} \end{bmatrix} = X_2 X_1^{-1} \begin{bmatrix} E_{1x}^{+} \\ E_{1y}^{+} \end{bmatrix} .$$

The reflection matrix is then

$$R = \frac{1}{\Delta} \begin{bmatrix} (k_{1z} - k_{2z1})(u_1 + u_{22}) + (k_{1z} - k_{2z2})(u_1 + u_{21}) & i2u_1 \dfrac{(k_{2z1} - k_{2z2})}{a_2} \\ -i2a_2k_{1z}(u_{21} - u_{22}) & (u_1 - u_{21})(k_{1z} + k_{2z2}) + (u_1 - u_{22})(k_{1z} + k_{2z1}) \end{bmatrix} , \qquad \text{(A-14)}$$

where

$$\Delta = (u_1 + u_{21})(k_{1z} + k_{2z2}) + (u_1 + u_{22})(k_{1z} + k_{2z1}) .$$

The reflection matrix in (A-14) is a function of frequency, ω, and of angle of incidence, θ. The angle of incidence comes into the reflection matrix by the relation

$$k_{1y} = \frac{\omega}{c}\sqrt{\varepsilon_1}\sin\theta ,$$

for propagation in the y-z plane. The boundary conditions for an electromagnetic wave require that the tangential component of the wave vector must be continuous across an interface. Thus,

$$k_{1y} = k_{2y} \equiv k_y .$$

Specifically, we get the relations

$$k_{1z}^2 = \left(\frac{\omega}{c}\right)^2 \varepsilon_1 - k_y^2 \quad \text{and} \quad k_{2zi} = \kappa_0 \sqrt{1 \pm \frac{g}{a_2}} \ , \tag{A-15}$$

where

$$\kappa_0 = \left(\frac{\omega}{c}\right)^2 \varepsilon_2 - k_y .$$

In addition to being a function of ω and θ, the reflection matrix, **R**, is also dependent upon the material parameters ε, ε_{12} and g.

As a check, we can show how **R** gives us the Fresnel reflection coefficients for a non-magnetic isotropic material. Non-magnetic means that g = 0 which leads to,

$$k_{2z1} = k_{2z2} = \kappa_{20}$$
$$u_{21} = u_{22} \equiv u_2$$

This makes the off-diagonal elements of **R** go to zero and hence, no mixing between x- and y-polarized light. Equation (A-14) then yields

$$E_{1x}^- = r_\perp E_{1x}^+ = \frac{k_{1z} - k_{2z}}{k_{1z} + k_{2z}} E_{1x}^+ \ , \tag{A-16a}$$

$$E_{1y}^- = r_\parallel E_{1y}^+ = \frac{u_1 - u_2}{u_1 + u_2} E_{1y}^+ \ , \tag{A-16b}$$

where $r_\perp$ and $r_\parallel$ are the perpendicular and plane polarized reflection coefficients. If we define the complex index of refraction to be

$$N_i^2 \equiv \varepsilon_i \ ,$$

then, by substitution for the u's and k's, we obtain

$$r_{\perp} = \frac{N_1 \cos\theta - \sqrt{N_2^2 - N_1^2 \sin^2\theta}}{N_1 \cos\theta + \sqrt{N_2^2 - N_1^2 \sin^2\theta}}$$

$$r_{\parallel} = \frac{N_2^2 \cos\theta - N_1\sqrt{N_2^2 - N_1^2 \sin^2\theta}}{N_2^2 \cos\theta + N_1\sqrt{N_2^2 - N_1^2 \sin^2\theta}} \qquad \text{(A-17)}$$

These are indeed the Fresnel reflection coefficients for an isotropic material.

As a simple example of the use of (A-14) for magneto-optical materials, we use the reflection matrix to analyze light reflected by an air/magneto-optic interface at normal incidence. This implies that $\theta = 0$ and $\varepsilon_1 = 1$. Upon substitution, we find that

$$R_{xx} = R_{yy} = \frac{-2\frac{\omega}{c}\left(1 - \varepsilon_2\sqrt{1-g^2}\right)}{\Delta}$$

$$R_{xy} = -R_{yx} = -i\frac{2\frac{\omega}{c}\sqrt{\varepsilon_2}\left(\sqrt{1-g} - \sqrt{1+g}\right)}{\Delta} \qquad \text{(A-18)}$$

where,

$$\Delta = -2\frac{\omega}{c}\left(1 + \sqrt{\varepsilon_2}\sqrt{1+g}\right)\left(1 + \sqrt{\varepsilon_2}\sqrt{1-g}\right) .$$

As stated previously, g is typically much smaller than 1 and so we expand out the above terms.

$$R_{xx} = \frac{1 - \sqrt{\varepsilon_2}}{1 + \sqrt{\varepsilon_2}} = -\frac{N-1}{N+1}$$

$$R_{xy} = i\frac{g\sqrt{\varepsilon_2}}{\left(1 + \sqrt{\varepsilon_2}\right)^2} = i\frac{Ng}{(N+1)^2} \qquad \text{(A-19)}$$

If the incident light is initially y-polarized, that is, in the plane of reflection, then,

$$E_x^r = R_{xy} E_y^i \ ,$$

$$E_y^r = R_{yy} E_y^i \quad .$$

The reflection coefficient for light polarized in the plane of reflection is

$$r_{\parallel} = \frac{E_y^r}{E_y^i} = R_{yy} = -\frac{N-1}{N+1} \quad ,$$

which is the Fresnel reflection coefficient for normal incident as can be deduced from (A-17). Thus, to first order in g, the reflectivity is unchanged by a magneto-optic effect.

The out-of-plane component of polarization produced by a magneto-optic effect is shown by the ratio

$$\frac{E_x^r}{E_y^i} = R_{xy} = i\frac{Ng}{(N+1)^2} \quad . \qquad \text{(A-20)}$$

Again, the magnitude of g is typically much less than one so that the magnitude of R_{xy} from Equation (A-20) is also much less than one.

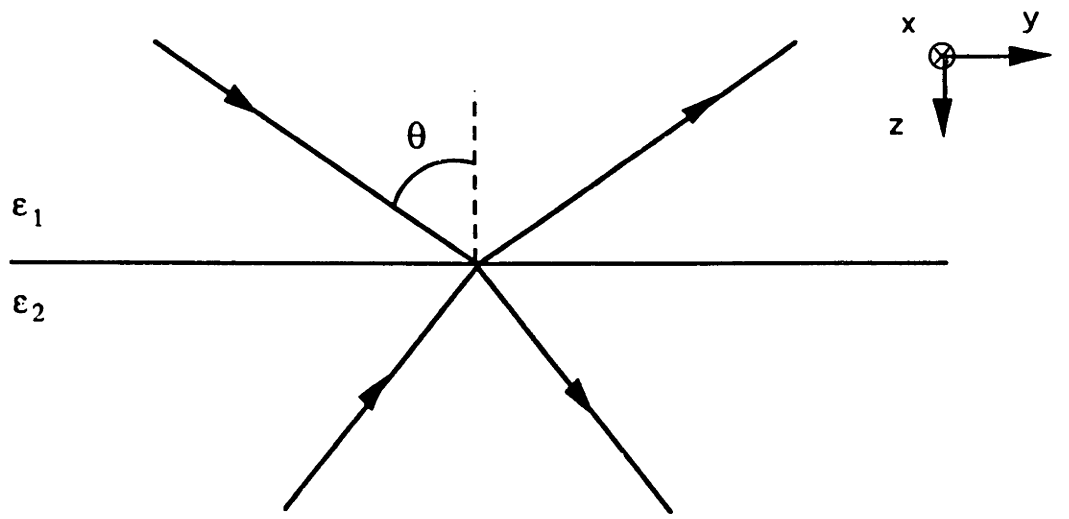

Figure A.1.

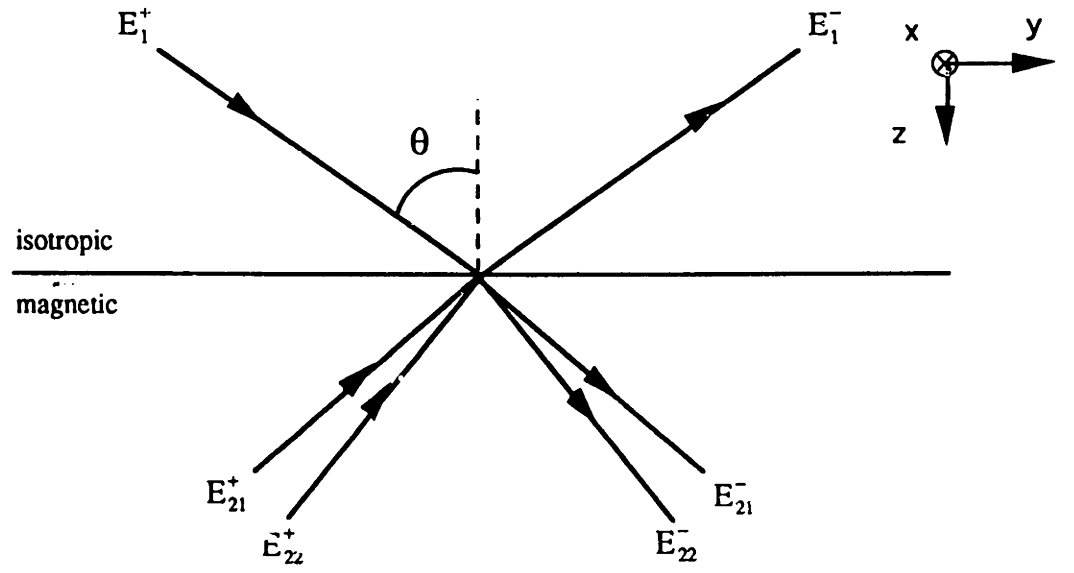

Figure A.2.

B. Ellipsometric Parameters for Isotropic Dielectrics

We wish to relate the experimentally obtained complex ellipticity, $\hat{\rho}$, of an isotropic material to its dielectric constant. We start with the complex Fresnel reflection coefficients of Equation (A-17):

$$r_{\perp} = \frac{N_1 \cos\theta - \sqrt{N_2^2 - N_1^2 \sin^2\theta}}{N_1 \cos\theta + \sqrt{N_2^2 - N_1^2 \sin^2\theta}} \quad ,$$

$$r_{\parallel} = \frac{N_2^2 \cos\theta - N_1 \sqrt{N_2^2 - N_1^2 \sin^2\theta}}{N_2^2 \cos\theta + N_1 \sqrt{N_2^2 - N_1^2 \sin^2\theta}} \quad , \tag{B-1}$$

where N_1 and N_2 are the complex indices of refraction for the ambient media and the isotropic material of interest, respectively, and θ is the angle of incidence. By definition of the ellipticity we find by substitution of Equations (B-1),

$$\hat{\rho} \equiv \rho e^{i\Delta} = \frac{r_{\parallel}}{r_{\perp}} = \frac{N_1 \sin^2\theta - \cos\theta \sqrt{N_2^2 - N_1^2 \sin^2\theta}}{N_1 \sin^2\theta + \cos\theta \sqrt{N_2^2 - N_1^2 \sin^2\theta}} \quad . \tag{B-2}$$

We can solve (B-2) for the complex dielectric constant of material two, which is, by definition, the index of refraction squared,

$$\varepsilon_2 \equiv N_2^2 = N_1^2 \sin^2\theta \left[1 + \left(\frac{1-\hat{\rho}}{1+\hat{\rho}} \right)^2 \tan^2\theta \right] \quad . \tag{B-3}$$

Equation (B-3) relates the ellipticity associated with the material to its dielectric constant. For the photoelastic modulated ellipsometer, however, the ellipsometric variables are not measured, but rather the quantities N, C and S which are defined as[46],

$$N = \frac{1-\rho^2}{1+\rho^2} \quad , \quad C = \frac{2\rho\cos\Delta}{1+\rho^2} \quad , \quad S = \frac{2\rho\sin\Delta}{1+\rho^2} \quad .$$

It would be more convenient if (B-3) were expressed in these quantities. This can be done by noting that

$$\frac{1-\hat{\rho}}{1+\hat{\rho}} = \left(\frac{1-\rho e^{i\Delta}}{1+\rho e^{i\Delta}}\right)\left(\frac{1+\rho e^{-i\Delta}}{1+\rho e^{-i\Delta}}\right) = \frac{1-\rho^2 - 2i\rho\sin\Delta}{1+\rho^2+2\rho\cos\Delta} = \frac{N - iS}{1+C} \quad . \tag{B-4}$$

Upon substitution of (B-4) into (B-3) we get

$$\varepsilon_2 = \varepsilon_1 \sin^2\theta\left[1 + \frac{N^2 - S^2 - i2NS}{(1+C)^2}\tan^2\theta\right] \quad . \tag{B-5}$$

For the case of the ellipsometer described in chapter four, where the ambient material is air and the angle of incidence is 45°, Equation (B-5) simplifies to,

$$\varepsilon_2 = \frac{1}{2}\left[1 + \frac{N^2 - S^2}{(1+C)^2}\right] - i\frac{NS}{(1+C)^2} \quad . \tag{B-6}$$

C. Corrections for PME Component Errors

In this appendix we derive the results of the PME configurations with non-ideal components. The non-idealness of the components is characterized by the three error parameters α, δ_0 and J_0. Also shown is the derivation of the quantities C, N and S from the measurements and the values of the error parameters.

The parameter, α, represents the leakage of the polarizer and analyzer. It is related to the extinction coefficients of these two components by the relation $2\alpha^2 =$ extinction coefficient. In terms of Jones' matrices, the polarizer and analyzer are represented by

$$\mathbf{P} = \mathbf{A} = \begin{bmatrix} 1 & 0 \\ 0 & \alpha \end{bmatrix} \quad , \tag{C-1}$$

where we have assumed that $\alpha \equiv \alpha_P = \alpha_A$.

Two parameters represent the errors from the modulator. The static birefringence of the modulator, δ_0, is the birefringence of the modulator in the absence of an applied electric field. The other parameter is a polarization-dependent transmission ratio, τ_0. In terms of a Jones' matrix

$$\mathbf{M} = \frac{1}{\sqrt{2}} \begin{bmatrix} 1 & 0 \\ 0 & \tau_0 e^{i(\delta_m + \delta_0)} \end{bmatrix} \quad , \tag{C-2}$$

where $\delta_m = A\sin\omega t$. It turns out that assuming $\tau_0 = 1$ is an excellent approximation as is explained in reference 46.

Finally, we include errors arising from $J_0(A) \neq 0$. This error causes the 2f component of the intensity to contribute to the dc intensity. Mathematically, this can be seen from the identity

$$\cos(A\sin\omega t) = J_0(A) + \sum_n 2J_{2n}(A)\cos 2n\omega t \quad . \tag{C-3}$$

Also, there is an error introduced by the compensator not having 90° retardance. This difference, δ_0, gives a Jones' matrix for the compensator of

$$\mathbf{C} = \frac{1}{\sqrt{2}}\begin{bmatrix} 1 & 0 \\ 0 & e^{i\left(\frac{\pi}{2}+\delta_c\right)} \end{bmatrix} \quad . \tag{C-4}$$

We look now at the intensities of the different ellipsometer configurations with the errors for the components included. We assume that α, δ_0, δ_C, $J_0 << 1$ and only save terms to first order in these quantities.

CS Configuration

The CS configuration can be expressed as a multiplication of Jones matrices of the non ideal components. The resultant electric field for this configuration is

$$\begin{aligned} \mathbf{E}_f &= \mathbf{A}\cdot\mathbf{R}(+45°)\cdot\mathbf{S}\cdot\mathbf{M}\cdot\mathbf{R}(-45°)\cdot\mathbf{P}\cdot\mathbf{E}_i \\ &= \frac{1}{2\sqrt{2}}\begin{bmatrix} 1+(1+\alpha)\rho e^{i(\Delta+\delta_m+\delta_0)} \\ -\alpha\left(1+e^{i(\Delta+\delta_m+\delta_0)}\right) \end{bmatrix} \quad . \end{aligned} \tag{C-5}$$

The intensity is proportional to $\mathbf{E}_f^* \cdot \mathbf{E}_f$ and is equal to

$$\begin{aligned} I^{CS} = \frac{1}{8}\big[&\left(1+\rho^2\right)-2\alpha\left(1-\rho^2\right)-2\left(\rho\sin\Delta+\delta_0\rho\cos\Delta\right)\sin\delta_m \\ &+2\left(\rho\cos\Delta-\delta_0\rho\sin\Delta\right)\cos\delta_m\big] \quad . \end{aligned} \tag{C-6}$$

We can separate the intensity into terms of the component frequencies of modulation by using the identities

$$\begin{aligned} \cos(A\sin\omega t) &= J_0(A)+\sum_n 2J_{2n}(A)\cos 2n\omega t \quad , \\ \sin(A\sin\omega t) &= \sum_n 2J_{2n+1}(A)\cos(2n+1)\omega t \quad . \end{aligned} \tag{C-7}$$

The results for the dc intensity and the first two harmonics are

$$\begin{aligned} I_{dc} &= \left(1+\rho^2\right)-2\alpha\left(1-\rho^2\right)+2J_0(A)\left(\rho\cos\Delta-\delta_0\rho\sin\Delta\right) \quad , \\ I_{1f} &= -2\left(\rho\sin\Delta+\delta_0\rho\cos\Delta\right)2J_1(A) \quad , \\ I_{2f} &= +2\left(\rho\cos\Delta-\delta_0\rho\sin\Delta\right)2J_2(A) \quad . \end{aligned} \tag{C-8}$$

This gives the following ratios:

$$R_{1f}^{+} \equiv \frac{I_{1f}}{I_{dc}} = -\frac{S'}{1-2\alpha N + C'J_0(A)} 2J_1(A) \quad ,$$
$$R_{2f}^{+} \equiv \frac{I_{2f}}{I_{dc}} = +\frac{C'}{1-2\alpha N + C'J_0(A)} 2J_2(A) \quad . \tag{C-9}$$

C, N and S have their usual definitions and C' and S' are defined as follows:

$$C' = C - \delta_0 S \quad ,$$
$$S' = S + \delta_0 C \quad . \tag{C-10}$$

We can modify the CS configuration slightly by orienting the analyzer to Ψ_A = -45° instead of to Ψ_A = +45°. This gives us similar results except for changes in sign of the terms. The intensity ratios of this new configuration are

$$R_{1f}^{-} = +\frac{S'}{1-2\alpha N - C'J_0(A)} 2J_1(A) \quad ,$$
$$R_{2f}^{-} = -\frac{C'}{1-2\alpha N - C'J_0(A)} 2J_2(A) \quad . \tag{C-11}$$

We now define the averages $\overline{R}_{1f}^{cs}$ and $\overline{R}_{2f}^{cs}$.

$$\overline{R}_{1f}^{cs} \equiv \tfrac{1}{2}\left[R_{1f}^{+} - R_{1f}^{-}\right] = S'(1+2\alpha N)2J_1(A)$$
$$\overline{R}_{2f}^{cs} \equiv \tfrac{1}{2}\left[R_{2f}^{+} - R_{2f}^{-}\right] = C'(1+2\alpha N)2J_2(A) \quad . \tag{C-12}$$

As can be seen, this averaging eliminates $J_0(A)$ (to first order) from the ratios and serves as one method for eliminating $J_0(A) \neq 0$ errors.

1f Calibration

The resultant electric field of the 1f calibration for the CS configuration is

$$\mathbf{E}_f = \mathbf{S}\cdot\mathbf{R}(-45°)\cdot\mathbf{A}\cdot\mathbf{R}(+45°)\cdot\mathbf{C}\cdot\mathbf{M}\cdot\mathbf{R}(-45°)\cdot\mathbf{P}\cdot\mathbf{E}_i$$

$$= \frac{1}{4\sqrt{2}}\begin{bmatrix} 1+ie^{i(\delta_m+\delta_0+\delta_c)} \\ \rho e^{i\Delta}\left[(1-2\alpha)+(1+2\alpha)ie^{i(\delta_m+\delta_0-\delta_c)}\right]\end{bmatrix} \quad . \tag{C-13}$$

The intensity is

$$I^{cal1f} = \frac{1}{16}(1+\rho^2)\left[1-\sin\delta_m-(\delta_0+\delta_c)\cos\delta_m\right] \quad , \tag{C-14}$$

which gives the ratios,

$$R_{1f}^{cal1f} = -2J_1(A) \quad ,$$

$$R_{2f}^{cal1f} = -(\delta_0+\delta_c)\delta_0 2J_2(A) \quad . \tag{C-15}$$

Here it is not necessary to average out any J_0 errors. Also note that δ_c does not contribute to the 1f channel, and so, the PME is not very sensitive to the compensator's retardance.

2f Calibration

The 2f calibration is primarily affected by J_0 errors. The resultant electric field for this configuration is

$$\mathbf{E}_f = \mathbf{S}\cdot\mathbf{R}(-45°)\cdot\mathbf{A}\cdot\mathbf{R}(+45°)\cdot\mathbf{M}\cdot\mathbf{R}(-45°)\cdot\mathbf{P}\cdot\mathbf{E}_i$$

$$= \frac{1}{4}\begin{bmatrix} \left(1+e^{i(\delta_m+\delta_0)}\right) \\ \rho e^{i\Delta}\left[(1-2\alpha)+(1+2\alpha)e^{i(\delta_m+\delta_0)}\right]\end{bmatrix} \quad . \tag{C-16}$$

The intensity is

$$I^{cal2f} = \frac{1}{8}(1+\rho^2)\left[1-\delta_0\sin\delta_m+\cos\delta_m\right] \quad , \tag{C-17}$$

giving the ratios

$$R_{1f}^{cal2f} = -\delta_0 \frac{2J_1(A)}{1+J_0(A)} \quad ,$$

$$R_{2f}^{cal2f} = +\frac{2J_2(A)}{1+J_0(A)} \quad . \tag{C-18}$$

Again, we can orient the analyzer at $\Psi_A = -45°$ to obtain a slightly different set of ratios.

$$R_{1f}^{cal2f-} = +\delta_0 \frac{2J_1(A)}{1-J_0(A)} \quad ,$$

$$R_{2f}^{cal2f-} = -\frac{2J_2(A)}{1-J_0(A)} \quad . \tag{C-19}$$

We define the averages $\overline{R}_{1f}^{cal2f}$ and $\overline{R}_{2f}^{cal2f}$.

$$\overline{R}_{1f}^{cal2f} \equiv \tfrac{1}{2}\left[R_{1f}^{+} - R_{1f}^{-}\right] = -\delta_0 2J_1(A) \quad ,$$

$$\overline{R}_{2f}^{cal2f} \equiv \tfrac{1}{2}\left[R_{2f}^{+} - R_{2f}^{-}\right] = 2J_2(A) \quad . \tag{C-20}$$

Again, this averaging eliminates errors from $J_0(A) \neq 0$.

N Configuration

The final electric field for the N configuration is

$$\mathbf{E}_f = \mathbf{S}\cdot\mathbf{R}(-45°)\cdot\mathbf{M}\cdot\mathbf{R}(+45°)\cdot\mathbf{P}\cdot\mathbf{E}_i \tag{C-21}$$

$$= \frac{1}{\sqrt{2}}\begin{bmatrix} 1+e^{i(\delta_m+\delta_0)} + \alpha\left(1-e^{i(\delta_m+\delta_0)}\right) \\ \rho e^{i\Delta}\left[\left(1-e^{i(\delta_m+\delta_0)}\right)+\alpha\left(1+e^{i(\delta_m+\delta_0)}\right)\right] \end{bmatrix} \quad .$$

The intensity is

$$I^{N} = \frac{1}{4}\left[\left(1+\rho^2\right) - \delta_0\left(1-\rho^2\right)\sin\delta_m + \left(1-\rho^2\right)\cos\delta_m\right] \quad , \tag{C-22}$$

yielding the ratios

$$R_{1f}^{N} = -\delta_0 \frac{N}{1+NJ_0(A)} 2J_1(A) \quad ,$$

$$R_{2f}^{N} = +\frac{N}{1+NJ_0(A)} 2J_2(A) \quad . \tag{C-23}$$

It would seem that we could average the results of this configuration with that of the configuration with the modulator oriented at Ψ_M = -45°. It turns out, however, that this configuration gives the same results as those for Ψ_M = +45°.

2f Calibration

The final electric field for the 2f calibration of the N configuration is

$$\mathbf{E}_f = \mathbf{S}\cdot\mathbf{A}\cdot\mathbf{R}(-45°)\cdot\mathbf{M}\cdot\mathbf{R}(+45°)\cdot\mathbf{P}\cdot\mathbf{E}_i \tag{C-24}$$

$$= \frac{1}{2\sqrt{2}}\begin{bmatrix} 1+e^{i(\delta_m+\delta_0)} + \alpha\left(1-e^{i(\delta_m+\delta_0)}\right) \\ \alpha\rho e^{i\Delta}\left(1-e^{i(\delta_m+\delta_0)}\right) \end{bmatrix} .$$

The intensity is

$$I^{cal2f} = \frac{1}{4}\left(1-\delta_0\sin\delta_m + \cos\delta_m\right) \quad , \tag{C-25}$$

leading to the ratios,

$$R_{1f}^{cal2f} = -\delta_0 \frac{1}{1+J_0(A)} 2J_1(A) \quad ,$$

$$R_{2f}^{cal2f} = +\frac{1}{1+J_0(A)} 2J_2(A) \quad . \tag{C-26}$$

As in the previous configuration, orienting the modulator to $\Psi_M = -45°$ gives the same results as those for $\Psi_M = +45°$.

Solving for C, N and S

The first step in solving for the quantities C, N and S is to measure the error parameters α, δ_0 and J_0.

The quantity α, as said before, is related to the extinction coefficient of the polarizers by

$$\text{extinction} = \frac{I_\perp}{I_\parallel} = 2\alpha^2 \quad , \tag{C-27}$$

for unpolarized incident light where parallel means parallel to the optical axis of the polarizer. Thus, α can be found by finding the extinction coefficient of the polarizers.

$J_0(A)$ can be found from the two 2f calibrations of the CS configuration by the equation

$$J_0(A) = -\frac{R_{2f}^{cal2f+} + R_{2f}^{cal2f+}}{R_{2f}^{cal2f+} - R_{2f}^{cal2f+}} \quad . \tag{C-28}$$

The static birefringence of the modulator, δ_0, can be found in a few different ways. Two such ways are the following:

$$\delta_0 = \frac{\overline{R}_{1f}^{cal2f}}{R_{1f}^{cal1f}} = \frac{R_{2f}^{cal1f}}{\overline{R}_{2f}^{cal2f}} \quad . \tag{C-29}$$

With the quantities α, δ_0 and J_0 known, we can now determine C, N and S from the measured values. The measured values C_{exp}, N_{exp} and S_{exp} are defined as follows:

$$\begin{aligned} C_{exp} &\equiv \frac{\overline{R}_{2f}^{cs}}{\overline{R}_{2f}^{cal2f}} = C'(1+2\alpha N) \quad , \\ N_{exp} &\equiv \frac{R_{2f}^{N}}{R_{2f}^{cal2f}} = N\left(1+(1-N)J_0(A)\right) \quad , \\ S_{exp} &\equiv \frac{R_{1f}^{cs}}{R_{1f}^{cal1f}} = S'(1+2\alpha N) \quad . \end{aligned} \tag{C-30}$$

We can invert these equations to find the desired quantities keeping only terms to first order in α, δ_0 and J_0.

$$
\begin{aligned}
N &= N_{exp}\left[1-\left(1-N_{exp}\right)J_0(A)\right] \quad , \\
C' &= C_{exp}\frac{1}{1+2\alpha N} \quad , \\
S' &= S_{exp}\frac{1}{1+2\alpha N} \quad ,
\end{aligned}
\tag{C-31}
$$

where

$$
\begin{aligned}
C &= C' + \delta_0 S' \quad , \\
S &= S' - \delta_0 C' \quad ,
\end{aligned}
$$

from the definitions of C' and S'.

D. PME Orientation Errors

We would like to determine the measurement errors of the optical constants measured by the ellipsometer. The quantities of interest are the complex dielectric constant $\varepsilon_0 = \varepsilon_0' + i\varepsilon_0''$, and the complex index of refraction $N = n + ik$. To determine the errors of these quantities, we start with the equations from Chapter 4.

$$\varepsilon_0'(N,C,S,\theta_i) = \sin^2\theta_i\left[1+\tan^2\theta_i\frac{N^2-S^2}{(1+C)^2}\right] \quad , \tag{D-1a}$$

$$\varepsilon_0''(N,C,S,\theta_i) = 2\sin^2\theta_i\tan^2\theta_i\frac{NS}{(1+C)^2} \quad , \tag{D-1b}$$

and

$$n(\hat{\varepsilon}_0) = \left[\tfrac{1}{2}\left(\varepsilon_0'^2+\varepsilon_0''^2\right)^{\frac{1}{2}}+\varepsilon_0'\right]^{\frac{1}{2}} \quad , \tag{D-1c}$$

$$k(\hat{\varepsilon}_0) = \left[\tfrac{1}{2}\left(\varepsilon_0'^2+\varepsilon_0''^2\right)^{\frac{1}{2}}-\varepsilon_0'\right]^{\frac{1}{2}} \quad . \tag{D-1d}$$

The uncertainty of ε_0' can be found by finding the partial derivatives of ε_0' with respects to the measured quantities[51];

$$d\varepsilon_0'(N,C,S,\theta_i) = \frac{\partial\varepsilon_0'}{\partial N}dN+\frac{\partial\varepsilon_0'}{\partial C}dC+\frac{\partial\varepsilon_0'}{\partial S}dS+\frac{\partial\varepsilon_0'}{\partial\theta_i}d\theta_i \quad . \tag{D-2}$$

The same approach can be applied to ε_0'', n and k. The determination of the partial derivatives in (D-2) is straightforward from (D-1). The uncertainties of the incident angle, $d\theta_i$, is determined by the experimental setup. The uncertainties in N, C and S (dN, dC and dS), however, are a little more involved.

The uncertainties in N, C and S arise from the misorientation of the optical components plus any statistical errors from measurement. To be rigorous, dN, dC and dS should be derived first by finding analytical forms of N, S and C and then using the partial derivative method used to determine (D-2). The partial derivatives are taken with

respects to the angle of orientation of the components. The author has tried this and found it to be cumbersome.

Another approach is to use modified Jones' matrices developed by O' Handley[49]. These matrices break up the modulated and unmodulated signal of each polarization, and in so doing, they lend themselves for use in numerical calculations. Bermudez[50] has taken advantage of this fact to produce a computer program that estimates the systematic errors of a measurement.

Here, however, we use a lazy man's approach to estimating the orientation errors of N, C and S. We assume that all orientation errors of the optical components are small angles. We then find the intensity of the measured signal to first order in the angular errors and compare it to the case of no errors. A useful Jones' matrix for doing this is the rotation matrix for small rotations:

$$\mathbf{R}(a << 1) = \begin{bmatrix} \cos a & \sin a \\ -\sin a & \cos a \end{bmatrix} \cong \begin{bmatrix} 1 & a \\ -a & 1 \end{bmatrix} \quad , \tag{D-3}$$

where we have expanded to first order in a.

The first quantity we want to look at is the 2f calibration for the CS measurement. We first calculate the resultant electric field of the configuration. Using a_P, a_M and a_A to represent the orientation errors of the polarizer, modulator and analyzer respectively, we get

$$\begin{aligned} \mathbf{E}_f = \mathbf{S} \cdot \mathbf{R}(-45°) \cdot \mathbf{R}(-a_A) \cdot \mathbf{A} \cdot \mathbf{R}(a_A) \cdot \mathbf{R}(45°) \cdot \mathbf{R}(-a_M) \cdot \mathbf{M} \\ \cdot \mathbf{R}(a_M) \cdot \mathbf{R}(-45°) \cdot \mathbf{R}(-a_P) \cdot \mathbf{P} \cdot \mathbf{E}_i \quad . \end{aligned} \tag{D-4}$$

The intensity of this electric field to first order in the errors is

$$I^{cal2f} = \frac{1}{8}\left[\left(1+\rho^2\right) - 2a_A\left(1-\rho^2\right)\right]\left[1+\cos\delta_m\right] \quad . \tag{D-5}$$

Thus,

$$R_{2f}^{+cal2f} = 2J_2(A) \quad . \tag{D-6}$$

We see that there are no errors in R_{2f}^{+cal2f} to first order. This is also true for the 2f calibration with the analyzer oriented at -45°:

$$R_{2f}^{cal2f} = -2J_2(A) \quad . \tag{D-7}$$

For the 1f calibration of the CS measurement, we introduce errors from the orientation of the compensator. The intensity of this configuration, retaining errors to first order, is

$$I^{cal1f} = \frac{1}{16}\left[\left(1+\rho^2\right) - 2a_A\left(1-\rho^2\right)\right]\left[1-\sin\delta_m\right] \quad , \tag{D-8}$$

yielding

$$R_{1f}^{cal1f} = -2J_1(A) \quad . \tag{D-9}$$

We see that the 1f calibration also has no first order orientation errors.

First order orientation errors *do* appear in the measurement of C and S. In the CS configuration with the analyzer at +45°, the intensity is

$$\begin{aligned} I^{CS} = \frac{1}{8}\Big[&\left(1+\rho^2\right) - 2\left(1-\rho^2\right)\left(a_P - a_M + a_A\right) - 2\rho\sin\Delta\sin\delta_m \\ &+\left[2\rho\cos\Delta - 2a_M\left(1-\rho^2\right)\right]\cos\delta_m\Big] \quad . \end{aligned} \tag{D-10}$$

This gives us the ratios, to first order in the errors, of

$$R_{1f}^{CS+} = -S\left[1+2N\left(a_A - a_M + a_P\right)\right]2J_1(A) \quad , \tag{D-11}$$

$$R_{2f}^{CS+} = +\left[C - 2a_M N + 2NC\left(a_A - a_M + a_P\right)\right]2J_2(A) \quad . \tag{D-12}$$

And for the CS measurement with the analyzer oriented at -45° we get the ratios,

$$R_{1f}^{CS-} = +S\left[1-2N\left(a_A + a_M - a_P\right)\right]2J_1(A) \quad , \tag{D-13}$$

$$R_{2f}^{CS-} = -\left[C + 2a_M N - 2NC\left(a_A + a_M - a_P\right)\right]2J_2(A) \quad . \tag{D-14}$$

We are now in the position to calculate the systematic errors in C and S. We start with the equations for C and S,

$$S = \frac{\overline{R}_{1f}^{cs}}{R_{1f}^{call\,f}} = \frac{\left|R_{1f}^{cs+}\right| + \left|R_{1f}^{cs-}\right|}{2R_{1f}^{call\,f}} \quad , \tag{D-15}$$

and

$$C = \frac{\overline{R}_{2f}^{cs}}{\overline{R}_{2f}^{cal2f}} = \frac{\left|R_{2f}^{cs+}\right| + \left|R_{2f}^{cs-}\right|}{2\overline{R}_{1f}^{cal2f}} \quad . \tag{D-16}$$

Since the calibration ratios do not contain errors, the systematic errors of C and S come from the numerators of (3). For the S measurement,

$$S_{exp} = S\left[1 + N\left(a_A^+ - a_M^+ + a_P^+\right) - N\left(a_A^- + a_M^- - a_P^-\right)\right] \quad . \tag{D-17}$$

As a worst case, we assume all errors are of maximum absolute value and have signs giving the largest possible error:

$$S_{exp} = S\left[1 \pm 2N(a_A + a_M + a_P)\right] \quad , \tag{D-18}$$

where the a's are all considered positive. This gives us an uncertainty in S of

$$\frac{dS}{S} = 2N(a_A + a_M + a_P) \quad . \tag{D-19}$$

Similarly, the uncertainty in C is

$$\frac{dC}{C} = 2N(a_A + a_M + a_P) \quad . \tag{D-20}$$

For the measurement of N and the 2f calibration, there are no first order orientation errors:

$$R_{2f}^{N} = N2J_2(A) \quad ,$$
$$R_{2f}^{cal2f} = 2J_2(A) \quad . \tag{D-21}$$

Thus,

$$dN = 0 \quad . \tag{D-22}$$

This discussion is only applicable for treating the systematic errors of measurements. There will of course be statistical errors associated with N.

Now that we have dN, dC and dS, we can plug these values into (D-2) and similar equations for ε_0'', n and k. The results are summarized here.

$$\begin{aligned}
d\varepsilon_0' &= \frac{1}{(1+C)^2}\left[|NdN| + |SdS| + \left|\frac{N^2 - S^2}{(1+C)}dC\right| + \left|\left[(1+C)^2 + 3\left(N^2 - S^2\right)\right]d\theta_i\right|\right] \quad , \\
d\varepsilon_0'' &= \varepsilon_0''\left[\left|\frac{dN}{N}\right| + \left|\frac{dS}{S}\right| + \left|\frac{2C}{1+C}\frac{dC}{C}\right| + |6d\theta_i|\right] \quad , \\
dn &= \frac{1}{4n\sqrt{\varepsilon_0'^2 + \varepsilon_0''^2}}\left[\left|\varepsilon_0' d\varepsilon_0'\right| + \left|\varepsilon_0'' d\varepsilon_0''\right|\right] + \frac{1}{2n}\left|d\varepsilon_0'\right| \quad , \\
dk &= \frac{1}{4k\sqrt{\varepsilon_0'^2 + \varepsilon_0''^2}}\left[\left|\left[\varepsilon_0' - 2\sqrt{\varepsilon_0'^2 + \varepsilon_0''^2}\right]d\varepsilon_0'\right| + \left|\varepsilon_0'' d\varepsilon_0''\right|\right] \quad ,
\end{aligned} \tag{D-23}$$

where

$$\begin{aligned}
dN &= dN|_{\text{statistical}} \quad , \\
dC &= 2NC(a_A + a_M + a_P) + dC|_{\text{statistical}} \quad , \\
dS &= 2NS(a_A + a_M + a_P) + dS|_{\text{statistical}} \quad .
\end{aligned}$$

E. Corrections for MOS Component Errors

This appendix deals with the errors that occur in the magneto-optic spectrometer (MOS) due to non-ideal components. The errors are characterized by the error parameters α, δ_0 and J_0 not being equal to zero. The origins of these parameters are discussed in appendix C and so the results are just listed here.

The leakage of unwanted polarization from a polarizer is characterized by α. The Jones' matrix for the polarizer and analyzer are

$$\mathbf{P} = \mathbf{A} = \begin{bmatrix} 1 & 0 \\ 0 & \alpha \end{bmatrix} \quad . \tag{E-1}$$

The static birefringence of the photoelastic modulator, δ_0, appears as an offset in the retardation of the modulator. The Jones' matrix for the modulator becomes

$$\mathbf{M} = \frac{1}{\sqrt{2}} \begin{bmatrix} 1 & 0 \\ 0 & e^{i(\delta_m + \delta_0)} \end{bmatrix} \quad , \tag{E-2}$$

where $\delta_m = A\sin\omega t$. Finally, $J_0(A)$ mixes the 2f signal with the dc signal according to the identity

$$\cos(A\sin\omega t) = J_0(A) + \sum_n 2J_{2n}(A)\cos 2n\omega t \quad . \tag{E-3}$$

As in the previous appendix, we assume all three parameters, α, δ_0 and J_0, to be much less than one.

Measurement

The configuration for the magneto-optic measurement yields an electric field according to the matrix equation

$$\mathbf{E}_i = \mathbf{A} \cdot \mathbf{S} \cdot \mathbf{M} \cdot \mathbf{R}(-45°) \cdot \mathbf{P} \cdot \mathbf{E}_i \quad , \tag{E-4}$$

where S is the magneto-optic sample matrix given in (5-1). We do not list the result here because it's yucky. The intensity of this electric field to first order in the error parameters is

$$I^{MO} = \frac{1}{4}(1 - 2\alpha\cos 2\varepsilon_K \cos 2\theta_K) + \frac{1}{4}(\sin 2\varepsilon_K + \delta_0 \cos 2\varepsilon_K \sin 2\theta_K)\sin\delta_m + \frac{1}{4}(\delta_0 \sin 2\varepsilon_K - \sin 2\theta_K \cos 2\varepsilon_K)\cos\delta_m \quad . \tag{E-5}$$

We are fortunate in the case of the MOS in that ε_K and θ_K are much less than one. Thus, we can further expand the intensity to first order in ε_K and θ_K and the result is

$$I^{MO} = \frac{1}{4}\left[(1 - 2\alpha) + (2\varepsilon_K + \delta_0 2\theta_K)\sin\delta_m - (2\theta_K - \delta_0 2\varepsilon_K)\cos\delta_m\right] \quad . \tag{E-6}$$

The frequency components of the intensity are found as they were in the previous appendix using the identities in (4-12). The dc intensity and the first two harmonics are

$$\begin{aligned} I^{dc} &= \frac{1}{4}\left[(1 - 2\alpha) - J_0(A)(2\theta_K - \delta_0 2\varepsilon)\right] \cong \frac{1}{4}(1 - 2\alpha) \quad , \\ I^{1f} &= \frac{1}{4}(2\varepsilon_K + \delta_0 2\theta_K)2J_1(A) \quad , \\ I^{2f} &= -\frac{1}{4}(2\theta_K - \delta_0 2\varepsilon_K)2J_1(A) \quad . \end{aligned} \tag{E-7}$$

Note that the second term in I_{dc} has been dropped since $J_0(A)$ times $2\theta_K$ and $2\varepsilon_K$ is a second order term. This is fortuitous in that it eliminates J_0 from our measurement. The intensity ratios are

$$\begin{aligned} R_{1f}^{MO} &= +2\frac{\varepsilon_K + \delta_0\theta_K}{1 - 2\alpha}2J_1(A) \quad , \\ R_{2f}^{MO} &= -2\frac{\theta_K - \delta_0\varepsilon_K}{1 - 2\alpha}2J_2(A) \quad . \end{aligned} \tag{E-8}$$

We could modify the above configuration by orienting the polarizer to $\psi_P = -45°$. This would give us the following ratios:

$$R_{1f}^{-} = -2\frac{\varepsilon_K + \delta_0\theta_K}{1+2\alpha}2J_1(A) \quad ,$$
$$R_{2f}^{-} = +2\frac{\theta_K - \delta_0\varepsilon_K}{1+2\alpha}2J_2(A) \quad . \qquad \text{(E-10)}$$

We could average these configurations as we have done previously. This would lead to the elimination of α to first order. However, α is a *fixed* parameter in the sense that it is a characteristic of the analyzer and polarizer and does not change from one experiment or scan to another. Thus, we need only measure α once and need not take an extra spectrum to eliminate it.

Calibrations

The intensity ratios for the 1f and 2f calibrations for the magneto-optic spectrometer are the same as those for the CS configuration of the PME. For the 1f calibration,

$$R_{1f} = -2J_1(A) \quad ,$$
$$R_{2f} = -\delta_0 2J_2(A) \quad . \qquad \text{(E-11)}$$

And, for the 2f calibration,

$$\overline{R}_{1f}^{cal2f} \equiv \tfrac{1}{2}\left[R_{1f}^{+} - R_{1f}^{-}\right] = \delta_0 2J_1(A) \quad ,$$
$$\overline{R}_{2f}^{cal2f} \equiv \tfrac{1}{2}\left[R_{2f}^{+} - R_{2f}^{-}\right] = 2J_2(A) \quad . \qquad \text{(E-12)}$$

Solving for ε_K and θ_K

The first step in determining ε_K and θ_K is to determine the error parameters α and δ_0 (J_0 is not a factor here). As shown in the previous appendix, α can be found from measuring the extinction coefficient of the polarizer and analyzer. The static birefringence, δ_0, can be found in a few different ways, two of which are

$$\delta_0 = \frac{\overline{R}_{1f}^{cal2f}}{R_{1f}^{call f}} = \frac{R_{2f}^{cal2f}}{\overline{R}_{2f}^{cal2f}} \quad . \qquad \text{(E-13)}$$

We can now express ε_K and θ_K in terms of the measured quantities E″ and R″.

$$E'' \equiv \frac{R_{1f}^{MO}}{R_{1f}^{cal1f}} = 2\frac{\varepsilon_K + \delta_0\theta_K}{1-2\alpha} \quad ,$$
$$R'' \equiv -\frac{R_{2f}^{MO}}{R_{2f}^{cal2f}} = 2\frac{\theta_K - \delta_0\varepsilon_K}{1-2\alpha} \quad . \tag{E-14}$$

By inverting these equations, we find ε_K and θ_K.

$$E = 2\varepsilon_K = (1-2\alpha)(E'' - \delta_0 R'') \quad ,$$
$$R = 2\theta_K = (1-2\alpha)(R'' + \delta_0 E'') \quad . \tag{E-15}$$

F. MOS Orientation Errors

We would like to determine the measurement errors of the optical constants measured by the magneto-optic spectrometer. The quantities of interest are the Kerr ellipticity, ε_K, and the Kerr rotation, θ_K. To determine the errors of these quantities, we start with the equations

$$\varepsilon_K = \frac{1}{2}\frac{R_{1f}^{MO}}{R_{1f}^{cal1f}} \quad ,$$
$$\theta_K = \frac{1}{2}\frac{R_{2f}^{MO}}{R_{2f}^{cal2f}} \quad . \qquad \text{(F-1)}$$

As is shown in Appendix D, the 1f and 2f calibration configurations are insensitive to the orientation errors of the components to first order. Thus, the orientation errors of the Kerr ellipticity and rotation come from the measurement configuration of the MOS. We use the small rotation matrix in Appendix D to find the intensity ratios of the measurement configurations.

The electric field for the measurement configuration is

$$\mathbf{E}_f = \mathbf{A}\cdot\mathbf{R}(a_A)\cdot\mathbf{S}_{MO}\cdot\mathbf{R}(-a_M)\cdot\mathbf{M}\cdot\mathbf{R}(a_M)\cdot\mathbf{R}(-45°)\cdot\mathbf{R}(-a_P)\cdot\mathbf{P}\cdot\mathbf{E}_i \quad , \qquad \text{(F-2)}$$

where a_P, a_M and a_A represent the misorientation errors of the polarizer, modulator and analyzer, respectively. The resultant intensity of this electric field to first order in the errors is

$$I^{MO} = \frac{1}{4}\left[1 - 2a_P + 2a_M + 2\varepsilon_K \sin\delta_m - (2\theta_K + 2a_M + 2a_A)\cos\delta_m\right] \quad . \qquad \text{(F-3)}$$

Thus, the intensity ratios to first order are

$$R_{1f}^{MO+} = 2\varepsilon_K(1 + 2a_P - 2a_M)2J_1(A) \quad ,$$
$$R_{2f}^{MO+} = -(2\theta_K + 2a_M + 2a_A)(1 + 2a_P - 2a_M)2J_2(A) \quad . \qquad \text{(F-4)}$$

When we reverse the magnetic field, ε_K and θ_K will change sign, but, the orientation errors will be unaffected:

$$R_{1f}^{MO-} = -2\varepsilon_K(1+2a_P-2a_M)2J_1(A) \quad ,$$
$$R_{2f}^{MO-} = +(2\theta_K-2a_M-2a_A)(1+2a_P-2a_M)2J_2(A) \quad . \tag{F-5}$$

By combining (F-4) and (F-5) as

$$R_{1f}^{MO} = \frac{1}{2}\left[R_{1f}^{MO+} - R_{1f}^{MO+}\right] = 2\varepsilon_K(1+2a_P-2a_M)2J_1(A) \quad ,$$
$$R_{2f}^{MO} = \frac{1}{2}\left[R_{2f}^{MO+} - R_{2f}^{MO+}\right] = -2\theta_K(1+2a_P-2a_M)2J_2(A) \quad , \tag{F-6}$$

we remove the analyzer misorientation as was explained in Chapter 5.

For both the ellipticity and the rotation, the error is the factor $(1+2a_P-2a_M)$. As a worst case, we assume all errors are of maximum absolute value and have signs giving the largest possible error:

$$\frac{d\varepsilon_K}{\varepsilon_K} = \frac{d\theta_K}{\theta_K} = \pm 2(a_P+a_M) \quad . \tag{F-7}$$

G. Determination of Off-diagonal Elements

From the ellipsometer and magneto-optic spectrometer measurements we can obtain the complex dielectric constant, ε_0, and the Kerr rotation and ellipticity, θ_K and ε_K, of a magneto-optic material. From these quantities, we would like to determine the off-diagonal elements of the material's dielectric tensor, ε_1' and ε_1''. Thus, we need to derive expressions for the real and imaginary parts of, ε_1, as a function of the four measured quantities,

$$\begin{aligned} \varepsilon_1' &= f(\varepsilon_0', \varepsilon_0'', \theta_K, \varepsilon_K) \quad , \\ \varepsilon_1'' &= g(\varepsilon_0', \varepsilon_0'', \theta_K, \varepsilon_K) \quad . \end{aligned} \tag{G-1}$$

To start, we make the assumptions that, in our magneto-optic measurements, we reflect light at normal incidence and that the off-diagonal elements of the dielectric tensor, represented by ε_1, are much smaller in magnitude than the diagonal elements,

$$|\varepsilon_1| << |\varepsilon_0| \quad .$$

With these two assumptions, equation (A-20) of Appendix A tells us that linear polarized light polarized in the y-direction of unit strength, will, upon reflection from a magnetic material, become polarized as,

$$\mathbf{E}_{reflected} = \frac{1}{(N+1)^2} \begin{bmatrix} iN \dfrac{\hat{\varepsilon}_1}{\hat{\varepsilon}_0} \\ N^2 - 1 \end{bmatrix} \quad . \tag{G-2}$$

This is an elliptically polarized wave. The orientation and ellipticity of this electric field are the Kerr rotation, θ_K, and Kerr ellipticity, ε_K, of the reflecting material.

One way in which the ellipticity and orientation of the reflected wave can be found is to transform the Jones vector of the electric field from a linear polarization basis to a circular polarization basis. The transformation matrix for transforming from an x-y basis to a left and right circular polarization basis is,

$$\mathbf{F}_{\rightarrow l,r} = \frac{1}{\sqrt{2}} \begin{bmatrix} 1 & i \\ 1 & -i \end{bmatrix} \quad .$$

With the electric field in terms of left and right circular polarized waves, the orientation and ellipticity of the electric field can be found from the following equations:

$$\theta = \frac{1}{2}\left(\mathrm{ph}(\mathbf{E}_l) - \mathrm{ph}(\mathbf{E}_r)\right) \quad ,$$
$$\varepsilon = \mathrm{Arcsin}\left[\frac{|\mathbf{E}_l| - |\mathbf{E}_r|}{\sqrt{2}|\mathbf{E}|}\right] \quad . \tag{G-3}$$

The expressions for θ_K and ε_K can be simplified by using the (valid) approximation that $|\varepsilon_1| << 1$. Assuming this, we can expand the expressions for θ_K and ε_K to first order in ε_1. The results are,

$$\theta = \frac{1}{D}\left[-\varepsilon_1'\left(k^3 + k - 3n^2k\right) + \varepsilon_1''\left(n^3 - n - 3nk^2\right)\right]$$
$$\varepsilon = \frac{1}{D}\left[\varepsilon_1'\left(n^3 - n - 3nk^2\right) + \varepsilon_1''\left(k^3 + k - 3n^2k\right)\right] \quad , \tag{G-4}$$

where,

$$D = \left(k^3 + k - 3n^2k\right)^2 + \left(n^3 - n - 3nk^2\right)^2 \quad .$$

Recall that $\sqrt{\varepsilon_0} = N = n + ik$. Solving these two simultaneous equations for ε_1' and ε_1'', we obtain our desired expressions for the off-diagonal elements of the dielectric tensor.

$$\varepsilon_1' = \varepsilon_K\left(n^3 - 3nk^2 - n\right) - \theta_K\left(k^3 - 3n^2k + k\right) \quad ,$$
$$\varepsilon_1'' = \varepsilon_K\left(k^3 - 3n^2k + k\right) + \theta_K\left(n^3 - 3nk^2 - n\right) \quad . \tag{G-5}$$

H. Alignment Procedures for PME

Alignment Laser

- Set the height of an iris to the height of the monochromator.
- Set height of the He-Ne alignment laser to height of the iris with the iris positioned very close to the laser.
- Set the height of a second iris with the laser beam with the iris positioned very close to the laser.
- With one iris at the beginning of the incident arm of the ellipsometer and the other at the end of the arm, align the laser beam to go through both irises.

Now the laser beam is parallel to the optical table and aligned with the center of the incident arm of the ellipsometer.

Polarizer

- Set the height of the polarizer so that it is centered with the laser beam.
- Set the angle of the polarizer so that the backreflection off the first surface of the polarizer returns to the laser.
- Set the height of the sample so that it is centered with the laser beam.
- Rotate sample to approximately a Brewster's angle of incidence; $\theta_B \approx \text{Arctan}(n)$.
- Orient the polarizer to approximately $\psi_P = 90°$ to polarize the laser beam in the plane of reflection of the sample.
- Adjust the orientation of the polarizer to obtain a minima in the light reflected from the sample.
- Adjust the angle of incidence to obtain a minima in the light reflected from the sample.
- Repeat the last two steps until you obtain the minimum minima.

The polarizer is now oriented to $\psi_P = 90°$. Please make a note of it.

Analyzer

- Set the height of the analyzer so that it is centered with the laser beam.
- Set the angle of the analyzer so that the backreflection off the first surface of the analyzer returns to the laser.
- Orient the polarizer to $\psi_P = 0°$.

- Orient the analyzer to obtain extinction of the light beam.

The analyzer is now oriented to $\psi_A = 90°$. Please make a note of it.

Modulator

- Set the height of the modulator so that it is centered with the laser beam.
- Set the angle of the modulator so that the backreflection off the first surface of the modulator returns to the laser.
- Orient the polarizer to $\psi_P = 0°$.
- Orient the analyzer to $\psi_P = 90°$.
- With the modulator on, orient the modulator to obtain extinction of the light beam. It will not matter at what retardation the modulator is set.

The modulator is now oriented to $\psi_M = 0°$. Please make a note of it.

Compensator

- Set the height of the compensator so that it is centered with the laser beam.
- Set the angle of the compensator so that the backreflection off the first surface of the compensator returns to the laser.
- Orient the polarizer to $\psi_P = 0°$.
- Orient the analyzer to $\psi_P = 90°$.
- Orient the compensator to obtain extinction of the light beam. It will not matter at what retardation the compensator is set.

The compensator is now oriented to $\psi_C = 0°$. Please make a note of it.

Sample

- Set the height of the sample so that it is centered with the laser beam.
- Set the angle of the sample so that the backreflection off the first surface of the sample returns to the laser.
- Mount the two irises at the beginning and end of the reflection arm of the ellipsometer with the same heights as before.
- Rotate the angle of incidence if the sample to send the laser beam through the two irises.

Now the laser beam is in a plane parallel to the optical table and aligned with the center of the two arms of the ellipsometer. Also, the angle of incidence on the sample is now 45°.

Lenses

Align the three lenses in the following manner an in the following order: Photodiode lens, recollimating lens, focusing lens.

- Mount lens with curved surface towards the laser beam. This makes alignment of the lenses much easier.
- Adjust height and angle of lens so that backreflection off the curved surface returns to the laser.

Irises

- Insert an iris between the analyzer position on the reflection arm and the photodiode lens.
- Insert the other iris before the polarizer.

Monochromator

- Remove laser beam.
- Reflect light from monochromator off aligning mirror so that it passes through both irises.

Endnotes

1 M. J. Freiser, IEEE Transactions on Magnetics **MAG-4**, 152 (1968).

2 W. Voigt, *Magneto- und Elektro-optik* (B. G. Teubner, Leipzig, 1908).

3 F. A. Jenkins and H. E. White, *Fundamentals of Optics 4d* (McGraw-Hill, New York, 1976), p.474.

4 C. J. Ballhausen, *Introduction to Ligand Field Theory* (McGraw-Hill, New York, 1962), p.211.

5 F. Bertaut and F. Forrat, Compt. Rend. **242**, 382 (1956).

6 S. Geller and M. A. Gilleo, Acta Crystal. **10**, 239 (1957).

7 J.F. Dillon, Jr., J. Phys. Radium **20**, 374 (1959).

8 F. J. Kahn, P. S. Pershan and J. P. Remeika, Phys. Rev. **186**, 891 (1969).

9 M. V. Chetkin, I. G. Morozova and G. K. Tyutneva, Soviet Physics - Solid State **9**, 2852 (1968).

10 C. Buhrer, J. Appl. Phys. **40**, 4500 (1969).

11 H. Matthews, S. Singh and R. C. LeCraw, Appl. Phys. Lett. **7**, 165 (1965).

12 S. Wittekoek and D. E. Lacklison, Physical Review Lett. **28**, 740 (1972).

13 For a review article, see P. Hansen and J. -P. Krumme, Thin Solid Films **114**, 69 (1984).

14 S. Wittekoek, T. J. A. Pompa, J. M. Robertson and P. F. Bongers, Phys. Rev. B **12**, 2777 (1975).

15 H. Takeuchi, Japan Journal of Applied Physics **14**, 1903 (1975).

16 S. Wittekoek and T. J. A. Pompa, J. Appl. Phys. **44**, 5560 (1973).

17 A review of these theories and the research conducted in this field upto 1976 is given in G. B. Scott and D. E. Lacklison, IEEE Transactions on Magnetics **MAG-12**, 292 (1976).

18 D. E. Lacklison, H. I. Ralph and G. B. Scott, Solid State Comm. **10**, 269 (1972).

19 D. E. Lacklison, G. B. Scott and J.L. Page, Solid State Comm. **14**, 861 (1974).

20 G. B. Scott, D. E. Lacklison and J. L. Page, Phys. Rev. B **10**, 971(1974).

21 G. B. Scott, D. E. Lacklison and J. L. Page, J. Phys. C **8**, 519 (1975).

22 S. Geller, H. J. Williams, R. C. Sherwood and G. P. Espinosa, J. Appl. Phys. **35**, 1754 (1964).

23 D. E. Lacklison, G. B. Scott, H. I. Ralph and J. L. Page, IEEE Transactions on Magnetics **MAG-9**, 457 (1973).

24 F. J. A. M. Greidanus and W. B. Zeper, Mat. Res. Soc. Bull. **15**, 31 (1990).

25 A. Paoletti, ed., *Physics of Magnetic Garnets* (North-Holland Publishing Company, Amsterdam, 1978).

26 Gerhard Winkler, *Magnetic Garnets* (Friedr. Vieweg and Sohn, Braunschweig/Weisbaden, 1981).

27 Landolt-Börnstein, "Magnetic and other properties of Oxides and Related Compounds: Garnets and Perovskites", *Numerical Data and Functional Relationships in Science and Technology, New Series, III/12a.* (Springer-Verlag, Berlin, 1978).

28 E. R. Czerlinsky, Phys. Stat. Sol. **34**, 483 (1969).

E. R. Czerlinsky and R. A. MacMillan, Phys. Stat. Sol. **41**, 333 (1970).

29 S. Geller, "Crystal and Static Magnetic Properties of Garnets", *Phys. s of Magnetic Garnets*, ed. A. Paoletti (North-Holland Publishing Company, Amsterda n, 1978) p.1.

30 Elmer E. Anderson, "Molecular Field Model and the Magnetization of YIG", Physical Review **134**, A1581 (1964).

31 Gerald F. Dionne, "Molecular Field Coefficients of Substituted Yttrium Iron Garnets", Journal of Applied Physics **41**, 4874 (1970).

32 G. B. Scott, "The Optical Absorption and Magneto-optical Spectra of $Y_3Fe_5O_{12}$", *Physics of Magnetic Garnets*, ed. A. Paoletti, (North-Holland Publishing Company, Amsterdam, 1978) p.445.

33 D. L. Wood and J. P. Remeika, J. Appl. Phys **38**, 1038 (1967).

34 K. A. Wickersheim and R. A. Lefever, J. Chem. Phys. **36**, 844 (1962).

35 S. H. Wemple, S. L. Blank, J. A. Seman and W. A. Biolsi, Phys. Rev. B **9**, 2134 (1974).

36 Y. Tanabe, S. Sugano, J. Phys.Society of Japan **9**, 753 (1954).

37 J. P. van der Ziel, J. F. Dillon and J. P. Remeika, Proc. 18th Conf. Mag. and Mag. Mat., 254 (1971).

38 G. B. Scott and J. L. Page, Phys. Stat. Solidi. b **79**, 203 (1977).

39 G. B. Scott, D. E. Lacklison and J. L. Page, Physical Review B **12**, 2562 (1975).

40 R. K. Pathria, Statistical Mechanics (Permagon Press, Oxford, 1985).

41 Y. R. Shen, The Principles of Nonlinear Optics, John Wiley and Sons, New York, p. 13 (1984).

42 J. D. Jackson, *Electrodynamics* (John-Wiley, New York, 1986).

43 For a review article on the history of ellipsometry, see A. C. Hall, Surface Science **16**, 1 (1969).

44 James C. Kemp, J. Opt. Soc. Am. **59**, 950 (1969).

45 S. N. Jasperson and Schnatterly, Rev Sci. Instr **40**, 761 (1969).

46 V. M. Bermudez and V. H. Ritz, Applied Optics **17**, 542 (1978).

47 R. C. Jones, J. Opt. Sci. Am. **31**, 488 (1941).

48 R. M. A. Azzam and N. M. Bashara, Ellipsometry and Polarized Light (North-Holland, Amsterdam, 1977).

49 R. C. O'Handley, J. Opt. Soc. Am. **63**, 523 (1973)

50 V. M. Bermudez, Comput. Phys. Commun. **13**, 207 (1977).

51 P. R. Bevington and D. K. Robinson, *Data Reduction and Error Analysis of the Physical Sciences* (McGraw-Hill, New York, 1992).

52 J. -P. Krumme, V. Doorman and C. -P. Klages, Applied Optics **23**, 1184 (1984).

53 Bi: S. Geller, H. J. Williams, G. P. Espinosa, R. C. Sherwood and M. A. Gilleo, Appl. Phys. Lett. **3**, 21 (1963). Al: reference 22. In: G. Winkler and P. Hansen, Phil. Res. Rept. **27**, 151 (1972).

54 Card 18-1472 in the Inorganic Powder Diffraction File, Joint Committee on Powder Diffraction Standards, 1974

55 National Bureau of Standards Certificate for Standard Reference Material 640b, 1987.

56 We have used the older value for the wavelength of the copper $K_{\alpha 1}$ line in order to be consistent with the references 53 from which we find the lattice constants. The most current value is l(CuKa1) = 1.5405981 Å from R. D. Deslattes and A. Hennins, Phys. Rev. Letts **31**, 972 (1973).

57 V. Doorman, J. P. Krumme and C. P. Klages, Appl. Phys. A **34**, 223 (1984).

58 G. F. Dionne and G. A. Allen, J. Appl. Phys. **73**, 6127 (1993).

59 W. Wettling, B. Andlauer, P. Koidl, J. Schneider and W. Tolksdorf, Physica Status Solidi B **59**, 63 (1973).

60 S. Wittekoek, T. J. A. Popma and J. M. Robertson, Proc. 18th Conf. Mag. and Mag. Mat., 944 (1973).

61 P. M. Grant and W. Ruppel, Solid State Communications **5**, 543 (1967).

62 R. Metselaar and P. K. Larsen, Solid State Communications **15**, 291 (1974).

63 G. F. Dionne and G. A. Allen, J. Appl. Phys. **75**, 6372 (1994).

64 A. M. Clogston, Journal de Physique et le Radium **20**, 151 (1959).

65 M. Wolfsberg and L. Helmholtz, J. Chem. Phys. **20**, 837 (1952).

66 H. J. Zeiger and G. W. Pratt, *Magnetic Interactions in Solids* (Clarendon Press, Oxford,1973), p.239.

67 G.J. Sprokel, Applied Optics **23**, 3983 (1984).

THE END ?